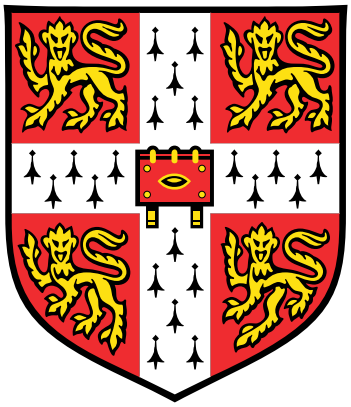

Modelling of colloidal dynamics in complex soft matter systems

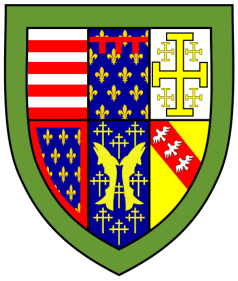

Luca Banetta

Supervisor: Prof. Alessio Zaccone

Co-supervisor: Prof. Markus Kraft

Department of Chemical Engineering & Biotechnology
University of Cambridge

This dissertation is submitted for the degree of
Doctor of Philosophy

Queens' College August 2020

This work is entirely dedicated to my family and my closest friends which always support me in every decision I take and allow me to become the person I am today.

Ad maiora!

Declaration

I hereby declare that except where specific reference is made to the work of others, the contents of this dissertation are original and have not been submitted in whole or in part for consideration for any other degree or qualification in this, or any other university. This dissertation is my own work and contains nothing which is the outcome of work done in collaboration with others, except as specified in the text and acknowledgements. This dissertation contains fewer than 65,000 words including appendices, footnotes, tables and equations and has fewer than 150 figures.

The thesis contains work that has been published:

1. L. Banetta, G. Storti, G. Hoggard, G. Simpson, A. Zaccone, *Predictive model of polymer reaction kinetics and coagulation behavior in seeded emulsion co- and ter-polymerizations*, Polymer Chemistry, https://doi.org/10.1039/D0PY01138J (2020);

2. L. Banetta, A. Zaccone, *Pair correlation function of charge-stabilized colloidal systems under strongly sheared conditions*, Colloid and Polymer Science **298**, 761-771 (2020);

3. L. Banetta, A. Zaccone, *Radial distribution function of Lennard-Jones fluids under shear flows from intermediate asymptotics*, Physical Review E **99**, 052606 (2019);

4. M. Lu, L. Banetta, L.J. Young, E.J. Smith, G.P. Bates, A. Zaccone, G.S. Kaminski-Schierle, A. Tunnacliffe, C.F. Kaminski, *Live-cell super-resolution microscopy reveals a primary role for diffusion in polyglutamine-driven aggresome assembly*, Journal of Biological Chemistry **294** (1), 257-268 (2019).

Luca Banetta
August 2020

Acknowledgements

The first acknowledgements need to go to Prof. Alessio Zaccone for his consistent and helpful support over the past three and a half years. As a main supervisor his knowledge of soft matter systems helped me a lot even in dealing with the most difficult case scenarios. Next I would also like to mention Prof. Daniele Luca Marchsio at Politecnico di Torino for informing me about this opportunity for the first time which has turned out to be the best all-around experience of my life until now.

At this point it is my pleasure to mention all the collaborators who play a crucial role in developing the works proposed in this thesis. I acknowledge Dr. Gareth Simpson for giving me the chance to work on one of their research projects and all the members of the R&D team at Synthomer (UK) Limited in Stallingborough including Dr. Christopher Davis, Dr. Lawrence Cook, Dr. Daniel Turner and Dr. George Hoggard for their support and availability to carry on the experimental procedures of Part II. Prof. Giuseppe Storti and Prof. Massimo Morbidelli are also acknowledged for all the useful discussions on emulsion polymerization kinetics for the theoretical development of Part II.

Finally, an important mention goes to Dr. Meng Lu, Prof. Clemens Kaminski and the whole Laser Analytics group for all the helpful conversations and support in providing the experimental evidence for the theoretical development of Part III.

I would also like to mention Prof. Markus Kraft to adopt me in the CoMo group and providing me with the logistic support I needed to finish my PhD. Next, of course, I would like to thank all of my friends, since they are not just colleagues, at the Department of Chemical Engineering & Biotechnology who have been a source of motivation and happiness throughout my whole PhD: Eric Bringley, Laura Pascazio, Danilo Russo, Mauro Malizia, Eugenia Biral, Francesco Monni, Maurin Salamanca, Gustavo Leon, Fernando Leon, Joseph Wong, Apoorv Jain, Dushanth Seevaratnam, Kimberly Bowal, SaiDarshan Adloor, Walter Kähm, Eduardo Nolasco, Maria Zacharopolou, Chung Lao, Angiras Meron, Ana Morgado, Luis Alberto Rocha.

Last but definitely not least, I want to show my appreciation to my dear friends Joshua Subel, Douglas Van Niekerk, and all the people from Queens' college because they filled my life

with great experiences who helped me becoming not only a better scientist, but also a better human being; *floreat domus*.

Abstract

This dissertation, divided into three parts and funded by the multinational company Synthomer LTD, is devoted to the modelling of the complex dynamics among colloidal particles in soft matter systems which are influenced by the interplay between Brownian motion, the common denominator among all the projects, and other phenomena such as inter-particle interactions and external fields.

Since the Brownian motion and its interplay with shear flow and physico-chemical interactions has a clear impact on the spatial arrangement, also called microstructure, of a colloidal suspension the first part of the thesis focuses on the proposal of a new theoretical framework which analyses the aforementioned feature of diverse dispersions under strongly sheared conditions by analytically solving the 2-Body Smoluchowski equation. The obtained solution is an extension of already existing theories and it is able to recover previous results for hard-spheres fluids under semi-dilute conditions. The new framework has also unveiled a new rich physical behavior by studying the microstructure of two paradigmatic cases of physically relevant interactions, the attractive Lennard-Jones potential and the Debye-Hückel or Yukawa potential for charge-stabilized particles.

The Brownian motion is also crucial in determining the aggregation behavior of colloidal particles: the mechanism proposed by Smoluchowski to study the collision rate between Brownian particles and a stationary one is used nowadays to describe the entry and exit of radicals during an emulsion polymerization. The second part of the thesis is then dedicated to the development of a mathematical model which, by using the pseudo-homopolymerization approach, describes the kinetics of this polymerization mode. By using the state-of-the-art models for radical entry and desorption the framework has the ultimate goal of predicting crucial kinetic variables such as the monomers conversions and latex composition throughout the process. The model foresees a series of unknown parameters which have been determined by extensive calibration on three different test cases of increasing complexity: a homo-polymerization of *n*-BA, a co-polymerization involving n-BA and methyl methacrylate (MMA) and, finally, a ter-polymerization of *n*-BA with MMA and 2-HydroxyEthyl Methacrylate (2-HEMA); the data for the first two series have been found in the literature, while the data for the ter-polymerization have been provided by Synthomer LTD. The predictive model

has been applied to study between the surfactant surface coverage of the particles as well as the total concentration of counterions in the system in order to rationalize the coagulation behavior during the whole polymerization process.
The third and final part focuses on a biological system: the self assembly of proteins *in vivo*. The work is focused on the growth dynamics of a poly-glutamine agglomerate, named aggresome, in a mammalian cell: through a numerical solution of the advection diffusion equation, the macroscopic equivalent of the Smoluchowski equation, it has been possible to disentangle the relative importance of Brownian diffusion and active directed cellular transport in the growth of the amyloid aggresome inside cells, thus unveiling the dominant role of diffusion over active transport.

Table of contents

List of figures **xvii**

List of tables **xxi**

1 General introduction **1**
1.1 Basics of the theory of Brownian motion 1
1.2 General outline 4
1.2.1 Part I: a new analytic framework to describe the microstructure of complex interacting particles under strongly sheared conditions . . 4
1.2.2 Part II: Predictive modelling of seeded emulsion homo-, co- and ter-polymerization kinetics and analysis of coagulation behavior of colloidal latexes 5
1.2.3 Part III: biological systems 7

I A new analytic framework to describe the microstructure of complex interacting particles under strongly sheared conditions **9**

2 Introduction **11**
2.1 3D formalism of the N-Body Smoluchowski equation 11
2.2 2-Body Smoluchowski equation 16
2.2.1 Hydrodynamic interactions 17
2.3 Literature review 23
2.3.1 Rheological and optical properties 24
2.3.2 Aggregation of colloids 30
2.3.3 Summary 33

3 Mathematical formalism **35**
3.1 Angular integral average 36

3.1.1 Compressing quadrants . . . 38
3.1.2 Extensional quadrants . . . 39
3.2 Singular perturbation methodology . . . 39
3.3 Outer solution . . . 40
3.3.1 Leading order term . . . 41
3.3.2 First order term . . . 42
3.3.3 Final remarks . . . 44
3.4 Inner Solution . . . 44
3.4.1 Dominant balancing . . . 44
3.4.2 Leading order term . . . 48
3.4.3 First order term . . . 48
3.4.4 Integration constants evaluation: asymptotic patching . . . 50
3.5 Summary . . . 52

4 Results, conclusions & future steps 55
4.1 Hard-Spheres model . . . 55
4.1.1 Validation of the theory . . . 56
4.1.2 Effect of the Péclet number . . . 57
4.2 Attractive fluids . . . 60
4.2.1 High Péclet number . . . 61
4.2.2 Intermediate Péclet number (Pe = 10) . . . 62
4.3 Charge stabilized colloids . . . 64
4.3.1 High Péclet numbers . . . 64
4.3.2 Intermediate Péclet number (Pe = 10) . . . 64
4.4 Conclusions . . . 67
4.5 Future steps . . . 67
4.5.1 Strongly sheared conditions . . . 67
4.5.2 Weakly sheared conditions . . . 68

II Predictive modelling of seeded emulsion homo-, co- and ter-polymerization kinetics and analysis of coagulation behavior of colloidal latexes 69

5 Introduction 71
5.1 What is an emulsion polymerization? . . . 71
5.1.1 Batch polymerization . . . 72
5.1.2 Semi-continuous polymerization . . . 74

5.2 Coagulum formation in emulsion polymerization . . . 75
5.2.1 Impact of the surfactant surface coverage . . . 78
5.2.2 Impact of saline content . . . 79
5.2.3 Impact of fluid motion: shear-induced aggregation . . . 81
5.3 Summary . . . 82

6 Description of the kinetic model 85
6.1 Choice of the modelling approach . . . 85
6.2 Description of the evaluation of the kinetic variables . . . 87
6.3 Initialization of the model . . . 88
6.4 Partitioning scheme . . . 89
6.5 Fundamental reactions . . . 90
6.5.1 Initiation . . . 91
6.5.2 Propagation . . . 92
6.5.3 Termination . . . 94
6.5.4 Chain transfer to monomer . . . 95
6.5.5 Backbiting . . . 96
6.6 Kinetic rates . . . 96
6.6.1 Rates in the particle phase . . . 97
6.6.2 Rates in the aqueous phase . . . 101
6.7 Quick recap . . . 101
6.8 Determination of the radical activity . . . 102
6.8.1 Termination rates . . . 103
6.8.2 Exit rates . . . 103
6.8.3 Entry rates . . . 105
6.9 Updates of the kinetic variables . . . 108
6.9.1 Conversions . . . 108
6.9.2 Latex composition . . . 108
6.9.3 Average particle size . . . 109
6.10 Monitoring of the surface coverage . . . 109
6.11 Monitoring of the salt content . . . 111
6.11.1 Strong salts . . . 111
6.11.2 Weak base: Ammonia . . . 112

7 Results, conclusions & future steps 115
7.1 Test cases . . . 115
7.2 Discussion of the evaluation of the kinetic variables . . . 117

7.2.1 *n*-BA homopolymerizations 118
7.2.2 *n*-BA/MMA co-polymerizations 121
7.2.3 *n*-BA/MMA/2-HEMA terpolymerizations 123
7.3 Interplay between surface coverage and salt content on coagulum formation 124
7.4 Conclusions 129
7.5 Future Steps 129
7.5.1 Quantitative prediction of coagulum formation 129
7.5.2 Extension to other polymerization modes 130

III Biological systems 133

8 Study of the *in vivo* growth dynamics of a Poly-glutamine 135
8.1 Introduction 135
8.2 Theoretical framework 136
8.2.1 Morphology of the aggresome 141
8.3 Mathematical methods 142
8.4 Discussion 145

9 Epilogue 147

References 151

Appendix A Supporting information of Part I 165
A.1 Derivation of the Einstein's diffusion equation 165
A.2 Stokes-Einstein-Smoluchowski correlation 166
A.3 Development of the calculations of Section 2.1 167
A.4 Gauge functions used in Sections 3.4.1 167

Appendix B Supporting Information of Part II 169
B.1 Evaluation of the diffusion coefficents of the monomers in water 169
B.2 Impact of the backbiting on the kinetic variables of BA/MMA copolymerizations 170
B.3 Polymerization procedure 171
B.3.1 Materials 171
B.3.2 Polymerization process 171
B.4 Latex characterizations 172
B.4.1 Free monomer evaluation 172

B.4.2 Particle size evaluation 172
B.4.3 Grit analysis 173

List of figures

1.1 An image of the flower of *Clarkia pulchella*. 1
1.2 Case study of the one-dimensional vibrating motion of a single particle. . . 3
1.3 Basic visual description of entry and exit of radicals during an emulsion polymerization. 6

2.1 Chaotic motion of N particles in an arbitrary volume V in the phase space. . 12
2.2 Schematic illustration of a pair of complex interacting Brownian particles interacting subjected to a simple shear flow in Cartesian coordinates. In particular **v** = (0,0,$\dot{\gamma}$y) in which $\dot{\gamma}$ is the shear rate the particles are exposed to and, finally, $\mathbf{F}^{\text{ext}} = \beta\ \nabla_{\mathbf{r}} U(\mathbf{r})$ 17
2.3 A single sphere moving towards a free surface located at the origin of a cylindrical reference frame. 19
2.4 Reference system for a pair of particles under simple shear flow. 21
2.5 Visual representation of the compressing (-) and extensional (+) quadrants of a sheared hard-spheres suspension, where the horizontal arrows represents the directions the external shear is applied. 23

3.1 Block diagram with the fundamental steps for the evaluation of the integration constants within $g_{\text{i}}^{\text{in}}(\tilde{r})$ 50

4.1 Comparison of $\text{g}_s(\tilde{r})$ evaluated from Eq.(4.2) with simulations (symbols) of Hard-Sphere suspensions at Pe = 1000 [25] at different volume fractions. . 56
4.2 Effect of the Péclet number on the trend of $\text{g}_c(\tilde{r})$ for the Hard-Spheres model. 58
4.3 Effect of the Péclet number on the trend of $\text{g}_e(\tilde{r})$ for the Hard-Sphere model. 59
4.4 Example of anisotropic microstructure: pair correlation function g(**r**) in the plane of shear for a suspension of polystyrene spheres in silicone oil in simple shear at $Pe = 3.0\ 10^5$. (adapted from [61]). 60
4.5 Effect of the interaction potential on the microstructure of compressing (left) and extensional (right) quadrants at Pe = 1000. 61

4.6 Average pcf related to the compressing quadrants at Pe = 10 for an hard-sphere suspension (lowest curve) and different values of λ. 62
4.7 Average pcf for extensional quadrants at Pe = 10 for an hard-sphere suspension (lowest curve) and different values of λ. 63
4.8 Effect of the repulsive DH potential on $g_c(\tilde{r})$ at high values of the Péclet number (Pe=1000): a) Compressing regions, b) Extensional regions. 65
4.9 Effect of the repulsive DH potential on $g_c(\tilde{r})$ at low values of the Péclet number (Pe=10). Left: effect of varying the coupling parameter Γ with $\kappa = 2$ fixed; right: effect of varying the Debye parameter with $\Gamma = 50$ kept fixed. . 65
4.10 Effect of the repulsive DH potential on $g_c(\tilde{r})$ at low values of the Péclet number (Pe=10): a) Effect of varying the coupling parameter Γ with $\kappa = 2$ fixed, b) Effect of varying the Debye parameter with $\Gamma = 50$ kept fixed. . . 66

5.1 Different mechanisms of particle formation. 72
5.2 Factors influencing the number of radicals in each particle during Interval II-III. 74
5.3 Major mechanisms to guarantee kinetic stability: steric (left) and electrostatic (right). 77
5.4 Screening effect between two charge stabilized particles 79
5.5 Values of the critical coagulation concentration (ccc) as a function of pH for a latex with the primary particle radius $R_P = 155$nm (adapted from [91]). . 81

6.1 Some of the main features of a latex dispersion which can be tracked by EP modelling; inside the red circle the features this work is focused on are highlighted. 86
6.2 A molecule of persulfate anion frequently used in the formation of radical precursors of an emulsion polymerization. 91
6.3 Reactions determining active chain type scheme for *n*-BA/MMA/2-HEMA ter-polymerization. 98

7.1 Comparison of X^{inst} vs X^{overall} obtained by the model (solid lines) and the respective experimental data (symbols) related to the homo-polymerization of *n*-BA adopting different feeding time. 119
7.2 Concentration of monomer swollen in the particles (left) and average number of radicals (right) for BA 1. 119
7.3 Comparison of X^{inst} vs X^{overall} obtained by the model (solid lines) and the respective experimental data (symbols) related to the homo-polymerization of *n*-BA adopting different amounts of initiator. 120

7.4 Entry rate ρ_I of oligomers per particle (left) and $\tilde{n}$ (right) for test cases BA 3 and BA 5-7. 121
7.5 Comparison of X^{inst} vs X^{overall} obtained from the model and the respective experimental data related to the co-polymerization of *n*-BA/MMA [119]. . . 122
7.6 Fundamental features influencing the co-polymerization test cases: average termination rate in bulk (left) and in the particle phase (right), together with the average number of radicals (bottom). 122
7.7 Evolution of the molar fractions of *n*-butyl acrylate in the different runs introduced in Table 7.3 compared to experimental data [119]. 123
7.8 Temporal trend of the predicted overall conversion during the ter-polymerization compared to experimental data. 124
7.9 Predicted average particle sizes compared to experimental data for all IC; each each trend has been normalized by the size of the respective seeds in order not to disclose sensitive information. 125
7.10 Surface coverage difference between IC 2 and IC 3. 126
7.11 Temporal evolution of the coagulation behavior from the grit analysis: on the left the plot is focused on the timespan of the feed additions, on the right the behavior during the whole polymerization process is shown. 127
7.12 Concentrations of counterions in the aqueous phase as a function of time during the polymerization process. The panel on the right is a zoomed in version of the plot on the left hand side focusing on the late stage of the process. The dashed lines indicate the lower and an upper bounds for the CCC, such that CCC $\approx 0.085/0.09$ [mol/L]. 127
7.13 Visual summary of the balance between the surface coverage and salt content on the energy barrier against aggregation in IC 2 (left) and IC 3 (right) at the end of the polymerization. 128

8.1 Scheme of the aggresome growth with the contemporary presence of vibrating Brownian motion inside the cytosol and active transport on the MTOC; it is possible to see the presence of the HDAC6 (yellow) and the dynein (pink). 137
8.2 One of the possible growing paths of the aggresome which is used to evaluate the parameters in Eq.(8.11) (adapted from [143]); the scale bar represents 1μm 140
8.3 Number of particles inside the growing aggresome N with respect to its dimensionless radius R/R_{P} (adapted by [143]). 142
8.4 Aggregates concentration profile inside the cytosol at the beginning of the process (black), after 4h (red), 8h (blue), 12h (magenta) and 16h (green). . . 144

8.5 Analysis of the contributions of the diffusive motion (dashed line), active transport (dashed-dot line) and their combined contribution (solid line) to the "aggresome" growth coupled with a comparison to experimental data (red dots and linked error bars). 145

B.1 Plots of Instantaneous vs Overall conversion for the co-polymerization test cases considering (solid lines) and neglecting (dashed lines) the presence of tertiary radicals in the reacting scheme. 170

List of tables

3.1 Coefficients appearing in Eq.(3.48) as they appear in the equation from left to right 47

6.1 Saturation values adopted to compute the missing partition coefficients . . . 90
6.2 Convention adopted for the subscripts of every reaction rate constant adopted in this work. 91
6.3 Arrhenius parameters for homo-propagation rates. 93
6.4 Collection of the adopted reactivity ratios. 94
6.5 Arrhenius parameters for the known termination rates. 95
6.6 Arrhenius parameters for the known termination rates. 96
6.7 Diffusion coefficients of the monomers in water. 104
6.8 Input parameters for the evaluation of the critical degree of oligomerization $\bar{z}$. 108
6.9 Input parameters for the absorption of the emulsifiers.. 111
6.10 List of all the initiators and surfactant in the formulation of the industrial test case. 112

7.1 Information about the masses [kg] of the homo-polymerization formulations [121]. 116
7.2 Different test cases for the homo-polymerization of *n*-BA [121]. 116
7.3 Information about the masses [kg] of the co-polymerization formulations [119] 116
7.4 Distinctive information about the co-polymerizations of *n*-BA/MMA. . . . 117
7.5 Nomenclature of the industrial test cases. 117
7.6 Compositions of the delayed additions for the industrial test cases: the percentages are related to the total mass of monomers. 117
7.7 Final values of the adjustable parameters at the end of the calibration. . . . 118

8.1 Input data adopted for the solution of the Cauchy problems. 139
8.2 Time and spatial steps adopted in the numerical frameworks. 144

B.1 Input data for Eq.(B.1). 169
B.2 Volumes of samples and water adopted in the successive dilutions. 173
B.3 Temporal trend of Polydispersity Indexes for IC 1 and IC 3 with time = 0 set as the beginning of the monomers' additions. 173

Chapter 1

General introduction

Throughout this work the reader will encounter a variety of projects which deal with the modelling of colloidal dynamics in complex soft matter systems covering diverse fields across science, going from fluid mechanics to growth of proteinaceous clusters linked to neurodegenerative diseases.
Since all of them share the interplay between the Brownian motion and other eventual phenomena such as inter-particle interactions or the application of external fields, this chapter proposes a brief historical resume of the fundamental theoretical aspects of the Brownian motion followed by a brief outline of the thesis where the links between it and each part of the manuscript will be highlighted.

1.1 Basics of the theory of Brownian motion

Fig. 1.1 An image of the flower of *Clarkia pulchella*.

The Brownian motion takes its name by the botanist Robert Brown [1] who was the first one to observe it in 1828: he described a jiggling movement in water of the pollen of *Clarkia pulchella*, a flowering plant in the Onagraceae family showed in Fig.1.1. Subsequently, the same phenomenon was identified for different types of sub-micron particles, both organic and inorganic, suspended in a liquid phase. At the time Brown could not provide with any explanations for this vibrating behaviour; actually it took almost 80 years to find an answer. On parallel, Adolf Fick [2] published the first theoretical study on diffusion where he correlated the flux of salt between two tanks filled with water with its concentration gradient $\partial C/\partial x$ between them obtaining what it is now called *Fick's first law*:

$$J = -D_0 \frac{\partial C}{\partial x} \tag{1.1}$$

where D_0 is the diffusion coefficient of an isolated particle expressed in area per unit time. Subsequently, combining Eq.(1.1) with the continuity equation he derived what today is known as *Fick's second law*:

$$\frac{\partial C(x,t)}{\partial t} = \frac{\partial}{\partial x}\left(D_0 \frac{\partial C(x,t)}{\partial x}\right). \tag{1.2}$$

Finally, Einstein published a seminal paper in 1905 [3] where he proposed a description of Brownian motion as the result of *collisions between the particles and the molecules constituting the solvent* and he linked the jiggling motion studied by Brown to the macroscopic diffusion analysed by Fick. Hypothesizing that the movement of one particle is not influenced by the others and that its displacement after a certain observation time τ is independent from the previous ones, the motion of the particle is described by the *probability* $Q(\Delta)$ for it to undergo a certain displacement $\Delta \in [-\infty, \infty]$ during τ. Einstein expressed C in a certain point x at $t + \tau$ as the sum over all the possible displacement at time t:

$$C(x, t+\tau) = \int_{-\infty}^{\infty} C(x+\Delta) Q(\Delta) d\Delta \tag{1.3}$$

After some mathematical manipulations proposed in Appendix A Einstein expressed D_0 as a function of the displacements by

$$D_0 = \frac{1}{\tau} \int_{-\infty}^{\infty} \frac{\Delta^2}{2} Q(\Delta) d\Delta \tag{1.4}$$

and he has found out that the temporal evolution of $C(x,t)$ is described by the Eq.(1.2) with constant D_0:

$$\frac{\partial C(x,t)}{\partial t} = D_0 \left[\frac{\partial^2 C}{\partial x^2} \right]. \tag{1.5}$$

Eq.(1.5) can then be adopted to study the 1D motion of a single particle with radius R_P in a fluid with viscosity η proposed in Fig.1.2: $C(x,t)$ can be related to the *probability*

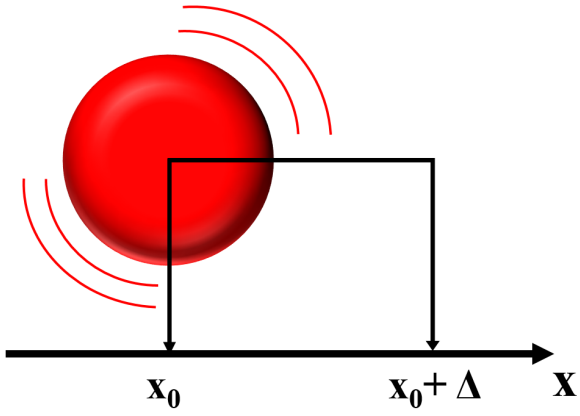

Fig. 1.2 Case study of the one-dimensional vibrating motion of a single particle.

distribution function $g(x,t)$, the probability for the particle to be in a certain position x at time starting from a known position x_0 at t = 0, so Eq.(1.5) becomes:

$$\frac{\partial g(x,t)}{\partial t} = D_0 \left[\frac{\partial^2 g(x,t)}{\partial x^2} \right]. \tag{1.6}$$

The impact of external contribution on a suspension under Brownian dynamics has been proposed first by Smoluchowski [4]: after having derived independently the same results obtained by Einstein he evaluated the impact of different external forces $\mathbf{F}^{\text{ext}}$ on the case study proposed in Fig.1.2. He has found out that their effect can be fully recovered by adding an extra drift term in Eq.(1.5) which depends on $\mathbf{F}^{\text{ext}}$; this new formalism takes the name of *Smoluchowski equation*:

$$\frac{\partial g(x,t)}{\partial t} = \frac{\partial}{\partial x} \left[D_0 \frac{\partial g(x,t)}{\partial x} - Z^{-1} \mathbf{F}^{\text{ext}} g(x,t) \right], \tag{1.7}$$

where $Z = 6\pi\eta R_P$ is the Stokes friction coefficient which can be related to the diffusion constant of a single particle D_0 through the famous *Stokes-Einstein-Smoluchowski* correlation (refer to Appendix A for the rigorous derivation):

$$D_0 = \frac{1}{\beta Z} = \frac{k_B T}{6\pi\eta R_P}, \tag{1.8}$$

where k_B is the Boltzmann constant and T the absolute temperature.

1.2 General outline

The following section is dedicated to a quick introduction on the three different parts the manuscript is divided in.

1.2.1 Part I: a new analytic framework to describe the microstructure of complex interacting particles under strongly sheared conditions

Eq.(1.7), which has been originally used to describe the 1D Brownian motion of a single particle, has then been extended to 3-dimensional spaces and to include ulterior external effects such as the application of shear stresses on the fluid the particles are dispersed into. Moreover, it has been modified so that it could be applied to more and more concentrated dispersions which are classified by the packed fraction ϕ, the total volume of the system actually occupied by particles with number concentration n and equal size R_P defined as:

$$\phi = \frac{4}{3}\pi R_P^3 \, n. \tag{1.9}$$

In the scenario of a many-body problem the probability distribution function becomes written as $g(\mathbf{r}_1, .., \mathbf{r}_N)$ and it is defined as the probability to find a specific particle in a certain position identified by the 3D vector $\mathbf{r}_i$ and it will describe the microstructure, that is the spatial arrangement, of the suspension of interest. This problem arises the necessity of describing the interactions among the particles since the hypothesis of an isolated object is not realistic anymore. They have been evaluated in scenarios where the Reynolds number is sufficiently low, so that possible inertial effects acting on the particles are negligible: the medium which fulfils this condition is said to be under *creeping flow* and the particles under *Stokesian dynamics* [5].
The first part of the thesis proposes a new analytic framework which describes the microstructure of complex interacting particles under strongly sheared conditions. Chapter 2 begins with a detailed description of the formalism behind the extension of the Smoluchowski equation to a system of a number N of particles under purely Brownian dynamics which has then been modified to include the effect of an external shear flow; the section ends with the expression of the equation which considers 2-Body dynamics with a detailed explanation of the considered hydrodynamic interactions. The chapter continues with a brief literature

review on analytic frameworks about the evaluation of the microstructure of sheared suspensions and its application in the analysis of crucial features such as the rheological and optical properties of colloidal suspensions.
In Chapter 3 the mathematical arrangement is described in full detail, meanwhile in Chapter 4 all the results are proposed and discussed: the new theory will be validated by predicting the microstructure of an hard-sphere suspension and compare it with Stokesian dynamics simulations. Afterwards the study will be extended to complex interacting systems, one attractive (12-6 Lennard-Jones potential) and one repulsive (Debye-Hückel potential) highlighting a new wealth of physical phenomena.

1.2.2 Part II: Predictive modelling of seeded emulsion homo-, co- and ter-polymerization kinetics and analysis of coagulation behavior of colloidal latexes

One of the most important applications of the kinetic theory of Brownian motion is the study of aggregation phenomena: everything started from the pioneering work by Smoluchowski who, inspired by Professor R. Zsigmondy and his studies on coagulation of gold solutions, has rigorously derived the binary collision rate between particles in diverse scenarios[6].
His first case study foresaw the presence of a stationary particle whose centre is at the origin of the reference frame: the starting point is the following 3D boundary value problem (BVP)

$$\begin{cases} \dfrac{\partial C}{\partial t} = D_0 \left[\nabla^2 C - \nabla \cdot (\beta \mathbf{F}^{\text{ext}}\, C) \right]; \\ C = 0 \quad r = R; \\ C = C_0 \quad r \to \infty; \\ C = C_0 \quad \forall r > R,\ t = 0. \end{cases} \tag{1.10}$$

Eq.(1.10) has been analytically solved for hard spheres ($\mathbf{F}^{\text{ext}} = \mathbf{0}$) under steady state conditions. Through the hypothesis of radial symmetry it is possible to obtain the following concentration profile C of Brownian particles at a radial distance r from the stationary one

$$C = C_0 \left(1 - \frac{R}{r} \right), \tag{1.11}$$

from which the calculation of the flow rate related to the colliding Brownian particles was straightforward:

$$F = 4\pi D R C_0 \tag{1.12}$$

This scenario can be associated to frequently encountered physical phenomena such as

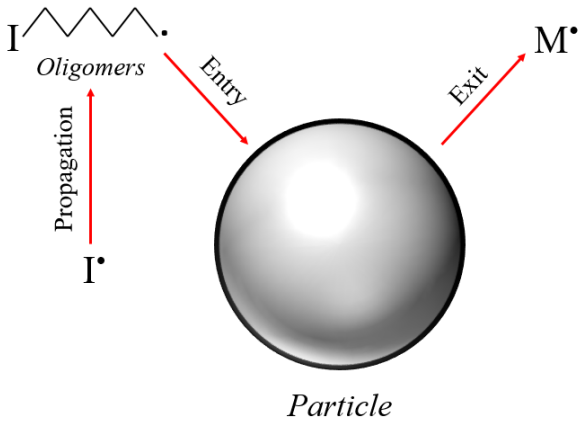

Fig. 1.3 Basic visual description of entry and exit of radicals during an emulsion polymerization.

the entry of oligomeric radicals and the desorption of monomeric ones during an emulsion polymerization showed in Fig.1.3.
The entry starts when the monomer dissolved in water reacts with precursors derived from an initiator $I^{\bullet}$ starting the formation of oligomers which are absorbed into the particles one they have become sufficiently hydrophobic [7].
It is straightforward to associate the latter with the "stationary" phase and the oligomers with the Brownian particles, so the expression for their flow rate can be evaluated as:

$$k_{\mathrm{e}}^{\mathrm{m}} = k_{\mathrm{ads}}[\mathrm{M}]_w = 4\pi D_0 R_{\mathrm{S}} N_{\mathrm{AV}}[\mathrm{M}]_{\mathrm{w}} \tag{1.13}$$

where D_0 is the diffusion coefficient of the oligomers, $[\mathrm{M}]_{\mathrm{w}}$ their molar concentration in the aqueous phase ($C_0 = N_{\mathrm{AV}}[\mathrm{M}]_{\mathrm{w}}$ where N_{AV} is the Avogadro number), meanwhile R_S the swollen radius of the particle.
Eq.(1.13) is the starting point to evaluate the desorption rate of monomeric radicals during an emulsion polymerization: by assuming conditions of equilibrium between the amount of monomer which enters and exits the particles, it is possible to write

$$\mathrm{Particle}-\mathrm{M}^{\bullet} \underset{k_{\mathrm{e}}^{\mathrm{m}}}{\overset{k_{\mathrm{exit}}}{\rightleftharpoons}} \mathrm{Particle} + \mathrm{M}^{\bullet} \tag{1.14}$$

The total rate of escaping particle per unit time can be formalized as:

$$k_{\mathrm{exit}} = k_{\mathrm{dm}} V_{\mathrm{S}} [\mathrm{M}]_{\mathrm{p}} N_{\mathrm{AV}}, \tag{1.15}$$

where $V_S = 4/3\pi R_S^3$ is the swollen volume of the particle and $[M]_p$ the molar concentration of monomer in the particle. If equilibrium conditions are considered, then the following expression for the desorption rate is obtained:

$$k_{exit}^m = k_e^m \rightarrow k_{dm} = \frac{4\pi D_w R_S [M]_w N_{AV}}{V_S [M]_p N_{AV}} = \frac{3D_w}{R_S^2} \frac{[M]_w}{[M]_p} \tag{1.16}$$

This link between Brownian motion and the entry and exit of radicals offers the opportunity to propose in Chapter 5-6-7 a kinetic model where these phenomena, together with state-of-the-art mechanisms, are included to study reaction kinetics of seeded emulsion homo-, co- and ter-polymerizations. Another innovation of this framework will be the use of a rigorous theoretical model to rationalize the interplay between the surface of the latexes actually covered by a surfactant and the salt content inside the reactor on the formation of undesired coagulum during industrial processes.

1.2.3 Part III: biological systems

Brownian dynamics have also found applications in biological studies: a classic problem linked to Brownian motion is the narrow escape problem. Basically, it is the evaluation of the mean escape time of a small Brownian element from a domain which is bounded by a reflecting boundary, except for a small window which is the only way out. This scenario has been recently associated to the motion of a single molecule (ion, protein) inside or outside a cellular membrane [8].

Moreover, the basic equations of Brownian motion have recently been applied to track single particle trajectories allowing the study of local biophysical properties such as density of obstacles inside the cells [9].

The final part of the thesis deals with an ulterior topic, that is the self-assembly of proteins *in vivo*: the topic of interest here is the growth dynamics of Poly-glutamine aggresome inside a mammalian cell whose the genes have been modified to generate an over-expression of the aforementioned protein [10].

Part I

A new analytic framework to describe the microstructure of complex interacting particles under strongly sheared conditions

Chapter 2

Introduction

As mentioned in Chapter 1 the aim of the first part of the thesis is proposing a new analytic framework whose ultimate goal is studying the microstructure, that is the spatial arrangement, of complex-interacting particles under strongly sheared conditions. First and foremost Section 2.1 is dedicated to present the general framework: the Smoluchowski equation related to a 3D system of N particles under sheared conditions according to the formalism showed in [11] from which the particular case valid for 2-Body dynamics is extracted (Section 2.2). This first step is necessary in order to introducer the proper terminology which will ease the analysis of the literature review in Section 2.3: it will be focused on the most important theoretical works related to the resolution of the aforementioned equations for different levels of applied shear. The chapter finishes with a summary in which the motivations behind the development of a new theoretical framework are highlighted.

2.1 3D formalism of the N-Body Smoluchowski equation

In chapter 1 the first attempts to describe the Brownian motion of a single particle have been proposed, instead the following section aims to provide with an intuitive way to derive the probability distribution function for an ensemble composed of N equal particles as showed in Fig.2.1.
The starting point is the classic equation of motion as proposed by Langevin in 1908 [12] which describes the temporal variation of the momentum $\mathbf{p}_i$ of each one of the N particles:

$$\frac{d\mathbf{p}_i}{dt} = \mathbf{F}_i^{\text{tot}} \quad \text{i} = 1,...,N. \tag{2.1}$$

The overall force $\mathbf{F}_i^{\text{tot}}$ acting on a single particle includes the superposition of a viscous force exercised by the fluid $\mathbf{F}^{\text{visc}}$ which is the source of the hydrodynamic interactions, a

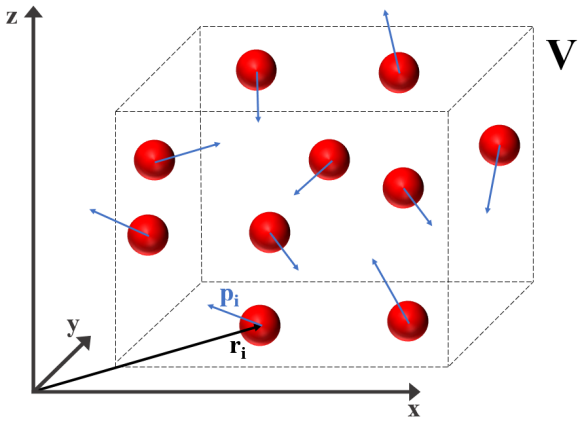

Fig. 2.1 Chaotic motion of N particles in an arbitrary volume V in the phase space.

stochastic one $\mathbf{F}^{\mathrm{Br}}$ which is the result of the collisions between the molecules of the solvent and the particle (the actual source of Brownian motion) and a third force $\mathbf{F}^{\mathrm{ext}}$ which takes into account the influence of eventual inter-particle interactions.

$$\frac{d\mathbf{p}_i}{dt} = \mathbf{F}_i^{\mathrm{visc}} + \mathbf{F}_i^{\mathrm{ext}} + \mathbf{F}_i^{\mathrm{Br}} \tag{2.2}$$

In the case scenario proposed in Fig.2.1 the probability density function is not dependent on positions only, but also on their momenta and the ensemble of these two state variables is known as *phase space* $\mathbf{X}$

$$\mathbf{X} = (\mathbf{r}_i, \mathbf{p}_i), \tag{2.3}$$

and its temporal variation can be consequently described as

$$\frac{d\mathbf{X}}{dt} = \left(\frac{d\mathbf{r}_i}{dt}, \frac{d\mathbf{p}_i}{dt}\right). \tag{2.4}$$

The definition of distribution function g($\mathbf{r}_i$,$\mathbf{p}_i$,t) = g($\mathbf{X}$,t) is then extended as the probability of finding each of the N particles not only in the positions $\mathbf{r}_i$, but also with momenta $\mathbf{p}_i$ at time t. Since g($\mathbf{X}$,t) must be conserved at any times in arbitrary volume $\mathbf{V} \in \mathbf{X}$ its temporal variation inside $\mathbf{V}$ must be equal to the flux across its external surface ∂V:

$$\frac{\partial}{\partial t}\left(\int_V g(\mathbf{X},t)d\mathbf{X}\right) = -\oint_{\partial V} d\mathbf{S}\cdot\left(\frac{d\mathbf{X}}{dt}\right)g(\mathbf{X},t). \tag{2.5}$$

Applying the Gauss divergence theorem it can be written that

$$\frac{\partial}{\partial t}\left(\int_V g(\mathbf{X},t)d\mathbf{X}\right) = -\int_V d\mathbf{X}\left[\nabla_{\mathbf{X}}\cdot\left(\frac{d\mathbf{X}}{dt}\right)g(\mathbf{X},t)\right] \tag{2.6}$$

which means

$$\frac{\partial g(\mathbf{X},t)}{\partial t} = -\nabla_{\mathbf{X}} \cdot \left(\frac{d\mathbf{X}}{dt}\right) g(\mathbf{X},t) \tag{2.7}$$

If the divergence of the phase space is expressed as the superposition of its two contributions with respect to the positions and momenta it can be written that

$$\frac{\partial g(\mathbf{X},t)}{\partial t} = -\sum_{i=1}^{N} \left[\nabla_{\mathbf{r}_i} \cdot \left(\frac{\mathbf{p}_i}{M}\, g(\mathbf{X},t) \right) + \nabla_{\mathbf{p}_i} \cdot \left(\mathbf{F}_i^{\text{tot}}\, g(\mathbf{X},t) \right) \right], \tag{2.8}$$

where M is the mass of the particles.

In order to move forward with the discussion, it is important to introduce the concept of time-scale, the minimum time resolution considered by an experiment rather than a theory: it is known that the typical time scale related to the collisions between particles and the molecules of the solvent is $\tau_{\text{solv}} \approx 10^{-14}$ s.

The Langevin equation is instead valid for time scales much longer than τ_{solv} because of the constraints on the random Brownian force $\mathbf{F}^{\text{Br}}$; the minimum time interval in this scenario is called *Fokker-Planck* time scale $\tau_{\text{FP}} >> \tau_{\text{solv}}$.

Finally, in the case of purely Brownian dynamics the considered time scale is $\tau_D \approx 10^{-9}$ s which is much longer than τ_{FP}: in these conditions $\tau_D >> M/Z$ (Z is recalled to be the Stokes friction coefficient) which means that their momenta are instantaneously equilibrated with the thermal bath due to the collisions with the solvent molecules between observation times $\tau_D, 2\tau_D, \ldots$.

The immediate consequence of this reasoning is the phase space distribution function to be dependent on the particle positions only in case of pure Brownian dynamics. This causes the acceleration term in the Langevin equation to become null ($d\mathbf{p}_i/dt = 0 \ \rightarrow \mathbf{F}_i^{\text{tot}} = 0$) which means that Eq.(2.2) can be implemented in its steady state form; Eq.(2.8) can subsequently be simplified as

$$\frac{\partial g(\mathbf{X},t)}{\partial t} = \frac{\partial g(\mathbf{r}_i,t)}{\partial t} = -\sum_{i=1}^{N} \left[\nabla_{\mathbf{r}_i} \cdot \left(\frac{\mathbf{p}_i}{M}\, g(\mathbf{r}_i,t) \right) \right]. \tag{2.9}$$

At this point, in order to explicitly write the expression for the momenta $\mathbf{p}_i$, it is necessary to introduce every contribution to the steady state approximation of Eq.(2.2) starting from the viscous force $\mathbf{F}_i^{\text{visc}}$.

At the time Langevin first proposed his formalism he hypothesized that the suspension was so diluted that the motion of each particle was never influenced by the movement of the

others, so the viscous force $\mathbf{F}_i^{\text{visc}}$ could simply be described as

$$\mathbf{F}_i^{\text{visc}} = -\underline{\mathbf{Z}}\frac{\mathbf{p}_i}{M}, \tag{2.10}$$

where $\underline{\mathbf{Z}}$ is the friction matrix, the 3D equivalent of the Stokes friction coefficient Z introduced in Eq.(1.7).
In case of many-body dynamics a new version of Eq.(2.10) has been proposed where the viscous force acting on the i-th particle $\mathbf{F}_i^{\text{visc}}$ is also influenced by the presence of the other N-1 particles:

$$\mathbf{F}_i^{\text{visc}} = \sum_{j=1}^{N} \underline{\mathbf{Z}}_{ij}(\mathbf{r}_i) \cdot \frac{\mathbf{p}_j}{M}. \tag{2.11}$$

$\underline{\mathbf{Z}}_{ij}(\mathbf{r}_i)$ is now every friction matrix which expresses the influence of momentum of the j-th one on the i-th particle through the application of a viscous force.

Concerning the formalism of $\mathbf{F}_i^{\text{ext}}$, it is defined by adopting the classical dependence on the gradient of the associated interaction potential $U(\mathbf{r}_i)$

$$\mathbf{F}_i^{\text{ext}} = -\nabla_{\mathbf{r}_i} U(\mathbf{r}_i), \tag{2.12}$$

and at this point the steady state Langevin equation can be expressed as

$$0 = \sum_{j=1}^{N} \underline{\mathbf{Z}}_{ij} \cdot \frac{\mathbf{p}_j}{M} - \nabla_{\mathbf{r}_i} U(\mathbf{r}_i) + \mathbf{F}_i^{\text{br}}. \tag{2.13}$$

It is now possible to express the velocities in Eq.(2.9) as function of the microscopic diffusion matrices $\underline{\mathbf{D}}_{ij}$ which are linked to the friction matrices $\underline{\mathbf{Z}}_{ij}$ by the procedure proposed in Appendix A:

$$\frac{\mathbf{p}_i}{M} = \sum_{j=1}^{N} \beta \underline{\mathbf{D}}_{ij} \cdot \left(\nabla_{\mathbf{r}_j} U(\mathbf{r}_1, ..., \mathbf{r}_N) - \mathbf{F}_j^{\text{br}} \right) \tag{2.14}$$

Replacing Eq.(2.14) into Eq.(2.9) is an ulterior step towards the formalization of the N-Body Smoluchowski equation:

$$\frac{\partial}{\partial t}\left(g(\mathbf{r}_i, t) \right) = -\sum_{i=1}^{N} \left[\nabla_{\mathbf{r}_i} \cdot \sum_{j=1}^{N} \beta \underline{\mathbf{D}}_{ij} \cdot \left(-\nabla_{\mathbf{r}_j} U(\mathbf{r}_1, ..., \mathbf{r}_N) + \mathbf{F}_i^{\text{br}} \right) g(\mathbf{X}, t) \right]. \tag{2.15}$$

The only missing piece of the puzzle is the identification of the constitutive equation for the Brownian force $\mathbf{F}_i^{\text{Br}}$. It is necessary at this point to impose a condition of dynamic equilibrium

where the pdf is hypothesized to assume the well known Maxwellian form:

$$g(\mathbf{r}_i,t) \sim \exp\left(-\beta U(\mathbf{r}_i)\right), \tag{2.16}$$

which leads to the following description of $\mathbf{F}_i^{\mathrm{Br}}$

$$\mathbf{F}_i^{\mathrm{Br}} = -\frac{1}{\beta}\nabla_{\mathbf{r}_i}\ln\left(g(\mathbf{r}_i,t)\right). \tag{2.17}$$

Replacing Eq.(2.17) into Eq.(2.15) the final structure of the N-body Smoluchowski equation is obtained:

$$\begin{aligned}\frac{\partial g(\mathbf{r}_i,t)}{\partial t} &= \sum_{i,j=1}^{N}\nabla_{\mathbf{r}_i}\cdot\left\{\beta\underline{\mathbf{D}}_{ij}\cdot\left[\nabla_{\mathbf{r}_j}U(\mathbf{r}_i)+\frac{1}{\beta}\nabla_{\mathbf{r}_j}\ln\left(g(\mathbf{r}_i,t)\right)\right]g(\mathbf{r}_i,t)\right\} = \\ &= \sum_{i,j=1}^{N}\nabla_{\mathbf{r}_i}\cdot\left\{\beta\underline{\mathbf{D}}_{ij}\cdot\left[\nabla_{\mathbf{r}_j}U(\mathbf{r}_i)g(\mathbf{r}_i,t)+\frac{1}{\beta}\nabla_{\mathbf{r}_j}g(\mathbf{r}_i,t)\right]\right\}.\end{aligned} \tag{2.18}$$

Eq.(2.18) has been derived for particles a fluid in quiescent conditions, but this work is mainly focused on strongly sheared systems for which the *Péclet number* Pe , the relative importance between advective and Brownian forces, is much higher than unity. These scenarios can be encountered in real life when it comes, for instance, to certain paints and coatings applications: the "spraying procedure" includes the application of very strong shear rates which can cause $Pe >> 1$, so the study of the microstructure and the rheology under these conditions is very important in order to properly determine the shear stability of these products. Moreover, the processing of colloidal systems is deeply affected by high shear stresses: during emulsion polymerizations, for instance, it is possible for the Péclet number to be higher than unity if critical thresholds of shear rate are passed. This causes shear-induced aggregation which needs to be avoided entirely because it leads to complete failure of the polymerization.
The main result of the application of a shear stress is the generation of a velocity flow field $\mathbf{V}_0$ which depends on the position vector $\mathbf{r}$ and the rate of strain tensor $\underline{\mathbf{E}}$:

$$\mathbf{V}_0 = \underline{\mathbf{E}}\cdot\mathbf{r}. \tag{2.19}$$

In this case the hydrodynamic force $\mathbf{F}_i$ acting on each particle has to be modified: first and foremost the friction matrices $\underline{\mathbf{Z}}_{ij}$ acts on the velocities of the particles relative to the local

fluid velocity as follows

$$\mathbf{F}_i^{\mathrm{h}} = \sum_{j=1}^{N} \underline{\mathbf{Z}}_{ij} \cdot \left(\frac{\mathbf{p}_j}{M} - \underline{\mathbf{E}} \cdot \mathbf{r}_j \right). \tag{2.20}$$

Moreover, the flow field around each particle is disturbed by the presence of the other N-1: this effect is represented by matrices of index-rank 3 $\underline{\underline{\mathbf{C}}}^i(\mathbf{r}_1, ..., \mathbf{r}_N)$, so the hydrodynamic forces assume the following final form:

$$\mathbf{F}_i^{\mathrm{h}} = \sum_{j=1}^{N} \underline{\mathbf{Z}}_{ij} \cdot \left(\frac{\mathbf{p}_j}{M} - \underline{\mathbf{E}} \cdot \mathbf{r}_j \right) + \underline{\underline{\mathbf{C}}}^i(\mathbf{r}_1, ..., \mathbf{r}_N) : \underline{\mathbf{E}}, \tag{2.21}$$

where : indicates the contraction operator with respect to adjacent indices of $\underline{\underline{\mathbf{C}}}^i$ and $\underline{\mathbf{E}}$.
In the end, by adopting the same procedure described in Appendix A it is possible to obtain the final form of the N-Body Smoluchowski equation under simple shear flow:

$$\frac{\partial g(\mathbf{r}_i,t)}{\partial t} = \sum_{i,j=1}^{N} \nabla_{\mathbf{r}_i} \cdot \left\{ \beta \underline{\mathbf{D}}_{ij} \cdot \left[\nabla_{\mathbf{r}_j} U(\mathbf{r}_i) + \frac{1}{\beta} \nabla_{\mathbf{r}_j} \ln\left(g(\mathbf{r}_i,t)\right) \right] g(\mathbf{r}_i,t) \right\} + \\ - \sum_{i=1}^{N} \nabla_{\mathbf{r}_i} \cdot \left(\mathbf{v}_i \, g(\mathbf{r}_i,t) \right), \tag{2.22}$$

where $\mathbf{v}_i$ is the contribution to the velocity of the particles due to the presence of the external stress:

$$\begin{cases} \mathbf{v}_i = \underline{\mathbf{E}} \cdot \mathbf{r}_i + \underline{\underline{\mathbf{C}}}^{\prime i} : \underline{\mathbf{E}}; \\ \underline{\underline{\mathbf{C}}}^{\prime i} = \beta \sum_n \underline{\mathbf{D}}_{in} \cdot \underline{\underline{\mathbf{C}}}^n, \end{cases} \tag{2.23}$$

where it is possible to highlight the contribution of the shear itself ($\underline{\mathbf{E}} \cdot \mathbf{r}_i$) and the one derived from the disturbance due to the presence of the other particles ($\underline{\underline{\mathbf{C}}}^{\prime i} : \underline{\mathbf{E}}$).

2.2 2-Body Smoluchowski equation

Since the ultimate goal of this work is finding an analytic description of the microstructure under strongly sheared conditions, the system has to be sufficiently diluted in order to transform Eq.(2.22) into its 2 Body equivalent:

$$\frac{\partial g(\mathbf{r}_i,t)}{\partial t} = \sum_{i,j=1}^{2} \nabla_{\mathbf{r}_i} \cdot \left[\underline{\mathbf{D}}_{ij} \cdot \left(\nabla_{\mathbf{r}_j} g(\mathbf{r}_i,t) + \beta \, \nabla_{\mathbf{r}_j} U(\mathbf{r}_i) g(\mathbf{r}_i,t) \right) \right] - \sum_{i=1}^{2} \nabla_{\mathbf{r}_i} \cdot \left(\mathbf{v}_i \, g(\mathbf{r}_i,t) \right). \tag{2.24}$$

At this point Eq.(2.24) needs to assume a new formalism which will be the starting point of our analytic treatment. It is necessary to adopt a new coordinate system like the one showed

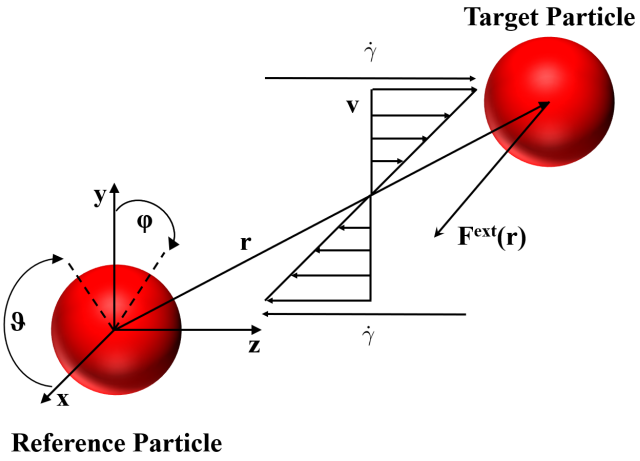

Fig. 2.2 Schematic illustration of a pair of complex interacting Brownian particles interacting subjected to a simple shear flow in Cartesian coordinates. In particular $\mathbf{v} = (0,0,\dot\gamma y)$ in which $\dot\gamma$ is the shear rate the particles are exposed to and, finally, $\mathbf{F}^{\text{ext}} = \beta\ \nabla_{\mathbf{r}} U(\mathbf{r})$.

in Fig.2.2. Its origin is located at the centre of one of the two particles which will be called "reference particle" and the other will be named "target particle". The formalism can now be rewritten as a function of the relative position of the target particle with respect to the reference one $\mathbf{r} = \mathbf{r}_2 - \mathbf{r}_1$:

$$\frac{\partial g(\mathbf{r},t)}{\partial t} = \nabla_{\mathbf{r}} \cdot \left[\underline{\mathbf{D}} \cdot \left(\nabla_{\mathbf{r}} g(\mathbf{r},t) + \beta\ \nabla_{\mathbf{r}} U(\mathbf{r}) g(\mathbf{r},t) \right) \right] - \nabla_{\mathbf{r}} \cdot \left(\mathbf{v}(\mathbf{r})\ g(\mathbf{r},t) \right). \tag{2.25}$$

From this point on the probability distribution function $g(\mathbf{r},t)$ will be renamed *pair correlation function* (pcf) [13, 14], the probability of finding the target particle in a certain position $\mathbf{r}$ with respect to the reference one. The final step is the introduction of the steady state approximation obtaining Eq.(2.26) which will be analytically solved in Chapter 3:

$$\nabla \cdot \left[\underline{\mathbf{D}} \cdot \left(\nabla g(\mathbf{r}) + \beta\ \nabla U(\mathbf{r}) g(\mathbf{r}) \right) \right] - \nabla \cdot \left(\mathbf{v}(\mathbf{r})\ g(\mathbf{r}) \right) = 0. \tag{2.26}$$

where $\nabla = \nabla_{\mathbf{r}}$.

2.2.1 Hydrodynamic interactions

Before proceeding with the literature review it is important to focus more attention on the hydrodynamic interactions which represent the link between the viscous forces acting

on the particles and their momenta as showed in Eq.(2.11); in this case only the pairwise hydrodynamic interactions of main interest in this work will be highlighted.
First, the ones due to the motion of the particles in a quiescent fluid are proposed which provides with the complete description of the microscopic diffusion matrix $\underline{\mathbf{D}}$, next the interactions derived from the scenario in which the fluid is under simple shearing motion are described whose final result is the formalism of the relative velocity $\mathbf{v}$.
Both these classes of interactions are evaluated by the resolution of the equations of motion of the fluid surrounding the particles under creeping conditions. These conditions can be found in many applications in colloidal science: one possible example is a suspension of colloidal particles with diameter $d_P \approx 0.1\mu m$ dispersed inside a reactor i.e. for emulsion polymerization purposes.
In this scenario the Reynolds number related to the particles is usually very low ($Re_p \approx 10^{-3} - 10^{-7}$), so it is possibler to neglect inertial effects. Moreover, if the characteristic length of the reactor L (usually its diameter) is much bigger than d_P, then eventual wall effects can be not taken into consideration as a first approximation and classic far-field boundary conditions (unperturbed motion) for the creeping flow can be implemented.
The cornerstone of this section will be the resolution of the well-known Stokes equations, which determine the proper velocity $\mathbf{u}$ and pressure P fields in the fluid under these conditions [15]:

$$\begin{cases} \nabla P = \mu \nabla^2 \mathbf{u}; \\ \nabla \cdot \mathbf{u} = 0, \end{cases} \tag{2.27}$$

Solving Eq.(2.27) with the proper boundary conditions leads to the evaluation of the viscous forces $\mathbf{F}^{\mathrm{visc}}$ and torques acting on a certain particle from which it is possible to extract the necessary information about the hydrodynamic interactions.

Quiescent fluid

$\underline{\mathbf{D}}$, the matrix which describes the relative diffusivity between the two particle, can be normalized with respect to its dilute limit, highlighting the hydrodynamic interactions along (D_{rr}) and tangentially ($D_{\theta\theta}$, $D_{\phi\phi}$) to the line of centres:

$$\underline{\mathbf{D}} = 2D_0 \begin{bmatrix} D_{\mathrm{rr}} & D_{\mathrm{r}\theta} & D_{\mathrm{r}\phi} \\ D_{\theta\mathrm{r}} & D_{\theta\theta} & D_{\theta\phi} \\ D_{\phi\mathrm{r}} & D_{\phi\theta} & D_{\phi\phi} \end{bmatrix} \sim 2D_0 \begin{bmatrix} D_{\mathrm{rr}} & 0 & 0 \\ 0 & D_{\theta\theta} & 0 \\ 0 & 0 & D_{\phi\phi} \end{bmatrix}. \tag{2.28}$$

D_{rr}, $D_{\theta\theta}$, $D_{\phi\phi}$ can be found in the literature through the procedure previously described for a series of different relative translating and rotating motions between the particles [16].

In this case it has been decided to describe the hydrodynamic disturbance along the line of centres D_{rr} since it is the only one actually used in this work; for now, the interactions tangential to the radial distance have been entirely neglected ($D_{\theta\theta} = D_{\phi\phi} = 0$). The following discussion will be divided into two different sections based upon the relative motion between the particles.

The scenario in which the particles are approaching each other has been studied by Brenner

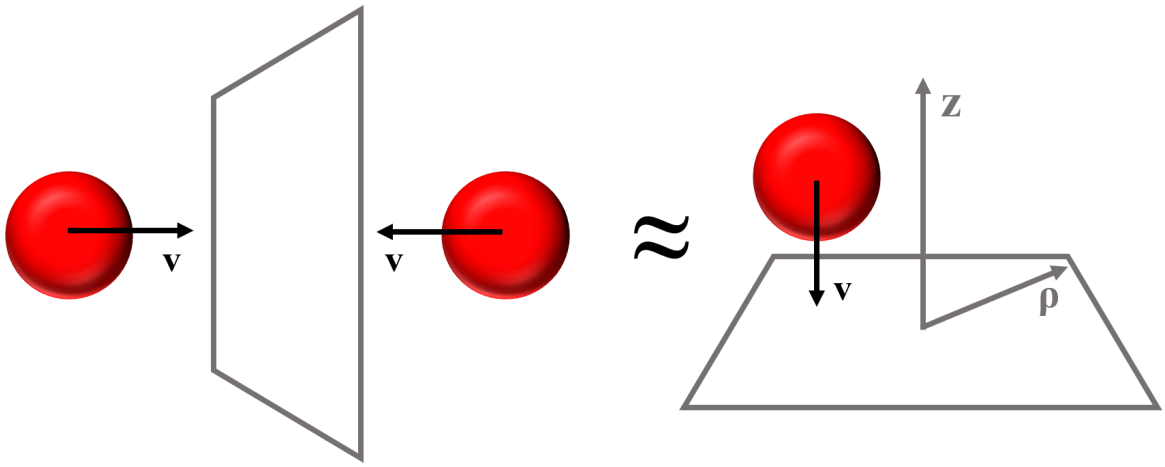

Fig. 2.3 A single sphere moving towards a free surface located at the origin of a cylindrical reference frame.

[17]: he considered the motion of a sphere with velocity **v** in a creeping fluid along the axial direction towards a free-surface where a cylindrical reference frame (ρ,ϕ,z) is located as showed on the right hand side of Fig.2.3. It has been unveiled that this representation can be a good approximation of the situation proposed on the left hand side of Fig. 2.3 which is the actual case study: the plane equidistant from the approaching particles can actually be interpreted as a free surface for which the following boundary conditions have been applied

$$\begin{cases} v_z = 0 \quad z = 0 \\ \dfrac{dv_\rho}{dz} = 0 \quad z = 0, \end{cases} \tag{2.29}$$

which represent the vanish of the axial velocities and of the tangential stresses at the free surface.

By solving the Stokes equations for this particular case it is possible to find the final form of the axial component of the hydrodynamic force, the only one which is not null, according to

the procedure proposed by Stimson and Jeffrey [18] :

$$\mathbf{F}^{\text{visc}} = (Z\chi_c)\mathbf{v}. \tag{2.30}$$

From visual analysis of Eq.(2.30) it can clearly be seen that χ_c is the hydrodynamic correction to the Stokes law, Eq.(2.10), whose final solution has been calculated as

$$\begin{cases} \chi_c(\alpha) = \dfrac{4}{3}\sinh(\alpha)\sum_{n=1}^{\infty}\dfrac{n(n+1)}{(2n-1)(2n+3)}\left[\dfrac{4\cosh^2(n+1/2)\alpha+(2n+1)^2\sinh^2(\alpha)}{2\sinh(2n+1)\alpha-(2n+1)\sinh(2\alpha)}-1\right]; \\ \alpha = \cosh\left(\dfrac{h}{R_P}\right); \end{cases} \tag{2.31}$$

where h is the normalized surface to surface distance.
Finally, it is possible to write down the relative radial diffusivity by recalling the definition of friction coefficient and correlating it to the diffusion matrix through the Stokes Einstein correlation Eq.(1.8):

$$\frac{1}{\beta(Z\chi_c)} = D_0\chi_c^{-1} \rightarrow D_{\text{rr}} = \chi_c^{-1}. \tag{2.32}$$

Since the ultimate goal is the development of an analytic framework, the rigorous solution for χ_c^{-1} will be replaced by a polynomial which can reproduce accurately its near- and far-field values and slopes [19, 20]:

$$\chi_c(h)^{-1} \sim \frac{6h^2+4h}{6h^2+13h+2}. \tag{2.33}$$

The description of the scenario in which the particles fade away from each other is instead straightforward: it is fair to say that there is no correction to the Stokes law for the viscous force and the particles translate without being reciprocally influenced

$$\chi_e(h)^{-1} = 1 \rightarrow D_{rr} = 1. \tag{2.34}$$

Simply sheared fluid

If the liquid environment is not quiescent, but under the effect of an external shear the velocity of the fluid $\mathbf{V_0}$ under unperturbed conditions is not null anymore. Let's consider the particular two-body dynamics scenario described in Fig.2.4: if the velocity of the fluid is assumed to be $\mathbf{V_0} = (0,0,\dot{\gamma}y)$ it means that the related rate of strain tensor $\underline{\mathbf{E}}$ and angular velocity Ω are

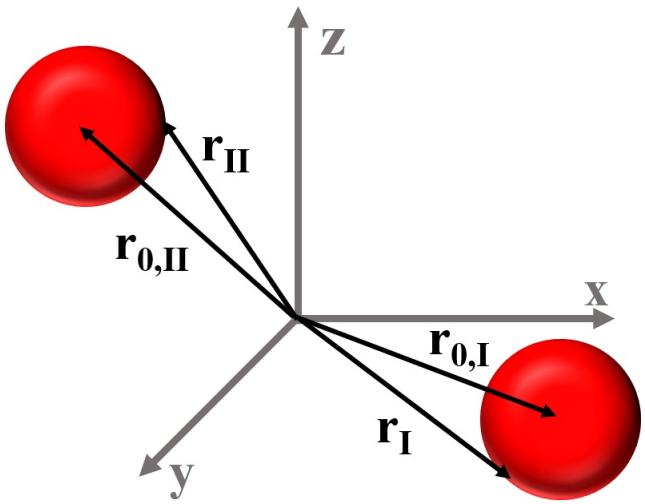

Fig. 2.4 Reference system for a pair of particles under simple shear flow.

linked to the shear rate $\dot{\gamma}$ through:

$$\underline{\mathbf{E}} = \begin{bmatrix} 0 & 0 & 0 \\ 0 & 0 & \frac{\dot{\gamma}}{2} \\ 0 & \frac{\dot{\gamma}}{2} & 0 \end{bmatrix} \qquad \Omega = \left(-\frac{\dot{\gamma}}{2}, 0, 0\right). \tag{2.35}$$

The two spheres (I and II) in Fig.2.4 have their positions identified by the vectors $\mathbf{r_{0,I}}$ and $\mathbf{r_{0,II}}$, respectively. The application of the shear induces a certain velocity on the particles which is composed of a translational $\mathbf{t_i}$ and a rotational component $\Omega_\mathbf{i}$ as follows:

$$\mathbf{V}_i = \mathbf{t_i} + \Omega_\mathbf{i} \times (\mathbf{r_i} - \mathbf{r_{0i}}) \quad \text{i = I,II.} \tag{2.36}$$

where $\mathbf{r_i}$ is the position vector from the origin to a certain point on the surface of the i-th sphere.
In order to evaluate **v**, the relative velocity of the target particle with respect to the reference one, a new set of the Stokes equations with identical structure to Eq.(2.27) needs to be solved,

$$\begin{cases} \nabla P' = \mu \nabla^2 \mathbf{u'} \\ \nabla \cdot \mathbf{u'} = 0, \end{cases} \tag{2.37}$$

but the fundamental variables $\mathbf{u'} = \mathbf{V} - \mathbf{V}_0$ and $P' = p - p_0$ are scaled by the velocity and pressure of the fluid with respect to its unperturbed conditions. By solving Eq.(2.37) adopting the following boundary conditions

1. **u'** $\to 0$ and $P' \to 0$ as $\mathbf{r} \to \infty$: the system recovers its unperturbed conditions when sufficiently far away form the particles;

2. no-slip conditions at the solid-liquid interfaces (Eq.(2.36)),

it is possible to know the pressure P' and the components of the velocity of the fluid **u'** which can then be used to evaluate the total force and torque exercised on each particles by the viscous medium.
Finally, by supposing that the overall force and torque acting on them are null (neutral buoynacy), it is possible to evaluate the trajectory of the target sphere with respect to the reference one from which the spherical components of the relative velocity $\mathbf{v}(\mathbf{r}) = [v_r, v_\theta, v_\phi]$ [21] can be expressed; for the case study proposed in Fig.2.2 it is obtained that

$$\begin{cases} v_r = dr/dt = \dot{\gamma} r(1 - A(r)) \sin^2(\theta) \sin(\phi) \cos(\phi); \\ v_\theta = r(d\theta/dt) = \dot{\gamma} r(1 - B(r)) \sin(\theta) \cos(\theta) \sin(\phi) \cos(\phi); \\ v_\phi = r \sin\theta (d\phi/dt) = \dot{\gamma} r \sin(\theta) \left(\cos^2(\phi) - \dfrac{B(r)}{2} \cos(2\phi) \right). \end{cases} \tag{2.38}$$

It is important to highlight that the relative velocity between the particles is the superposition of two effects: one is due to the motion of the fluid because of the applied shear, the second is a a distortion of the flow field around one particle due to the presence of the other which is caused by the hydrodynamic interactions represented by the functions A(r) and B(r) [22] which are the representation of the disturbance matrices $\underline{\underline{\mathbf{C}}}^i$ introduced in the previous section for the particular 2-body dynamics case. Near- or far-field asymptotic expressions for the two hydrodynamic functions are usually adopted in theoretical frameworks, but in this case a pair of fitting functions which reproduce the numerical data proposed by Batchelor [23] will be adopted [24]:

$$\begin{cases} A(r) = \dfrac{113.2568894}{(r/R_P)^5} + \dfrac{307.8264828}{(r/R_P)^6} - \dfrac{2607.54064288}{(r/R_P)^7} + \dfrac{3333.72020041}{(r/R_P)^8}; \\ \\ B(r) = \dfrac{0.96337157}{((r/R_P) - 1.90461683)^{1.99517070}} - \dfrac{0.93850774}{((r/R_P) - 1.90378420)^{2.01254004}}. \end{cases} \tag{2.39}$$

An important observation needs to be done and it has been visually outlined in Fig.2.5. A simple shear flow field includes two possible relative motions between the particles based upon the sign of the radial velocity v_r: on the one hand there are two *compressing quadrants* where the particles approach each other which correspond to a negative sign of v_r, on the other there are two *extensional regions* where the particles instead are being pulled away

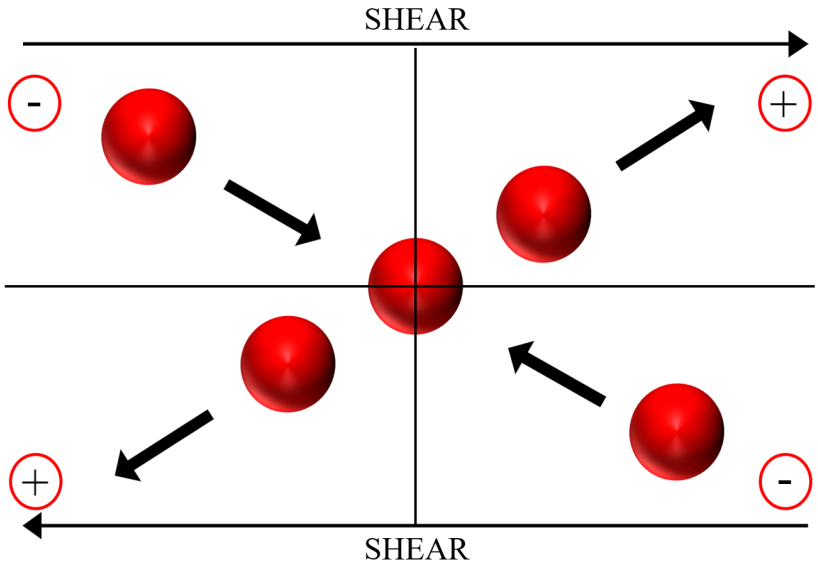

Fig. 2.5 Visual representation of the compressing (-) and extensional (+) quadrants of a sheared hard-spheres suspension, where the horizontal arrows represents the directions the external shear is applied.

from each other by the induced flow field.
Moreover, the hydrodynamic interactions always create an opposite effect with respect to the induced flow: in the compressing quadrants they represent the squeezing of the fluid between the particles which opposes resistance to their approach, meanwhile they provide with an attractive contribution in the extensional regions where the particles are being separated.

2.3 Literature review

Once every component of the 2-Body Smoluchowski equation has been explained it is important to define the proper boundary conditions (BCs) in order for the microstructure to be fully unveiled. The following literature review is divided into two different sections based upon the different near-field conditions adopted to solve Eq.(2.26) and, subsequently, the properties of the suspension of interest; in order for the discussion to be as simple as simple all the particles will have the same radius R_P. Every section also considers different ratios between shear- and Brownian- induced contributions which are described by the Péclet number formalized as [25]

$$\mathrm{Pe} = \frac{\dot{\gamma} R_P^2}{D_0} = \frac{6\pi\eta R_P^3 \dot{\gamma}}{k_B T} : \tag{2.40}$$

in case of weakly sheared conditions Pe $\ll 1$, meanwhile Pe $\gg 1$ for strongly sheared systems; it is important to highlight that this review will mainly focus on theoretical frameworks, so references to experimental works rather than simulations will be done only if necessary.

2.3.1 Rheological and optical properties

If the properties of interest are rheological rather than optical, the first BC is classic "far-field" condition

$$g(\mathbf{r}) = 1 \quad |\mathbf{r}| = r \to \infty, \tag{2.41}$$

which means that the particles are not influenced by each other at sufficiently long distances. Concerning the "near-field" condition, it is formalized as a balance between Brownian- and shear-induced fluxes along the line of centres at the surface of the reference particle:

$$\mathbf{n} \cdot \nabla \cdot \underline{\mathbf{D}} \cdot \left(\beta \nabla U g(\tilde{\mathbf{r}}) + \nabla g(\mathbf{r}) \right) = \mathbf{n} \cdot \nabla \cdot \left(\mathbf{v}(\mathbf{r}) g(\mathbf{r}) \right) \quad r \to 2, \tag{2.42}$$

where $\mathbf{n}$ is the unit vector along the line of centres.
Once the boundary value problem composed of Eq.(2.26, 2.41, 2.42) is solved, the pcf can be used to study the rheology of the suspension by computing the overall bulk stress of the suspension Σ

$$\underline{\Sigma} = -P\underline{\mathbf{I}} + 2\eta_0 \underline{\mathbf{E}} + \Sigma_P = -P\underline{\mathbf{I}} + 2\eta_0 \underline{\mathbf{E}} + \underline{\Sigma}_P^H + \underline{\Sigma}_P^B + \underline{\Sigma}_P^P, \tag{2.43}$$

which depends on the stresses originated by the fluid ($-P\underline{\mathbf{I}} + 2\eta_0 \underline{\mathbf{E}}$) and by the suspension Σ_P which is in turn divided into an hydrodynamic Σ_P^H, Brownian Σ_P^B and inter-particle Σ_P^P contributions [26]. The final step is writing explicitly the bulk stress as a function of the rate of strain from which it is possible to find correlations among the viscosity of the suspension η, the one of the ambient fluid η_0 and other crucial features such as the concentration of particles, usually represented by their packed fraction ϕ, and the rate of strain $\underline{\mathbf{E}}$:

$$\underline{\Sigma} = -P\underline{\mathbf{I}} + 2\eta(\phi)\underline{\mathbf{E}}. \tag{2.44}$$

For instance, the first approximation which correlates η to η_0 and ϕ for a dilute suspension of hard-spheres is the well known expression found by Einstein:

$$\eta = \eta_0 \left(1 + \frac{5}{2}\phi + O(\phi^2) \right). \tag{2.45}$$

On the other hand, the fundamental feature related to the optical properties is the *structure factor*, the Fourier transform of g(**r**) [14]:

$$S(\mathbf{k}) = 1 + n \int d\mathbf{r}(g(\mathbf{r}) - 1) \exp(i\mathbf{k} \cdot \mathbf{r}), \tag{2.46}$$

where **k** is the scattering vector and n the number density of the particles.

Weakly sheared conditions

In case of weakly sheared conditions, the solution for the pcf is usually found as a series whose structure is proposed in Eq.(2.47):

$$g(\mathbf{r}) = g_{\text{eq}}(r) + f(\mathbf{r}) + ... \tag{2.47}$$

Eq.(2.47) is also called *perturbative series*, where $f(\mathbf{r})$ represents the anisotropic perturbation which breaks the symmetry of the equilibirum microstructure g_{eq} due to the application of an external stress; before starting it is important to highlight that all the following frameworks are related to hard-sphere models which means that $\nabla U = 0$.
The first framework which predicted this effect was published by Batchelor [27] who noticed that, for a suspension of hard-spheres under low shear stresses, $g_{\text{eq}} = 1$ and $f(\mathbf{r})$ is linear with respect to the dimensionless rate of strain tensor $\underline{\tilde{\mathbf{E}}} = \underline{\mathbf{E}}/\dot{\gamma}$. This means that Eq.(2.47) can be rewritten as a power series whose base is the Péclet number:

$$g(\mathbf{r}) = 1 - \frac{R_P^2 \dot{\gamma}}{D_0} \frac{\mathbf{r} \cdot \underline{\tilde{\mathbf{E}}} \cdot \mathbf{r}}{r^2} g_1(r) = 1 - \text{Pe} \frac{\mathbf{r} \cdot \underline{\tilde{\mathbf{E}}} \cdot \mathbf{r}}{r^2} g_1(r), \tag{2.48}$$

g_1 was then calculated by replacing Eq.(2.48) into Eq.(2.26) and solving the resulting equation by the means of a numerical procedure. The microstructure has then been used to compute the bulk stress by considering hydrodynamic contributions only ($\underline{\Sigma}_P^B = \underline{\Sigma}_P^P = \underline{0}$), finding the hydrodynamic limit η_∞ which is an extension to order ϕ^2 of Eq.(2.45):

$$\eta_\infty = \eta_0 \left(1 + \frac{5}{2}\phi + 5.0\phi^2 + O(\phi^3) \right). \tag{2.49}$$

Afterwards, the calculations were repeated by considering strong Brownian motion (Pe $\to 0$), so Σ_P^B was evaluated and η followed as

$$\eta = \eta_0 \left(1 + \frac{5}{2}\phi + 6.2\phi^2 + O(\phi^3) \right). \tag{2.50}$$

By comparing η with η_∞ the influence of the Brownian motion on the viscosity was too small to be measured experimentally [27], so other works have tried to extend the discussion to more concentrated systems in order to evaluate a non-negligible contribution of the Brownian dynamics to the rheology.
A common procedure foresees the application of an integral average which, applied to a certain property $A(\mathbf{r}_1,...,\mathbf{r}_N)$, is formalized as

$$g(\mathbf{r}_1,\mathbf{r}_2)\langle A\rangle = N(N-1)\int A g(\mathbf{r}_1,\mathbf{r}_2,\mathbf{r}_3)d\mathbf{r}_3...d\mathbf{r}_N. \tag{2.51}$$

The N-Body Smoluchowski equation is basically transformed in its 2-Body equivalent in which all the fundamental properties involving the two particles are conditionally averaged over the other N-2. This procedure adds a series of terms dependent on the triplet distribution function which are subsequently truncated in order to guarantee a closure to the problem. The conditional averaged Smoluchowski equation, now written as a function of the relative distance $\mathbf{r}$, becomes

$$\nabla\cdot\langle\underline{\mathbf{D}}\rangle\cdot\nabla g(\mathbf{r}) - \nabla\cdot\Big(\langle\mathbf{v}(\mathbf{r})\rangle\ g(\mathbf{r})\Big) = 0. \tag{2.52}$$

A first attempt to solve Eq.(2.52) has been proposed by Gast and Russel [28]: their work, as the one proposed by Batchelor, includes pairwise hydrodynamic interactions only and, for this reason, their resolution introduced considerable errors when compared to experimental data of very concentrated systems, especially related to the viscosity. An attempt to refine this theory has been conducted by Lionberger and Russel [29] by introducing approximate descriptions of many-body hydrodynamics near contact which provided more reliable predictions for both the microstructure and rheology.
Another fundamental work has been conducted by Brady [30] who started from this alternative form of Eq.(2.47)

$$g(\mathbf{r},\phi) = g_{\mathrm{eq}}(r,\phi)(1+f'(\mathbf{r})+...). \tag{2.53}$$

He considered the many-body hydrodynamic interactions in the description of $f'(\mathbf{r})$ with a self diffusion coefficient $D_{0,s}(\phi)$ which scales with the packed fraction ϕ:

$$f'(\mathbf{r}) = -\frac{R_P^2\dot{\gamma}}{D_{0,s}(\phi)}\frac{\mathbf{r}\cdot\underline{\tilde{\mathbf{E}}}\cdot\mathbf{r}}{r^2}g_1. \tag{2.54}$$

The transient version of Eq.(2.52) has then been rewritten as

$$g_{\mathrm{eq}}\frac{dg_1(r)}{dt} = \nabla\cdot\langle\underline{\mathbf{D}}\rangle g_{\mathrm{eq}}\cdot\nabla g_1(r) - \nabla\cdot\langle\mathbf{v}\rangle g_{\mathrm{eq}}. \tag{2.55}$$

Experiments based on tracer measurements by the means of photon correlation spectroscopy have provided with the necessary information for $D_{0,s}(\phi)$ [31], meanwhile Stokesian dynamics simulations have given the necessary data for η_∞ and $g_{\mathrm{eq}}(r,\phi)$ [32], so the perturbation of the microstructure has been evaluated and, subsequently, a new scaling law for η has followed as

$$\eta = \eta_\infty + \eta_0 \frac{12}{5} \frac{D_0}{D_{0,s}(\phi)} \phi^2 g_{\mathrm{eq}}(r,\phi), \tag{2.56}$$

finding very good agreement with experimental data.
For now, the terms involving the triplet distribution function have always been truncated in order to make the problem solvable. Nazockdast and Morris have instead included three particle hydrodynamic interactions by assuming pairwise additivity of the viscous forces [33]. In order to close the problem the triplet distribution function $g(\mathbf{r}_1,\mathbf{r}_2,\mathbf{r}_3)$ has been correlated to the pair correlation function $\mathrm{g}(\mathbf{r}_1,\mathbf{r}_2)$ through a modified version of the Kirkwood integrals [34]. Finally, an extra term representative of a shear-induced diffusion has been added to Eq.(2.52) which is scaled as a function of the volume fraction as proposed by Brady.
The microstructure is then obtained numerically by the means of an iterative procedure and validated by comparison with Stokesian dynamics simulations providing with good results for $0.1 \leq \mathrm{Pe} \leq 100$ (it is not a typical range for weakly sheared conditions, but the lower limit of the range of the Péclet numbers can be considered as sufficiently low). The authors have also described the rheology through the computation of the shear viscosity. In particular they found that for $\mathrm{Pe} \leq 10$ the viscosity decreases with the shear: this happens because the stress Σ_P decreases due to the reduction of the Brownian contribution Σ_P^B which overwhelms the increase of the hydrodynamic term Σ_P^H. On the other hand, if $\mathrm{Pe} > 10$ the increase of Σ_P^H becomes dominant and the viscosity starts increasing with the applied shear rate causing a shear-thickening behavior.
Other theoretical frameworks, instead, dealt with the complete N-Body Smoluchowski equation by applying the Mode-Coupling theory in order to study the rheology of fluids close to glass transition [35–37].

Concerning the effect of the shear on the optical properties, it can be observed as a distortion of the structure factor which has been observed experimentally for the first time by Ackerson & Clark [38, 39]: they reported small distortions in the distribution of the intensity of the light scattered by a dispersion of hard-spheres; in order to describe this effect plenty of theoretical approaches have been proposed. All of the following frameworks did not include any hydrodynamic interactions under the approximation for the shear stresses to be sufficiently low in magnitude and the systems to be diluted enough.
Their procedure instead involved approximated descriptions of direct interactions among

the particles in order to derive expressions for the distortion of the structure factor from its equilibrium form S_{eq} adopting the same type of power series as previously seen for Eq.(2.47):

$$S(\mathbf{k}) = S_{eq} + \varepsilon(\mathrm{Pe})S_1 + ... \tag{2.57}$$

For instance, Ronis [40] has used a **k**-dependent diffusion constant, which depends on the equilibrium structure factor S_{eq} as well, in their approach based on the "fluctuating diffusion equation model" and he stated that the distortion of the structure factor scales with the first power of Pe:

$$\varepsilon(\mathrm{Pe}) = \mathrm{Pe}. \tag{2.58}$$

This work also provided the complete evaluation of S_{eq} and S_1 which resulted in satisfying qualitative results when compared to experimental data [41], but it is also suggested that considering the hydrodynamic interactions can improve the evaluation of the distortion.
Another approach proposed the replacement of the diffusion term in Eq.(2.26) with a relaxation time τ_a directly dependent on the distortion of the microstructure [42] which is the starting point for the evaluation of $S(\mathbf{k})$ whose structure is predicted to be perturbed with the same scale predicted by Ronis.
The theoretical knowledge has been extended by Dhont [43] who solved the Fourier transform of Eq.(2.26): he derived the results found in [40] as a particular case of his more general calculations and he demonstrated that Ronis provides with reliable results only outside a "boundary layer" located at $\mathbf{k} = 0$, where the description of the distortion of S(**k**) does not scale anymore with Pe, but $S_1 \propto \sqrt{\mathrm{Pe}}$. The author himself admitted that the distortion described by him was minimal due to the very dilute conditions and small shear rates, but his work is clearly a first step towards a more general description of the effect of shear on the structure factor.
Another important work is the one conducted by Blawzdziewicz [44]: more recent experimental evidence [45] together with simulations of Brownian dynamics [46] suggested the presence triggering of an additional distortion along the plane perpendicular to the direction of the flow, a feature which is not foreseen by the aforementioned theories. By solving Eq.(2.26) neglecting again hydrodynamic interactions by the induced sources method he was capable of reproducing the aforementioned new feature. The results also include a rheological study through the evaluation of the shear stress finding a shear thinning behavior which is consistent with previously described frameworks [33].

Strongly sheared conditions

The literature related to theoretical frameworks which describes the microstructure and rheology of strongly sheared systems has its pioneering work in a paper published by Batchelor and Green [47] who derived an analytic solution of the 2-Body version of Eq.(2.26) for Pe $\rightarrow \infty$ under steady state assumption:

$$\nabla \cdot \left(\mathbf{v}(\mathbf{r}) g(\mathbf{r}) \right) = 0, \tag{2.59}$$

in which the relative velocity $\mathbf{v}(\mathbf{r})$ has been described according to Eq.(2.38).
Since it is a first order ODE, only one BC is needed which in this case is the far-field one Eq.(2.41). The main observation is that the microstructure has been found to have a complete spherical symmetry:

$$g(\mathbf{r}) \approx g(r) = \frac{1}{1-A(r)} \exp\left(\int_r^{\infty} \frac{3(B(r)-A(r))}{r(1-A(r))} dr \right). \tag{2.60}$$

This was explained by the fact that, for a pure straining motion, all the trajectories around one particle are open which means that one sphere approaches the other from infinite distance. They then adopted Eq.(2.60) as input for the evaluation of Σ_P and build the following new extension of the Einstein theory for the suspension viscosity:

$$\eta_{\infty} = \eta_0 \left(1 + \frac{5}{2}\phi + 7.6\phi^2 + O(\phi^3) \right). \tag{2.61}$$

On the other hand, they could not complete the calculation for a system under simple shearing motion because in this case some trajectories are closed and the spherical symmetry of the microstructure is subsequently lost.
Twenty years later, Brady and Morris [48] started filling this gap by proposing a new analytic framework in which they analysed the microstructure of strongly sheared suspensions. In order to destroy the region of closed streamlines typical of a simple shear flow, they included a new dimensionless parameter $b > 0$ which is a representation of the excluded volume interactions which keep the particles to a minimum distance $2R_P + b$. It becomes part of a new dimensionless parameter b/R_P which can be interpreted as an indicator of the relative importance between hydrodynamic interactions and Brownian motion together with interparticle interactions: if its value is close to 0 then the microstructure is dominated by hydrodynamics, otherwise the influence of the lubrication forces get progressively negligible and the thermodynamic forces, the Brownian one among all, become dominant [49].
They proposed a new analytic solution for Eq.(2.26) inside a small boundary layer with width

$\delta \propto O(1/\mathrm{Pe})$ near the reference particle whose presence has been identified by numerical frameworks as well [49]. Within the layer the pcf varies quite suddenly and reaches a contact value g(2b) = O(Pe) in the compressing regions, meanwhile in the extensional quadrants it is supposed to be O(1), but without any actual rigorous calculations. The contact value of the micro-structure has then been used to study the rheology of the suspension under dilute conditions observing that, if $\mathrm{b}/R_P \to 0$, the suspension experiences a shear thickening behavior, an effect mainly due to the presence of the presence of the boundary layer [33].

2.3.2 Aggregation of colloids

Even if it is a topic which is not directly faced in this work a brief literature review about the aggregation of colloids under sheared conditions is proposed.
As mentioned in Chapter 1, the pair correlation function is linked to the concentration of particles in the liquid medium through

$$C(\mathbf{r}) = g(\mathbf{r})C_0, \tag{2.62}$$

where C_0 is the concentration of particles in the bulk. As previously mentioned, all the frameworks study the simplest possible scenario: pairwise coagulation of particles with equal size R_P. By applying Eq.(2.62) Eq.(2.26) becomes

$$\nabla \cdot \underline{\mathbf{D}} \cdot \Big(\beta \nabla U C(\mathbf{r}) + \nabla C(\mathbf{r}) \Big) - \nabla \cdot \Big(\mathbf{v}(\mathbf{r}) C(\mathbf{r}) \Big) = 0. \tag{2.63}$$

The two boundary conditions, the far- and near-field, are respectively written as

$$\begin{cases} C(\mathbf{r}) = C_0 & r \to \infty \\ C(\mathbf{r}) = 0 & r \to 2R_P \end{cases} \tag{2.64}$$

The far-field BC is exactly the equivalent as Eq.(2.41), meanwhile the near-field one represents the *immediate stick* condition between the approaching particles. Once the boundary value problem Eq.(2.63-2.64) is solved the coagulation rate is calculated as the surface integral of the resulting flux:

$$J = \oint \left[\underline{\mathbf{D}} \cdot \Big(\beta \nabla U C(\mathbf{r}) + \tilde{\nabla} C(\mathbf{r}) \Big) - \mathbf{v}(\mathbf{r}) C(\mathbf{r}) \right] \cdot \mathbf{n} \, dS \tag{2.65}$$

Weakly sheared conditions

The pioneering work conducted by Smoluchowski and introduced in Chapter 1 for the aggregation of Brownian particles with a stationary one [6] was extended to scenarios in which all the considered particles were under Brownian dynamics. This new physical system was described by simply replacing in the 2-Body Smoluchowski equation the diffusion coefficient of an isolated particle D_0 with the relative diffusion coefficient $D_{12} = 2D_0 D_{rr}$ related to a pair of particles [50].
Finally, it has been hypothesized that Eq.(2.63) is under purely Brownian conditions ($\mathbf{v}(\mathbf{r}) = \mathbf{0}$) and dependent on the radial coordinate r only:

$$\frac{1}{r^2}\frac{d}{dr}\left(r^2 D_{12}\frac{dC}{dr} + \beta D_{12}\frac{dU}{dr}C\right) = 0, \tag{2.66}$$

The boundary value problem including the boundary conditions in Eq.(2.64) can be easily solved finding the following result for the concentration C(r)

$$\frac{C(r)}{C_0} = \frac{\exp\int_{2R_P}^{r}\exp(\beta U)/(r^2 D_{12})dr}{\exp\int_{2R_P}^{\infty}\exp(\beta U)/(r^2 D_{12})dr}\exp(-\beta U) \tag{2.67}$$

which can then be used to calculate the flux J through Eq.(2.65), recovering the original result obtained by Smoluchowski for the diffusion-limited coagulation of hard spheres (U = 0) in absence of hydrodynamic interactions ($D_{rr} = 1$)

$$J^{\mathrm{DL}} = 8\pi D_{12} R_P C_0, \tag{2.68}$$

and the results obtained by Spielman [51]:

$$J^{\mathrm{RL}} = \frac{J^{\mathrm{DL}}}{W}. \tag{2.69}$$

J^{RL} is the flow rate considering the influence of inter-particle interactions on the aggregation this time defined to happen under *reaction-limited* conditions. The role of the inter-particle interactions, represented by the potential U, is quantitatively represented by W, the Fuchs stability ratio, which is defined as:

$$W = \int_{2\,R_P}^{\infty}\frac{\exp(\beta U)}{D_{\mathrm{rr}} r^2}dr. \tag{2.70}$$

Later works have then extended the discussion to scenarios where Brownian motion and

application of external shears happen at the same time.
The first attempt has been conducted by Swift & Frielander [52] which postulated that the Brownian- and shear-induced contributions to the aggregation are independent and the overall kernel is simply the superposition of Eq.(2.69) and the aggregation rate under purely sheared conditions (See Eq.(5.12) down below):

$$J = J^{\mathrm{RL}}\left(1 + \mathrm{Pe}\frac{2W}{3}\right) \tag{2.71}$$

This hypothesis has been proved to be incorrect and now it is widely accepted that, as also showed in the section related to the rheological and optical properties, Brownian- and shear-induced contributions are coupled.
Van de Ven & Mason [53] have found a solution to Eq.(2.63) for a system under dilute conditions through the use of matched asymptotics. They suggested that the flow rate does not vary with the first power of the Péclet number, as indicated by the previous theory [52], but with its square root which is clear evidence that the two processes are not linearly independent:

$$J = J^{\mathrm{RL}}(1 + \sqrt{\mathrm{Pe}}\, B_0 W), \tag{2.72}$$

where B_0 is a numerical parameter depending on the type of applied field.
Zaccone et al [54] instead proposed a rigorous analytic framework around the resolution of Eq.(2.63) inside a boundary layer with width $\delta = O(\mathrm{Pe}^{-1/2})$ considering complex interacting particles. Their ultimate result is a modified Fuchs Stability ratio in which the presence of the shear flow is taken into account as follows:

$$W = \int_{2R_P}^{\delta} \frac{1}{D_{rr} r^2} \exp\left[\int_{\delta}^{r} (\beta U + \mathrm{Pe} v_r) dr\right] dr \tag{2.73}$$

Their results have been compared to numerical simulations [24] obtaining both good qualitative and quantitative matching for $\mathrm{Pe} \leq 100$. Above this range the discrepancy between the theory and simulations is mainly dependent on the lack of hydrodynamic interactions in the analytic formalism which has been demonstrated to play a crucial role in determining the microstructure [47, 48] under very strong shear conditions.

Strongly sheared conditions

In case of strongly sheared conditions,the initial point has been another work made by Smoluchowski which considered $\mathrm{Pe} \to \infty$ and total absence of hydrodynamic interactions

leading to the straightforward evaluation of the pcf:

$$C(r) = \Big(1 - H(2-r)\Big)C_0, \tag{2.74}$$

where H is the Heaviside step function. The subsequent integration by Eq.(2.65) leads to the well-known orthokinetic aggregation rate:

$$J_S = \frac{32}{3}\dot{\gamma}R_P^3 C_0. \tag{2.75}$$

An attempt to include the influence of inter-particle interactions, described by the DLVO theory, for the limit $\mathrm{Pe} \to \infty$ has been done by Van de Ven & Mason [56] by adding a capture efficiency α_r to Eq.(2.75).
The effect of Brownian motion has also been considered by Feke and Schowalter [57]: their solution is built as as a power series whose base is the inverse of the Péclet number:

$$C(\mathbf{r}) = C_0(\mathbf{r}) + \mathrm{Pe}^{-1}C_1(\mathbf{r}) + ..., \tag{2.76}$$

where C_0 is the solution of Eq.(2.63) for $\mathrm{Pe} \to \infty$, meanwhile C_1 represents the influence of Brownian-induced contributions on the orthokinetic limit. Their approach is an approximate perturbative methodology which includes three different regions, Once both of the leading terms have been evaluated, the overall flow rate can be calculated as

$$J = J_0 + \mathrm{Pe}^{-1}J_1 + ... \tag{2.77}$$

where J_0 and J_1 are calculated through Eq.(2.65) by using $C = C_0(\mathbf{r})$ and $C = C_1(\mathbf{r})$, respectively. Their results clearly showed hat the Brownian- and shear-induced contributions are not independent and need to be coupled in order for their respective effects to be considered properly.

2.3.3 Summary

In the previous section the most important theoretical frameworks involving the evaluation of the microstructure of sheared hard-sphere suspensions adopting different boundary conditions based upon the properties of interest have been proposed.
At this point, focusing on the section related to strongly sheared conditions, it is possible to put on evidence the motivations behind the development of this new theoretical framework. It can be noticed that there is still a lack of a completely analytic procedure in describing a

three dimensional microstructure of a suspension under strong shearing motion: Batchelor and Green did not include this effect [47] limiting their analysis to purely strained conditions, meanwhile Brady & Morris did not propose an analytic solution for the pair correlation function outside the boundary layer or for the extensional quadrants [48]. Moreover their work suppose the contact value of the pcf to scale with the first power of the Péclet number, a result which has been reconsidered based on Stokesian dynamics simulations [25] which found a weaker dependence and highlighted the decrease of the peak with ϕ. Moreover, even if a complete analytic solution is found, its most common use is the starting point for a numerical evaluation of the microstructure in order to compute the properties of interest such as the aggregation rate [57]. Finally, the vast majority of the works are related to hard-sphere suspensions with little attention paid to the effect of eventual inter-particle interactions.
On the contrary, this work has the intent to propose a completely analytic framework which is capable of studying, first, the perturbation of the Brownian motion for every region of the sheared fluid and, finally, to what extent interparticle potentials can affect the microstructure of a colloidal dispersion under these conditions.

Chapter 3

Mathematical formalism

After having introduced the formalism behind the 2-Body Smoluchowski equation, the literature review and the motivations behind this work, this chapter includes an accurate step-by-step description of the mathematical procedure adopted to analytically evaluate the microstructure under strongly sheared conditions.
The new analytic methodology starts from the following boundary value problem which is the union of Eq.(2.25, 2.41, 2.42):

$$\begin{cases} \nabla \cdot \left[\underline{\mathbf{D}} \cdot \left(\nabla g(\mathbf{r}) + \beta \ \nabla U(\mathbf{r}) g(\mathbf{r}) \right) \right] - \nabla \cdot \left(\mathbf{v}(\mathbf{r}) \ g(\mathbf{r}) \right) = 0; \\ g(\mathbf{r}) = 1 \quad r \to \infty; \\ \mathbf{n} \cdot \nabla \cdot \left[\underline{\mathbf{D}} \cdot \left(\beta \ \nabla U(\mathbf{r}) g(\mathbf{r}) + \nabla g(\mathbf{r}) \right) - \left(\mathbf{v}(\mathbf{r}) g(\mathbf{r}) \right) \right] \quad r \to r_c = \sigma + b. \end{cases} \tag{3.1}$$

The near-field condition has been expressed as a function of the hard-sphere diameter $\sigma = 2R_P$ and b, which is the closest distance the two particles can approach and it describes the relative balance between Brownian and hydrodynamic forces [48]. Since the hydrodynamic interactions play a very important role, the value of b needs to be close to zero; in this work it has been decided to fix $b = 5\ 10^{-5}\sigma$ because it is the same strength of the excluded volume interactions adopted by the Stokesian dynamics simulations the theory will be compared to [25] in the next chapter.

The first step is making the master equation in Eq.(3.1) dimensionless by introducing

$$\begin{cases} \tilde{r} = r/\sigma; \\ \tilde{U} = \beta U; \\ \mathbf{v(r)} = \dot{\gamma}\sigma\tilde{\mathbf{v}}(\tilde{\mathbf{r}}); \\ \underline{\mathbf{D}} = 2D_0\underline{\tilde{\mathbf{D}}} = 2\dfrac{k_BT}{6\pi\eta R_\mathrm{P}}\underline{\tilde{\mathbf{D}}} \end{cases} \tag{3.2}$$

Replacing all the previously introduced terms in Eq.(2.26) and rearranging it is obtained that

$$2\tilde{\nabla}\cdot\underline{\tilde{\mathbf{D}}}\cdot\left(\tilde{\nabla}\tilde{U}g(\tilde{\mathbf{r}})+\tilde{\nabla}g(\tilde{\mathbf{r}})\right)-\tilde{\nabla}\cdot\left(4\frac{6\pi\eta\dot{\gamma}R_\mathrm{P}^3}{k_BT}\tilde{\mathbf{v}}(\tilde{\mathbf{r}})g(\tilde{\mathbf{r}})\right)=0. \tag{3.3}$$

Introducing the Péclet number according to Eq.(2.40) it can be written that:

$$\tilde{\nabla}\cdot\underline{\tilde{\mathbf{D}}}\cdot\left(\tilde{\nabla}\tilde{U}g(\tilde{\mathbf{r}})+\tilde{\nabla}g(\tilde{\mathbf{r}})\right)-2\,\mathrm{Pe}\tilde{\nabla}\cdot\left(\tilde{\mathbf{v}}(\tilde{\mathbf{r}})g(\tilde{\mathbf{r}})\right)=0. \tag{3.4}$$

By applying the linearity of the divergence operators Eq.(3.4) can be written as follows:

$$\frac{1}{\mathrm{Pe}}\left[\tilde{\nabla}\cdot\left(\underline{\tilde{\mathbf{D}}}\cdot\tilde{\nabla}g(\tilde{\mathbf{r}})\right)+\tilde{\nabla}\cdot\underline{\tilde{\mathbf{D}}}\cdot\left(\tilde{\nabla}\tilde{U}g(\tilde{\mathbf{r}})\right)\right]-2\left(\tilde{\mathbf{v}}\cdot\tilde{\nabla}g(\tilde{\mathbf{r}})+g(\tilde{\mathbf{r}})\tilde{\nabla}\cdot\tilde{\mathbf{v}}\right)=0. \tag{3.5}$$

At this point, the mathematical procedure to make the problem analytically solvable is presented.

3.1 Angular integral average

The mathematical treatment is based on reducing a 3D problem to a one-dimensional equivalent in which all the major features reported in Eq.(3.5) are dependent on the radial coordinate $\tilde{r}$ only.
The first step is the application of an angular average $\langle\cdots\rangle$ over a certain portion of the solid angle Ω to Eq.(3.5); its main result is the introduction of an angular averaged pcf over Ω which depends on $\tilde{r}$ only:

$$g(\tilde{r}) = \langle g(\tilde{\mathbf{r}})\rangle = \frac{1}{4\pi}\int g(\tilde{\mathbf{r}})d\Omega. \tag{3.6}$$

Since both $\underline{\tilde{\mathbf{D}}}$ and $\tilde{U}$ have no angular dependence it can be written that

$$\frac{1}{\mathrm{Pe}}\left[\tilde{\nabla}\cdot\left(\underline{\tilde{\mathbf{D}}}\cdot\tilde{\nabla}g(\tilde{r})\right)+\tilde{\nabla}\cdot\underline{\tilde{\mathbf{D}}}\cdot\left(\tilde{\nabla}\tilde{U}g(\tilde{r})\right)\right]-2\left(\langle\tilde{\mathbf{v}}\cdot\tilde{\nabla}g(\tilde{\mathbf{r}})\rangle+\langle g(\tilde{\mathbf{r}})\tilde{\nabla}\cdot\tilde{\mathbf{v}}\rangle\right)=0. \tag{3.7}$$

Next, it is necessary to apply a *decoupling* procedure: supposing that the velocity and the pair correlation function are weakly correlated the average of the scalar product can be replaced by the scalar product of the averages as follows:

$$\langle\tilde{\mathbf{v}}\cdot\tilde{\nabla}g(\tilde{\mathbf{r}})\rangle+\langle g(\tilde{\mathbf{r}})\tilde{\nabla}\cdot\tilde{\mathbf{v}}\rangle\approx\langle\tilde{\mathbf{v}}\rangle\cdot\tilde{\nabla}g(\tilde{r})+g(\tilde{r})\langle\tilde{\nabla}\cdot\tilde{\mathbf{v}}\rangle. \tag{3.8}$$

finally completing the transition from a 3D problem to a 1D equivalent:

$$\frac{1}{\mathrm{Pe}}\left[\tilde{\nabla}\cdot\left(\underline{\tilde{\mathbf{D}}}\cdot\tilde{\nabla}g(\tilde{r})\right)+\tilde{\nabla}\cdot\underline{\tilde{\mathbf{D}}}\cdot\left(\tilde{\nabla}\tilde{U}g(\tilde{r})\right)\right]-2\left(\langle\tilde{\mathbf{v}}\rangle\cdot\tilde{\nabla}g(\tilde{r})+g(\tilde{r})\langle\tilde{\nabla}\cdot\tilde{\mathbf{v}}\rangle\right)=0. \tag{3.9}$$

Nevertheless, a correct definition of the solid angles where the average is applied is of pivotal importance and they can be found through the analysis of the radial velocity v_r.
In the previous chapter it has been introduced how a simple shear flow can be separated into *compressing* sectors of solid angle (radial velocity between the particles is negative) and *extensional* regions where the particles move away from each other (positive sign of the radial velocity).
The solid angles are then chosen so that the overall microstructure g(**r**) is replaced by a duo of angular average pair correlation functions: one, named $g_{\mathrm{c}}(\tilde{r})$, represents the spatial arrangement of the suspension in the compressing regions, meanwhile $g_{\mathrm{e}}(\tilde{r})$ describes the microstructure related to the extensional sectors; the price to pay for it is the impossibility to produce deformed contour plots to highlight the angle-dependent pcfs. From this point on every angular average quantity will be represented according to the following formalism: $\langle\ldots\rangle_{\mathrm{i}}$, where i = c refers to the compressing quadrants, meanwhile i = e indicates the extensional regions.
Another consequence of the angular integral average procedure is the replacement of the actual **v** and $\tilde{\nabla}\cdot\tilde{\mathbf{v}}$ with their angular averaged equivalents. The new angular averaged radial velocity $\langle\tilde{\mathbf{v}}\rangle_{\mathrm{i}}$ can be written as

$$\begin{aligned}\langle\tilde{\mathbf{v}}\rangle_{\mathrm{i}}=\tilde{r}(1-A(\tilde{r}))\frac{1}{4\pi}\Bigg[&\int_{\theta_1}^{\theta_2}\sin^2(\theta)\sin(\theta)d\theta\times\\&\times\left(\int_{\phi_1}^{\phi_2}\sin(\phi)\cos(\phi)d\phi+\int_{\phi_3}^{\phi_4}\sin(\phi)\cos(\phi)d\phi\right)\Bigg]=\alpha_i\tilde{r}(1-A(\tilde{r})),\end{aligned} \tag{3.10}$$

where θ_1 and θ_2 together with ϕ_1, ϕ_2, ϕ_3 and ϕ_4 are, respectively, the borders of the polar and azimuthal coordinate which respect the compressional/extensional condition; they will be used to compute α_i, the coefficient which describes the angular averaged effect of the flow field.
At the same time the angular averaged divergence $\langle \nabla \cdot \tilde{\mathbf{v}} \rangle$ is evaluated starting from its formal definition in spherical coordinates:

$$\tilde{\nabla} \cdot \tilde{\mathbf{v}} = \frac{1}{\tilde{r}^2} \frac{\partial}{\partial \tilde{r}} \left(\tilde{r}^2 \tilde{v}_r \right) + \frac{1}{\tilde{r} \sin(\theta)} \frac{\partial}{\partial \theta} \left(\sin(\theta) \tilde{v}_\theta \right) + \frac{1}{\tilde{r} \sin\theta} \frac{\partial}{\partial \phi} \left(\tilde{v}_\phi \right). \tag{3.11}$$

Adopting the correlations in Eq.(2.38), it can be expressed as

$$\tilde{\nabla} \cdot \tilde{\mathbf{v}} = \left[3(B(\tilde{r}) - A(\tilde{r})) - \tilde{r} \frac{\mathrm{d}A}{\mathrm{d}\tilde{r}} \right] \sin^2\theta \sin\phi \cos\phi. \tag{3.12}$$

Applying the same angular average procedure seen for Eq.(3.10) it is obtained that

$$\langle \tilde{\nabla} \cdot \tilde{\mathbf{v}} \rangle_{\mathrm{i}} = \alpha_i \left[3(B(\tilde{r}) - A(\tilde{r})) - \tilde{r} \frac{\mathrm{d}A}{\mathrm{d}\tilde{r}} \right]; \tag{3.13}$$

thus, for each quadrant the following angular average velocity and divergence are obtained:

$$\begin{cases} \langle \tilde{\mathbf{v}} \rangle_{\mathrm{i}} = \alpha_i (1 - A(\tilde{r})) \tilde{r}, \\ \langle \tilde{\nabla} \cdot \tilde{\mathbf{v}} \rangle_{\mathrm{i}} = \alpha_i \left(3(B(\tilde{r}) - A(\tilde{r})) - \tilde{r} \dfrac{dA(\tilde{r})}{d\tilde{r}} \right). \end{cases} \tag{3.14}$$

3.1.1 Compressing quadrants

To evaluate $\langle \tilde{\mathbf{v}} \rangle$ in the region where the particles are approaching each other, the θ_i and ϕ_i which cause $\tilde{v}_r$ to be negative need to be found.
Starting from the definition of the radial velocity

$$\tilde{v}_r = \tilde{r} \sin^2(\theta) \sin(\phi) \cos(\phi), \tag{3.15}$$

it can be noticed by inspection that, imposing $\tilde{r} > 0$, the $\theta-$dependent part is positive $\forall \theta \in [0, \pi]$. As a consequence, $\tilde{v}_r$ can be negative only if

$$\sin(\phi) \cos(\phi) < 0; \tag{3.16}$$

Eq.(3.16) is satisfied by $\phi \in [\pi/2, \pi]$ and $\phi \in [3\pi/2, 2\pi]$.
This makes perfect sense: the medium point of the interval $[\pi/2\pi]$ is $\phi_c = 3\pi/4 = 135^\circ$

which corresponds to the values of the compressional axes of the straining portion of the shear flow [25].
Eq.(3.10) can then be applied:

$$\langle\tilde{\mathbf{v}}\rangle_{\mathrm{c}} = \tilde{r}(1-A(\tilde{r}))\frac{1}{4\pi}\left[\int_0^{\pi}\sin^2(\theta)\sin(\theta)d\theta\times \right.$$
$$\left.\times\left(\int_{\pi/2}^{\pi}\sin(\phi)\cos(\phi)d\phi+\int_{3\pi/2}^{2\pi}\sin(\phi)\cos(\phi)d\phi\right)\right], \quad (3.17)$$

and the following result is obtained

$$\alpha_c = -\frac{1}{3\pi}. \quad (3.18)$$

3.1.2 Extensional quadrants

In this case the opposite condition is imposed: $\tilde{v}_r > 0$. Following the same procedure it can be found that $\phi \in [0,\pi/2]$ and $\phi \in [\pi, 3\pi/2]$; in this case the medium of $[0\pi/2]$ is $\phi_e = \pi/4 = 45°$, which corresponds to the extensional axes of a simple shear flow.
Applying Eq.(3.10) to the new quadrant it is found that

$$\alpha_e = \frac{1}{3\pi}. \quad (3.19)$$

3.2 Singular perturbation methodology

After having applied all the steps seen in the previous section, it is useful to recall the master equation for each quadrant:

$$\frac{1}{\mathrm{Pe}}\left[\tilde{\nabla}\cdot\left(\underline{\tilde{\mathbf{D}}}\cdot\tilde{\nabla}g_{\mathrm{i}}(\tilde{r})\right)+\tilde{\nabla}\cdot\left(\underline{\tilde{\mathbf{D}}}\cdot\tilde{\nabla}\tilde{U}\right)g_{\mathrm{i}}(\tilde{r})+\left(\underline{\tilde{\mathbf{D}}}\cdot\tilde{\nabla}\tilde{U}\right)\cdot\tilde{\nabla}g_{\mathrm{i}}(\tilde{r})\right]+$$
$$-2\left(\langle\tilde{\mathbf{v}}\rangle_{\mathrm{i}}\cdot\tilde{\nabla}g_{\mathrm{i}}(\tilde{r})+g_{\mathrm{i}}(\tilde{r})\langle\tilde{\nabla}\cdot\tilde{\mathbf{v}}\rangle_{\mathrm{i}}\right)=0 \quad (3.20)$$

and isolate the dependence on the radial coordinate only

$$\frac{1}{\mathrm{Pe}}\left[\frac{1}{\tilde{r}^2}\frac{\mathrm{d}}{\mathrm{d}\tilde{r}}\left(\tilde{r}^2\chi_i(\tilde{r})^{-1}\frac{\mathrm{d}g_{\mathrm{i}}(\tilde{r})}{\mathrm{d}\tilde{r}}\right)+\frac{1}{\tilde{r}^2}\frac{\mathrm{d}}{\mathrm{d}\tilde{r}}\left(\tilde{r}^2\chi_i(\tilde{r})^{-1}\frac{\mathrm{d}\tilde{U}}{\mathrm{d}\tilde{r}}\right)g_{\mathrm{i}}(\tilde{r})+\chi_i(\tilde{r})^{-1}\frac{\mathrm{d}\tilde{U}}{\mathrm{d}\tilde{r}}\frac{\mathrm{d}g_{\mathrm{i}}(\tilde{r})}{\mathrm{d}\tilde{r}}\right]+$$
$$-2\left(\langle\tilde{\mathbf{v}}\rangle_{\mathrm{i}}\frac{\mathrm{d}g_{\mathrm{i}}(\tilde{r})}{\mathrm{d}\tilde{r}}+g_{\mathrm{i}}(\tilde{r})\langle\tilde{\nabla}\cdot\tilde{\mathbf{v}}\rangle\right)=0. \quad (3.21)$$

In the end, by introducing a parameter ε known as *perturbation parameter*:

$$\varepsilon = \frac{1}{\mathrm{Pe}} \tag{3.22}$$

and by adding the proper boundary conditions, the final BVP can be written as:

$$\begin{cases} \varepsilon\left[\chi_i^{-1}\left(\dfrac{\mathrm{d}^2 g_\mathrm{i}}{\mathrm{d}\tilde{r}^2}+\dfrac{2}{\tilde{r}}\dfrac{\mathrm{d}g_\mathrm{i}}{\mathrm{d}\tilde{r}}\right)+\dfrac{\mathrm{d}(\chi_i^{-1})}{\mathrm{d}\tilde{r}}\dfrac{\mathrm{d}g_\mathrm{i}}{\mathrm{d}\tilde{r}}+g_\mathrm{i}\dfrac{\mathrm{d}\tilde{U}}{\mathrm{d}\tilde{r}}\dfrac{\mathrm{d}(\chi_i^{-1})}{\mathrm{d}\tilde{r}}+\chi_i^{-1}\left(\dfrac{2}{\tilde{r}}\dfrac{\mathrm{d}\tilde{U}}{\mathrm{d}\tilde{r}}+\dfrac{\mathrm{d}^2\tilde{U}}{\mathrm{d}\tilde{r}^2}\right)g_\mathrm{i}+ \right. \\ \left. +\chi_i^{-1}\dfrac{\mathrm{d}\tilde{U}}{\mathrm{d}\tilde{r}}\dfrac{\mathrm{d}g_\mathrm{i}}{\mathrm{d}\tilde{r}}\right]-2\left(\langle\tilde{\mathbf{v}}\rangle_\mathrm{i}\dfrac{\mathrm{d}g_\mathrm{i}}{\mathrm{d}\tilde{r}}+g_\mathrm{i}\langle\tilde{\nabla}\cdot\tilde{\mathbf{v}}\rangle_\mathrm{i}\right)=0, \\ \\ g_\mathrm{i}(\tilde{r}\to\infty)=1, \\ \chi_i(\tilde{r}_c)^{-1}\left(\dfrac{\mathrm{d}g_\mathrm{i}}{\mathrm{d}\tilde{r}}\right)_{\tilde{r}=\tilde{r}_c}+\left(\chi_i(\tilde{r}_c)^{-1}\dfrac{\mathrm{d}\tilde{U}}{\mathrm{d}\tilde{r}}-2\mathrm{Pe}\langle\tilde{\mathbf{v}}\rangle_\mathrm{i}\right)g_\mathrm{i}(\tilde{r}_c)=0. \end{cases} \tag{3.23}$$

From inspection of Eq.(3.23) it can immediately be seen that the perturbation parameter is linked with the highest order derivative of the ordinary differential equation (ODE). If its value is small enough, the problem is said to be *singularly perturbed* and it can be solved by the application of the boundary layer theory [58].
The approach, also called *intermediate asymptotics methodology*, consists of the evaluation of two different power series related to two different regions of the domain: the first is the outer layer, the furthest region from the reference particle, where the solution is slowly changing with $\tilde{r}$, meanwhile the second is the inner region, also called boundary layer, which is the closer to the reference particle where the solution is steeply and very rapidly changing with the normalized radial coordinate.

3.3 Outer solution

The outer solution for each quadrant will be written as a power series in the small parameter ε:

$$g_\mathrm{i}^{\mathrm{out}} = g_{0,\mathrm{i}}^{\mathrm{out}} + \varepsilon g_{1,\mathrm{i}}^{\mathrm{out}} + \varepsilon^2 g_{2,\mathrm{i}}^{\mathrm{out}} + \ldots, \tag{3.24}$$

where $g_{0,\mathrm{i}}^{\mathrm{out}}$ is the leading order term, $g_{1,\mathrm{i}}^{\mathrm{out}}$ is the first order one and so on; within this work calculations have been carried on up to the first order for both of the outer and the inner solutions.

3.3.1 Leading order term

To find $g_{0,\mathrm{i}}^{\mathrm{out}}$ it is supposed that the solution is characterized by sufficiently low values of its derivatives, so that they become negligible if multiplied by a small parameter such as ε; this concept is practically implemented by imposing $\varepsilon = 0$ in Eq.(3.23).
The immediate consequence is the reduction of the order of the ODE, so only boundary condition can be imposed: since the boundary layer is close to $\tilde{r}_c$ far-field one is chosen, ending up with the following boundary value problem:

$$\begin{cases} \langle \tilde{\mathbf{v}} \rangle_{\mathrm{i}} \dfrac{\mathrm{d}g_{0,\mathrm{i}}^{\mathrm{out}}(\tilde{r})}{\mathrm{d}r} + g_{0,\mathrm{i}}^{\mathrm{out}}(\tilde{r}) \langle \tilde{\nabla} \cdot \tilde{\mathbf{v}} \rangle_{\mathrm{i}} = 0. \\ g_{0,\mathrm{i}}^{\mathrm{out}}(\tilde{r} \to \infty) = 1 \end{cases} \tag{3.25}$$

Mathematical steps

Rewriting Eq.(3.25) as

$$\frac{\mathrm{d}g_{0,\mathrm{i}}^{\mathrm{out}}(\tilde{r})}{\mathrm{d}\tilde{r}} + g_{0,\mathrm{i}}^{\mathrm{out}}(\tilde{r}) \frac{\langle \tilde{\nabla} \cdot \tilde{\mathbf{v}} \rangle_{\mathrm{i}}}{\langle \tilde{\mathbf{v}} \rangle_{\mathrm{i}}} = 0. \tag{3.26}$$

This first order ODE can be solved through the introduction of an integrating factor $\mu(\tilde{r})$:

$$\mu(\tilde{r}) = \exp \int \left(\frac{\langle \tilde{\nabla} \cdot \tilde{\mathbf{v}} \rangle_{\mathrm{i}}}{\langle \tilde{\mathbf{v}} \rangle_{\mathrm{i}}} \right) d\tilde{r} = \exp \left[- \int_{\tilde{r}}^{\infty} \left(\frac{\langle \tilde{\nabla} \cdot \tilde{\mathbf{v}} \rangle_{\mathrm{i}}}{\langle \tilde{\mathbf{v}} \rangle_{\mathrm{i}}} \right) d\tilde{r} \right] \tag{3.27}$$

Replacing Eq.(3.17) and Eq.(3.13) it is obtained

$$\mu(\tilde{r}) = \exp \int_{\tilde{r}}^{\infty} - \left[\frac{3(B(\tilde{r}) - A(\tilde{r}))}{\tilde{r}(1 - A(\tilde{r}))} - \frac{\mathrm{d}A/\mathrm{d}\tilde{r}}{1 - A(\tilde{r})} \right] d\tilde{r} \tag{3.28}$$

Multiplying both sides of Eq.(3.26) by $\mu(\tilde{r})$ and considering the far field boundary condition the following can be written

$$\begin{cases} \dfrac{d(g_{0,\mathrm{i}}^{\mathrm{out}}\, \mu(\tilde{r}))}{d\tilde{r}} = 0 \\ g_{0,\mathrm{i}}^{\mathrm{out}} = 1 \quad \tilde{r} \to \infty \end{cases} \tag{3.29}$$

which leads to the straightforward calculation

$$g_{0,\mathrm{i}}^{\mathrm{out}} = \frac{1}{\mu(\tilde{r})} = \exp \int_{\tilde{r}}^{\infty} \left[\frac{3(B(\tilde{r}) - A(\tilde{r}))}{\tilde{r}(1 - A(\tilde{r}))} - \frac{\mathrm{d}A/\mathrm{d}\tilde{r}}{1 - A(\tilde{r})} \right] d\tilde{r} \tag{3.30}$$

Rearranging Eq.(3.30) it can be noticed that the leading order term for both the compressing and extensional regions is the same, which means that the microstructure is featured by a spherical symmetry and is easy to observe that it corresponds to the solution proposed by

Batchelor and Green for pure straining motion [23]:

$$g_{0,\mathrm{i}}^{\mathrm{out}} = \frac{1}{1-A(\tilde{r})} \exp\left[\int_{\tilde{r}}^{\infty} \left(\frac{3(B-A)}{\tilde{r}(1-A)}\right) d\tilde{r}\right], \tag{3.31}$$

an evidence that our approach include previous theoretical frameworks and improve them by considering the perturbation of the Brownian-induced contributions by evaluating the next order term.

3.3.2 First order term

To evaluate $g_{1,\mathrm{i}}^{\mathrm{out}}$ the first and second derivative of $g_{\mathrm{i}}^{\mathrm{out}}$ needs to be developed

$$\begin{cases} \dfrac{\mathrm{d}g_{\mathrm{i}}^{\mathrm{out}}}{\mathrm{d}\tilde{r}} = \dfrac{\mathrm{d}g_{0,\mathrm{i}}^{\mathrm{out}}}{\mathrm{d}\tilde{r}} + \varepsilon \dfrac{\mathrm{d}g_{1,\mathrm{i}}^{\mathrm{out}}}{\mathrm{d}\tilde{r}} + \dots \\ \dfrac{\mathrm{d}^2 g_{\mathrm{i}}^{\mathrm{out}}}{\mathrm{d}\tilde{r}^2} = \dfrac{\mathrm{d}^2 g_{0,\mathrm{i}}^{\mathrm{out}}}{\mathrm{d}\tilde{r}^2} + \varepsilon \dfrac{\mathrm{d}^2 g_{1,\mathrm{i}}^{\mathrm{out}}}{\mathrm{d}\tilde{r}^2} + \dots \end{cases} \tag{3.32}$$

and replaced together with Eq.(3.24) in Eq.(3.23) and grouped all the terms linked with the same power of the perturbation parameter.
Since the task of $g_{1,\mathrm{i}}^{\mathrm{out}}$ is the evaluation of the impact of the Brownian motion on a purely sheared suspension, ε can not be null. So, the only way to find the n-th order coefficient of Eq.(3.24) is to impose the coefficient related to the n-th power of ε to be zero. $g_{1,\mathrm{i}}^{\mathrm{out}}$ can be found by isolating the coefficient which multiplies the first power of ε:

$$\begin{cases} \left[\chi_i^{-1}\left(\dfrac{\mathrm{d}^2 g_{0,\mathrm{i}}^{\mathrm{out}}}{\mathrm{d}\tilde{r}^2} + \dfrac{2}{\tilde{r}}\dfrac{\mathrm{d}g_{0,\mathrm{i}}^{\mathrm{out}}}{\mathrm{d}\tilde{r}}\right) + \dfrac{\mathrm{d}(\chi_i^{-1})}{\mathrm{d}\tilde{r}}\dfrac{\mathrm{d}g_{0,\mathrm{i}}^{\mathrm{out}}}{\mathrm{d}\tilde{r}} + g_{0,\mathrm{i}}^{\mathrm{out}}\dfrac{\mathrm{d}\tilde{U}}{\mathrm{d}\tilde{r}}\dfrac{\mathrm{d}(\chi_i^{-1})}{\mathrm{d}\tilde{r}} + \right. \\ \left. + \chi_i^{-1}\dfrac{\mathrm{d}\tilde{U}}{\mathrm{d}\tilde{r}}\dfrac{\mathrm{d}g_{0,\mathrm{i}}^{\mathrm{out}}}{\mathrm{d}\tilde{r}} + \chi_i^{-1}\left(\dfrac{2}{\tilde{r}}\dfrac{\mathrm{d}\tilde{U}}{\mathrm{d}\tilde{r}} + \dfrac{\mathrm{d}^2\tilde{U}}{\mathrm{d}\tilde{r}^2}\right) g_{0,\mathrm{i}}^{\mathrm{out}}\right] - 2\left(\langle\tilde{\mathbf{v}}\rangle_{\mathrm{i}}\dfrac{\mathrm{d}g_{1,\mathrm{i}}^{\mathrm{out}}}{\mathrm{d}\tilde{r}} + g_{1,\mathrm{i}}^{\mathrm{out}}\langle\tilde{\nabla}\cdot\tilde{\mathbf{v}}\rangle_{\mathrm{i}}\right) = 0, \\ \\ g_{1,\mathrm{i}}^{\mathrm{out}}(\tilde{r}\to\infty) = 0. \end{cases} \tag{3.33}$$

The boundary condition in Eq.(3.33) represents the independence of far-field boundary condition from the Péclet number.

Mathematical steps

It is possible to solve Eq.(3.33) analytically by expressing the first and the second order derivative of $g_{0,\mathrm{i}}^{\mathrm{out}}$ as

$$\begin{cases} \dfrac{\mathrm{d}g_{0,\mathrm{i}}^{\mathrm{out}}}{\mathrm{d}\tilde{r}} = -\dfrac{\langle\tilde{\nabla}\cdot\tilde{\mathbf{v}}\rangle_{\mathrm{i}}}{\langle\tilde{\mathbf{v}}\rangle_{\mathrm{i}}} g_{0,\mathrm{i}}^{\mathrm{out}} = -\left[\dfrac{3(B(\tilde{r})-A(\tilde{r}))}{\tilde{r}(1-A(\tilde{r}))} - \dfrac{\mathrm{d}A/\mathrm{d}\tilde{r}}{1-A(\tilde{r})}\right] g_{0,\mathrm{i}}^{\mathrm{out}} = Y(\tilde{r}) g_{0,\mathrm{i}}^{\mathrm{out}} \\ \dfrac{\mathrm{d}^2 g_{0,\mathrm{i}}^{\mathrm{out}}}{\mathrm{d}\tilde{r}^2} = \left(Y^2(r) + \dfrac{\mathrm{d}Y(\tilde{r})}{\mathrm{d}\tilde{r}}\right) g_{0,\mathrm{i}}^{\mathrm{out}} \end{cases} \tag{3.34}$$

By replacing the derivatives in Eq.(3.33) it is readily obtained that

$$\frac{g_{0,\mathrm{i}}^{\mathrm{out}}(\tilde{r})}{2\langle\tilde{\mathbf{v}}\rangle_{\mathrm{i}}}\left\{\chi_i^{-1}\left(Y^2+\frac{\mathrm{d}Y}{\mathrm{d}\tilde{r}}\right)+\left[\chi_i^{-1}\left(\frac{2}{\tilde{r}}+\frac{\mathrm{d}\tilde{U}}{\mathrm{d}\tilde{r}}\right)+\frac{\mathrm{d}(\chi_i^{-1})}{\mathrm{d}\tilde{r}}\right]Y+ \right. \\ \left. +\chi_i^{-1}\left(\frac{\mathrm{d}^2\tilde{U}}{\mathrm{d}\tilde{r}^2}+\frac{2}{\tilde{r}}\frac{\mathrm{d}\tilde{U}}{\mathrm{d}\tilde{r}}\right)+\frac{\mathrm{d}(\chi_i^{-1})}{\mathrm{d}\tilde{r}}\frac{\mathrm{d}\tilde{U}}{\mathrm{d}\tilde{r}}\right\} = \frac{\mathrm{d}g_{1,\mathrm{i}}^{\mathrm{out}}}{\mathrm{d}\tilde{r}} + g_{1,\mathrm{i}}^{\mathrm{out}}\left(\frac{\langle\tilde{\nabla}\cdot\tilde{\mathbf{v}}\rangle_{\mathrm{i}}}{\langle\tilde{\mathbf{v}}\rangle_{\mathrm{i}}}\right). \tag{3.35}$$

Equation (3.35) can be solved analytically by adopting the same integrating factor $\mu(\tilde{r})$ introduced in Eq.(3.27-3.28) which simplifies it as:

$$\frac{\mathrm{d}}{\mathrm{d}\tilde{r}}\left(\mu(\tilde{r})g_{1,\mathrm{i}}^{\mathrm{out}}\right) = \frac{1}{2\langle\tilde{\mathbf{v}}\rangle_{\mathrm{i}}}\left\{\chi_i^{-1}\left(Y^2+\frac{\mathrm{d}Y}{\mathrm{d}\tilde{r}}\right)+\left[\chi_i^{-1}\left(\frac{2}{\tilde{r}}+\frac{\mathrm{d}\tilde{U}}{\mathrm{d}\tilde{r}}\right)+\frac{\mathrm{d}(\chi_i^{-1})}{\mathrm{d}\tilde{r}}\right]Y+ \right. \\ \left. +\chi_i(\tilde{r})^{-1}\left(\frac{\mathrm{d}^2\tilde{U}}{\mathrm{d}\tilde{r}^2}+\frac{2}{\tilde{r}}\frac{\mathrm{d}\tilde{U}}{\mathrm{d}\tilde{r}}\right)+\frac{\mathrm{d}(\chi_i^{-1})}{\mathrm{d}\tilde{r}}\frac{\mathrm{d}\tilde{U}}{\mathrm{d}\tilde{r}}\right\}. \tag{3.36}$$

Finally it is possible to integrate the previous equation within the interval $[\tilde{r},\infty]$ obtaining the final form of $g_{1,\mathrm{i}}^{\mathrm{out}}$:

$$g_{1,\mathrm{i}}^{\mathrm{out}} = -g_{0,\mathrm{i}}^{\mathrm{out}}\int_{\tilde{r}}^{\infty}\frac{1}{2\langle\tilde{\mathbf{v}}\rangle_{\mathrm{i}}}\left\{\chi_i^{-1}\left[Y^2+\frac{\mathrm{d}Y}{\mathrm{d}\tilde{r}}+\left(\frac{2}{\tilde{r}}+\frac{\mathrm{d}\tilde{U}}{\mathrm{d}\tilde{r}}\right)Y+\frac{\mathrm{d}^2\tilde{U}}{\mathrm{d}\tilde{r}^2}+\frac{2}{\tilde{r}}\frac{\mathrm{d}\tilde{U}}{\mathrm{d}\tilde{r}}\right]+ \right. \\ \left. +\frac{\mathrm{d}(\chi_i^{-1})}{\mathrm{d}\tilde{r}}\left(Y+\frac{\mathrm{d}\tilde{U}}{\mathrm{d}\tilde{r}}\right)\right\}\mathrm{d}\tilde{r}. \tag{3.37}$$

3.3.3 Final remarks

By expressing Eq.(3.31) and Eq.(3.37) into Eq.(3.24) the complete form of the outer solution is obtained:

$$g_{\mathrm{i}}^{\mathrm{out}}(\tilde{r}) = \left[1-\varepsilon\left(\int_{\tilde{r}}^{\infty}\frac{1}{2\langle\tilde{\mathbf{v}}\rangle_{\mathrm{i}}}\left\{\chi_i^{-1}\left[Y^2+\frac{\mathrm{d}Y}{\mathrm{d}\tilde{r}}+\left(\frac{2}{\tilde{r}}+\frac{\mathrm{d}\tilde{U}}{\mathrm{d}\tilde{r}}\right)Y+\right.\right.\right.$$
$$\left.\left.\left.+\frac{\mathrm{d}^2\tilde{U}}{\mathrm{d}\tilde{r}^2}+\frac{2}{\tilde{r}}\frac{\mathrm{d}\tilde{U}}{\mathrm{d}\tilde{r}}\right]+\frac{\mathrm{d}(\chi_i^{-1})}{\mathrm{d}\tilde{r}}\left(Y+\frac{\mathrm{d}\tilde{U}}{\mathrm{d}\tilde{r}}\right)\right\}\mathrm{d}\tilde{r}\right)\right]g_{0,\mathrm{i}}^{\mathrm{out}}+O(\varepsilon^2), \quad (3.38)$$

where $g_{0,\mathrm{i}}^{\mathrm{out}}$ is recalled to be the spherical symmetric solution obtained by Batchelor & Green:

$$g_{0,\mathrm{i}}^{\mathrm{out}} = \frac{1}{1-A(\tilde{r})}\exp\left[\int_{\tilde{r}}^{\infty}\left(\frac{3(B-A)}{\tilde{r}(1-A)}\right)d\tilde{r}\right]. \quad (3.39)$$

Eq.(3.38) is a novel extension of [47], valid for regions sufficiently far away from the reference particle, which considers the anisotropic perturbation from Brownian-induced contributions, whose weight is determined by the perturbation parameter $\varepsilon = O(\mathrm{Pe}^{-1})$, on an isotropic microstructure initially generated by a purely straining motion.

3.4 Inner Solution

Focusing now on the small section of the domain where the solution varies dramatically with $\tilde{r}$, the first step is the application of change of variable called *inner transformation*. Since it is known that the region where the rdf varies the most is close to the reference particle, the inner coordinate ξ will be defined as

$$\xi = \frac{\tilde{r}-\tilde{r}_c}{\delta(\varepsilon)}, \quad (3.40)$$

where $\delta(\varepsilon)$ is the order of magnitude of the width of the boundary layer.

3.4.1 Dominant balancing

Before turning to the evaluation of the inner solution $g_{\mathrm{i}}^{\mathrm{in}}$ the relationship between $\delta(\varepsilon)$ and the perturbation parameter ε itself has to be found; this procedure is called *dominant balancing*

[58, 59]. At first, the inner transformation has to be applied to Eq.(3.23):

$$\varepsilon\Bigg[\chi_i^{-1}(\xi)\left(\frac{\mathrm{d}^2 g_{\mathrm{i}}^{\mathrm{in}}(\xi)/\mathrm{d}\xi^2}{\delta^2(\varepsilon)}+\frac{2}{(\xi\,\delta(\varepsilon)+\tilde{r}_c)}\frac{\mathrm{d}g_{\mathrm{i}}^{\mathrm{in}}/\mathrm{d}\xi}{\delta(\varepsilon)}\right)+\frac{(\mathrm{d}(\chi_i^{-1})/\mathrm{d}\xi)(\mathrm{d}g_{\mathrm{i}}^{\mathrm{in}}/\mathrm{d}\xi)}{\delta(\varepsilon)^2}+$$
$$+\chi_i^{-1}(\xi)\left(\frac{\mathrm{d}^2\tilde{U}/\mathrm{d}\xi^2}{\delta(\varepsilon)^2}+\frac{2}{(\xi\,\delta(\varepsilon)+\tilde{r}_c)}\frac{\mathrm{d}\tilde{U}/\mathrm{d}\xi}{\delta(\varepsilon)}\right)+\chi_i^{-1}(\xi)\frac{(\mathrm{d}\tilde{U}/\mathrm{d}\xi)(\mathrm{d}g_{\mathrm{i}}^{\mathrm{in}}/\mathrm{d}\xi)}{\delta(\varepsilon)^2}+$$
$$+g_{\mathrm{i}}^{\mathrm{in}}\frac{(\mathrm{d}\tilde{U}/\mathrm{d}\xi)(\mathrm{d}(\chi_i^{-1})/\mathrm{d}\xi)}{\delta(\varepsilon)^2}\Bigg]-2\left(\frac{\langle\tilde{\mathbf{v}}(\xi)\rangle_{\mathrm{i}}}{\delta(\varepsilon)}\mathrm{d}g_{\mathrm{i}}^{\mathrm{in}}/\mathrm{d}\xi+g_{\mathrm{i}}^{\mathrm{in}}\langle\tilde{\nabla}\cdot\tilde{\mathbf{v}}(\xi)\rangle_{\mathrm{i}}\right)=0. \quad (3.41)$$

The crucial point of the dominant balancing is finding the asymptotic behaviour of all the functions in the above ODE with respect to $\delta(\varepsilon)$ and ε. For this reason a set of "gauge functions" which represent the asymptotic trend of every term in Eq.(3.41) as $\varepsilon\to 0$ [60] has to be found.
At first, focusing the attention on the angular-averaged quantities proposed in Eq.(3.42):

$$\begin{cases}\langle\tilde{\mathbf{v}}\rangle_{\mathrm{i}}=\alpha_i(\xi\,\delta+\tilde{r}_c)(1-A(\xi)),\\[2ex]\langle\tilde{\nabla}\cdot\tilde{\mathbf{v}}(\xi)\rangle_{\mathrm{i}}=\alpha_i\left[3(B(\xi)-A(\xi))-\dfrac{(\xi\,\delta+\tilde{r}_c)}{\delta(\varepsilon)}\dfrac{\mathrm{d}A}{\mathrm{d}\xi}\right].\end{cases} \quad (3.42)$$

It can be observed that $\langle\tilde{\mathbf{v}}\rangle_{\mathrm{i}}$ tends a finite value as $\delta\to 0$, so its gauge function will be a finite number, represented as $O(1)$.
To establish the gauge function related to $\langle\tilde{\nabla}\cdot\tilde{\mathbf{v}}(\xi)\rangle$ an ulterior function for $\mathrm{d}A/\mathrm{d}\xi$ is needed. Starting from the definition of A(r) provided in Eq.(2.39):

$$A(r)=\frac{113.2568894}{(2\tilde{r})^5}+\frac{307.8264828}{(2\tilde{r})^6}-\frac{2607.54064288}{(2\tilde{r})^7}+\frac{3333.72020041}{(2\tilde{r})^8}. \quad (3.43)$$

Now, it is necessary to apply the inner transformation Eq.(3.40), and then the derivative with respect to the inner variable can be computed as:

$$\frac{\mathrm{d}A}{\mathrm{d}\xi}=\delta\left(\frac{-104.179+142.6(\mathrm{r}_c+\delta\xi)-28.8587(\mathrm{r}_c+\delta\xi)^2}{(\mathrm{r}_c+\delta\xi)^9}-\frac{17.6964}{(\mathrm{r}_c+\delta\xi)^6}\right)=$$
$$=\delta A_r(\xi). \quad (3.44)$$

From inspection it is evident that A_r is bounded as $\varepsilon\to 0$, so $A_r=\mathrm{O}(1)$ and, as a consequence, $\mathrm{d}A/\mathrm{d}\xi=\mathrm{O}(\delta(\varepsilon))$ as $\delta\to 0$, therefore $\langle\tilde{\nabla}\cdot\tilde{\mathbf{v}}(\xi)\rangle_{\mathrm{i}}=O(1)$ as $\varepsilon\to 0$.
Next, the hydrodynamic functions $\chi_i^{-1}(\xi)$ and their respective derivatives $d\chi_i^{-1}/d\xi$ are

analysed:

$$\begin{cases} \chi_c^{-1}(\xi) = \dfrac{24(\xi\delta+\tilde{r}_c-1)^2+8(\xi\delta+\tilde{r}_c-1)}{24(\xi\delta+\tilde{r}_c-1)^2+26(\xi\delta+\tilde{r}_c-1)+2}; \\ \dfrac{\mathrm{d}\chi_c^{-1}}{\mathrm{d}\xi} = \dfrac{4\delta(\varepsilon)}{11}\left(\dfrac{2}{(\xi\delta+\tilde{r}_c)^2}+\dfrac{9}{(\xi\delta+12\tilde{r}_c-11)^2}\right) = \delta(\varepsilon)\chi_{r,c}^{-1}; \\ \chi_e = 1; \\ \dfrac{\mathrm{d}\chi_e^{-1}}{\mathrm{d}\xi} = 0 \rightarrow \chi_{r,e}^{-1} = 0. \end{cases} \tag{3.45}$$

From inspection of Eq.(3.45) it can be found that $\chi_i^{-1} = O(1)$ and $d\chi_i^{-1}/d\xi = O(\delta(\varepsilon))$ as $\varepsilon \rightarrow 0$ for both the quadrants.

At this point, only the gauge functions related to the first and second order derivatives of the interaction potentials $\mathrm{d}\tilde{U}/\mathrm{d}\xi$ and $\mathrm{d}^2\tilde{U}/\mathrm{d}\xi^2$ have to be found. It has been demonstrated in the appendix A that, for all the considered potentials, the gauge functions assume the same trend:

$$\begin{cases} \dfrac{\mathrm{d}\tilde{U}}{\mathrm{d}\xi} = O(\delta(\varepsilon)) = \delta(\varepsilon)W(\xi); \\ \dfrac{\mathrm{d}^2\tilde{U}}{\mathrm{d}\xi^2} = O(\delta(\varepsilon)^2) = \delta(\varepsilon)^2X(\xi). \end{cases} \tag{3.46}$$

where $W(\xi)$ and $X(\xi)$ are bounded functions (= O(1) as $\varepsilon \rightarrow 0$) which depend on the considered potential.

Recapping, the following gauge functions have been obtained:

$$\begin{cases} \dfrac{\mathrm{d}\tilde{U}}{\mathrm{d}\xi} = \delta(\varepsilon)W(\xi) = O(\delta(\varepsilon)), \quad \dfrac{\mathrm{d}^2\tilde{U}}{\mathrm{d}\xi^2} = \delta(\varepsilon)^2X(\xi) = O(\delta(\varepsilon)^2); \\ \langle\tilde{\mathbf{v}}\rangle_\mathrm{i} = O(1), \quad \langle\tilde{\nabla}\cdot\tilde{\mathbf{v}}(\xi)\rangle_\mathrm{i} = O(1); \\ \chi_\mathrm{i}^{-1} = O(1) \quad \dfrac{\mathrm{d}(\chi_i)^{-1}}{\mathrm{d}\xi} = \delta(\varepsilon)\chi_{r,i}^{-1} = O(\delta(\varepsilon)). \end{cases} \tag{3.47}$$

(i)	(ii)	(iii)	(iv)	(v)
$O(\varepsilon/\delta(\varepsilon))$	$O(\varepsilon)$	$O(\varepsilon\delta(\varepsilon))$	O(1)	$O(\delta(\varepsilon))$

Table 3.1 Coefficients appearing in Eq.(3.48) as they appear in the equation from left to right

.

Upon replacing all the above expressions in Eq.(3.41) and rearranging it is obtained that

$$\frac{\varepsilon}{\delta(\varepsilon)}\left(\chi_i^{-1}(\xi)\frac{\mathrm{d}^2 g_{\mathrm{i}}^{\mathrm{in}}}{\mathrm{d}\xi^2}\right)+\varepsilon\left(\frac{2\chi_i^{-1}(\xi)}{(\xi\,\delta(\varepsilon)+\tilde{r}_c)}+\chi_i^{-1}(\xi)W(\xi)+\chi_{\mathrm{r,i}}^{-1}(\xi)\right)\frac{\mathrm{d}g_{\mathrm{i}}^{\mathrm{in}}}{\mathrm{d}\xi}+$$
$$+\varepsilon\;\delta(\varepsilon)\left[\chi_i^{-1}\left(\frac{2}{(\xi\,\delta(\varepsilon)+\tilde{r}_c)}W(\xi)+X(\xi)\right)+W(\xi)\chi_{\mathrm{r,i}}^{-1}(\xi)\right]g_{\mathrm{i}}^{\mathrm{in}}+$$
$$-2\left(\langle\tilde{\mathbf{v}}\rangle_{\mathrm{i}}\frac{\mathrm{d}g_{\mathrm{i}}^{\mathrm{in}}}{\mathrm{d}\xi}+\delta(\varepsilon)g_{\mathrm{i}}^{\mathrm{in}}\langle\tilde{\nabla}_\xi\cdot\tilde{\mathbf{v}}\rangle_{\mathrm{i}}\right)=0. \quad (3.48)$$

The gauge functions representing the orders of magnitude of the terms in Eq.(3.48) are listed in Table 3.1; the coefficient (iv) is the one related to the relative velocity shown to be $O(1)$. The aim of the dominant balancing is finding the pair of coefficients of Eq.(3.48) which counts the most as $\varepsilon\to 0$ through a "trial and error" procedure; immediately it can be noticed that, since both ε and $\delta(\varepsilon)$ are much less then unity, (iii) is going to be for sure less dominant than the other terms, so it will be discarded.

Mathematical development

Let's suppose that the pair of terms that dominate are (ii) and (iv): this choice is unreasonable since at the beginning of the derivation it has been assumed that $\varepsilon \ll 1$. Now let's suppose that (i) and (ii) are the dominant as $\varepsilon\to 0$: this would mean that $\delta(\varepsilon)=O(1)$. In this case (i), (ii), (iv) and (v) become respectively $O(\varepsilon)$, O(ε), O(1) and O(ε): it is evident that the second last term, considered to be negligible, is actually the most important one as $\varepsilon\to 0$, so even this hypothesis is unreasonable.
Finally, supposing that (i) and (iv) are the most dominant terms leads to $\delta(\varepsilon)=O(\varepsilon)$. This final assumption is the correct one because (i), (ii), (iv) and (v) become $O(1)$, $O(\varepsilon)$, $O(1)$ and O(ε) respectively; in this case the excluded terms are negligible compared to the other two as $\varepsilon\to 0$. For this reason the following expression for the boundary layer will be considered:

$$\delta(\varepsilon)=O(\varepsilon)=O(\mathrm{Pe}^{-1}). \quad (3.49)$$

Eq.(3.49) provides an estimate of the width of the boundary layer which is in agreement with the results provided in the literature [57] for strongly sheared suspensions of hard-spheres, but it has been derived here in a rigorous way for the first time. Based upon the previous

results, the differential equation for the evaluation of $g_{\mathrm{i}}^{\mathrm{in}}$ can be written in its final form as:

$$\chi_i^{-1}(\xi)\frac{\mathrm{d}^2 g_{\mathrm{i}}^{\mathrm{in}}}{\mathrm{d}\xi^2}+\varepsilon\left[\left(\frac{2\chi_i^{-1}(\xi)}{(\xi\varepsilon+\tilde{r}_c)}+\chi_i^{-1}(\xi)W(\xi)+\chi_{\mathrm{r,i}}^{-1}(\xi)\right)\frac{\mathrm{d}g_{\mathrm{i}}^{\mathrm{in}}(\xi)}{\mathrm{d}\xi}-2\langle\tilde{\nabla}_\xi\cdot\tilde{\mathbf{v}}(\xi)\rangle_{\mathrm{i}}\, g_{\mathrm{i}}^{\mathrm{in}}(\xi)\right]+$$
$$+\varepsilon^2 g_{\mathrm{i}}^{\mathrm{in}}(\xi)\left(X(\xi)\chi_i^{-1}(\xi)+2\frac{\chi_i^{-1}(\xi)W(\xi)}{(\xi\varepsilon+\tilde{r}_c)}+\chi_{\mathrm{r,i}}^{-1}(\xi)W(\xi)\right)-2\langle\tilde{\mathbf{v}}(\xi)\rangle_{\mathrm{i}}\frac{\mathrm{d}g_{\mathrm{i}}^{\mathrm{in}}(\xi)}{\mathrm{d}\xi}=0. \tag{3.50}$$

Since the inner solution is a series based on the powers of the boundary layer, the result previously obtained in Eq.(3.49) can be adopted to describe the structure of $g_{\mathrm{i}}^{\mathrm{in}}$ as :

$$g_{\mathrm{i}}^{\mathrm{in}}=g_{0,\mathrm{i}}^{\mathrm{in}}+\varepsilon g_{1,\mathrm{i}}^{\mathrm{in}}+\varepsilon^2 g_{2,\mathrm{i}}^{\mathrm{in}}+\ldots \tag{3.51}$$

3.4.2 Leading order term

It is possible to evaluate g_0^{in} under the same hypothesis made for the outer solution: by imposing $\varepsilon=0$ in Eq.(3.50)

$$\frac{\mathrm{d}^2 g_{0,\mathrm{i}}^{\mathrm{in}}}{\mathrm{d}\xi^2}-2\frac{\langle\tilde{\mathbf{v}}(\varepsilon=0)\rangle_{\mathrm{i}}}{\chi_i^{-1}(\varepsilon=0)}\frac{\mathrm{d}g_{0,\mathrm{i}}^{\mathrm{in}}}{\mathrm{d}\xi}=0, \tag{3.52}$$

a second order ODE is obtained which can be immediately solved:

$$g_{0,\mathrm{i}}^{\mathrm{in}}=C_1+C_0\int_0^{\xi}\exp\left[\left(\int_0^{\xi}2\frac{\langle\tilde{\mathbf{v}}(\varepsilon=0)\rangle_{\mathrm{i}}}{\chi_i^{-1}(\varepsilon=0)}d\xi\right)\right]d\xi, \tag{3.53}$$

where C_0 and C_1 are integration constants which will be evaluated in subsection 3.4.4.

3.4.3 First order term

In order to calculate $g_{1,\mathrm{i}}^{\mathrm{in}}$ the first and the second order derivatives of the inner solution

$$\begin{cases}\dfrac{\mathrm{d}g_{\mathrm{i}}^{\mathrm{in}}}{\mathrm{d}\xi}=\dfrac{\mathrm{d}g_{0,\mathrm{i}}^{\mathrm{in}}}{\mathrm{d}\xi}+\varepsilon\dfrac{\mathrm{d}g_{1,\mathrm{i}}^{\mathrm{in}}}{\mathrm{d}\xi}+\varepsilon^2\dfrac{\mathrm{d}g_{2,\mathrm{i}}^{\mathrm{in}}}{\mathrm{d}\xi}+\ldots. \\ \dfrac{\mathrm{d}^2 g_{\mathrm{i}}^{\mathrm{in}}}{\mathrm{d}\xi^2}=\dfrac{\mathrm{d}^2 g_{0,\mathrm{i}}^{\mathrm{in}}}{\mathrm{d}\xi^2}+\varepsilon\dfrac{\mathrm{d}^2 g_{1,\mathrm{i}}^{\mathrm{in}}}{\mathrm{d}\xi^2}+\varepsilon^2\dfrac{\mathrm{d}^2 g_{2,\mathrm{i}}^{\mathrm{in}}}{\mathrm{d}\xi^2}+\ldots\end{cases} \tag{3.54}$$

have to be replaced into Eq.(3.50). Then, it is necessary to apply the same procedure used for the outer solution: group together all the terms linked with the same power of ε and set them

separately equal to zero. This means that the following equation for $g_{1,\mathrm{i}}^{\mathrm{in}}$ has to be solved:

$$\frac{\mathrm{d}^2 g_{1,\mathrm{i}}^{\mathrm{in}}}{\mathrm{d}\xi^2} - 2\frac{\langle\tilde{\mathbf{v}}(\xi)\rangle_{\mathrm{i}}}{\chi_i^{-1}(\xi)}\frac{\mathrm{d}g_{1,\mathrm{i}}^{\mathrm{in}}}{\mathrm{d}\xi} + \left[\left(\frac{2}{(\xi\varepsilon+\tilde{r}_c)} + W(\xi) + \frac{\chi_{\mathrm{r,i}}^{-1}}{\chi_i^{-1}}\right)\frac{\mathrm{d}g_{0,\mathrm{i}}^{\mathrm{in}}}{\mathrm{d}\xi} - 2\frac{\langle\tilde{\nabla}_\xi\cdot\tilde{\mathbf{v}}(\xi)\rangle_{\mathrm{i}}}{\chi_i^{-1}(\xi)} g_{0,\mathrm{i}}^{\mathrm{in}}(\xi)\right] = 0. \tag{3.55}$$

Mathematical steps

By introducing the following change of variable

$$p_1 = \frac{\mathrm{d}g_{1,\mathrm{i}}^{\mathrm{in}}}{\mathrm{d}\xi}, \tag{3.56}$$

Eq.(3.55) becomes

$$\begin{aligned}\frac{\mathrm{d}p_1}{\mathrm{d}\xi} - \frac{2\langle\tilde{\mathbf{v}}(\xi)\rangle_{\mathrm{i}}}{\chi_i^{-1}(\xi)}p_1 = \\ = -\left[\left(\frac{2}{(\xi\varepsilon+\tilde{r}_c)} + W(\xi) + \frac{\chi_{\mathrm{r,i}}^{-1}}{\chi_i^{-1}}\right)\frac{\mathrm{d}g_{0,\mathrm{i}}^{\mathrm{in}}}{\mathrm{d}\xi} - 2\frac{\langle\tilde{\nabla}_\xi\cdot\tilde{\mathbf{v}}(\xi)\rangle_{\mathrm{i}}}{\chi_i^{-1}(\xi)} g_{0,\mathrm{i}}^{\mathrm{in}}(\xi)\right] = 0.\end{aligned} \tag{3.57}$$

It is possible to treat this equation as a first order ODE which will be solved through the introduction of an integrating factor:

$$\mu(\xi) = \exp\left[\left(\int_0^\xi -2\frac{\langle\tilde{\mathbf{v}}(\xi)\rangle_{\mathrm{i}}}{\chi_i^{-1}(\xi)}d\xi\right)\right], \tag{3.58}$$

which transforms the above mentioned equation as

$$\frac{\mathrm{d}[\mu(\xi)p_1]}{\mathrm{d}\xi} = -\left[\left(\frac{2}{(\xi\varepsilon+\tilde{r}_c)} + W(\xi) + \frac{\chi_{\mathrm{r,i}}^{-1}}{\chi_i^{-1}(\xi)}\right)\frac{\mathrm{d}g_{0,\mathrm{i}}^{\mathrm{in}}}{\mathrm{d}\xi} - 2\frac{\langle\tilde{\nabla}_\xi\cdot\tilde{\mathbf{v}}(\xi)\rangle_{\mathrm{i}}}{\chi_i^{-1}(\xi)} g_{0,\mathrm{i}}^{\mathrm{in}}\right]\mu(\xi). \tag{3.59}$$

The previous equation can be solved analytically, ending up with

$$\begin{aligned}p_1\mu(\xi) - C_2 = \frac{\mathrm{d}g_{1,\mathrm{i}}^{\mathrm{in}}}{\mathrm{d}\xi}\mu(\xi) - C_2 = \int_0^\xi\left[\left(\frac{2}{(\xi\varepsilon+\tilde{r}_c)} + W(\xi) + \frac{\chi_{\mathrm{r,i}}^{-1}}{\chi_i^{-1}}\right)\frac{\mathrm{d}g_{0,\mathrm{i}}^{\mathrm{in}}}{\mathrm{d}\xi} + \right. \\ \left. - 2\frac{\langle\tilde{\nabla}_\xi\cdot\tilde{\mathbf{v}}(\xi)\rangle_{\mathrm{i}}}{\chi_i^{-1}(\xi)} g_{0,\mathrm{i}}^{\mathrm{in}}\right]\mu(\xi)\mathrm{d}\xi.\end{aligned} \tag{3.60}$$

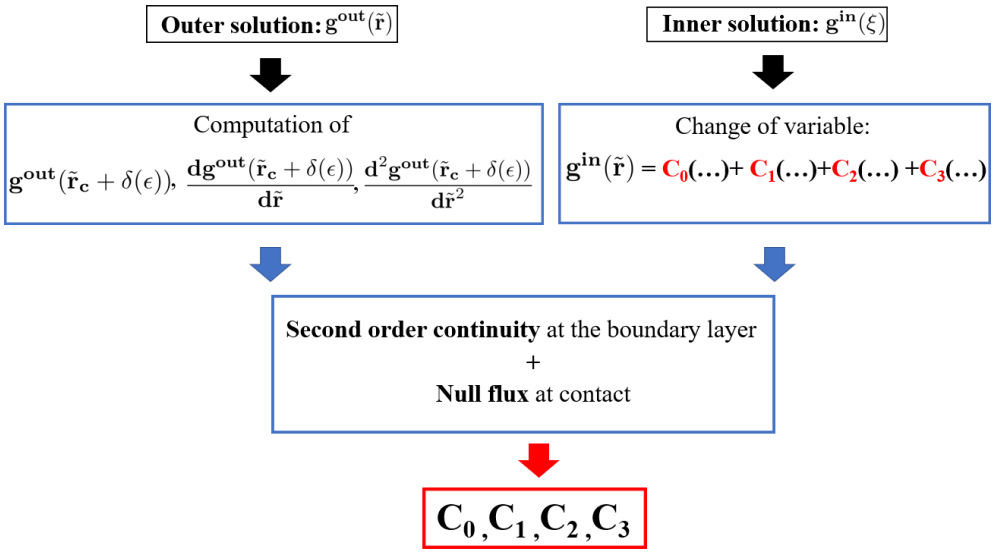

Fig. 3.1 Block diagram with the fundamental steps for the evaluation of the integration constants within $g_{\mathrm{i}}^{\mathrm{in}}(\tilde{r})$

Finally, it is possible to solve Eq.(3.60) through a final straightforward integration obtaining:

$$g_{1,\mathrm{i}}^{\mathrm{in}} = C_3 + \int_0^{\xi}\left\{C_2 - \int_0^{\xi}\left[\left(\frac{2}{(\xi\varepsilon+\tilde{r}_c)} + W(\xi) + \frac{\chi_{\mathrm{r,i}}^{-1}}{\chi_i^{-1}}\right)\frac{\mathrm{d}g_{0,\mathrm{i}}^{\mathrm{in}}}{\mathrm{d}\xi} + \right.\right.$$
$$\left.\left. - 2\frac{\langle\tilde{\nabla}_\xi\cdot\tilde{\mathbf{v}}(\xi)\rangle_{\mathrm{i}}}{\chi_i^{-1}(\xi)}g_{0,\mathrm{i}}^{\mathrm{in}}\right]\exp\left(\int_0^{\xi} -2\frac{\langle\tilde{\mathbf{v}}(\xi)\rangle_{\mathrm{i}}}{\chi_i^{-1}(\xi)}\mathrm{d}\xi\right)\mathrm{d}\xi\right\}\exp\left(\int_0^{\xi} 2\frac{\langle\tilde{\mathbf{v}}(\xi)\rangle_{\mathrm{i}}}{\chi_i^{-1}(\xi)}d\xi\right)\mathrm{d}\xi. \quad (3.61)$$

where C_2 and C_3 are integration constants whose evaluation is the task of the next subsection.

3.4.4 Integration constants evaluation: asymptotic patching

To summarize two different series, $g_{\mathrm{i}}^{\mathrm{in}}$ and $g_{\mathrm{i}}^{\mathrm{out}}$, have been evaluated which describe the behaviour of the solution in two different adjacent sections of the integration domain of each quadrant. The final step is the evaluation of the integration constants C_0, C_1, C_2 and C_3 present in the inner solution whose full procedure is summarized in Fig. 3.1.

Since four unknown parameters are needed, it is necessary to introduce four equations to determine them: the first one is Eq.(3.68), the near-field boundary condition of zero flux at the reference particle surface, a constraint which must be respected. The other three can be obtained from the *patching* procedure [58] whose general principle is as follows: if two solutions share a common border, one of the two is completely known and the other has N constants to be evaluated, it is necessary to apply a continuity of order $N-1$.

This principle is suitable for our case since the full behavior of the outer solution is calculated,

and it is necessary to fix a second order continuity between $g_{\mathrm{i}}^{\mathrm{out}}$ and $g_{\mathrm{i}}^{\mathrm{in}}$ at their shared border, that is $\tilde{r} = \tilde{r}_c + \varepsilon$ in order to find the three remaining constants.
After having obtained the complete structure of the inner solution, all the coefficients related to each integration constant needs to be grouped; for clarity the following mathematical notation will be adopted:

$$\begin{cases} \mathrm{Int}_0(\xi) = \exp\int_0^\xi 2\dfrac{\langle\tilde{\mathbf{v}}(\varepsilon=0)\rangle}{\chi_i^{-1}(\varepsilon=0)}\mathrm{d}\xi, \quad \mathrm{IntInt}_0(\xi) = \int_0^\xi \mathrm{Int}_0(\xi)\mathrm{d}\xi; \\ \mathrm{Int}_1(\xi) = \exp\int_0^\xi 2\dfrac{\langle\tilde{\mathbf{v}}(\xi)\rangle_{\mathrm{i}}}{\chi_i^{-1}(\xi)}\mathrm{d}\xi, \quad \mathrm{T}(\xi) = 2\dfrac{\langle\tilde{\nabla}_\xi\cdot\tilde{\mathbf{v}}\rangle}{\chi_i^{-1}(\xi)\mathrm{Int}_1(\xi)}; \\ \mathrm{Z}(\xi) = 2\dfrac{\langle\tilde{\nabla}_\xi\cdot\tilde{\mathbf{v}}\rangle}{\chi_i^{-1}(\xi)}, \ \ \mathrm{R}(\xi) = \mathrm{Z}(\xi)\mathrm{IntInt}_0 - \left(\dfrac{2}{\xi\varepsilon+\tilde{r}_c} + W(\xi) + \dfrac{\chi_{\mathrm{r,i}}^{-1}(\xi)}{\chi_i^{-1}(\xi)}\right)\mathrm{Int}_0; \\ \mathrm{Q}(\xi) = \left[\mathrm{T}(\xi)\mathrm{IntInt}_0 - \left(\dfrac{2}{\xi\varepsilon+\tilde{r}_c} + W(\xi) + \dfrac{\chi_{\mathrm{r,i}}^{-1}(\xi)}{\chi_i^{-1}(\xi)}\right)\mathrm{Int}_0\right](\mathrm{Int}_1)^{-1}. \end{cases} \tag{3.62}$$

So, $g_{\mathrm{i}}^{\mathrm{in}}(\xi)$ can be written as

$$\begin{aligned} g_{\mathrm{i}}^{\mathrm{in}}(\xi) = C_0\left\{\mathrm{IntInt}_0(\xi) + \varepsilon\left[\int_0^\xi\left(\int_0^\xi \mathrm{Q}(\xi)\mathrm{d}\xi\right)\mathrm{Int}_1\mathrm{d}\xi\right]\right\} + \\ + C_1\left\{1 + \varepsilon\left[\int_0^\xi\left(\int_0^\xi \mathrm{T}(\xi)\mathrm{d}\xi\right)\mathrm{Int}_1\mathrm{d}\xi\right]\right\} + C_2\delta(\varepsilon)\int_0^\xi \mathrm{Int}_1(\xi)\mathrm{d}\xi + C_3\varepsilon. \end{aligned} \tag{3.63}$$

To find the integration constants it is necessary to transform ξ back to the radial coordinate $\tilde{r}$:

$$\begin{aligned} g_{\mathrm{i}}^{\mathrm{in}}(\tilde{r}) = C_0\left\{\mathrm{IntInt}_0(\tilde{r}) + \frac{1}{\varepsilon}\left[\int_{\tilde{r}_c}^{\tilde{r}}\left(\int_{\tilde{r}_c}^{\tilde{r}} \mathrm{Q}(\tilde{r})\mathrm{d}\tilde{r}\right)\mathrm{Int}_1\mathrm{d}\tilde{r}\right]\right\} + \\ + C_1\left\{1 + \frac{1}{\varepsilon}\left[\int_{\tilde{r}_c}^{\tilde{r}}\left(\int_{\tilde{r}_c}^{\tilde{r}} \mathrm{T}(\tilde{r})\mathrm{d}\tilde{r}\right)\mathrm{Int}_1\mathrm{d}\tilde{r}\right]\right\} + C_2\int_{\tilde{r}_c}^{\tilde{r}} \mathrm{Int}_1(\tilde{r})\mathrm{d}\tilde{r} + C_3\varepsilon \end{aligned} \tag{3.64}$$

Next, the first and the second order derivative of $g_{\mathrm{i}}^{\mathrm{in}}(\tilde{r})$ are expressed as:

$$\begin{aligned} \frac{\mathrm{d}g_{\mathrm{i}}^{\mathrm{in}}(\tilde{r})}{\mathrm{d}\tilde{r}} = C_0\left[\mathrm{Int}_0(\tilde{r}) + \frac{1}{\varepsilon}\left(\int_{\tilde{r}_c}^{\tilde{r}} \mathrm{Q}(\tilde{r})\mathrm{d}\tilde{r}\right)\mathrm{Int}_1(\tilde{r})\right] + \\ + C_1\left[\frac{1}{\varepsilon}\left(\int_{\tilde{r}_c}^{\tilde{r}} \mathrm{T}(\tilde{r})\mathrm{d}\tilde{r}\right)\mathrm{Int}_1(\tilde{r})\right] + C_2\mathrm{Int}_1(\tilde{r}); \end{aligned} \tag{3.65}$$

$$\frac{\mathrm{d}^2 g_{\mathrm{i}}^{\mathrm{in}}(\tilde{r})}{\mathrm{d}\tilde{r}^2} = C_0\left[\frac{\mathrm{dInt}_0(\tilde{r})}{\mathrm{d}\tilde{r}} + \frac{1}{\varepsilon}\left(\int_{\tilde{r}_c}^{\tilde{r}} \mathrm{Q}(\tilde{r})\mathrm{d}\tilde{r}\right)\frac{\mathrm{dInt}_1(\tilde{r})}{\mathrm{d}\tilde{r}} + R(\tilde{r})\right] + \\ + C_1\left[\frac{1}{\varepsilon}\left(\int_{\tilde{r}_c}^{\tilde{r}} \mathrm{T}(\tilde{r})\mathrm{d}\tilde{r}\right)\frac{\mathrm{dInt}_1(\tilde{r})}{\mathrm{d}\tilde{r}} + Z(\tilde{r})\right] + C_2\frac{\mathrm{dInt}_1(\tilde{r})}{\mathrm{d}\tilde{r}}. \quad (3.66)$$

It is now possible to evaluate all the integration constants C_0, C_1, C_2 and C_3 by solving the following linear system which is composed of the actual patching procedure

$$\begin{cases} g_{\mathrm{i}}^{\mathrm{out}}(\tilde{r} = \tilde{r}_c + \varepsilon) = g_{\mathrm{i}}^{\mathrm{in}}(\tilde{r} = \tilde{r}_c + \varepsilon); \\ \dfrac{\mathrm{d}g_{\mathrm{i}}^{\mathrm{out}}(\tilde{r} = \tilde{r}_c + \varepsilon)}{\mathrm{d}\tilde{r}} = \dfrac{\mathrm{d}g_{\mathrm{i}}^{\mathrm{in}}(\tilde{r} = \tilde{r}_c + \varepsilon)}{\mathrm{d}\tilde{r}}; \\ \dfrac{\mathrm{d}^2 g_{\mathrm{i}}^{\mathrm{out}}(\tilde{r} = \tilde{r}_c + \varepsilon)}{\mathrm{d}\tilde{r}^2} = \dfrac{\mathrm{d}^2 g_{\mathrm{i}}^{\mathrm{in}}(\tilde{r} = \tilde{r}_c + \varepsilon)}{\mathrm{d}\tilde{r}^2}, \end{cases} \quad (3.67)$$

together with the application of the boundary condition related to the balance between Brownian- and shear-induced effects at $\tilde{r} \to \tilde{r}_c$:

$$0 = \chi_i(\tilde{r}_c)^{-1}\frac{\mathrm{d}g_{\mathrm{i}}^{\mathrm{in}}}{\mathrm{d}\tilde{r}}(\tilde{r}_c) + \left(\chi_i(\tilde{r}_c)^{-1}\frac{\mathrm{d}\tilde{U}}{\mathrm{d}\tilde{r}}(\tilde{r}_c) - 2\mathrm{Pe}\langle\tilde{\mathbf{v}}\rangle_{\mathrm{i}}\right)g_{\mathrm{i}}^{\mathrm{in}}(\tilde{r}_c). \quad (3.68)$$

3.5 Summary

In this chapter the full mathematical procedure to analytically solve the 2-Body Smoluchowski equation under strongly sheared conditions has been proposed.
It is based on the application of an angular average procedure which allows the evaluation of two microstructures $g_{\mathrm{i}}(\tilde{r})$, one representing the spatial arrangement in the compressing quadrants, where the shear stress pushes the particles towards each other, and the other in the extensional sectors, where the flow field pulls the particles away from one another:

$$\begin{cases} g_c(\tilde{r}) & \theta \in [0,\pi]\ \phi \in [\pi/2,\pi],\ \phi \in [3\pi/2, 2\pi] \quad \text{Compressing regions;} \\ g_e(\tilde{r}) & \theta \in [0,\pi]\ \phi \in [0,\pi/2],\ \phi \in [\pi, 3\pi/2] \quad \text{Extensional regions.} \end{cases} \quad (3.69)$$

Each solution $g_{\mathrm{i}}(\tilde{r})$ is calculated by a singular perturbation methodology which makes the overall solution composed of two different power series with base $\varepsilon = \mathrm{Pe}^{-1}$:

$$g_{\mathrm{i}}(\tilde{r}) = \begin{cases} g_{\mathrm{i}}^{\mathrm{in}}(\tilde{r}) = g_{0,i}^{\mathrm{in}} + \varepsilon g_{1,i}^{\mathrm{in}} + O(\varepsilon^2) & \tilde{r} < \mathrm{r}_c + \varepsilon \\ g_{\mathrm{i}}^{\mathrm{out}}(\tilde{r}) = g_{0,i}^{\mathrm{out}} + \varepsilon g_{1,i}^{\mathrm{out}} + O(\varepsilon^2) & \tilde{r} \geq \mathrm{r}_c + \varepsilon. \end{cases} \quad (3.70)$$

$g_{\mathrm{i}}^{\mathrm{out}}(\tilde{r})$ is the outer solution which describes the pair correlation function in the section of each quadrant further away from the reference particle where the solution is supposed to change sufficiently slowly with the radial coordinate. It represents an extension of the solution previously found by Batchelor & Green for pure straining motion which now includes the distortion of the spherical symmetry recorded in the pure hydrodynamic limit due to the influence of Brownian-induced contributions.
$g_{\mathrm{i}}^{\mathrm{in}}(\tilde{r})$ is the inner solution valid for a small region, named boundary layer with width $\delta = O(\varepsilon)$ near the reference particle surface in which the solution varies quite steeply with the radial coordinate. It has been found as a function of the *inner variable* $\xi = (\tilde{r} - \tilde{r}_c)/\delta$ and it includes four integration constants (C_0, C_1, C_2 and C_3) which have been found by *asymptotic patching*.

Chapter 4

Results, conclusions & future steps

After having explained step-by-step the analytical procedure adopted to evaluate the microstructures over the compressing and extensional quadrants, this chapter is focused on the discussion of the results provided by the theory starting from the analysis of an Hard-Spheres (HS) suspension: first the theory will be compared to Stokesian dynamics simulations, next it will be shown the impact of the Brownian induced contributions on the spatial arrangement of the dispersion in the compressing and extensional regions; moreover the effect of different Péclet numbers on the microstructures will also be proposed.
The second part is instead dedicated to analyse the impact of different types of complex interacting particles by comparing the $g_{\mathrm{i}}(\tilde{r})$ obtained for hard-spheres with the one calculated for two different complex-interacting systems: the first is an attractive fluid in which the particles interact with a 12-6 Lennard-Jones potential, the second a suspension of charge-stabilized particles which interact with a screened Coulomb, also known as Yukawa, potential.
The third and final part will be instead focused on the address of some potential directions for future work.

4.1 Hard-Spheres model

The Hard-Spheres model will be represented by introducing the following formalism into the master equation Eq.(3.23):

$$\begin{cases} \tilde{U}(\tilde{r}) = \infty & \tilde{r} < \tilde{r}_c; \\ \tilde{U}(\tilde{r}) = 0 & \tilde{r} \geq \tilde{r}_c. \end{cases} \tag{4.1}$$

and proceed with the calculations which, for the sake of brevity, will not reported for any of the following case studies.

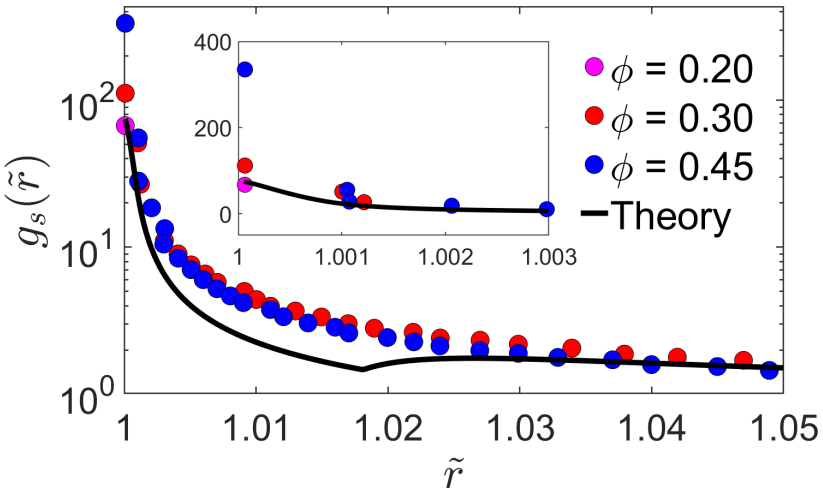

Fig. 4.1 Comparison of $g_s(\tilde{r})$ evaluated from Eq.(4.2) with simulations (symbols) of Hard-Sphere suspensions at Pe = 1000 [25] at different volume fractions.

4.1.1 Validation of the theory

In order to show that the theory provides with a reliable description of the microstructure of hard-spheres an overall angular average pcf $g_s(\tilde{r})$ is evaluated for strongly sheared conditions (Pe = 1000):

$$g_s(\tilde{r}) = \frac{g_c(\tilde{r}) + g_e(\tilde{r})}{2}, \tag{4.2}$$

It is then compared in Fig. 4.1 to the spherical average pair correlation function obtained by Stokesian dynamics simulations of concentrated strongly sheared suspensions [25] under the same Péclet number.

It is seen that, at distances from the surface of the reference particle from $\tilde{r}_c$ to $\tilde{r} = 1.0015$, the theory respects the trends provided by the simulations, which is featured by the presence of a peak whose maximum is located at $\tilde{r} = \tilde{r}_c$. The theory reasonably underestimates the peak obtained by the simulations since they are related to concentrated systems in which the packed fraction ϕ varies from 0.30 to 0.45, meanwhile the theory works for semidilute conditions for which $\phi \approx 0.20$: it can be seen that the peak of $g_s(\tilde{r})$ as it is shown in Fig. 4.1 is caught quite well by the theory; unfortunately no information about the whole spherical average microstructure has been found for this case..

Moreover, the value of the peak could still be a little bit overestimated for two possible reasons: the first is the fact that the theory does not consider the vorticity typical of a simple shear flow, the second is linked to the neglect of the effect of angular diffusion which provides the particles with the possibility to escape the boundary layer in the compressing regions. [49].

There is one final point to address: there is a clear discontinuity in the trend at $\tilde{r} \approx 1.018$. This artifact is due to the fact that $g_{\mathrm{s}}(\tilde{r})$ is a simple arithmetic average between $g_{\mathrm{c}}(\tilde{r})$ and $g_{\mathrm{e}}(\tilde{r})$ which present very different trends because of the anisotropy typical of strongly sheared conditions which will be discussed in the next section.
Nonetheless, Fig. 4.1 confirms the reliability of the theory which correctly represents the most important features of the microstructure under strongly sheared suspensions with no adjustable parameters.

4.1.2 Effect of the Péclet number

This section is intended to propose the singular trends for the quadrant dependent microstructures $g_c(\tilde{r})$ and $g_e(\tilde{r})$. Moreover, it will be shown how their trends are modified by decreasing the strength of the advective forces represented by a progressive reduction of the Péclet number.
First, the pcfs related to the compressing regions are proposed in Fig. 4.2: the balance between the advective forces which push the particles towards each other and the hydrodynamic interactions which represent the overall resistance opposed by the squeezing of the fluid between them causes the presence of an accumulation peak. Its contact value $g_c(\tilde{r}_c)$ naturally decreases with the Péclet number because of the decrease of the strength of the shear forces. Moreover weaker advective forces cause a slower rate of increase of the peaks, an aspect also influenced by the increase of the width of the boundary layer since the Brownian-induced contributions become more and more important.
On the other hand, in Fig. 4.3 the microstructure for the extensional quadrants is shown: in this scenario the advective forces tend to flatten the profile of $g_{\mathrm{e}}(\tilde{r})$ to unity, which indicates that the motions of the two particles are completely independent from one another. This tendency is put even more on evidence by the fact that the viscous forces linked to the Brownian motion of the particles are negligible ($\chi_e^{-1} = 1$). For Pe = 1000 it is possible to observe a small accumulation zone near the contact region: this effect can be explained by the hydrodynamic interactions encoded by the functions $A(\tilde{r})$ and $B(\tilde{r})$ which, recalling Section 2.2.1, provide always an opposite effect to the induced flow, so in this case they assume an attractive nature causing the small peak near contact. On the other hand, when the Péclet number decreases the peak disappears and it is possible to observe that the width of the depletion region near the reference particle, where the pair correlation function assumes null values, keeps increasing because of the smaller and smaller impact of the attractive effect of the hydrodynamic contributions.
To conclude, one final overall observation needs to be done on $g_{\mathrm{c}}(\tilde{r})$ and $g_{\mathrm{e}}(\tilde{r})$. Even if the leading order for both the outer solutions $g_{0,\mathrm{i}}^{\mathrm{out}}$ is the same, that is the spherical symmetric

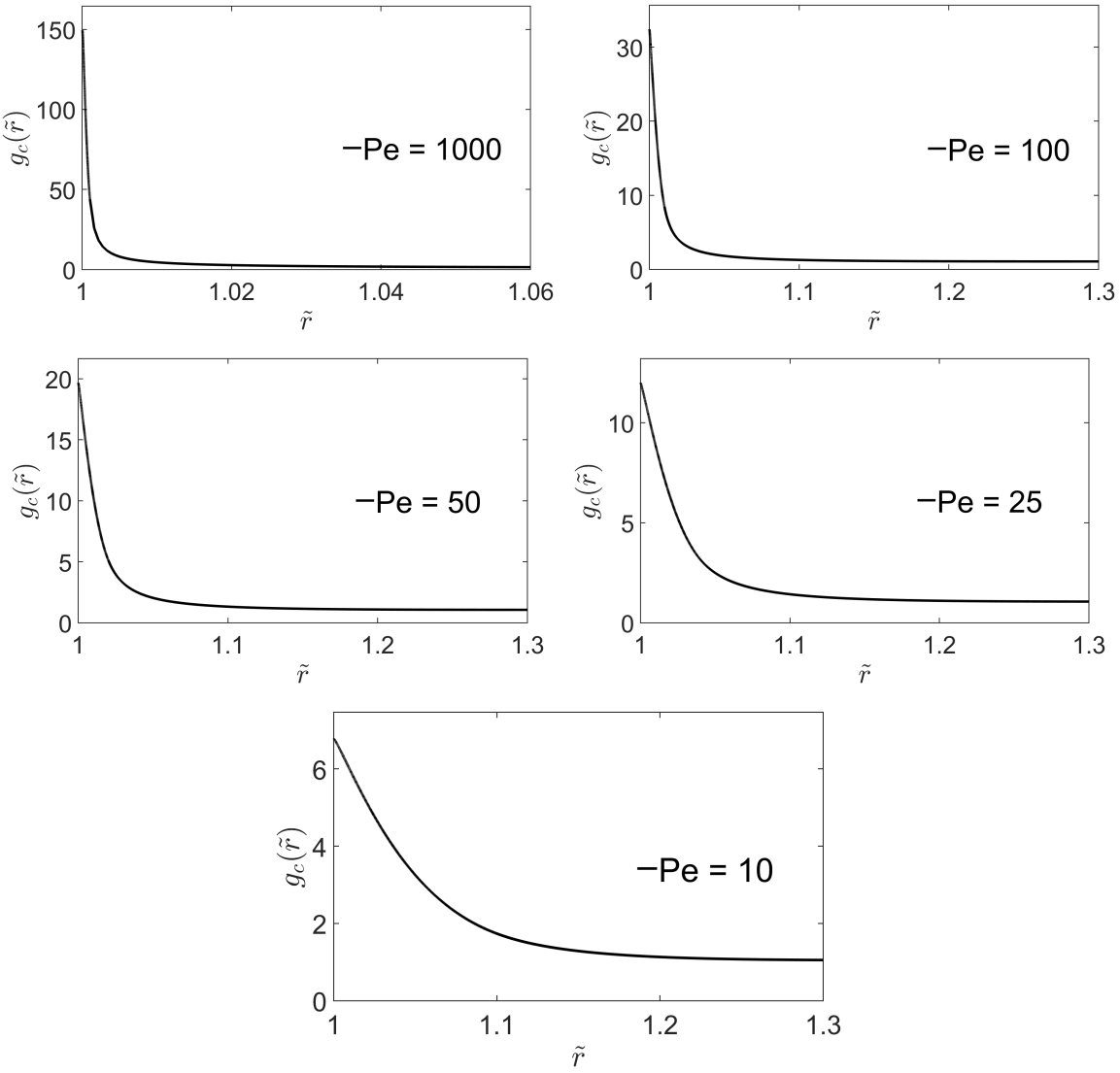

Fig. 4.2 Effect of the Péclet number on the trend of $g_c(\tilde{r})$ for the Hard-Spheres model.

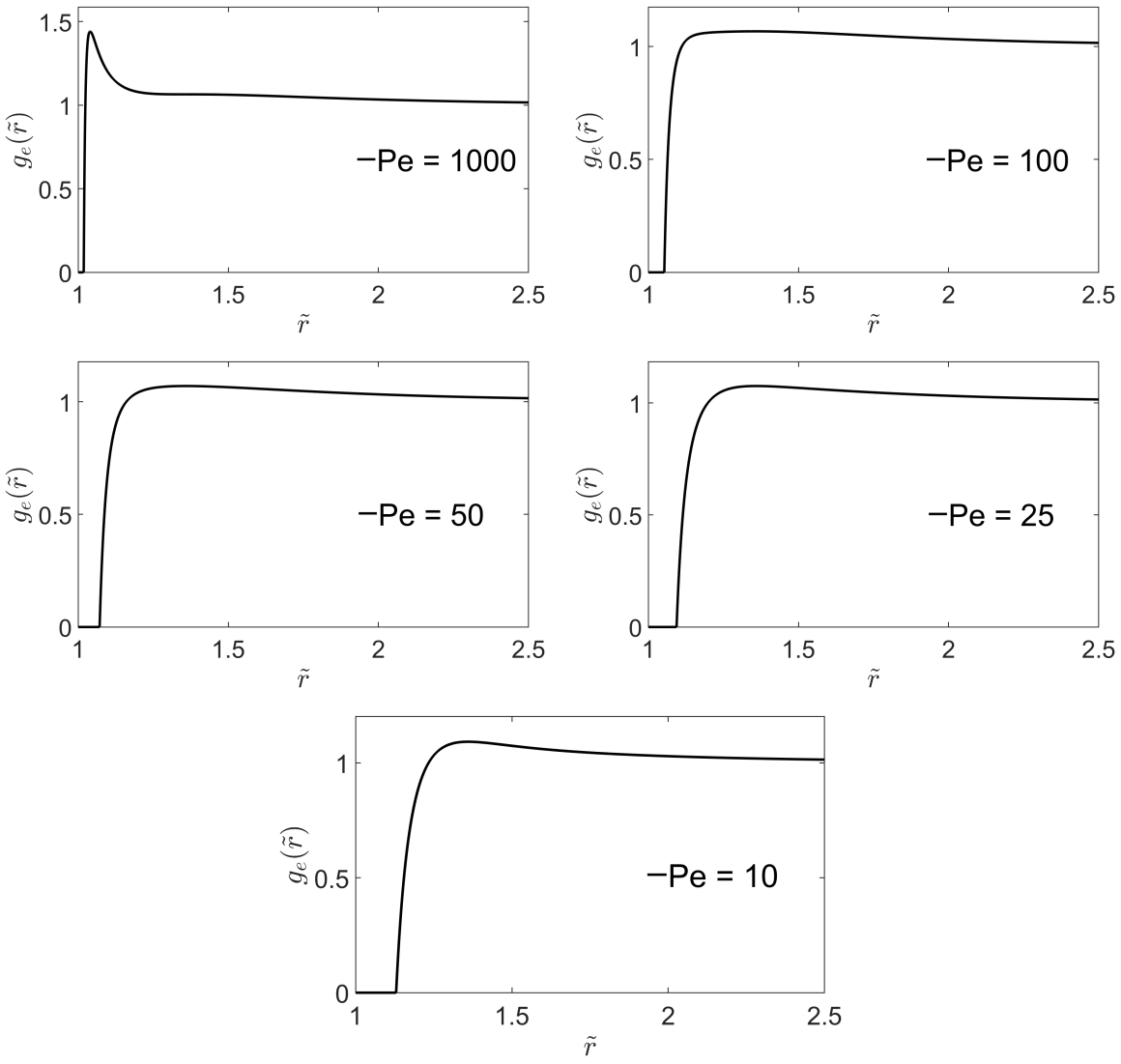

Fig. 4.3 Effect of the Péclet number on the trend of $g_e(\tilde{r})$ for the Hard-Sphere model.

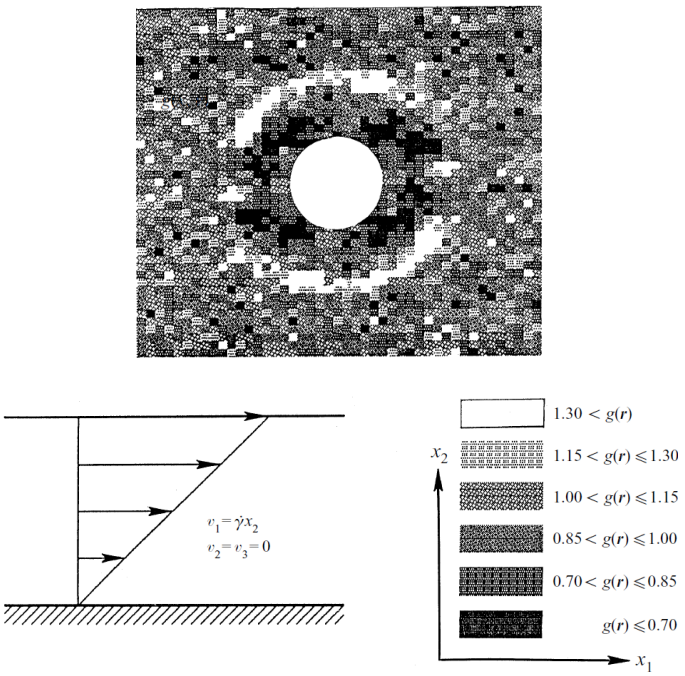

Fig. 4.4 Example of anisotropic microstructure: pair correlation function g(**r**) in the plane of shear for a suspension of polystyrene spheres in silicone oil in simple shear at $Pe = 3.0\ 10^5$. (adapted from [61]).

solution obtained by Batchelor & Green, the final microstructure is strongly anisotropic after Brownian-induced contributions are taken into account by the evaluation of $g^{\text{out}}_{1,\text{i}}$ and the subsequent calculation of the inner solutions: in the compressing sectors the pcf assumes values higher than unity which increases with higher Péclet numbers, meanwhile in the extensional quadrants the peak reaches O(1) only and a depletion region has been detected. This description agrees with results published in both experimental [61] and numerical procedures [32]: in Fig.4.4 the pcf of a hard-spheres suspension under creeping flow conditions ($Re = 3.0\ 10^{-7}$) has been obtained by the means of digital image analysis. It is possible to observe that the values of the pcf are not homogeneous, but it is possible to observe accumulation areas in correspondence of the compressing sectors featured by higher values of the pcf (white areas), meanwhile lower values of g(**r**), which corresponds to depletion sectors, can be observed in the extensional regions (darker areas).

4.2 Attractive fluids

Attractive suspensions under induced flow fields have recently received a lot of attention because of the wealth of different identified rheological behaviours such as wall slips [62]

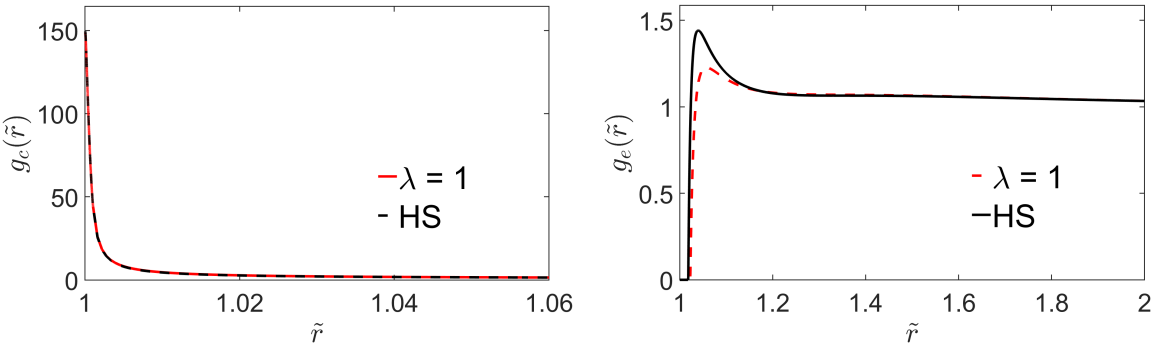

Fig. 4.5 Effect of the interaction potential on the microstructure of compressing (left) and extensional (right) quadrants at Pe = 1000.

and flow heterogeneities [63]. Recent experiments conducted in confined geometries show self-organization of the particles into log-rolling flocs [64] which can significantly reduce electronic properties of batteries [65] which have been linked to hydrodynamic coupling between the flocs and the confining boundaries [66].
Anyway, the single theoretical framework, to my knowledge, related to the study of rheology of attractive systems has been proposed by Varga & Swan [67] which is focused on weakly sheared conditions only, meanwhile there is absence of any rigorous analytic approach dealing with strongly sheared conditions; the following discussion aims to start filling this gap.
The effect of attractive interactions is implemented by a 12-6 Lennard-Jones interaction potential, a paradigm for many liquids, but the study can easily be extended to other potentials such as the Asakura–Oosawa formulation [68], which is frequently used in studies involving attractive suspensions. Since the spheres are supposed to be impenetrable, the same excluded volume interactions considered for the previous case study have been included, so $\tilde{U}(\tilde{r})$ is defined as

$$\begin{cases} \tilde{U}(\tilde{r}) = \infty \quad \tilde{r} < \tilde{r}_c; \\ \tilde{U}(\tilde{r}) = \tilde{U}_{\min}\left(\tilde{r}^{-12} - \tilde{r}^{-6}\right) = 4\lambda\left(\tilde{r}^{-12} - \tilde{r}^{-6}\right) \quad \tilde{r} \geq \tilde{r}_c. \end{cases} \tag{4.3}$$

where λ is the minimum of the interaction potential between the particles.

4.2.1 High Péclet number

It is expected that, for large values of the Péclet number, the effect of the shear flow is completely dominant on the microstructure related to both quadrants. This is demonstrated

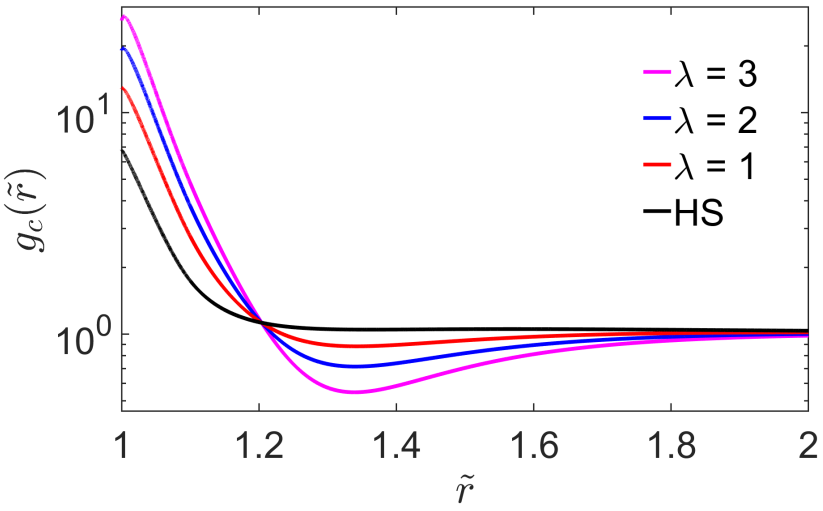

Fig. 4.6 Average pcf related to the compressing quadrants at Pe = 10 for an hard-sphere suspension (lowest curve) and different values of λ.

in Fig. 4.5 where the $g_c(\tilde{r})$ for the calculation including the LJ potential is exactly the same as for the hard sphere calculation, meanwhile there is a small difference concerning the microstructure related to extensional quadrants, but it is basically negligible. This aspect is confirmed by experimental observations as well: in studies related to the rheology of attractive emulsions under shear it has been proved that shear rates over a certain threshold prevent any possibility for the particles to interact and form clusters [64].

4.2.2 Intermediate Péclet number (Pe = 10)

On the other hand, if the Péclet number is sufficiently small, the effect of the interparticle interactions on the microstructure is not negligible anymore.

In Fig. 4.6 the effect of the Lennard-Jones potential on the microstructure related to the compressing quadrants is proposed. In this case the pair correlation function can be divided into three different radial regions: in the one furthest away from the reference particle a significant undershoot and a minimum in $g_c(\tilde{r})$ can be observed, which becomes deeper upon increasing the attraction energy of the LJ potential. Interestingly, this feature is absent in the hard sphere case: this minimum represents a depletion region in which the synergy between the attractive force of the LJ and the action of the shear flow is pushing the particles towards each other without encountering any resistance from the fluid, giving origin to a "black-hole" effect. When the particles get sufficiently close to each other the repulsive lubrication forces due to the squeezing of the fluid are not negligible any more and they oppose resistance against the approach between the particles causing the formation of an

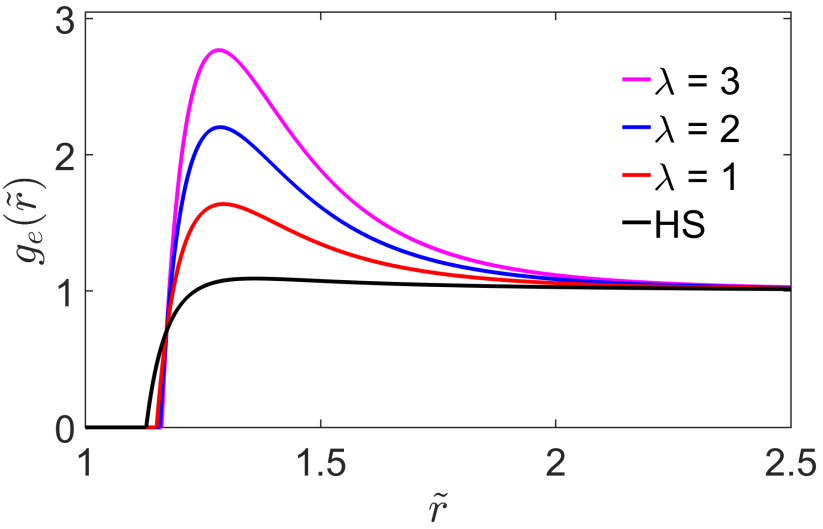

Fig. 4.7 Average pcf for extensional quadrants at Pe = 10 for an hard-sphere suspension (lowest curve) and different values of λ.

accumulation peak. Finally, once the peak is passed, the third region is featured by a decrease of the pcf which is smooth and non-singular, in contrast with the one of the HS system which features a singularity at the point of maximum: this feature is to be attributed to the short-range repulsive part of the interaction of the LJ potential which causes the pair correlation function to approach zero as $\tilde{r} \to \tilde{r}_c$.

It is important to highlight that the depth of the undershoot, the height of the peak and the slope of $g_c(\tilde{r})$ before and after the maximum, all increase with the attraction parameter λ: a deeper well of potential corresponds to stronger attractive long-range interactions and also, at the same time, to stronger short-range repulsive contributions.

A completely different scenario is encountered when attention is paid to Fig. 4.7 where the microstructure related to the extensional quadrants is proposed: it is recalled that for the case of HS the particles are pulled away from each other by the shear which flattens the profile of the pcf.

The microstructure is drastically modified when the contribution of the LJ potential is taken into account: the long range attractive forces start interacting with the advective ones which in this case provide with a repulsive contribution. Again, this balance leads to the formation of an accumulation peak which is, intuitively, much smaller than the one foreseen for the compressing regions and directly proportional to λ.

Once the peak is reached the pcf quickly reaches null values, in particular the slopes of the curves tend to be steeper and steeper with the increase of λ because, as already mentioned in the discussion of $g_c(\tilde{r})$, the stronger the long range attractive interactions are, the strongest the short-range repulsions will consequently be.

4.3 Charge stabilized colloids

The current theory is also extended to systems in which the particles interact by the means of a purely repulsive interaction potential such as the screened Coulomb (Debye Hückel or DH) potential which is coupled by the usual excluded volume interactions:

$$\begin{cases} \tilde{U}(\tilde{r}) = \infty \quad \tilde{r} < \tilde{r}_c; \\ \tilde{U}(\tilde{r}) = \dfrac{(Z^* e)^2}{4\pi\varepsilon_r\varepsilon_0\sigma k_B T}\dfrac{\exp(-\kappa\tilde{r})}{\tilde{r}} = \Gamma\dfrac{\exp(-\kappa\tilde{r})}{\tilde{r}} \quad \tilde{r} \geq \tilde{r}_c. \end{cases} \tag{4.4}$$

Z^* is the effective charge, e the electron charge, ε_r the medium relative dielectric permittivity, ε_0 the dielectric permittivity of vacuum, and κ the dimensionless Debye screening parameter in units of σ^{-1}. The inverse of κ is the Debye length κ^{-1}, which is the length scale within which the interactions are non-negligible. The parameter Γ is known as the coupling constant and controls the strength of the repulsion.
The literature proposes plenty of works involving sheared charge-stabilized colloids, but the vast majority of them involves the use of Brownian dynamics [46, 69], where the hydrodynamic interactions have not been considered at all. On the other hand, their presence in these scenarios have been considered by Nazockdast and Morris who have extended their work described in Chapter 2 from Hard-Spheres to repulsive interacting systems [70]. Anyway, their theory is valid in a range of Péclet number different from the one proposed in this work and its results start becoming less and less reliable when the suspension approaches the semidilute limit, for which instead this work has been demonstrated to be accurate.

4.3.1 High Péclet numbers

Fig. 4.8 shows that also the repulsive interactions provide null or very small differences in the microstructure for both the compressing and extensional regions in case of strongly sheared conditions (Pe = 1000).

4.3.2 Intermediate Péclet number (Pe = 10)

As previously seen for the attractive fluids, the effect of inter-particle interactions is absolutely non-negligible if the conditions are weaker than the one described in Section 4.3.1. Here the influence of the coupling parameter Γ and the screening parameter κ on the angular average microstructures will be described.
In Fig. 4.9 the results for $g_c(\tilde{r})$ are proposed: in the left hand side the contribution of the repulsive DH interaction causes the peak of the pcf to decrease with the increase of the

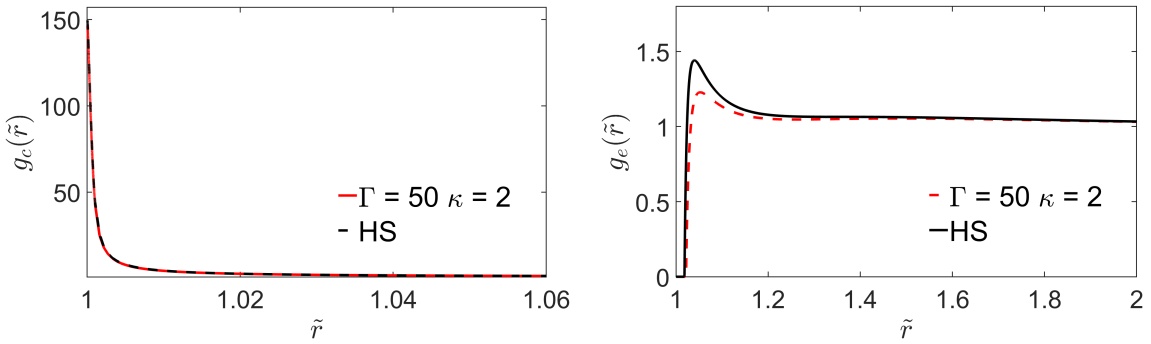

Fig. 4.8 Effect of the repulsive DH potential on $g_c(\tilde{r})$ at high values of the Péclet number (Pe=1000): a) Compressing regions, b) Extensional regions.

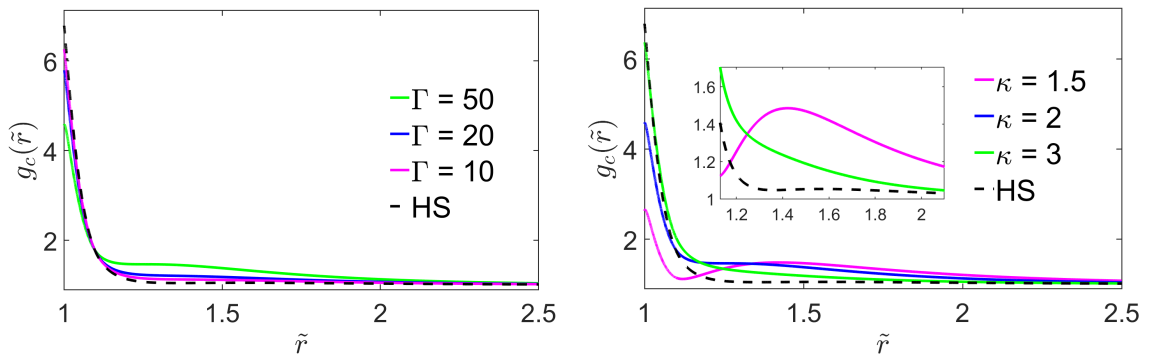

Fig. 4.9 Effect of the repulsive DH potential on $g_c(\tilde{r})$ at low values of the Péclet number (Pe=10). Left: effect of varying the coupling parameter Γ with $\kappa = 2$ fixed; right: effect of varying the Debye parameter with $\Gamma = 50$ kept fixed.

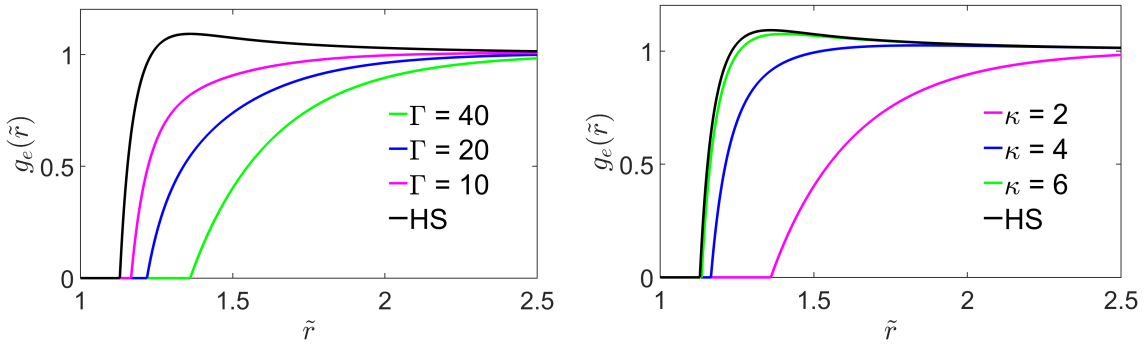

Fig. 4.10 Effect of the repulsive DH potential on $g_c(\tilde{r})$ at low values of the Péclet number (Pe=10): a) Effect of varying the coupling parameter Γ with $\kappa = 2$ fixed, b) Effect of varying the Debye parameter with $\Gamma = 50$ kept fixed.

coupling parameter Γ: since the screened-Coulomb interactions clearly opposes a resistance to the approach of the particles the stronger the repulsions are, the more difficult will be for the particles to get closer.

The right hand side shows instead the effect of the Debye screening parameter κ: increasing κ means decreasing the screening length κ^{-1} which sets the length scale for the decay of the DH repulsion. A new effect is predicted here: as the Debye length decreases, a secondary maximum appears for $\kappa = 1.5$ (in units of σ) at a position $r = 1.4\sigma$, which is slightly less than the Debye length $(1+\kappa^{-1})\sigma \approx 1.67\sigma$. This effect can be interpreted as a local accumulation of particles advected by the flow towards the electrostatic repulsive wall; if the Debye length is too short this effect cannot be seen.

Finally, as a consistency check, it is possible to see that the microstructure of repulsive interacting particles gets closer to the hard-sphere limit if Γ goes to zero or κ goes to infinity.

In Fig. 4.10 the effects of the screened Coulomb interaction potential on the microstructure related to the extensional regions are proposed. First of all, considering this order of magnitude for the Péclet number, there is no accumulation peak near the surface of the reference particle, a common feature with the Hard-Spheres model treated previously, which is due to the tendency of the advective forces to pull the particles away from each other.

It can be observed that the synergy between the "repulsive-like" flow and the screened-Coulomb interaction leads to a *depletion layer* near contact, within which the probability of finding a particle is identically zero. It can also be noticed that its width increases with the stronger repulsions, represented by an increase of their strength controlled by Γ rather than their range represented by κ^{-1}. Again, the micro-structure tends to approach the behaviour of hard-spheres if $\kappa^{-1} \to \infty$ or $\Gamma \to 0$.

4.4 Conclusions

In this work a new analytic method to solve the two body Smoluchowski equation with shear flow by means of an intermediate asymptotics method has been proposed. The final result is the evaluation of two angular averaged pair correlation functions, which describe the microstructure of colloidal suspensions in two different regions of flow field under simple shear motion. The theory has been used first to describe the behavior of an Hard-Spheres suspension obtaining reliable results which are also consistent with Stokesian dynamics simulations.
The theory has then been applied to attractive fluids predicting an important feature of the pcf of attractive fluids in compressing quadrants: the presence of a pronounced depletion effect resulting in a minimum or undershoot in the pcf at separations right after the accumulation peak. This effect is already visible at modest values of the attraction energy, and becomes more and more important upon increasing the attraction. Concerning the extensional sectors the balance between the "repulsive" action of the advective forces and the attractive effect of the Lennard-Jones interactions generate an accumulation peak whose height is of course lower than its counterpart in the compressing regions.
Afterwards, the attention is switched from attractive to repulsive fluids studying the effect of screened-Coulomb (Debye-Hückel) interactions on the spatial arrangement of the particles. In the compression sectors the accumulation peak near contact is lowered upon increasing the repulsion parameters of the Debye-Hückel potential. As the Debye length increases a secondary maximum, which occurs at separations comparable to the Debye length, appears which is due to the competition between the attractive action of the advective forces and the effect of screened electrostatic repulsion. In the extensional sectors, instead, no accumulation peak is visible, but it is observed the occurrence of a depletion layer (where the pair correlation function is identically zero) whose width increases with either the charge repulsion strength or the Debye length.

4.5 Future steps

4.5.1 Strongly sheared conditions

In the literature review it has been showed that the microstructure has been widely used to study the rheology of the suspensions, so one possibility is using the current data evaluated for the microstructure to calculate the overall bulk stress of the suspension and its viscosity in order to reproduce typical behavior of strongly shear suspensions such as shear thickening and look for the impact of inter-particle interactions at these level of shear stresses.

Another possibility is the extension of the theory to more concentrated suspensions by start including many-body hydrodynamic interactions: the most straightforward way to do so is by adopting a volume-fraction dependent self-diffusion coefficient [30] into the formulations which leads to a new scaling of the Péclet number:

$$\overline{\mathrm{Pe}} = \frac{\dot{\gamma} R_P^2}{D_{0,s}(\phi)}. \tag{4.5}$$

This procedure can lead the way to study, for instance, the microstructure of denser and ordered systems [71].
A final possibility is to study the aggregation behavior of colloids by applying the intermediate asymptotics methodology to the BVP composed of Eq.(2.63-2.64). The idea is finding the impact of different types of interparticle interactions on the aggregation behavior of colloids by evaluating the concentration profiles and using them in Eq.(2.65) to compute the resulting flow rates.

4.5.2 Weakly sheared conditions

It is also possible to apply the methodology to weakly sheared conditions: in this case the perturbation parameter ε will be put equal to the Péclet number, obtaining

$$\tilde{\nabla} \cdot \underline{\tilde{\mathbf{D}}} \cdot \left(\tilde{\nabla} \tilde{U} g(\tilde{\mathbf{r}}) + \tilde{\nabla} g(\tilde{\mathbf{r}}) \right) - 2\varepsilon \tilde{\nabla} \cdot \left(\tilde{\mathbf{v}}(\tilde{\mathbf{r}}) g(\tilde{\mathbf{r}}) \right) = 0. \tag{4.6}$$

In this case from preliminary calculations it emerges a singularity of the flow field for $r \to \infty$ [43]. A possibility to avoid it is solving the Fourier transform of this equation following the procedure adopted by Dhont and extend his theoretical work to complex interacting systems and monitor the distortion of the structure factor $S(q)$ due to the applied shear.
Across the literature there is already experimental evidence related to the spatial arrangement of this type of systems under weakly sheared conditions which can be utilized as a possible validation [72]. Furthermore, this analytical theory can be used as the starting point to describe several physical systems such as plasmas and dusty plasmas [73]and , also, to predict and model controlled self-assembly of nanoparticles using shear flow [74].

Part II

Predictive modelling of seeded emulsion homo-, co- and ter-polymerization kinetics and analysis of coagulation behavior of colloidal latexes

Chapter 5

Introduction

In Chapter 1 It has been highlighted how the aggregation of Brownian particles with a stationary one has been adopted to model the entry of oligomers and the desorption of monomeric radical species during an Emulsion Polymerization (EP) (see section 1.2.2).
This part of the thesis will be focused on this polymerization mode and it will be centred on a kinetic model for externally seeded emulsion polymerizations which includes new updated mechanisms for critical kinetic phenomena such as radical entry and exit. Another goal of this project is trying to optimize operative conditions to minimize the formation of undesired coagulum which is one of the major causes of reactor fouling.
The following chapter will first provide with a brief description of the main mechanistic aspects of an EP followed by a quick review on the main possible causes for which particles could start aggregating uncontrollably and form coagulum.

5.1 What is an emulsion polymerization?

An EP is an heterogeneous free-radical procedure (FRP) which is mainly driven by sequential addition of monomeric units to active propagating chains happening in a population of particles dispersed in an aqueous phase. It starts from an initial charge of water where a surfactant, an initiator (usually a water-soluble inorganic salt) and one or more monomers are mixed; some sort of agitation must be provided, of course, to avoid phase separation. There is great interest from the industrial community in improving the description of this process since it has become the most popular option for the production of a great variety of polymeric products, usually known as latexes, with broad application range, from adhesives, paints and additives for paper [75]. Its popularity derives from a multitude of advantages when compared to other FRPs: the use of water as liquid medium instead of organic solvents is more gentle towards the environment and eases the removal of the heat produced during

the reaction. Moreover, it guarantees the possibility to obtain waterborne dispersions with a solid content over 50%, a feature highly desirable for many products because of lower costs for transport and faster medium evaporation.
There are several different methodologies to implement it: the more straightforward one is the *batch procedure* where all the ingredients are added at the beginning of the process. This procedure is not the one the model is focused on, but its description is useful to understand the basic mechanisms of an EP.

5.1.1 Batch polymerization

The process starts from an the aqueous phase which is immediately mixed with a monomeric charge, an emulsifier and an initiator. Since the adopted monomers are usually hydrophobic they quickly saturate the liquid environment and subsequently form droplets which are surrounded by the surfactant. Another organic phase is eventually formed if the remaining amount of dissolved emulsifier passes its critical micelle concentration threshold: a high number of micelles dispersed in the liquid environment are formed which are quickly saturated by monomers diffusing from the droplets. According to the more established mechanistic description an EP is divided into three different intervals [76].

Interval I

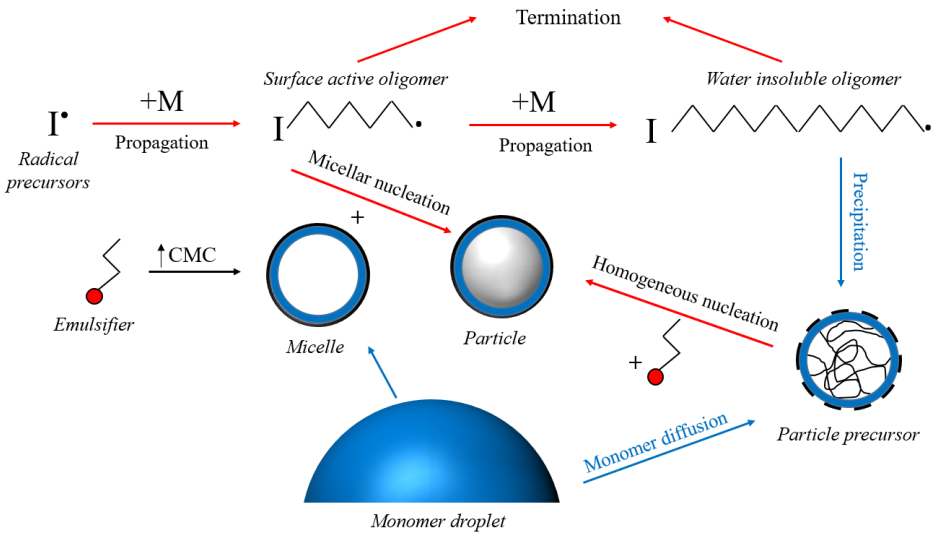

Fig. 5.1 Different mechanisms of particle formation.

Interval I, whose fundamental mechanisms are proposed in Fig. 5.1, is centred on the formation of the particles. It starts from the decomposition of the initiator into radical precursors: since they are too hydrophilic to interact with any organic phase they start reacting with the monomer dissolved in the aqueous phase. The newly formed oligomers can, in turn, (i) keep propagating with other monomer or (ii) terminate with another oligomer in the aqueous phase. If they become sufficiently hydrophobic, also defined as *surface active*, they can leave the aqueous phase and be absorbed by one of the organic ones. Since it is very common that the total surface area of the micelles is orders of magnitude higher than the one of the droplets, it is much more likely for an oligomer to enter a micelle giving birth to a polymer particle; this mechanism has been named *micellar* or *heterogeneous nucleation* [77]. More than 20 years later with respect to the discovery of the aforementioned mechanism, it has been established that the formation of new particles can also happen in the absence of micelles [78, 79]: the oligomers can actually keep growing even after they pass the limit for the surface activity until their hydrophobicity is so high that they become completely water-insoluble. At this point their inevitable fate is to precipitate and, since they have become part of an hydrophobic phase, to be surrounded by the molecules of emulsifier still dissolved in water and saturated by monomer forming new particles; this mechanism has been called *homogeneous nucleation*.

Interval II-III

As soon as Interval I is over all of the micelles have disappeared and the total number of particles N_P inside the aqueous phase is constant the particle growth starts and it covers the remaining Intervals II-III. Even if micelles are absent the surfactant has a role of paramount importance in making sure that aggregation does not take place by stabilizing the particle phase electrostatically, if an ionic surfactant is adopted, rather than steric, if a non-ionic emulsifier is used; a better explanation on these mechanisms will be provided in Section 5.2. One of the crucial aspects at this point of the polymerization is accurately monitoring how each monomer is distributed among the phases present at that time. During Interval II there is still a droplet phase, so the particles are saturated by the monomers which start reacting with the propagating chains: when a certain amount of monomer is consumed it is immediately replaced by other diffusing from the droplets. Once the droplets are depleted, Interval III begins: the majority of the monomers happen to be in the particle phase, so their concentration will consistently decrease over time until the conversion is completed or reached a steady value.

It is widely accepted that, to model how each monomer is split among the phases, its transport from one phase to the other is much quicker than any chemical reaction involving it,

a principle which will be the starting point to model the partitioning scheme in Section 6.4.
The second crucial aspect is the description of the mechanisms influencing the number of

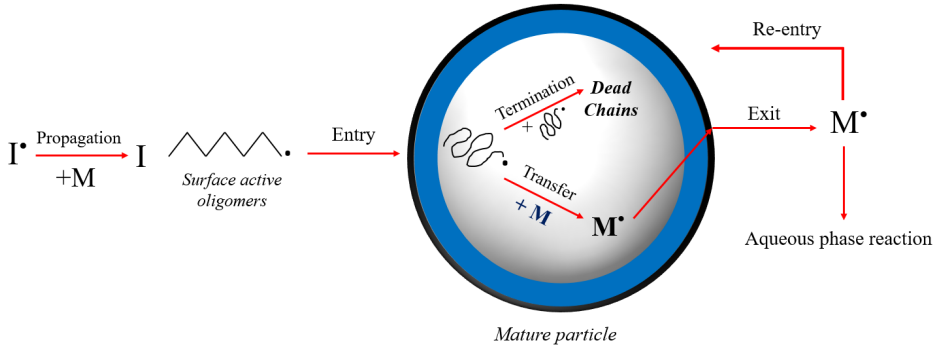

Fig. 5.2 Factors influencing the number of radicals in each particle during Interval II-III.

radicals contained in each particle during Interval II-III which are graphically introduced in Fig. 5.2. There can be a loss of radical activity in the particle phase because two chains encounter each other triggering the reaction of termination. Alternatively, it is possible that monomeric radicals derived from a radical chain transfer are capable of exiting a particle and, once they are in the liquid medium, can subsequently propagate or terminate within the aqueous phase.
On the other hand there are also mechanisms which help boosting the reactivity inside a particle by increasing the total number of propagating chains: it is possible for some of these desorbed monomers to actually re-enter another particle and then convert more monomer. At the same time in the aqueous phase radical precursors and dissolved monomers keep forming surface active oligomers with the same mechanism introduced in Interval I for the heterogeneous nucleation but, instead of entering micelles, they will enter the already formed polymer particles and increase the overall radical activity.

5.1.2 Semi-continuous polymerization

Even if the batch mode is very helpful to describe all the different mechanisms and phenomena happening during an EP it is rarely used in mass-scale industrial productions because of the difficulty in controlling the polymer features and the reaction conditions as well. For instance, if the polymerization involves multiple monomeric species with very different reactivity ratios a phenomenon named *compositional drift* happens: at the beginning of the process the more reactive monomer will be converted more easily causing an inhomogeneous composition in the latex between the beginning and the end of the batch. This is highly undesired because it affects the end-use properties of a latex i.e. a 95/5 wt/wt *n*-Butyl

Acrylate/Methyl Methacrylate is an adhesive, meanwhile a 50/50 latex is a binder for paints, so in case compositional drift happens during its production it is neither one material nor the other [80]. Moreover, FRPs are well-known to be exothermic reactions: in scenarios where the conversion of monomers release extreme amounts of heat, especially during the earlier stages of a batch, cooling down the reactor is non-trivial and this exposes the system to run away reactions which will put the safety of the plant at risk.
A convenient solution to avoid these issues is to operate under *semi-continuous* conditions where all the reactants are consistently dosed over a pre-determined time span.
There are two possible strategies: the first foresees an initial charge of a fraction of the reactants in order to allow particle formation to happen followed by a slow dosage of the complementary reaction mixture; in this case the process is called *internal seeded EP*. Alternatively, Interval I can be entirely skipped by charging the reactor with an already made latex followed by a slow additions of the reactants; this mode is called *external seeded EP*. In a semi-continuous procedure it is possible to optimize the flow rate of each monomer to prevent the compositional drift and it guarantees a much better control over the particle size distribution by accurately selecting the total fraction of the reactants initially charged. Moreover, the external seeded EP guarantees also a great control on the particle size since the polymer particle number N_P and the total mass of the monomer additions can be decided a priori.
Finally, the heat produced by the reaction per unit of time will be more gradual and consistent, making the temperature inside the reactor much easier to control; in this thesis attention will be paid to *external seeded polymerizations*.

5.2 Coagulum formation in emulsion polymerization

One of the major issues when it comes to the production of latexes is that the polymer suspension is thermodynamically unstable: the reduction of the Gibbs free energy related to the system, the indicator for the transition from an unstable to a more stable state, is linked to the reduction of the total interfacial area of the particles which inevitably leads to coagulation.
On the other hand, latexes are kinetically stable which means that they can be properly treated to delay their transition to thermodynamic equilibrium and guarantee a product with the desired properties (such as tackiness, peeling resistance or shear resistance for adhesives, the main products studied in this work) and avoiding any aggregation, if not desired. The concept of kinetic stability is linked to the presence of an energy barrier which discourages the particles to approach each other and colliding with enough energy to coagulate. If this

principle is not respected there can be uncontrolled aggregation during the production of the latex which leads to the formation of both microscopic and macroscopic coagulum due to which the final product cannot achieve the required design features.
There are several possible causes for coagulum to form which are based on aggregation phenomena or related to the polymerization kinetics. This last category includes the so-called *secondary nucleation*: it is basically a second wave of particle formation meanwhile mature particles are already present in the system which can lead to system destabilization. Anyway, this phenomenon is relevant if the number concentration of mature particles in the reactor is $[N_P] \approx 10^{14}$ L^{-1} or lower [75], meanwhile the EPs used to analyse coagulum formation are featured by $[N_P]$ two order of magnitudes or more higher than this limit throughout the whole polymerization, so this eventuality has not been considered.
In the end it has been decided to focus on aggregation phenomena between mature particles only. The first ever study about it has been proposed in Chapter 2: in that particular case the flow rate of particles J through Eq.(2.65) has been evaluated. In this particular scenario it is more of interest the aggregation rate β_{ij} between two particles with radiuses R_i and R_j which can be related to J as

$$J = \frac{1}{2}\beta_{ij}C_0. \tag{5.1}$$

According to the aforementioned correlation the collision rate under diffusion-limited conditions can be generalized as:

$$\beta_{ij}^{\mathrm{DL}} = \frac{2k_BT}{3\eta}(R_i+R_j)\left(\frac{1}{R_i}+\frac{1}{R_j}\right). \tag{5.2}$$

To add the effect of the energy barrier on the aggregation kinetics, which is now defined to be under *reaction-limited* conditions, it is necessary to add the Fuchs stability ratio [51] to Eq.(5.2):

$$\beta_{ij}^{\mathrm{RL}} = \frac{\beta_{ij}^{\mathrm{DL}}}{W_{ij}} = \frac{2k_BT}{3\eta W_{ij}}(R_i+R_j)\left(\frac{1}{R_i}+\frac{1}{R_j}\right) \tag{5.3}$$

$$W_{ij} = (R_i+R_j)\int_{(R_i+R_j)}^{\infty}\frac{\exp\left(U/k_{\mathrm{B}}T\right)}{\chi_c^{-1}(r)r^2}\mathrm{d}r, \tag{5.4}$$

where U is the interaction potential describing the energy barrier between two particles, k_{B} the Boltzmann constant, T the absolute temperature, r the centre-to-centre distance between the particles normalized by their size, and χ_c^{-1} the function representing the hydrodynamic interactions between the particles explained in Section 2.2.1; now it is necessary to focus on the possible contributions to U which is usually modelled, according to the DLVO theory, as

a superposition of two different effects:

$$U = U_{\text{vdw}} + U_{\text{rep}}. \tag{5.5}$$

U_{vdw} is the potential related to the attractive interactions collectively known as van der Walls forces which arise from the presence of different dipole-dipole interactions which are described by the well-known Hamaker equation [81]

$$U_{\text{vdw}} = -\frac{H}{6}\left[\frac{2R_iR_j}{r^2-(R_i+R_j)^2} + \frac{2R_iR_j}{r^2-(R_i-R_j)^2} + \ln\left(\frac{r^2-(R_i+R_j)^2}{r^2-(R_i-R_j)^2}\right)\right], \tag{5.6}$$

where H is the Hamaker constant.
U_{rep}, instead, represents the repulsive forces which are the foundations for kinetic stability; the two most common mechanisms to guarantee it are proposed in Fig. 5.3.
Some formulations foresee the use of non-ionic surfactants such as ethoxyaltes or certain

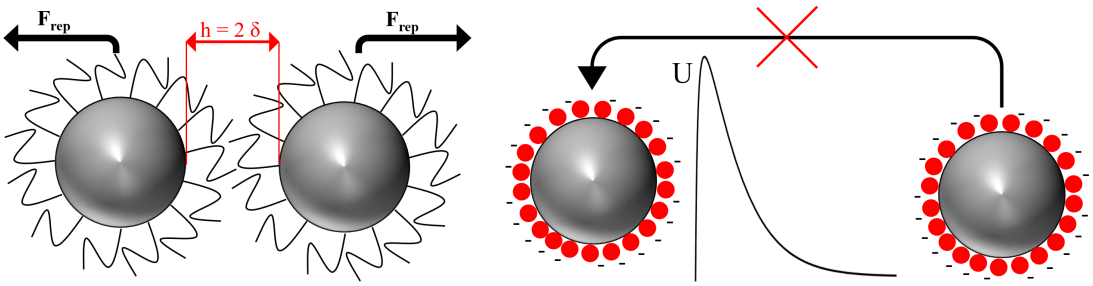

Fig. 5.3 Major mechanisms to guarantee kinetic stability: steric (left) and electrostatic (right).

particular polymers such as Poly(Ethylene Oxide) or Poly(Vynil Alcohol) to guarantee *steric stabilization* [82]: their absorption on the surface of the particles foresees the creation of an hairy layer with a certain width δ. If the surface-to surface distance h becomes less than 2δ, the layers will be compressed and generate a repulsive mechanical force F_{rep}, associated to the repulsive potential U_{rep}, which causes the particles to literally bounce off each other.
Another possibility is the *electrostatic* approach: it involves the use of ionic surfactants, usually anionic, whose absorption builds an electric double layer (EDL) providing the particles with a net negative surface charge density $\sigma_{\text{net},i}$ and surface potential ζ_i which generates the repulsive contribution to the energy barrier U. A quantitative expression for U_{rep} can be found for sufficiently low potentials (< 60 mV) and thin EDLs according to Hogg,

Healey and Furstenau [83]:

$$U_{\text{rep}} = \frac{\pi\varepsilon_0\varepsilon_r R_i R_j(\zeta_i^2+\zeta_j^2)}{(R_i+R_j)}\left\{\frac{2\zeta_i\zeta_j}{(\zeta_i^2+\zeta_j^2)}\ln\left[\frac{1+\exp\left(-\kappa(r-R_i-R_j)\right)}{1-\exp\left(-\kappa(r-R_i-R_j)\right)}\right]+\right.$$
$$\left.+\ln\left\{1-\exp\left[-2\kappa(r-R_i-R_j)\right]\right\}\right\} \quad (5.7)$$

where ε_0 is the vacuum dielectric constant and ε_r the relative medium permittivity. Finally, κ represents the inverse of the Debye length, an indicator of the range where the electrostatic interactions around one particle are actually effective:

$$1/\kappa = \sqrt{\frac{\varepsilon_r\varepsilon_0 k_B T}{2N_{\text{AV}}e^2 I}}, \quad (5.8)$$

where e is the electron charge and $I[\text{mol m}^{-3}]$ is the ionic strength in the liquid medium which depends on the contribution of every ionic species C_i in the liquid medium and their respective valences z_i

$$I = \frac{1}{2}\sum_i z_i^2 C_i, \quad (5.9)$$

5.2.1 Impact of the surfactant surface coverage

One of the most intuitive aspects of electrostatic stabilization is the fact that the surface charge density is strictly dependent on the fraction of the total surface of the particles which is actually covered by the surfactant. Melis et al. [84] started their description of the colloidal stability of a Poly-Vynil Acetate latex by correlating the surface charge density to the surface coverage θ, which is the ratio between the surface of the particles actually covered and the one considering saturation conditions, through:

$$\sigma_0 = z_{\text{E}}\theta\Gamma_\infty e N_{\text{AV}}, \quad (5.10)$$

where Γ_∞ is the emulsifier concentration at saturation conditions, z_{E} is the valence of the absorbed molecules of surfactant and N_{AV} is recalled to be the Avogadro number. Then, they calculated the net charge σ_{net} by subtracting the screening effect due to absorbed counterions in the EDL allowing them to evaluate the zeta potential ζ and, subsequently, the Fuchs Stability ratios through Eq.(5.4).

A simplified approach has also been proposed by Unzueta and Forcada which correlates W_{ij}

to the surface coverage for a *n*-Butyl Acrylate/Methyl Methacrylate co-polymerization [85]:

$$W_{ij} = K' \exp\left(K"\sqrt{\theta}\right), \tag{5.11}$$

where K' and K" are adjustable parameters.
The correlation between surface coverage and surface charge density has also been proved experimentally. Mayer et al. [86] analysed the coagulation of poly-styrene stabilized by DRAS: they have figured out that a minimum surface coverage θ_{cr} must be provided in order for the coagulation to be prevented. The same principle has been reported by Sajjadi [87] for a seeded homopolymerization of *n*-Butyl Acrylate for which $\theta_{cr} = 0.25$ must be guaranteed. Sňupárek and coworkers [88] have also analysed the effect of various dosages of surfactant during semi-continuous polymerizations of different acrylic monomers: by varying the ratio between the emulsifier initially charged (R) and the one subsequently added after particle formation (E) he has reported a considerable increase of coagulum formation with increasing R/E. This observation makes perfect sense because the higher the emulsifier at the beginning the higher the number of particles will be generated during Interval I and, subsequently, less emulsifier per particle will be available to guarantee stability during the growth.
From these investigations it clearly emerges that having an excessively "naked" surface reduces the height of the energy barrier provided by exposing the particles to a higher number of successful collisions on the hydrophobic polymer spots, which leads to coagulation [89].

5.2.2 Impact of saline content

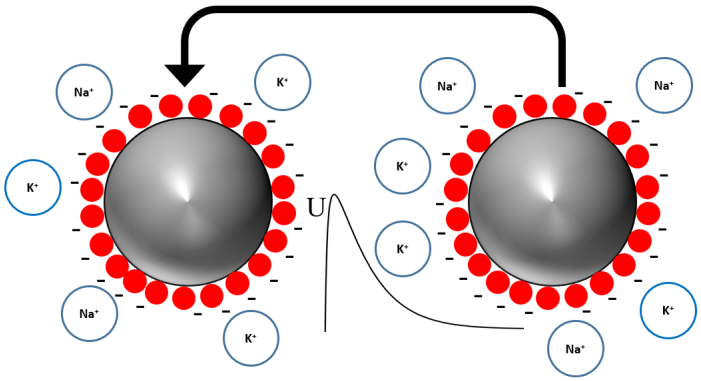

Fig. 5.4 Screening effect between two charge stabilized particles

An insufficient surface coverage is not the only possible cause which can weaken the energy barrier: from the analysis of Eq.(5.8-5.9) it is clear that an increase of the ionic strength, the indicator of the overall saline content in the system, causes the reduction of the

Debye length and, subsequently, of the energy barrier; this phenomenon is represented in Fig. 5.4 and it is often referred to as *screening effect*.
Let's suppose to have stabilized the suspension with an anionic emulsifier: the presence of cationic species inside the liquid medium hides the negative charges absorbed on the particles, so the range where they can reject each other is smaller and it is easier for the particles to get sufficiently close to pass the energy barrier and coagulate. The consideration of this aspect is of paramount importance in an emulsion polymerization since in both lab and industrial formulations a considerable amount of salts are used: some very common initiators are divalent salts such as persulfates, which can be coupled with potassium, sodium or ammonium. Moreover there is the necessity to include additions of buffer solutions, such as ammonia or sodium bicarbonate for various reasons, among which there is pH-control, and even the emulsifier itself dissolves cationic species in the liquid medium since it is usually adopted as an organic salt.
This effect has been widely studied across the literature: Melis et al. [84] analyzed the effect of different amounts of sodium chloride on the aggregation behavior of Poly-Vynil Acetate latex through Population Balance Modelling, confirming an increasing aggregation rate with higher saline content. Moreover, they stated that salt-induced aggregation is the more dominant coagulation mechanism in the typical operative conditions of an EP, so any shear-induced contribution has been neglected. Jia and coworkers [90] introduced another possible approach as they considered the influence of different salts on a carboxylic latex surface. They proposed that the cationic species not only screened the negative charges on the particles, but also reduced the number of active surface charge groups by establishing association equilibria with the absorbed molecules of emulsifier which ultimately caused an ulterior reduction of the colloidal stability. By comparing the results from their model to experimental data derived from Static Light Scattering (SLS), they accurately predicted the aforementioned decrease of W with the increase of total salt concentration.
Ehrl et al. [91] have extended this study with the intent of predicting the Critical Coagulation Concentration (CCC) for certain pairs salts/carboxyl-stabilized colloids. The CCC is the molar concentration of counterions which causes the energy barrier to disappear, causing the aggregation to speed-up and becoming diffusion-limited. They have predicted the CCC value for a charge stabilized latex under different pH by finding the concentration of each salt which causes W to be around 1.5 and compared their results to experimental data provided in the literature [92] finding a very good agreement, as it is showed in Fig. 5.5.

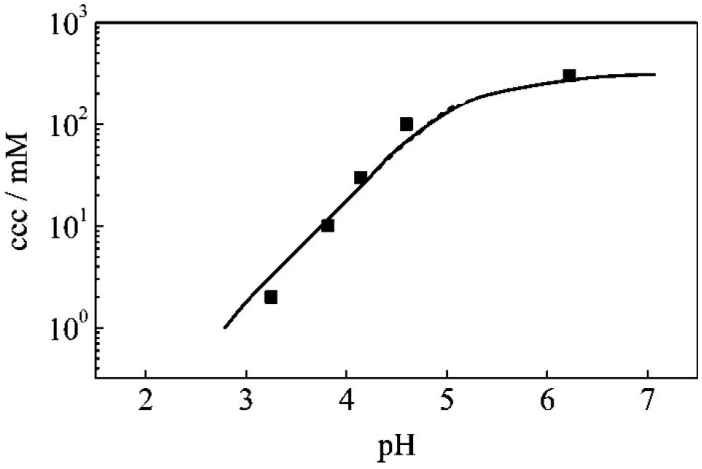

Fig. 5.5 Values of the critical coagulation concentration (ccc) as a function of pH for a latex with the primary particle radius $R_P = 155$nm (adapted from [91]).

5.2.3 Impact of fluid motion: shear-induced aggregation

Because of the simultaneous presence of hydrophilic and hydrophobic phases the reaction environment must be stirred to avoid phase separation between the phases and to guarantee reaction conditions as homogeneous as possible inside the reactor. On the other hand, careful attention must be paid to this aspect: the particles inside the liquid medium experience shear rates due to the fluid motion which push them towards each other. In extreme cases the shear rate is sufficiently strong that particles can get over the energy barrier leading to orthokinetic aggregation.

This phenomenon has already been discussed in the Section 2.3, so it will not repeated here; the onyl necessary recall is the extension of the orthokinetic limit Eq.(5.12) to particles with generic sizes R_i and R_j proposed by Smoluchowski under laminar flow [93] which has been extended to three dimensions by Camp and Stein [94]:

$$\beta_{ij} = \frac{4}{3} G (R_i + R_j)^3 \tag{5.12}$$

where G is the spatially averaged shear rate which can be related to the agitation power P by

$$G = \sqrt{\frac{P}{\mu V}}, \tag{5.13}$$

where μ is the suspension dynamic viscosity, V the volume of the liquid phase inside the reactor; this approach can also be used for turbulent flows according to [94]

$$G = \sqrt{\frac{2\varepsilon}{15\pi\nu}}, \tag{5.14}$$

where ε the energy dissipation rate and ν the kinematic viscosity. Eq.(5.12) has been adopted by Matějíček and co-workers [95] to study the influence of the reactor agitation on the appearance of coagulum during the ter-polymerization of styrene/butyl acrylate/acrylic acid: an initial increase of P the fouling thanks to a better mixing but, above a certain power threshold, the coagulum increases because of the increasingly important contribution of the shear-induced aggregation process.
On the same hand Krutzer et al. [96] adopted the same approach to shear-induced coagulation under different regimes, going from laminar to isotropic turbulent flow and compare their results to existing theories finding out that usually theoretical approaches underestimate experimental evidence.
Finally, it is worth mentioning the work by Lowry and co-workers [97]: they have observed an increase of fouling with increasing power provided to the impeller because more frequent collisions become capable of overcoming the energy barrier between the particles. They rationalized their findings by proposing a semi-empirical model for the collision rate

$$\beta_{ij} = \frac{4Gf(\phi)}{\pi W_{ij}}, \tag{5.15}$$

where $f(\phi)$ is a function dependent on the volume fraction ϕ of the solids. Even if a complete and quantitative understanding of such phenomena is quite difficult, it can be said that the impelling power during a polymerization should be sufficient to ensure homogeneous mixing conditions inside the reactor, as it has also been proved by Zubitur at al. [98], but at the same time it must not be too strong to generate shear-induced aggregation.

5.3 Summary

In this chapter the basics of an emulsion polymerization and the main possible reasons for coagulum formation have been proposed. Even if plenty of effort has been put to study how different phenomena affect the formation of coagulum and, in spite of these extensive efforts, there are currently no studies in the literature which address the intimate link between the polymerization kinetics, the reaction environment and the coagulation process which, on the other hand, will be the ultimate goal of the project which sees this work as its first step;

moreover the proposes new recently developed mechanisms to describe crucial phenomena happening during an EP such as the radical exit from the particles.
Chapter 6 is focused on the explanation of every mechanistic aspect included in the model which describes the polymerization kinetics involving multi-radicalic species by adopting the well-known *pseudo-homopolymerization* approach with a particular focus on the new mechanisms of radical entry and exit. Moreover, the kinetic model will be coupled with two functions which tracks the surface coverage θ and the total amount of counterions added to the system at any time; for now no possible scheme to detect actual aggregation is implemented, but the intent is to visualize the operative conditions which can be related to a *possible loss of colloidal stability*.
In Chapter 7 the resulting framework has been calibrated extensively with two different series of test cases from the literature, one of homo-polymerizations of *n*-Butyl Acrylate followed by one of co-polymerizations involving *n*-Butyl Acrylate and Methyl Methacrylate; it will guarantee an accurate reproduction of crucial features such as *conversion*, *composition* and *particle size* through a very limited number of adjustable parameters and the validation is combined with explanation about the most important kinetic aspects related to each series.
The attention has then focused on an industrial test case, a *n*-Butyl Acrylate / Methyl Methacrylate / 2-HydroxyEthyl Methacrylate ter-polymer. After having verified once again that the model can monitor the overall kinetic variables of interest, it analyses two different test cases where different amounts of an anionic emulsifier have been used with the ultimate goal of studying the interplay between different surface coverages and saline contents on the formation of coagulum during the polymerization.

Chapter 6

Description of the kinetic model

As mentioned at the end of the previous chapter, the following one will provide an accurate description of the reaction kinetics and mechanisms adopted in the model which will be used in emulsion homo-, co- and ter-polymerizations involving *n*-Butyl Acrylate(*n*-BA), Methyl Methacrylate (MMA) and 2-HydroxyEthyl Methacrylate (2-HEMA): in particular a new recently developed mechanism for the exit rates together with an approximate, but analytic, approach for the radical entry have been included for the first time in a rigorous kinetic model.
The main monomer adopted in the polymerizations is n-Butyl Acrylate which is often used, combined with other monomers including MMA, in the formulation of outdoor paints, coatings or pressure sensitive adhesives [99]. The formulations are really versatile: an increase of *n*-Butyl Acrylate helps low temperature properties and flexibility since its glass transition temperature T_g is really low ($T_g = 228$ K). On the other hand an higher presence of harder monomers such as MMA ($T_g \sim 378$K) improves hardness and cohesive strength. This means that the composition of the product can be tailored based upon the end-use properties of the product; other functional monomers, such as 2-HEMA, can be added for improving adhesion properties and facilitate cross-linking if needed [99].

6.1 Choice of the modelling approach

Every emulsion polymerization model falls into two big subgroups based upon the fact that the framework can monitor the Particle Size Distribution (PSD) of a latex or not [100]: Type-2 models track it by solving Population Balance Equations [101, 102], on the other hand Type-1 approaches [103, 104] do not by respecting the following hypotheses

1. The suspension is considered monodisperse at any time;

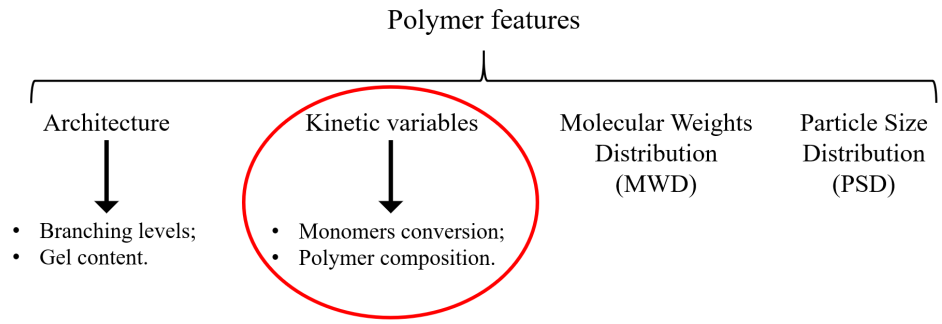

Fig. 6.1 Some of the main features of a latex dispersion which can be tracked by EP modelling; inside the red circle the features this work is focused on are highlighted.

2. The reactor is perfectly mixed.

The choice between Type-1 or 2 strictly depends on the features the modeller is interested in and Fig. 6.1 reports some of the most important ones.
The PSD has a crucial impact on the rheology and maximum solid content achievable by the latex, two features which control the quality of the mixing and the capability of the system to exchange heat: some interesting works have linked a multimodal PSD to the packed fraction ϕ of the suspension [105]. This information is then utilized to evaluate the rheological properties of the latex which ultimately leads to the determination of the maximum packed fraction the latex can achieve.
Even if a Type-1 approach is more approximative than a Type-2 it can still reproduce accurately important features. Among them there is the Molecular Weights Distribution (MWD) which has a crucial impact on the design properties of adhesives: for instance their tackiness is highly favoured by low Molecular Weights (MWs), meanwhile their resistance to peel is eased by intermediate MWs and high MWs improves the resistance against shear [106], making a hard challenge to find the optimal balance between the three depending upon the applications of each product. There are also other characteristics, for instance related to the architecture of the polymer itself, which can deeply influence the end-use properties: it has been verified that a certain fraction *n*-Butyl Acrylate based latexes can become completely water-insoluble during the reaction forming then a gel phase which plays an important role in determining the shear resistance of certain adhesives [107] and in enhancing binding strength of some paper coatings [108].
Despite their importance the aforementioned features have not been included at this stage of the modelling and it has been decided to adopt a Type-2 approach: since one of the main targets of this project is an accurate modelling of the surfactant surface coverage, only the features linked to the particle growth such as *monomers conversion* and *average particle size* have been included. Nonetheless the developed model can correctly predict, if necessary, the

latex *composition* which is linked to the glass transition temperature T_g and, subsequently, the Minimum Film Forming Temperature which is an important parameter in order to properly formulate a product which needs to cure under specific conditions.

6.2 Description of the evaluation of the kinetic variables

The first operation the model executes is gathering information from the initial charge which consists of an aqueous phase containing a certain mass $m_{\mathrm{P},0}$ of the external seed from which it initializes the volumes of the present phases and the total number of particles N_{P}.
Afterwards, it checks which additions are happening at each timestep and updates masses and volumes of every component influencing the kinetics (water, monomers and initiators). Finally, it processes this information providing with an evaluation of the amount of monomer consumed at each timestep which allows the evaluation of the kinetic variables:

1. monomers conversion from which the average particle size can be computed;
2. composition of the latex.

The model monitors these variables by solving a series of mass balances involving the N_m monomers present in the system

$$\frac{dm_{\mathrm{j}}}{dt} = \dot{m}_{\mathrm{in}} - C_{\mathrm{p}}^{\mathrm{j}}, j = 1, ..., N_m, \tag{6.1}$$

where m_{j} is the total mass of each free monomer in the reactor at time t, $\dot{m}_{\mathrm{in}}$ its mass entry rate at time t foreseen by the formulation and $C_{\mathrm{p}}^{\mathrm{j}}$ its consumption due to the polymerization whose evaluation is the fundamental point of the whole model:

$$C_{\mathrm{p}}^{\mathrm{j}} = f(R_{\mathrm{prop,p}}^{\mathrm{j}}, [\mathrm{R}_{\mathrm{TOT}}^{\bullet}]_{\mathrm{p}}). \tag{6.2}$$

It depends on $R_{\mathrm{prop,p}}^{\mathrm{j}}$, the propagation rate related to each monomer in the particle phase, and $[\mathrm{R}_{\mathrm{TOT}}^{\bullet}]_{\mathrm{p}}$ the total concentration of active chains in the aforementioned phase which in an EP can be rewritten according to the principle of compartmentalization as

$$[\mathrm{R}_{\mathrm{TOT}}^{\bullet}]_{\mathrm{p}} = \frac{\tilde{n} N_{\mathrm{P}}}{N_{\mathrm{AV}} V^{\mathrm{p}}}, \tag{6.3}$$

where $\tilde{n}$ is the average number of radicals per particle, N_{P} the total number of particles and V^{p} the volume of the particle phase, where all the polymerization is considered to take place. What follows describes the methodologies of evaluation of every feature of the system which

plays a crucial role in determining $R^{j}_{prop,p}$ and the total radical activity.
It is important to remember that $\tilde{n}$ is determined by three fundamental events: it is increased by the entry of surface active oligomeric radicals from the liquid environment whose rate is influenced by the overall propagation $R_{prop,w}$ and termination $R_{term,w}$ rates in the aqueous phase. On the other hand the radical activity is decreased by reactions happening in the particle phase: the first is the encounter between two active chains which leads to their termination happening with rate $R_{term,p}$. The presence of radicals in the particles is also decreased by the exit of monomeric radicals: since only oligomers can enter their presence in the particles is exclusively due to chain transfer to monomer happening with rate R^{j}_{fm}.
Every introduced kinetic rate depends on two different features: the respective rate constants and the concentrations of the monomeric species they are referred to. In Section 6.4 the procedure with which the concentrations of interest are obtained after each timestep will be described and in Section 6.5 the rate constants related to all the fundamental reactions influencing the target properties of the model will be introduced. At this point it is finally possible to introduce the methodologies with which the rate constants and the concentrations have been linked to to evaluate $R^{j}_{prop,p}$ and all the other reaction rates in Section 6.6. Finally, in Section 6.8 it is described the procedure with which the now computed rates influence the average number of radicals $\tilde{n}$.
At this point the model is capable of computing the consumptions C^{j}_{p} which will be used in the post-processing section described in Section 6.9 in order for the model to update the target variables.

6.3 Initialization of the model

The initial stage foresees the charge of a certain volume of water V_{water} in which a predefined volume $V_{pol,0}$ of an already made latex with known particle size $R_{p,0}$ is dispersed.
The first computed quantity is the total number of particles N_P:

$$N_P = \frac{V_{pol,0}}{\frac{4}{3}\pi R^3_{P,0}}. \tag{6.4}$$

$V_{pol,0}$ can be found by the knowledge of the total mass of the seed $m_{p,0}$ and its density $\rho_{P,0}$ which is approximated by an average of the densities ρ_{Pi} of their respective homo-polymers weighted by the mass fractions ω_i of each monomer in the seed:

$$\rho_{P,0} = \sum_{i=1}^{N_m} \rho_{Pi}\ \omega_i; \tag{6.5}$$

from this point on N_P will be considered constant throughout the whole reaction.
Immediately after the model initializes the volumes of the aqueous $V^\mathrm{w} = V_\mathrm{water}$ and the particle phase $V^\mathrm{p} = V_\mathrm{pol,0}$.

6.4 Partitioning scheme

Every timestep starts from the update of the volumes of free monomers V_j and water V_water from every foreseen addition and the total amount of the latex V_pol derived from the calculations of the previous timestep.
The partitioning scheme has the task of calculating the following variables:

1. the total volume of the droplet V^d, particle V^p and water phase V^w;
2. the volume fraction of every monomer in each phase ϕ_j^k;
3. the volume fraction of polymer present in the particles $\phi_\mathrm{pol}^\mathrm{p}$;
4. the volume fraction of the water in the aqueous phase ϕ_water^w.

Since there is the necessity to compute $3\,N_m + 5$ variables, an equivalent number of equations is needed: first and foremost the volume balances for each V_j, the water and the polymer together with the conservation of the volume fractions of every component in each phase are considered.

$$\begin{cases} V_\mathrm{j} = \phi_\mathrm{j}^p V^p + \phi_\mathrm{j}^d V^d + \phi_\mathrm{j}^w V^w, \ j = 1,...,N_m; \\ \phi_\mathrm{water}^w V^w = V_\mathrm{water}; \\ \phi_\mathrm{pol}^p V^p = V_\mathrm{pol}; \\ \sum_{j=1}^{\mathrm{N}_m} \phi_\mathrm{j}^p + \phi_\mathrm{pol}^p = 1; \\ \sum_{j=1}^{\mathrm{N}_m} \phi_\mathrm{j}^d = 1; \\ \sum_{j=1}^{\mathrm{N}_m} \phi_\mathrm{j}^w + \phi_\mathrm{water}^w = 1; \end{cases} \tag{6.6}$$

Still $2\,N_m$ equations are necessary to make the system solvable, so it is necessary to find correlations among the volume fractions related to the monomeric species ϕ_j^k. Assuming negligible mass transport resistances, the correlations between them are determined by using partition coefficients K_j^k, defined as the ratio of the concentration of the j-th component between the k-th and the aqueous phase:

$$K_j^k = \frac{\phi_{j,\mathrm{sat}}^k}{\phi_{j,\mathrm{sat}}^w} \sim \frac{\phi_j^k}{\phi_j^w} \quad j = 1,...,N_m. \tag{6.7}$$

Property	Value	Source
$\phi^p_{\text{MMA,sat}}$	0.73	[109]
$\phi^w_{\text{MMA,sat}}$	0.028	[110]
$\phi^w_{\text{2-HEMA,sat}}$	0.094	[111]
K^p_{BA}	480	[112]
K^d_{BA}	740	[112]
$K^p_{\text{2-HEMA}}$	3.51	[113]
$K^d_{\text{2-HEMA}}$	10.70	Eq.(6.7)
K^p_{MMA}	26	Eq.(6.7)
K^d_{MMA}	36	Eq.(6.7)

Table 6.1 Saturation values adopted to compute the missing partition coefficients

The series of K^k_j coefficients should be specific for the monomers-copolymer system of study. However, since it was not possible to experimentally evaluate them, the partitioning coefficients of each component in its homopolymer have been applied as found in the literature as for *n*-BA, or calculated by knowing the appropriate volume fractions at saturation conditions as it has been done for MMA and 2-HEMA; every input variable and the adopted values of the partition coefficients are proposed in Table 6.1. At this point it is possible to solve the algebraic system Eq.(6.6-6.7) and, once every ϕ^k_j is known, to compute the molar concentrations of interest as

$$[\mathrm{J}]_k = \frac{\text{number of moles of the j-th monomer in the k-th phase}}{V^k} = \frac{\rho_{\mathrm{m,j}}}{\mathrm{MW_j}} \frac{V^k_{\mathrm{j}}}{V^k} = \frac{\rho_{\mathrm{m,j}}}{\mathrm{MW_j}} \phi^k_{\mathrm{j}}, \tag{6.8}$$

where $\rho_{\mathrm{m,j}}$ are densities and $\mathrm{MW_j}$ the molecular weights of each monomer; it is also important to highlight the update of the volume fraction of the polymer ϕ^p_{pol} which will be adopted in the definition of the termination rate in the particle phase $R_{\text{term,p}}$ later on.

6.5 Fundamental reactions

After the volumes, volume fractions and molar concentrations are updated, the model is ready to calculate the reaction rates, so this section is dedicated to the introduction of all the elements constituting the overall reaction scheme together with all the kinetic rate constants used as inputs by the model.

In a FRP every chemical process involving organic species is centred on polymeric chains whose nomenclature is expressed as: $\mathrm{R^{\bullet}_{k,i}}$. Its two main features are the number k of monomeric units inside it also called degree of polymerization and the type of reactive

Type of monomer	**Type of active chain**
n-BA $\rightarrow 1$	$R^{\bullet}_{k,SPR} \rightarrow 1$
	$R^{\bullet}_{k,MCR} \rightarrow 2$
MMA $\rightarrow 3$	$R^{\bullet}_{k,MMA} \rightarrow 3$
2-HEMA $\rightarrow 4$	$R^{\bullet}_{k,2\text{-}HEMA} \rightarrow 4$

Table 6.2 Convention adopted for the subscripts of every reaction rate constant adopted in this work.

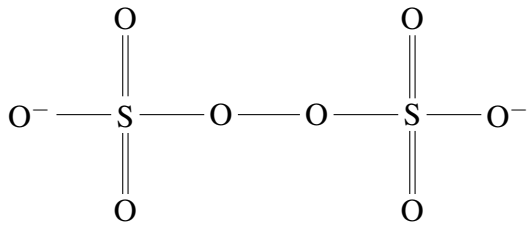

Fig. 6.2 A molecule of persulfate anion frequently used in the formation of radical precursors of an emulsion polymerization.

terminal end i, the only part the chain which can interact or with other chains or single monomeric units; in Table 6.2 the convention adopted to indicate every terminal end and monomer in the kinetic rate constants is proposed.
In every test case a maximum of three monomers among n-BA, MMA and 2-HEMA will be present, but there is a maximum of four possible reactive sites because, meanwhile Methyl Methacrylate and 2-HydroxyEthyl Methacrylate allow secondary forms only ($R^{\bullet}_{k,MMA}$ and $R^{\bullet}_{k,2\text{-}HEMA}$), n-Butyl Acrylate can assume a secondary ($R^{\bullet}_{k,SPR}$) or a tertiary ($R^{\bullet}_{k,MCR}$) form because it can undergo intramolecular chain transfer to polymer also known as *backbiting* (see Section 6.5.5).

Finally, since the reaction temperature can vary from case to case, the rate constants are proposed according to the Arrhenius equation:

$$F = A \exp\left(-\frac{E_a}{RT}\right). \tag{6.9}$$

6.5.1 Initiation

For now the discussion has been centred on the monomers, so this section is focused on another fundamental reaction which does not involve monomeric species: the initiation which involves the production of radical precursors $I^{\bullet}$ from an initiator I which will then propagate with the monomers dissolved in water and, subsequently, entry the particles once the oligomers becomes surface active.

Although there are different mechanisms for this to happen, the *thermal* one will be described only since it is the single one adopted in this work.
A thermal initiator is a particular water-soluble inorganic salt such as a persulfate whose anion proposed in Fig. 6.2. This mechanism is based on an homolitic breakage of the O-O bridge between the sulphates due to an increase of temperature which causes the formation of a pair of radical precursors:

$$S_2O_8{}^{2-} \xrightarrow{f\,k_d} 2\,SO_4{}^{-\bullet}, \tag{6.10}$$

where k_d is the related decomposition rate and f the initiator decomposition efficiency (f=0.6 for the persulphate [7]) which are the basic components for the evaluation of the total rate of consumption of initiator which is the starting point for the description of the entry process of oligomers into the particles:

$$R_I = 2fk_dI. \tag{6.11}$$

The values of k_d adopted in this work derive from an Arrhenius-type correlation found from the fitting of experimental data obtained by Boristov et al. [114]:

$$k_d\ [s^{-1}] = 10^{13.488} \exp\left(\frac{-118.638\ [kJ/(mol\ K)]}{RT}\right) \tag{6.12}$$

Eq.(6.12) has been found for $T \in [353K - 368K]$, but the range of temperatures of the polymerizations goes from 343 K to 351 K. Nonetheless Eq.(6.12) has been extended to 343 K because good agreement has been found between the extrapolated values and other decomposition rates reported in the literature: for instance at 348 K Eq.(6.12) gives as a result $k_d = 4.73\ \ 10^{-5} s^{-1}$ which is very similar to the value in equivalent conditions reported in the literature ($k_d = 4.345\ 10^{-5}\ s^{-1}$) [7].

6.5.2 Propagation

The propagation is the process by which active chains increase their degree of polymerization by adding new monomeric units M_j:

$$R_i^{\bullet} + M_j \xrightarrow{k_{p,ij}} R_j^{\bullet} \tag{6.13}$$

$k_{p,ij}$ is the propagation rate constant between the propagating chain with an i-th terminal end and M_j is the added j-th monomeric unit which will then become the new reactive site of the chain.

Rate	**A** $[\mathbf{L}/(\mathbf{mol\ s})]$	$\mathbf{E_a}$**[kJ/mol]**	**Ref**
$k_{p,11}$	$2.24\ 10^7$	17.9	[116]
$k_{p,21}$	$9.20\ 10^5$	28.3	[117]
$k_{p,33}$	$2.67\ 10^6$	22.40	[115]
$k_{p,44}$	$8.89\ 10^6$	21.9	[118]

Table 6.3 Arrhenius parameters for homo-propagation rates.

Homo-propagation rates $k_{p,ii}$ are available from the literature: Pulsed-Laser-Polymerization coupled with Size-Exclusion-Chromatography (PLP-SEC) is usually adopted to evaluate the desired rate constants at different temperatures from the knowledge of the Molecular Weight Distribution at low conversion stages [115], which is exactly what it has been done for the values of MMA and 2-HEMA reported in Table 6.3. Unfortunately, this procedure does not provide with reliable results for the two acrylic monomers: PLP-SEC fails in determining the propagation rate constants related to n-BA at temperatures over 303 K because of the presence of multiple radical species due to the previously mentioned intramolecular chain transfer to polymer . For this reason it is assumed that the Arrhenius parameters related to $k_{p,11}$, which have been found to be valid at temperatures below 303 K, are considered to be valid even in the temperature range of the simulations in absence of other alternatives.
Also because of the simultaneous presence of multiple radical species related to n-BA, it is not possible to use the classic PLP-SEC to determine $k_{p,21}$: a possible alternative is the Single Pulse-Pulsed Laser Polymerization coupled with Electron Paramagnetic Resonance spectroscopy (SP-PLP-EPR) which allows the simultaneous evaluation of the concentration of both the radicalic species at different temperatures which leads to the evaluation of the propagation rate constant of mid chain radicals by PREDICI refinement [117]. The final values of the Arrhenius parameters related to the homo-propagation rate constant n-BA and radical species are proposed in Table 6.3 as well.
Since co- and ter-polymerizations are also involved in the modelling it is also important to determine the cross-propagation rates $k_{p,ij}$ by adopting the related reactivity ratios

$$r_{ij} = \frac{k_{p,ii}}{k_{p,ij}} \tag{6.14}$$

which express the tendency of a j-th monomer to react with an i-th terminal end whose numerical values are proposed in Table 6.4.
They are usually found by running a series of polymerizations with different monomer ratios in the feed and correlating them with the composition of the obtained co-polymer.

$r_{i\text{-}j}$	Value	Ref
r_{13}	0.41	[119]
r_{31}	2.24	[119]
r_{14}	0.17	[120]
r_{41}	5.40	[120]
r_{34}	0.29	[120]
r_{43}	1.02	[120]

Table 6.4 Collection of the adopted reactivity ratios.

6.5.3 Termination

When two propagating chains encounter each other they lose their radical activity undergoing *termination* and become *dead chains*.
The most dominant mechanism is the combination: the two unpaired electrons of the active chains $R_{k,i}^{\bullet}$ and $R_{w,j}^{\bullet}$ create a covalent bond leading to the formation of a dead chain P_{k+w}.

$$R_{k,i}^{\bullet} + R_{w,j}^{\bullet} \xrightarrow{k_{ij}^{tc}} P_{k+w} \tag{6.15}$$

The second mechanism is by disproportionation, where one of the unpaired electrons is transferred from one chain to the other leading to the formation of two dead chains:

$$R_{k,i}^{\bullet} + R_{w,j}^{\bullet} \xrightarrow{k_{ij}^{td}} P_k + P_w \tag{6.16}$$

The distinction between combination and disproportionation is important only for the modelling of specific features such as the MWD [121], but since this model aims to describe the particle growth only, a unique bimolecular termination rate constant will be considered which is formalized as the superposition of the two mechanisms:

$$k_{t,ij} = k_{ij}^{tc} + k_{ij}^{td} \tag{6.17}$$

Termination rate constants for the homo-polymerization of 2-HEMA $k_{t,44}$ has been evaluated by fitting experimental data reported in the appropriate reference. On parallel, the termination rate constants for MMA and n-BA chain end radicals have been evaluated by the means of SP-PLP-EPR. Finally, the Arrhenius parameters related to the termination of mid chain radicals have been obtained by fitting polymerization rate vs monomer concentration data related to n-BA polymerizations through the knowledge of the proper reaction scheme. The final values are proposed in Table 6.5 together with the appropriate references. Instead the evaluation of "cross-termination" rate constants, if there is no information available in the

Rate	**A** $[\mathbf{L}/(\mathbf{mol\ s})]$	$\mathbf{E_a}$**[kJ/mol]**	**Ref**
$k_{t,11}$	$1.3 \cdot 10^{10}$	8.4	[117]
$k_{t,22}$	$9.0 \cdot 10^{6}$	5.6	[117]
$k_{t,12}$	$4.2 \cdot 10^{9}$	6.6	[117]
$k_{t,33}$	$2.33 \cdot 10^{10}$	8.44	[122]
$k_{t,44}$	$3.91 \cdot 10^{7}$	6.6	[118]

Table 6.5 Arrhenius parameters for the known termination rates.

literature, is done by using a geometric average between the respective homo-termination rate constants:

$$k_{ij}^{t} = \sqrt{k_{ii}^{t}\, k_{jj}^{t}}. \tag{6.18}$$

6.5.4 Chain transfer to monomer

This reaction, as the name suggests, is the shift of the reactive site from a propagating chain to a singular monomeric unit:

$$R_{k,i}^{\bullet} + M_j \xrightarrow{k_{fm,ij}} P_k + M_j^{\bullet}, \tag{6.19}$$

$k_{fm,ij}$ is the relative rate constant which is usually proposed in the literature as a "transfer constant" $C_m = k_{fm,ij}/k_{p,ij}$. Unfortunately C_m can rarely be found by standard PLP-SEC procedure [115]. In order to measure it, careful attention needs to be paid to the design of the polymerization systems: the choice falls on emulsion polymerizations not initiated by pulsed lasers but by redox initiators, in which the shape of the measured MWD (by Size Exclusion Chromatography, for instance) is influenced by radical entry and chain transfer to monomer only [123]. In Table 6.6 the Arrhenius parameter for the transfer to monomer rate $k_{fm,ij}$ have already been converted by considering the appropriate propagation constants: the values for $k_{fm,ij}$ related to MMA have been found by considering the transfer constants found by Stickler and Meyerhoff [124] normalized by the propagation constants found by Beuermann [115].
Finally, it is important to highlight that no cross-chain transfer has been considered ($k_{fm,ij} = 0 i \neq j$) and no information about the chain transfer to monomer related to 2-HEMA has been found, so it has been assumed $k_{fm,44} = 0$.

Rate	A $[\mathrm{L}/(\mathrm{mol\ s})]$	$\mathrm{E_a}[\mathrm{kJ/mol}]$	Ref
$k_{\mathrm{fm},11}$	$0.016\ k_{\mathrm{p},11}$	15.2	[123]
$k_{\mathrm{fm},21}$	$0.016\ k_{\mathrm{p},22}$	15.2	[123]
$k_{\mathrm{fm},33}$	$2.0 \cdot 10^5$	46.1	[125]
$k_{\mathrm{fm},44}$	0	0	Assumed
$k_{\mathrm{fm},31}$	0	0	Assumed
$k_{\mathrm{fm},32}$	0	0	Assumed
$k_{\mathrm{fm},12}$	0	0	Assumed

Table 6.6 Arrhenius parameters for the known termination rates.

6.5.5 Backbiting

The final reaction is relevant to *n*-BA only in this work and it is the intramolecular chain transfer to polymer also known as "backbiting": it is the transition of a secondary radical form to a tertiary (or mid-chain) radical form expressed as

$$\mathrm{R}^{\bullet}_{\mathrm{k,SPR}} \xrightarrow{\mathrm{k_{fp,2}}} ,\mathrm{R}^{\bullet}_{\mathrm{k,MCR}} \tag{6.20}$$

where $k_{\mathrm{fp},2}$ is the related rate constant whose Arrhenius parameters have been evaluated by SP-PLP-EPR [117].

$$k_{\mathrm{fp},2}[\mathrm{L\ mol^{-1}s^{-1}}] = 1.6\ 10^8 \exp\left(\frac{-34.7[\mathrm{kJ\ mol^{-1}}]}{RT}\right). \tag{6.21}$$

6.6 Kinetic rates

Once the reaction rate constants have been introduced the model can calculate the reactions rates of interest.

The major difficulty to overcome is the dealing with multiple monomers and/or terminal ends at the same time: even the simplest case, the homo-polymerization of *n*-BA, is *de-facto* a co-polymerization because of the multiple radical active sites due to the backbiting.

This problem is faced into two different ways in the particle and aqueous phase: in the first case the well known pseudo-homopolymerization approach is used [126] because the long chain approximation is supposed to be valid, meanwhile in the aqueous phase a more simplified approach will be proposed since only short oligomers are present.

6.6.1 Rates in the particle phase

The pseudo-homopolymerization approach allows the model to express every rate as it is formalized for an homo-polymerization, but all the specific kinetic rate parameters will be averaged based upon the probabilities for each chain P_i to have a certain i-th terminal end formally defined as the concentration of each type of chain $[R_i^\bullet]_p$ normalized by the concentration of every chain $[R_{TOT}^\bullet]_p$. Since there are four different reactive sites ($N_r = 4$) four different P_i are introduced:

$$P_1 = \frac{[R_{SPR}^\bullet]_p}{[R_{TOT}^\bullet]_p} \quad P_2 = \frac{[R_{MCR}^\bullet]_p}{[R_{TOT}^\bullet]_p} \quad P_3 = \frac{[R_{MMA}^\bullet]_p}{[R_{TOT}^\bullet]_p} \quad P_4 = \frac{[R_{2\text{-}HEMA}^\bullet]_p}{[R_{TOT}^\bullet]_p}, \tag{6.22}$$

where the subscripts have been defined according to the nomenclature adopted for the terminal ends in Table 6.2.

As it can be seen from Figure 6.3 the transition from one "active site" to the other can happen by "cross-propagation" with a different monomer or by backbiting. Here it is important to discuss the effect of the intramolecular chain transfer to polymer on the reaction kinetics: across the literature it has been highlighted that the effect provided by the intramolecular chain transfer to polymer on the polymerization kinetics can be suppressed or, however, provide a very small contribution to the reaction kinetics [127, 128] according to H-NMR measurements carried on a n-Butyl Acrylate/Styrene copolymer with a minimal mole fraction of styrene of 0.3 in the final composition of the latexes.

For this reason a sensitivity analysis on the impact of the backbiting on the kinetics of the BA/MMA co-polymerization has been conducted and the results have been discussed in Appendix B: it can be demonstrated that the impact of the intramolecular chain transfer to polymer on the kinetic variables is basically negligible when the mole fraction of methyl methacrylate is comparable to the one of styrene adopted in the aforementioned studies, meanwhile the backbiting still plays an important role when the mole fraction of *n*-BA is 90% or more. For these reasons it has been decided to consider the effect of the backbiting for every co- and ter-polymerization discussed in the next chapter.

Given this set of reactions and assuming their dominant role among all the reactions

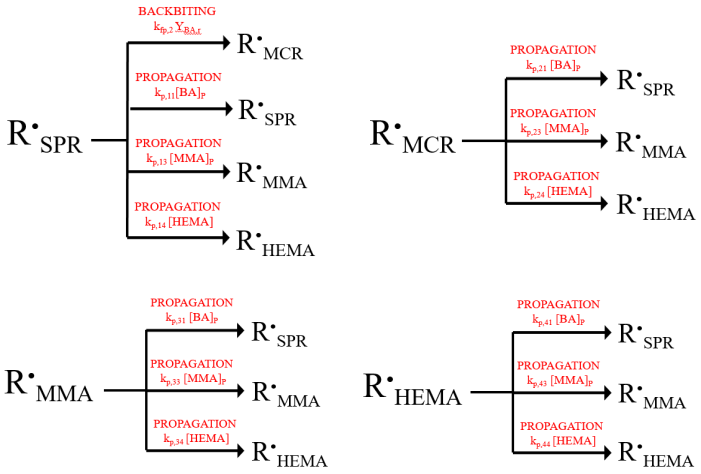

Fig. 6.3 Reactions determining active chain type scheme for *n*-BA/MMA/2-HEMA terpolymerization.

involving active chains, the following balances can be written:

$$\begin{cases} \dfrac{dP_2}{dt} = 0 = P_1\left(k_{\mathrm{fp},2}\,Y_{\mathrm{BA,inst}}\right) - P_2\left(k_{\mathrm{p},21}[\mathrm{BA}]_\mathrm{p} + k_{\mathrm{p},23}[\mathrm{MMA}]_\mathrm{p} + k_{\mathrm{p},24}[\text{2-HEMA}]_\mathrm{p}\right); \\ \dfrac{dP_3}{dt} = 0 = P_1\left(k_{\mathrm{p},13}[\mathrm{MMA}]_\mathrm{p}\right) + P_2\left(k_{\mathrm{p},23}[\mathrm{MMA}]_\mathrm{p}\right) - P_3\left(k_{\mathrm{p},31}[\mathrm{BA}]_\mathrm{p} + k_{\mathrm{p},34}[\text{2-HEMA}]_\mathrm{p}\right) + \\ \quad + P_4\left(k_{\mathrm{p},43}[\mathrm{MMA}]_\mathrm{p}\right); \\ \dfrac{dP_4}{dt} = 0 = P_1\left(k_{\mathrm{p},14}[\text{2-HEMA}]_\mathrm{p}\right) + P_2\left(k_{\mathrm{p},24}[\text{2-HEMA}]_\mathrm{p}\right) + P_3\left(k_{\mathrm{p},34}[\text{2-HEMA}]_\mathrm{p}\right) + \\ \quad - P_4\left(k_{\mathrm{p},41}[\mathrm{BA}]_\mathrm{p} + k_{\mathrm{p},43}[\mathrm{MMA}]_\mathrm{p}\right); \\ P_1 + P_2 + P_3 + P_4 = 1. \end{cases} \tag{6.23}$$

In particular, $Y_{\mathrm{BA,inst}}$ is instantaneous composition expressed in terms of the fraction of the consumption of *n*-Butyl Acrylate compared to the overall amount of converted monomer at each time t:

$$Y_{\mathrm{BA,r}}(t) = \frac{C_{\mathrm{p,BA}}}{\sum_{i=1}^{N_m} C_{\mathrm{p,j}}}, \tag{6.24}$$

By solving Eq.(6.23) it is possible to find the complete set of P_i from which it is possible to evaluate the pseudo-homopolymerization rates.

The first one will be $R^{\mathrm{j}}_{\mathrm{prop,p}}$ whose formal expression can be found by formally defining the consumption of every monomer as

$$C^{\mathrm{j}}_{\mathrm{p}} = \left(\sum_{i=1}^{N_r} k_{\mathrm{p,ij}} [\mathrm{R}^{\bullet}_{\mathrm{i}}]_{\mathrm{p}} \right) [\mathrm{J}]_{\mathrm{p}} \mathrm{MW}_{\mathrm{j}}. \tag{6.25}$$

By replacing $[\mathrm{R}^{\bullet}_{\mathrm{i}}]_{\mathrm{p}}$ according to the pseudo-homopolymerization approach (Eq.(6.22)) it can be rewritten as

$$C^{\mathrm{j}}_{\mathrm{p}} = \left(\sum_{i=1}^{N_r} k_{\mathrm{p,ij}} P_i \right) [\mathrm{J}]_{\mathrm{p}} [\mathrm{R}^{\bullet}_{\mathrm{TOT}}]_{\mathrm{p}} \tag{6.26}$$

and it is possible to isolate the following propagation rate:

$$R^{\mathrm{j}}_{\mathrm{prop,p}} = \left(\sum_{i=1}^{N_r} k_{\mathrm{p,ij}} P_i \right) [\mathrm{J}]_{\mathrm{p}} = \overline{k}_{\mathrm{p,j}} [\mathrm{J_p}]. \tag{6.27}$$

The effect of the pseudo-homopolymerization approach relies on the fact that every reaction rate related to a single j-th monomer is written exactly as in a homopolymerization, but with a modified propagation rate constant $\overline{k}_{\mathrm{p,j}}$ which is an average of all the possible propagation events weighted by the probabilities for the j-th monomer to encounter a chain with an i-th terminal end.
The same principle adopted for $R^{\mathrm{j}}_{\mathrm{prop,p}}$ is used to find the equivalent expression for the pseudo-homotransfer to monomer rate $R^{\mathrm{j}}_{\mathrm{fm,p}}$ and the correlated rate constants $\overline{k}_{\mathrm{fm,j}}$:

$$R^{\mathrm{j}}_{\mathrm{fm,p}} = \sum_{i=1}^{N_r} k_{\mathrm{fm,ij}} P_i [\mathrm{J}]_{\mathrm{p}} = \overline{k}_{\mathrm{fm,j}} [\mathrm{J}]_{\mathrm{p}}. \tag{6.28}$$

For the bimolecular termination rate the derivation is slightly different because only radical chains are involved:

$$R^{\mathrm{j}}_{\mathrm{term,p}} = \sum_{\mathrm{i=1}}^{N_r} k^{\mathrm{p}}_{\mathrm{t,ij}} [\mathrm{R}^{\bullet}_{\mathrm{i}}]_{\mathrm{p}} [\mathrm{R}^{\bullet}_{\mathrm{j}}]_{\mathrm{p}}, \tag{6.29}$$

where $k^{\mathrm{p}}_{\mathrm{t,ij}}$ are the termination rate constants in the particle phase: it is important to differentiate them from $k_{\mathrm{t,ij}}$ proposed in Table 6.5 because the latter are usually evaluated under bulk conditions, when the monomer conversion is close to zero, meanwhile the formers are related to the particle phase. In this phase the presence of a growing solid phase hinders the approach of propagating chains slowing down the whole termination process: this phenomenon is called "gel effect" whose influence on the overall termination kinetics is proposed later in the discussion.
In this case the application of the pseudo-homopolymerization approach causes the termina-

tion rate for each terminal end to be written as

$$R^{\mathrm{j}}_{\mathrm{term,p}} = \sum_{\mathrm{i}=1}^{N_r} k^{\mathrm{p}}_{\mathrm{t,ij}} P_i P_j [\mathrm{R}^{\bullet}_{\mathrm{TOT}}]^2_{\mathrm{p}} \tag{6.30}$$

from which it is possible to find the pseudo-homotermination rate related to each active chain:

$$\overline{k}^{\mathrm{p}}_{\mathrm{t,j}} = \sum_{i=1}^{N_r} k^{\mathrm{p}}_{\mathrm{t,ij}} P_i P_j \tag{6.31}$$

It is also possible to formalize the overall termination rate $R_{\mathrm{term,p}}$ as a function of $[\mathrm{R}^{\bullet}_{\mathrm{TOT}}]_{\mathrm{p}}$ and of an average overall termination rate $\langle k_{\mathrm{t}} \rangle_{\mathrm{p}}$:

$$R_{\mathrm{term,p}} = \langle k_{\mathrm{t}} \rangle_{\mathrm{p}} [\mathrm{R}^{\bullet}_{\mathrm{TOT}}]^2_{\mathrm{p}}. \tag{6.32}$$

$\langle k_{\mathrm{t}} \rangle_{\mathrm{p}}$ is linked to the overall termination rate under bulk conditions $\langle k_{\mathrm{t,b}} \rangle$ which is expressed as function of the $k_{\mathrm{t,ij}}$ proposed in Table 6.5:

$$\langle k_{\mathrm{t,b}} \rangle = \sum_{i=1}^{N_r} \sum_{j=1}^{N_r} k_{\mathrm{t,ij}} P_i P_j, \tag{6.33}$$

when the monomer conversion is close to zero (negligible polymer concentration).
The aforementioned movement of the chains hindered by the growing solid phase which causes the so-called gel effect is represented in Eq.(6.33) by the addition of the exponential term:

$$\langle k_{\mathrm{t,p}} \rangle = \langle k_{\mathrm{t,b}} \rangle \exp \left[\left(- \sum_{i=1}^{N_m} a_i Y_i \right) \phi^{p}_{\mathrm{pol}} \right]. \tag{6.34}$$

It is designed to depend on the amount of growing polymer in the particle phase through the corresponding volume fraction ϕ^{p}_{pol}, evaluated in the partitioning scheme, and on its composition. Different amounts of converted monomers actually provide with distinct influences on the gel effect through monomer-specific coefficients a_i weighted by their respective mole fractions $Y_{\mathrm{i}}(t)$ in the polymer:

$$Y_{\mathrm{i}}(t) = \frac{(m_{\mathrm{r},i} + m_{\mathrm{s},i})\ \mathrm{MW_i}}{\sum_{j=1}^{N_m} (m_{\mathrm{r},j} + m_{\mathrm{s},j})\ \mathrm{MW_j}}, \tag{6.35}$$

where $m_{\mathrm{r},i}$ is the mass of each monomer reacted until time t and $m_{\mathrm{i,s}}$ are the respective residual masses in the initial seed.

6.6.2 Rates in the aqueous phase

On the other hand, in the aqueous phase the long chain approximation, one of the hypotheses the homo-polymerization approach is built upon, is not valid anymore.
The total propagation rate in the aqueous phase can be written as

$$R^{\mathrm{j}}_{\mathrm{prop,w}} = \sum_{i=1}^{N_r} k_{\mathrm{p,ij}} [\mathrm{R}^{\bullet}_{\mathrm{i}}]_{\mathrm{w}} [\mathrm{J}]_{\mathrm{w}}, \tag{6.36}$$

but this time the average propagation rate constants related to each monomer $\overline{k}_{\mathrm{p,j}}$ are evaluated by a simple geometric average among the rate constants between every terminal end which can interact with the j-th monomer:

$$\begin{cases} R^{\mathrm{j}}_{\mathrm{prop,w}} = \sum_{i=1}^{N_r} k^{\mathrm{w}}_{\mathrm{p,ij}} [\mathrm{R}^{\bullet}_{\mathrm{i}}]_{\mathrm{w}} [\mathrm{J}]_{\mathrm{w}} \sim \overline{k}^{\mathrm{w}}_{\mathrm{p,j}} [\mathrm{J}]_{\mathrm{w}} [\mathrm{R}^{\bullet}_{\mathrm{TOT}}]_{\mathrm{w}} \\ \overline{k}^{\mathrm{w}}_{\mathrm{p,j}} = \left(\prod_{i=1}^{N_r} k_{\mathrm{p,ij}} \right)^{1/N_r} \end{cases} \tag{6.37}$$

Concerning the bimolecular termination events, the approach is even simpler because the rate will be described as a function of the geometric average of the termination rates for the respective homo-polymerizations $k^{\mathrm{i}}_{\mathrm{t,w}}$:

$$\begin{cases} R_{\mathrm{term,w}} = \langle k_{\mathrm{t,w}} \rangle [\mathrm{R}^{\bullet}_{\mathrm{TOT}}]^2_{\mathrm{w}}; \\ \langle k_{\mathrm{t,w}} \rangle = \left(\prod_{i=1}^{N_m} k^{\mathrm{i}}_{\mathrm{t,w}} \right)^{1/N_m}, \end{cases} \tag{6.38}$$

where $\langle k_{\mathrm{t,w}} \rangle$ is the average termination rate in the aqueous phase which is introduced as a geometric average of the termination rate constants for the respective homopolymers: the values for MMA and 2-HEMA, $k^{\mathrm{MMA}}_{\mathrm{t,w}}$ $k^{\text{2-HEMA}}_{\mathrm{t,w}}$, are readily available ($k_{\mathrm{t,33}}$ and $k_{\mathrm{t,44}}$ respectively), meanwhile the situation is more complicated for the evaluation of $k^{\mathrm{BA}}_{\mathrm{t,w}}$ since *n*-BA can assume multiple radical forms and their corresponding rate constants $k_{\mathrm{t,11}}$ and $k_{\mathrm{t,22}}$ differ by two orders of magnitude [117]. Therefore $k^{\mathrm{BA}}_{\mathrm{t,w}}$ is treated as an adjustable parameter with a value chosen in between those reported for the secondary and the tertiary radical types.

6.7 Quick recap

Before continuing, it is important to remind the reader with the most important features of the chapter until this point. Until this point all of the fundamental reactions, rates and physical variables necessary to find the consumption rate of each monomer have been introduced. $C^{\mathrm{j}}_{\mathrm{p}}$,

assembling Eq.(6.3 - 6.26), can be expressed as

$$C_{\mathrm{p}}^{\mathrm{j}} = \sum_{i=1}^{N_r} k_{\mathrm{p,ij}} P_i [\mathrm{J}]_{\mathrm{p}} \mathrm{MW}_{\mathrm{j}} \frac{\tilde{n} N_{\mathrm{P}}}{N_{\mathrm{AV}}}. \tag{6.39}$$

The propagation rate constants $k_{\mathrm{p,ij}}$ have been provided in Table 6.3, the probabilities P_i from Eq.(6.23) and the concentrations $[\mathrm{J}]_{\mathrm{p}}$ from the partitioning scheme explained in Eq.(6.6 - 6.7); finally, the total number of particles N_{P} is calculated from the information related to the seed discussed in Section 6.3.
The only feature still remaining to be addressed is the radical activity represented by $\tilde{n}$, the average number of radicals, whose evaluation is the focal point of the next section.

6.8 Determination of the radical activity

The radical activity is quantitatively described by the popular Smith-Ewart (SE) equations [77] which monitor the time evolution of the number concentration $[N_i]$ of particles with state i which represents the number of propagating chains inside them. Since the total number of particles is constant, it is possible to define the probability for each particle to have a state i N_i by normalizing $[N_i]$ with the overall concentration of particles in the reactor

$$N_i = \frac{[N_i]}{[N_{\mathrm{P}}]}, \tag{6.40}$$

from which it is then possible to formalize the Smith-Ewart equations as

$$\frac{dN_i}{dt} = \rho N_{i-1} + \overline{k}_{i+1}(i+1)N_{i+1} + c(i+2)(i+1)N_{i+2} - \Big(\rho + \overline{k}_i i + ci(i-1)\Big)N_i. \tag{6.41}$$

The first source term of Eq.(6.41) represents the increase of the number of particles with state i due to entry of a oligomeric radical in a particle with $i-1$ propagating chains with rate ρ, meanwhile the second the exit of a monomeric radical from a particle with state $i+1$ with a state-dependent rate equal to $\overline{k}_{i+1}$; finally the third term represent the formation of particle with i active chains due to a termination event in a particle with state $i+2$ happening with rate c. On the other hand, the loss terms in Eq.(6.41) represent the same phenomena all happening to a particle with state i which subsequently reduce N_i due to the entry of a radical inside it, the exit of a monomeric radical from it or a termination between two chains contained in it, respectively.
Eq.(6.41) is supposed to be a system of infinite ordinary differential equations (ODEs), so the

maximum value of i will be set equal to i_{cr}, and large enough to ensure that the contribution of states with $i > i_{cr}$ to $\tilde{n}$ is negligible. Finally, the average number of radicals $\tilde{n}$ can be computed as

$$\tilde{n} = \sum_i N_i i. \tag{6.42}$$

6.8.1 Termination rates

c, the bimolecular termination rate between two propagating chains inside a particle, is defined as:

$$c = \frac{\langle k_{t,p} \rangle}{2N_{AV}V_s} = \frac{\langle k_{t,p} \rangle}{2N_{AV}(V^p/N_P)}, \tag{6.43}$$

where $\langle k_{t,p} \rangle$ is the rate constant of bimolecular termination already introduced in Eq.(6.34) and V_s is the swollen volume of each particle.

6.8.2 Exit rates

The ensemble of state-dependent exit rates of monomeric radicals $\overline{k}_i$ are written as a superposition of the exit rates of the single monomers involved [103]:

$$\overline{k}_i = \sum_{j=1}^{N_m} k_i^j \tag{6.44}$$

Note that the desorption of 2-HEMA has been neglected because it was not possible to find any reliable value of the corresponding chain transfer to monomer rate coefficient. However, the impact of this assumption on the model predictions is expected to be minimal, given the low amount of 2-HEMA in the test cases where it is present.
The starting point for the evaluation of $\overline{k}_i$ is the definition of the desorption rates of monomer j from a particle with state i $R'_{dm,ij}$ [129]:

$$R'_{dm,ij} = \left[\left(\sum_{k \in N'_r} k_{fm,kj} P_k [J]_p \right) i[N_i] + \rho_{re,j}[N_{i-1}] \right] Q_i^j. \tag{6.45}$$

First, it is important to specify a convention specifically adopted in this section: N'_r is the number of radical species a certain monomer can have: as mentioned earlier n-BA can assume both secondary and tertiary radical forms, so $N'_r = 1,2$, while $N'_r = 3$ for MMA.
$R'_{dm,ij}$ depends on the modes with which monomeric radicals can appear inside a particle which are expressed within the square brackets: the first term is related to the chain transfer to monomer, while the second represents the possibility of a previously desorbed radical

Monomer	$\mathbf{D_{w,j}}[\mathbf{m^2 s^{-1}}]$
n-BA	$2.53\ 10^{-9}$
MMA	$3.07\ \ 10^{-9}$

Table 6.7 Diffusion coefficients of the monomers in water.

to re-enter another particle with rate $\rho_{\mathrm{re,j}}$. Next, Q_i^j represents the probability for every monomeric radical in a certain state to desorb rather than propagate with another monomer or terminate with another chain:

$$Q_i^j = \frac{k_{\mathrm{d,j}}}{k_{\mathrm{d,j}} + R^{\mathrm{j}}_{\mathrm{prop,p}} + 2c^{\mathrm{j}}(i-1)}. \tag{6.46}$$

$k_{\mathrm{d,j}}$ is the rate with which a monomer desorbs [7] (see Chapter 1 for the whole derivation)

$$k_{\mathrm{d,j}} = \frac{3D_{\mathrm{w,j}}}{R_S^2}\frac{[\mathrm{J}]_{\mathrm{w}}}{[\mathrm{J}]_{\mathrm{p}}}, \tag{6.47}$$

where $D_{\mathrm{w,j}}$ are the diffusion coefficients of monomers in the aqueous phase which are proposed in Table 6.7 and they have been evaluated according to the Wilke-Chang formula; see Appendix B for the complete procedure.

Moreover, $R^{\mathrm{j}}_{\mathrm{prop,p}}$ represents the propagation rate

$$R^{\mathrm{j}}_{\mathrm{prop,p}} = \sum_{j\in N'_r}\sum_{k=1}^{N_m}\left(k_{\mathrm{p,jk}}P_j[\mathrm{K}]_{\mathrm{P}}\right), \tag{6.48}$$

meanwhile c^{j} the respective termination rate

$$c^{\mathrm{j}} = \frac{\sum_{j\in N'_r}P_j\left(\sum_{l=1}^{N_r}k_{\mathrm{t,jl}}P_l\right)}{2N_{\mathrm{AV}}V_S}\exp\left[-\left(\sum_{i=1}^{N_m}a_iY_i\right)\phi^P_{\mathrm{pol}}\right]. \tag{6.49}$$

The re-entry rate $\rho_{\mathrm{re,j}}$ is expressed as a function of a state-average desorption coefficient $\langle k^j\rangle$, the average number of radicals inside each particle $\tilde{n}$ and a fate parameter β_j which represents the probability for a desorbed radical to react in the aqueous phase (terminate or propagate) instead of re-entering another particle. Once all of these fundamental quantities have been formalized it is finally time to express the constitutive equation for each single desorption rate as

$$R'_{\mathrm{dm,ij}} = k_i^j i[N_i] = \left(\sum_{k\in N'_r}k_{\mathrm{fm,kj}}P_k[\mathrm{J}]_{\mathrm{p}}i[N_i] + \rho_{\mathrm{re,j}}[N_{i-1}]\right)Q_i^j \tag{6.50}$$

which means

$$k_i^j = \left[\sum_{k \in N_r'} k_{\mathrm{fm,kj}} P_k [\mathrm{J}]_\mathrm{p} + \left(\frac{\langle k^j \rangle \tilde{n} (1-\beta_j)[N_{i-1}]}{i[N_i]} \right) \right] Q_i^j. \tag{6.51}$$

A formal expression for $\langle k^j \rangle$ still needs to be provided and, to do so, it is necessary to introduce the overall desorption rate for each monomer across all the states and interpret it as a function of the state average exit rate $\langle k^j \rangle$, the average number of radicals and the total concentration of particles $[N_P]$:

$$R'_{\mathrm{dm,tot,j}} = \langle k^\mathrm{j} \rangle \tilde{n} [N_\mathrm{P}] = \sum_{i=1}^{i_\mathrm{cr}} R'_{\mathrm{dm,ij}} = \sum_{i=1}^{i_\mathrm{cr}} \left(\sum_{k \in N_r'} k_{\mathrm{fm,kj}} P_k [\mathrm{J}]_\mathrm{p} i[N_i] + \langle k^j \rangle \tilde{n} (1-\beta_j)[N_{i-1}] \right) Q_i^j. \tag{6.52}$$

From the previous expression the evaluation of $\langle k^j \rangle$ is straightforward

$$\langle k^j \rangle = \left(\sum_{k \in N_r'} k_{\mathrm{fm,kj}} P_k [\mathrm{J}]_\mathrm{p} \right) \frac{\sum_i i N_i Q_i^j}{\tilde{n}[1 - (1-\beta_j) \sum_i N_{i-1} Q_i^j]} \tag{6.53}$$

By replacing Eq.(6.53) into Eq.(6.51) it is possible to write down the final version of the exit rate for the single monomers

$$k_i^j = \left(\sum_{k \in N_r'} k_{\mathrm{fm,kj}} P_k [\mathrm{J}]_\mathrm{p} \right) Q_i^j \left(1 + (1-\beta_j) \frac{N_{i-1}}{i N_i} \frac{\sum_{i=1}^{\infty} i Q_i^j N_i}{1 - (1-\beta_j) \sum_{i=1}^{\infty} Q_i^j N_{i-1}} \right). \tag{6.54}$$

6.8.3 Entry rates

The entry rate of Eq.(6.41) is divided into two contributions:

$$\rho = \sum_{j=1}^{N_m} \rho_{\mathrm{re,j}} + \rho_I. \tag{6.55}$$

The first one is related to the re-entry of previously desorbed radicals which has been introduced in the previous section and briefly recalled here:

$$\rho_{\mathrm{re,j}} = \langle k^j \rangle \tilde{n} (1-\beta_j). \tag{6.56}$$

In this scenario complete re-entry has been assumed as the ultimate fate of the desorbed radicals, an hypothesis already adopted in the homo-polymerizations of *n*-Butyl Acrylate [130] and Methyl Methacrylate [131], which means $\beta_j = 0$ for both the radicals.
The second contribution derives from the oligomeric radicals originated by the decomposition of the initiator I. According to the mechanism described in Section 6.5.1 the appropriate

mole balance for I can be formalized as follows:

$$\frac{d\mathrm{I}}{dt} = \dot{n}_{\mathrm{I}} - R_{\mathrm{I}}, \tag{6.57}$$

where $\dot{n}_{\mathrm{I}}$ is the mole rate of initiator foreseen by the formulation, meanwhile R_{I} the rate of production of precursors $\mathrm{I}^{\bullet}$ according to the thermal initiation mechanism quantified by Eq.(6.11).

The presence of $\mathrm{I}^{\bullet}$ triggers the formation of oligomeric radicals which can (i) keep propagating with other monomers or (ii) terminate with one of the other chains whose total concentration in the liquid medium is $[\mathrm{T}^{\bullet}]$. Once they reach a critical degree of oligomerization z, they have become sufficiently surface active to instantaneously migrate to a particle and enter it with rate ρ_I [132].

The starting point is the description of the reacting scheme which pivots around the reactions involving propagating chains with degree of polymerization k independently from the type of active site:

$$\begin{cases} \mathrm{I} \xrightarrow{f\,\mathrm{k_d}} 2\,\mathrm{I}^{\bullet} \\ \mathrm{I}^{\bullet} + \mathrm{J} \xrightarrow{\mathrm{k^w_{p,Ij}}} \mathrm{R^{\bullet}_{1,tot}} \quad \mathrm{j} = 1,...,N_m \\ \mathrm{R^{\bullet}_{k,tot}} + \mathrm{J} \xrightarrow{\bar{k}^{\mathrm{w}}_{\mathrm{p,j}}} \mathrm{R^{\bullet}_{tot,k+1}} \quad 1 \leq \mathrm{k} < z, \;\; \mathrm{j} = 1,...,N_m \\ \mathrm{R^{\bullet}_{k,tot}} + \mathrm{T}^{\bullet} \xrightarrow{\langle \mathrm{k_{t,w}} \rangle} \mathrm{Dead\,Chains} \quad 1 \leq \mathrm{k} < z \\ \mathrm{R^{\bullet}_{z,tot}} + \mathrm{Particle} \xrightarrow{\rho_{\mathrm{I}}} \mathrm{Entry} \end{cases} \tag{6.58}$$

in which $\mathrm{R^{\bullet}_{k,tot}} = \sum_{j=1}^{N_r} \mathrm{R^{\bullet}_{k,j}}$.

From Eq.(6.58) it is possible to write down the following balances according to the approximations introduced in Section 6.6.2:

$$\begin{cases} \dfrac{d\mathrm{I}^{\bullet}}{dt} = 2fk_{\mathrm{d}}\mathrm{I} - \sum_{j=1}^{N_m} k_{\mathrm{p,Ij}}[\mathrm{J}]_{\mathrm{w}}\mathrm{I}^{\bullet} \\ \dfrac{d\mathrm{R^{\bullet}_{1,tot}}}{dt} = \sum_{j=1}^{N_m} k_{\mathrm{p,Ij}}[\mathrm{J}]_{\mathrm{w}}\mathrm{I}^{\bullet} - \sum_{j=1}^{N_m} \bar{k}^{\mathrm{w}}_{\mathrm{p,j}}[\mathrm{J}]_{\mathrm{w}}\mathrm{R^{\bullet}_{1,tot}} - 2\langle k^{\mathrm{t}}_{\mathrm{w}} \rangle [\mathrm{T}^{\bullet}]\mathrm{R^{\bullet}_{1,tot}} \\ \dfrac{d\mathrm{R^{\bullet}_{k,tot}}}{dt} = \sum_{j=1}^{N_m} \bar{k}^{\mathrm{w}}_{\mathrm{p,j}}[\mathrm{J}]_{\mathrm{w}}\mathrm{R^{\bullet}_{k\text{-}1,tot}} - \sum_{j=1}^{N_m} \bar{k}^{\mathrm{w}}_{\mathrm{p,j}}[\mathrm{J}]_{\mathrm{w}}\mathrm{R^{\bullet}_{k,tot}} - 2\langle k^{\mathrm{t}}_{\mathrm{w}} \rangle [\mathrm{T}^{\bullet}]\mathrm{R^{\bullet}_{k,tot}} \\ \dfrac{d\mathrm{R^{\bullet}_{z,tot}}}{dt} = \sum_{j=1}^{N_m} \bar{k}^{\mathrm{w}}_{\mathrm{p,j}}[\mathrm{J}]_{\mathrm{w}}\mathrm{R^{\bullet}_{tot,z-1}} - \rho_I \dfrac{N_{\mathrm{P}}}{N_{\mathrm{AV}}} \end{cases} \tag{6.59}$$

from which, by using the steady state approximation, it is possible to find the following expressions for every $R^{\bullet}_{tot,k}$:

$$\begin{cases} R^{\bullet}_{tot,1} = \dfrac{2fk_d I}{\sum_{j=1}^{N_m} k_{p,Ij}[J]_w I^{\bullet} + 2\langle k_w^t \rangle [T^{\bullet}]} \\ \\ R^{\bullet}_{tot,k} = \dfrac{\sum_{j=1}^{N_m} \bar{k}_{p,j}^{w}[J]_w}{\sum_{j=1}^{N_m} \bar{k}_{p,j}^{w}[J]_w + 2\langle k_w^t \rangle [T^{\bullet}]} R^{\bullet}_{tot,k-1} = \left(1 + \dfrac{2\langle k_w^t \rangle [T^{\bullet}]}{\sum_{j=1}^{N_m} \bar{k}_{p,j}^{w}[J]_w}\right)^{-1} R^{\bullet}_{tot,k-1} \end{cases} \tag{6.60}$$

If the mixture of monomers is sufficiently hydrophobic the total concentration of radical chains $[T^{\bullet}]$ can be approximated as

$$[T^{\bullet}] \sim \sqrt{\frac{fk_d[I]_w}{\langle k_w^t \rangle}}, \tag{6.61}$$

and it is possible to obtain the following modified version for the entry rate ρ_I:

$$\rho_I = \frac{2fk_d I N_{AV}}{N_p}\left(\frac{2\sqrt{fk_d[I]_w\langle k_w^t\rangle}}{\sum_{j=1}^{N_m}\bar{k}_{p,j}^{w}[J]_w}+1\right)^{1-\bar{z}} = \frac{R_I N_{AV}}{N_p}\left(\frac{2\sqrt{fk_d[I]_w\langle k_w^t\rangle}}{\sum_{j=1}^{N_m}\bar{k}_{p,j}^{w}[J]_w}+1\right)^{1-\bar{z}} \tag{6.62}$$

Note that Eq.(6.62) has been modified by adopting a variable critical length $\bar{z}$, which is defined as

$$\bar{z} = \sum_{j=1}^{N_m} \frac{\phi_j^w}{\sum_{i=1}^{N_m}\phi_i^w} z_j, \tag{6.63}$$

in order to take into account the different relative presence of the various monomers which plays an impact on when the produced oligomers will become surface active enough to interact with the particle phase.

Every z_j has been chosen as an intermediate value between the minimum degree of polymerization for surface activity and the one which will cause incipient water insolubility according to the following expressions derived from thermodynamic considerations [132] :

$$1 + \mathrm{int}\left(\frac{-23[\mathrm{kJ/(mol\ K)}]}{RT\ln[J]_{w,sat}}\right) \leq z_j \leq 1 + \mathrm{int}\left(\frac{-55[\mathrm{kJ/(mol\ K)}]}{RT\ln[J]_{w,sat}}\right), \tag{6.64}$$

where $[J]_{w,sat}$ is the molar concentration of every monomer at saturation conditions and int is a function which approximates the value in the brackets to the smallest integer; the final values for $[J]_{w,sat}$ and z_j adopted in this work are reported in Table 6.8.

Property	Value	Source
$[\mathrm{BA}]_{\mathrm{w,sat}}$ [mol L^{-1}]	0.0289	[110]
$[\mathrm{MMA}]_{\mathrm{w,sat}}$ [mol L^{-1}]	0.2606	[110]
$[\text{2-HEMA}]_{\mathrm{w,sat}}$ [mol L^{-1}]	0.7684	[111]
z_{BA}	3	Eq.(6.64)
z_{MMA}	6	Eq.(6.64)
$z_{\text{2-HEMA}}$	31	Eq.(6.64)

Table 6.8 Input parameters for the evaluation of the critical degree of oligomerization $\bar{z}$.

6.9 Updates of the kinetic variables

Once the average number of radicals is computed it is possible to calculate the consumptions $C_{\mathrm{p}}^{\mathrm{j}}$ by Eq.(6.39) and proceed to the evaluation of the kinetic variables.

6.9.1 Conversions

By solving the mass balances for each monomer,Eq.(6.1), it is possible to compute their mass in the reactor m_j at every time which is the fundamental feature for the evaluation of the conversions. In this work two different types will be considered: the *instantaneous* conversion X^{inst}, which is the ratio between the total amount of monomer consumed up to time t with respect to referred to the mass of monomers added until t m_{j}^{t} and its *overall* equivalent X^{overall} where the denominator is the total amount of monomers foreseen by the formulation $m_{\mathrm{j}}^{\mathrm{tot}}$:

$$\begin{cases} X^{\mathrm{inst}} = \dfrac{\sum_{j=1}^{\mathrm{N}_m}(m_{\mathrm{j}}^{\mathrm{t}} - m_{\mathrm{j}}) + m_{\mathrm{P,0}}}{\sum_{j=1}^{\mathrm{N}_m} m_{\mathrm{j}}^{\mathrm{t}} + m_{\mathrm{P,0}}}; \\ \\ X^{\mathrm{overall}} = \dfrac{\sum_{j=1}^{\mathrm{N}_m}(m_{\mathrm{j}}^{\mathrm{t}} - m_{\mathrm{j}}) + m_{\mathrm{P,0}}}{\sum_{j=1}^{\mathrm{N}_m} m_{\mathrm{j}}^{\mathrm{tot}} + m_{\mathrm{P,0}}}; \end{cases} \tag{6.65}$$

$m_{\mathrm{P,0}}$ is instead the total mass of the seed in the initial charge.

6.9.2 Latex composition

From the knowledge of the consumption it is also possible to update the amount of each monomer reacted at time t $m_{\mathrm{r,i}}(t)$ by

$$\frac{dm_{\mathrm{r,i}}}{dt} = C_{\mathrm{p}}^{\mathrm{j}}, \tag{6.66}$$

which is used for the evaluation of the product composition expressed or as mass fraction ω_i or mole fraction Y_{i} of every monomer in the latex:

$$\begin{cases} \omega_i = \dfrac{m_{\mathrm{r,i}} + m_{\mathrm{s,i}}}{\sum_{j=1}^{N_m}(m_{\mathrm{r,j}} + m_{\mathrm{s,j}})}; \\ \\ Y_{\mathrm{i}} = \dfrac{(m_{\mathrm{r,i}} + m_{\mathrm{i,s}})\mathrm{MW}_i}{\sum_{j=1}^{N_m}(m_{\mathrm{r,j}} + m_{s,j})\mathrm{MW}_{\mathrm{j}}}, \end{cases} \tag{6.67}$$

where $m_{\mathrm{s,j}}$ are recalled to be the masses of each monomer contained in the seed.

6.9.3 Average particle size

Finally the volume balance for the growing polymer V_{pol} can be expressed as a function of the consumptions $C_{\mathrm{p}}^{\mathrm{j}}$ as follows:

$$\frac{dV_{\mathrm{pol}}}{dt} = \left[\sum_{j=1}^{\mathrm{N}_m}\left(\sum_{i=1}^{\mathrm{N}_r} k_{\mathrm{p,ij}} P_i\right)[\mathrm{J}]_{\mathrm{p}}\mathrm{MW}_{\mathrm{j}}\right] \frac{\tilde{n} N_{\mathrm{p}}}{N_{\mathrm{AV}}\rho_{\mathrm{P}}}, \tag{6.68}$$

where ρ_P is the density of the latex updated by adopting the same procedure seen in Section 6.3:

$$\rho_P = \sum_{i=1}^{N_m} \omega_i \, \rho_{P,i}. \tag{6.69}$$

In the end, the average particle size R_{p} is readily evaluated:

$$R_{\mathrm{p}}(t) = \left(\frac{3}{4\pi}\,\frac{V_{\mathrm{pol}}}{N_{\mathrm{P}}}\right)^{1/3}. \tag{6.70}$$

6.10 Monitoring of the surface coverage

As declared in the introduction one of the intents of this work is finding links between the surface coverage θ and the stability of the product against formation of coagulum, so this section is dedicated to its modelling during the polymerizations.

The features reported in this section will be adopted for the industrial cases only, whose formulation includes two surfactants: an alkyl sulphate sodium salt (Surfactant A) covers the seed and a carboxylate salt of potassium is adopted during the delayed additions (Surfactant B).

The starting point is a simple mole balance related to each emulsifier:

$$\frac{dS_i}{dt} = \dot{n}_{\mathrm{S,i}}, \tag{6.71}$$

where $\dot{n}_{\mathrm{S,i}}$ are their mole rates foreseen by the formulation.
Every time a certain amount of emulsifier in the reactor is charged it partitions itself between the particle and the aqueous phase under the assumption that its adsorption on eventual droplets is negligible since the total surface area of the particles is much higher than the one of the droplets:

$$S_i(t) = S_{\mathrm{p,i}}(t) + S_{\mathrm{w,i}}(t) = A_{\mathrm{P}}\Gamma_i + S_{\mathrm{w,i}}(t), \tag{6.72}$$

where $S_{\mathrm{p,i}}$ represents the moles of emulsifier absorbed on the particles and $S_{\mathrm{w,i}}$ the amount dissolved in water.
$S_{\mathrm{p,i}}$ depends on the total surface area of the latex $A_{\mathrm{P}} = 4\pi R_{\mathrm{P}}^2 N_P$ and on Γ_i, the concentration of absorbed surfactant [mol m^{-2}].
Since surfactant A plays a minor role in the current model, it has been decided to describe the surface coverage provided by it supposing that all of the emulsifer is absorbed on the particles:

$$\theta_A(t) = \frac{n_{\mathrm{mol,A}}(t)}{A_{\mathrm{P}}\,\Gamma_{\infty,A}}, \tag{6.73}$$

where $n_{\mathrm{mol,A}}(t)$ are the total moles added until time t and $\Gamma_{\infty,A}$ the emulsifier concentration at saturation conditions which can be determined by surface tension evaluations. This hypothesis has been proved to be reasonable if, as it will be shown in Section 7.3, θ_A is sufficiently low.
On the other hand, the surface coverage provided by surfactant B is modelled by adopting a two-step Langmuir adsorption model:

$$\theta_B = \frac{\Gamma_{\mathrm{B}}}{\Gamma_{\infty,B}} = \frac{k_1[S]_{\mathrm{B,w}}(n^{-1} + k_2[S]_{\mathrm{B,w}}^{n-1})}{1 + k_1[S]_{\mathrm{B,w}}(1 + k_2[S]_{\mathrm{B,w}}^{n-1})}, \tag{6.74}$$

where $[S]_{\mathrm{B,w}}$ is the molar concentration of surfactant in the aquoeus phase, k_1 the adsorption of single surfactant molecules on the surface of the particles, while k_2 represents the formation rate of hemimicelles with aggregation number n; the emulsifier concentration at saturation conditions $\Gamma_{\infty,B}$ has been evaluated by using the same surface tension procedure used for surfactant A.
All the necessary information to compute the different surface coverages are proposed in Table 6.9: usually the emulsifier concentration at saturation conditions $\Gamma_{\infty,i}$ is expressed in

Property	**Value**	**Ref**
n	5.73	[89]
k_1 [L mol^{-1}]	$1.44 \cdot 10^5$	[89]
k_2 [(L mol^{-1})$^{1-n}$]	$1.6 \cdot 10^{20}$	[89]
$a_{s,B}$ [m^2]	$26 \cdot 10^{-20}$	[89]
$a_{s,A}$ [m^2]	$35 \cdot 10^{-20}$	[133]

Table 6.9 Input parameters for the absorption of the emulsifiers..

relation to the area occupied by a single molecule of surfactant $a_{s,i}$ through

$$\Gamma_{\infty,i} = \frac{1}{N_{\mathrm{AV}}\, a_{s,i}}. \tag{6.75}$$

Once both θ_A and θ_B have been evaluated, it is supposed that there is no competitive absorption between the emulsifiers, so the total surface coverage is simply the sum of the two contributions:

$$\theta = \theta_A + \theta_B. \tag{6.76}$$

6.11 Monitoring of the salt content

Finally, the model is also capable of tracking the total concentration of cationic species in the liquid medium: the use of anionic surfactants provide the particles with a negative surface charge so, subsequently, the presence of positive counterions in the aqueous phase "screens" the particles which can lead to a destabilization of the latex. The following scheme will be adopted in the test cases involving the *n*-BA/MMA/2-HEMA ter-polymer: the overall amount of counterions in the aqueous phase is calculated as the superposition of all the concentrations of the N_c different cations $[C_i]$ present in the system:

$$[\mathrm{CI}] = \sum_{i=1}^{N_c} [\mathrm{C}_i^+]; \tag{6.77}$$

for now the model does not take into account the different type of ionic species, an aspect which can be explored in future work.

6.11.1 Strong salts

The necessary information on the adopted initiators and surfactants are listed in Table 6.10 where the type and valence of counterions is put on evidence: since they are considered as

Compound	C_i	m_i
Sodium Persulfate	Na^+	2
Ammonium Persulfate	$NH_4{}^+$	2
Surfactant A	Na^+	1
Surfactant B	K^+	1

Table 6.10 List of all the initiators and surfactant in the formulation of the industrial test case.

strong salts, once they enter the liquid phase they separate in monovalent cationic C_i^+ and multivalent anionic A^{m-} species according to

$$C_i^m A \rightarrow m_i\, C_i^+ + A^{m-}. \tag{6.78}$$

The model checks for each time step which salt is added and it updates the total moles of each C_i^+ and A^{m-} depending upon the mole rate of the considered salt $\dot{n}_{C_i^m A}$:

$$\frac{dC_i^+}{dt} = \sum_{i=1}^{N_s} m_i\, \dot{n}_{C_i^m A}, \tag{6.79}$$

from which the concentration of every species is readily updated:

$$[C_i]_{\mathrm{w}} = \frac{C_i^+}{V^{\mathrm{w}}}. \tag{6.80}$$

6.11.2 Weak base: Ammonia

In the considered formulations ammonia is used to control the pH of the system. Since it is a weak base it undergoes the following equilibrium:

$$NH_3 + H_2O \underset{\leftarrow}{\overset{\gamma}{\rightleftharpoons}} NH_4{}^+ + OH^-, \tag{6.81}$$

where $\gamma = 1.88\ 10^{-5}$mol/L is the dissociation constant.
The model first updates the total moles of ammonia according to the following mole balance

$$\frac{dn_{NH_3}}{dt} = \dot{n}_{NH_3} \tag{6.82}$$

and then updates of the concentration of ammonia $[NH_3]_{\mathrm{w}} = n_{NH_3}/V^{\mathrm{w}}$.
According to LeChatelier principle, if $[NH_3]_{\mathrm{w}} > ([NH_4]^+_{\mathrm{w}} + [OH^-])$ the equilibrium goes

towards the production of ammonium ions:

$$\gamma = \frac{[NH_4]_w^+ [OH^-]_w}{[NH_3]_w}. \tag{6.83}$$

If the opposite is verified, then the equilibrium move towards the production of ammonia

$$\frac{K_w}{\gamma} = \frac{[NH_3]_w [H^+]_w}{[NH_4^+]_w}, \tag{6.84}$$

where K_w is the dissociation of water which has been calculated as a function of temperature through the following empirical law:

$$K_w = 1.204184539\ 10^{-22}\ \exp\left(0.06043\ \mathrm{T[K]}\right) \tag{6.85}$$

pH control

The monitoring of the salt content represents also the opportunity to monitor the overall pH of the system by the well known formula:

$$\mathrm{pH} = -\log_{10}\left(\frac{K_w}{[OH^-]_w}\right). \tag{6.86}$$

Chapter 7

Results, conclusions & future steps

In the previous chapter the theoretical aspects of the model have been presented with a detailed description of every mechanistic aspects included in it, meanwhile this chapter will show the results the framework can provide.
Once all the test cases are introduced in Section 7.1 the tuning of the adopted adjustable parameters during the description of the model is proposed in Section 7.2 where extensive comparisons between the kinetic variables calculated in Section 6.9 with data taken from the literature for the homo- and co-polymerization test cases or, in case of the ter-polymerization, measured experimentally by the procedures described in Appendix B.
Next, Section 7.3 is focused on the impact of the influence between different surface coverages and salt contents in the formation of coagulum.
Finally, Section 7.4 a quick review of the major results obtained in this work are proposed and Section 7.5 proposes the future steps with which the model can be developed in order to quantitatively minimize reactor fouling and be extended to other polymerization modes rather than trhe external seeded one.

7.1 Test cases

The test cases adopted in this work are presented in order of increasing complexity, from the homo-polymerizations of *n*-Butyl Acrylate to the *n*-BA/MMA/2-HEMA ter-polymerizations.

The formulations for the homo-polymerization runs have been gathered from the work made by Plessis et al [121]: all of them foresee the same initial seed size $R_{p,0} = 43\ 10^{-9}$ m, reaction temperature T = 348 K and equal composition of the additions which is reported in Table 7.1. The test cases can be distinguished by the different amounts of dosed initiator and feeding times of Addition 1 and Addition 2 which are highlighted in Table 7.2.

Next, the series of test cases of the *n*-BA/MMA copolymerizations conducted by of Elizalde

	Initial Charge	**Addition 1**	**Addition 2**
Water	0.0975	0.020	0.255
$m_{p,0}$	0.020	0	0
n-BA	0	0	0.2254
$K_2S_2O_8$	$m_I/2$	$m_I/2$	0

Table 7.1 Information about the masses [kg] of the homo-polymerization formulations [121].

[a] With respect to the total mass of added monomer.

Case	**Feeding time [min]**	$\mathbf{m_I}^a$
BA 1	60	0.30 %
BA 2	120	0.30 %
BA 3	180	0.30 %
BA 4	240	0.30 %
BA 5	180	0.0375 %
BA 6	180	0.075 %
BA 7	180	0.15 %

Table 7.2 Different test cases for the homo-polymerization of *n*-BA [121].

et al [119] is presented: the runs foresaw a reaction temperature T = 343 K and a feeding time of 180 minutes for the additions whose compositions are proposed in Table 7.3. The main differences among the the initial sizes and compositions of the seeds, the total amount of added initiator (potassium persulfate), and the composition of the feeds; all of this information is highlighted in Table 7.4.

Finally, the validation of the *n*-BA/MMA/2-HEMA terpolymerization includes four different runs conducted at Synthomer (UK) Limited in Stallingborough by adopting the materials and the procedure described in Appendix B. Their main features are proposed in Table 7.5: the three seeds are identical in composition (which cannot be disclosed for proprietary reasons), but their particles sizes $R^i_{p,0}$ and total amounts of added monomers $M_{m,i}$ vary from case to case: in particular $R^3_{p,0}$ is three times the size of $R^2_{p,0}$ and this means a gap of one order of magnitude in the particle number N_P which naturally affects the total consumption of monomer, especially during the earlier stages. The composition of all of the additions

	Initial Charge	**Addition 1**	**Addition 2**
Water	0.617	0	0.0325
$m_{p,0}$	0.063	0	0
n-BA+MMA[a]	0	0.540	0
$K_2S_2O_8$	$m_{tot,I}$	0	0

Table 7.3 Information about the masses [kg] of the co-polymerization formulations [119]

[a] Mole fraction of *n*-BA in the seed is equal to the one in the feed.

Case	$\mathbf{R_{p,0}}$ **[m]**	$\mathbf{m_{tot,I}}$ **[kg]**	$\mathbf{Y_{BA,s}}$[a]
BA-MMA 1	$42\ 10^{-9}$	0.002	0.9
BA-MMA 2	$49.5\ 10^{-9}$	0.002	0.7
BA-MMA 3	$42.1\ 10^{-9}$	0.001	0.5

Table 7.4 Distinctive information about the co-polymerizations of *n*-BA/MMA.

[a] With respect to the total mass of monomers in the formulation of the seed;
[b] With respect to the respective $M_{\mathrm{m,i}}$.

Case	***n*-Butyl Acrylate %**[a]	**Initial Size**	**Surfactant B %**[b]	**Total mass of monomers**
IC 1	~ 50 %	$R^0_{\mathrm{p,1}}$	0.8 %	$M_{\mathrm{m,1}}$
IC 2	~ 50 %	$R^0_{\mathrm{p,2}}$	0.8 %	$M_{\mathrm{m,2}}$
IC 3	~ 50 %	$R^0_{\mathrm{p,2}}$	0.97%	$M_{\mathrm{m,2}}$
IC 4	~ 50 %	$R^0_{\mathrm{p,3}}$	0.8 %	$M_{\mathrm{m,2}}$

Table 7.5 Nomenclature of the industrial test cases.

is instead the same and introduced in Table 7.6: again, for proprietary reasons, the exact percentage of each initiator and water in the respective additions can not be openly disclosed.

7.2 Discussion of the evaluation of the kinetic variables

As explained in the previous chapter, the adjustable parameters of the model are the termination rate of *n*-BA $k^{\mathrm{BA}}_{\mathrm{t,w}}$ in the aqueous phase and the monomer-specific coefficients a_i which expresses the hindering effect of the presence of the polymer on the bimolecular termination

[a] $M_{\mathrm{I,A}} + M_{\mathrm{I,B}} = 0.3\%\ M_{\mathrm{m,i}}$.

	Initial Charge	**Addition 1**	**Addition 2**	**Addition 3**	**Addition 4**
Water	-	-	-	-	-
Seed	0.20%	0	0	0	0
Monomers	0	0	100%	0	0
Surfactant B	0	0	Table 7.5	0	0
Initiator A	0	-[a]	0	0	0
Initiator B	0	0	0	-[a]	0
NH_3	0	0	0	0	0.75%

Table 7.6 Compositions of the delayed additions for the industrial test cases: the percentages are related to the total mass of monomers.

Variable	Value
$k_{t,w}^{BA}$ [L (mol s)$^{-1}$]	3.8·10^6
a_{BA}	6.3
a_{MMA}	16
$a_{2\text{-HEMA}}$	75

Table 7.7 Final values of the adjustable parameters at the end of the calibration.

rate. Their final values after the calibration procedure are proposed in Table 7.7 and what follows is the discussion which has led to their estimation.

7.2.1 *n*-BA homopolymerizations

The procedure starts from the evaluation of the parameters related to the *n*-Butyl Acrylate considering the experimental trends of X^{inst} vs $X^{overall}$ found in the literature.
The first part of this discussion involves the choice of the termination rate in the aqueous phase for *n*-BA $k_{t,w}^{BA} = 3.8\ 10^6$ [L mol^{-1}s^{-1}]. According to the Arrhenius parameters provided in Table 6.5 the termination rates for *n*-BA secondary and tertiary radicals are $k_{t,11} = 7.14\ 10^8$ [L mol^{-1}s^{-1}] and $k_{t,22} = 1.26\ 10^6$ [L mol^{-1}s^{-1}], respectively. The decision to select a value much closer to $k_{t,22}$ derives from an analysis of the relative presence of secondary and tertiary radicalic species with respect to the reaction temperature. It has been verified experimentally that at temperatures near 213 K almost all of the radicals assumes the secondary form, meanwhile at temperatures close to the ones of the formulations, around 343 K, the vast majority of the radicals are tertiary [134]; for this reason it has been decided to fix a value for $k_{t,w}^{BA}$ with the same order of magnitude as $k_{t,22}$.
Next, the *n*-BA-specific gel effect coefficient is tuned in order for the model to correctly describe the trends X^{inst} vs $X^{overall}$ for BA 1 to BA 7; this procedure ends up with a final value of $a_{BA} = 6.3$.
First, in Fig. 7.1 the comparison between the model predictions and the experimental data related to test cases BA 1 to BA 4, where the difference among the formulations is the feeding time of the delayed additions, is proposed. Even if the model slightly underestimates the data at lower conversions for BA 3 and BA 4 an overall satisfactory match is reached for every test case where the increase of X^{inst} at equal $X^{overall}$ with longer feeding times is correctly reproduced, evidence that the model can reliably predict the amount of monomer converted at any time during the reaction.
Nonetheless, the trends proposed in Fig. 7.1 are non-trivial and they need a deeper analysis; the discussion will be focused on BA 1, but the explanation can be extended to all the homo- and co-polymerization test cases.

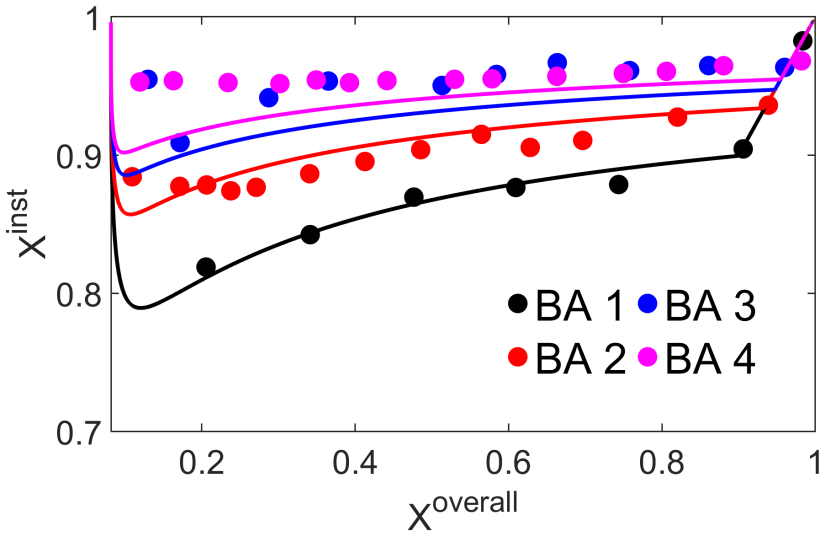

Fig. 7.1 Comparison of X^{inst} vs X^{overall} obtained by the model (solid lines) and the respective experimental data (symbols) related to the homo-polymerization of *n*-BA adopting different feeding time.

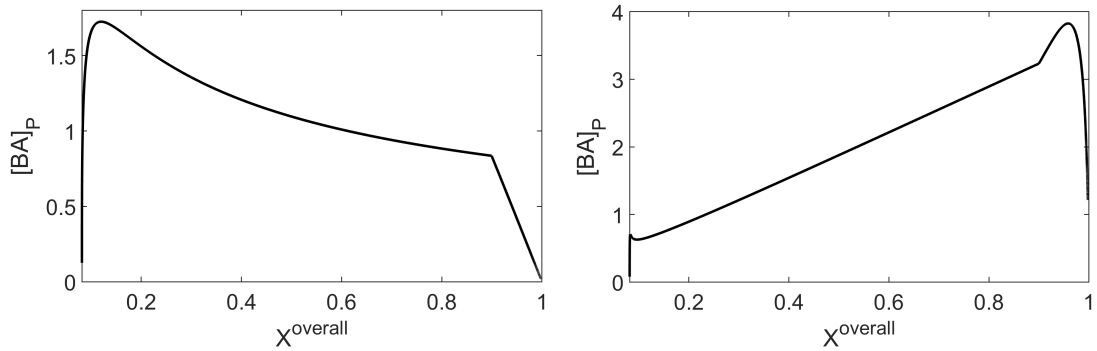

Fig. 7.2 Concentration of monomer swollen in the particles (left) and average number of radicals (right) for BA 1.

The instantaneous conversion is influenced by two opposed contributions: on the one hand X^{inst} is inversely proportional to the feeding rate because higher rates increase m^t_{BA}, the total mass of monomer added up until a certain time t, which causes the instantaneous conversion to decrease according to its formal definition in Eq.(6.65). On the other hand X^{inst} is directly proportional to the radical activity represented by the average number of radicals $\tilde{n}$, which increases the consumption of monomer C_{p}^{BA} according to Eq.(6.39).
At the beginning the amount of monomer provided is higher than its consumption, so X^{inst} starts decreasing, a feature confirmed by the increasing of the amount of *n*-Butyl Acrylate swollen into the particle phase highlighted by the left hand side of Fig.7.2 where the concentration of *n*-BA in the particle phase is proposed. In the meanwhile, the consistent increase of radical activity proposed on the right hand side of Fig. 7.2 causes C_{p}^{BA} to increase up until X^{inst} starts progressively increasing; this event is also confirmed by the decrease of the concentration of monomer in the particle phase. In the end it can be observed a discontinuity in the trend of Fig.7.1 which corresponds to the end of the delayed additions from which, by definition, $X^{\text{inst}} = X^{\text{overall}}$. This moment is also visible in Fig.7.2 where the concentration of *n*-BA in the particle phase suddenly drops because no more monomer is added and the average number of radicals experience a quick increase before dropping down. This last feature is due to the delicate interplay between the overall entry rate ρ and termination rate c in determining the radical activity: once the additions are over the decrease of the termination rate due to the gel effect is predominant over the decrease of the entry rate ρ due to the depletion of the monomer dissolved in the aqueous phase until the maximum is reached. Afterwards the scenario is inverted and the decrease of the entry rate of oligomeric radicals becomes predominant causing the radical activity to reduce.

In Fig. 7.3 the model predictions with test cases BA 3 and BA 5-7 are proposed: they are featured by the same feeding time for the delayed additions, but different amounts of initiators. In this case the model can correctly predict the increase of instantaneous conversion when a more substantial content of initiator is added. This effect is due to an increase of the entry rate of oligomeric radicals (ρ_I) according to the procedure described in Section 6.8.3 which is showed on the left side of Fig. 7.4. This subsequently leads to an higher radical activity detected by the increase of the average number of radicals $\tilde{n}$ which is proposed on the right hand side of Fig. 7.4 with the immediate consequence of incrementing the consumption of *n*-BA at each time step causing the increase in X^{inst}.

7.2.2 *n*-BA/MMA co-polymerizations

The adjustable parameters for the homo-polymerizations are now used as input data for the co-polymerization test cases where a_{MMA} is tuned in order to reproduce the same type of

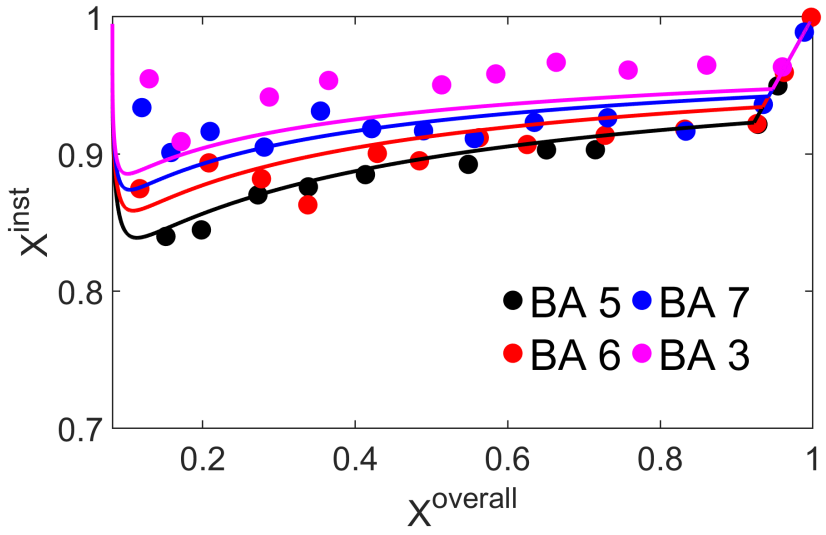

Fig. 7.3 Comparison of X^{inst} vs X^{overall} obtained by the model (solid lines) and the respective experimental data (symbols) related to the homo-polymerization of *n*-BA adopting different amounts of initiator.

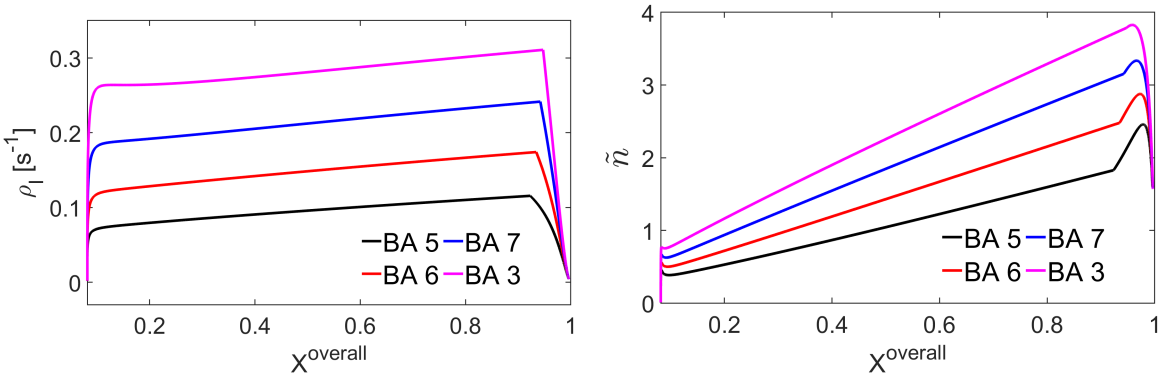

Fig. 7.4 Entry rate ρ_I of oligomers per particle (left) and $\tilde{n}$ (right) for test cases BA 3 and BA 5-7.

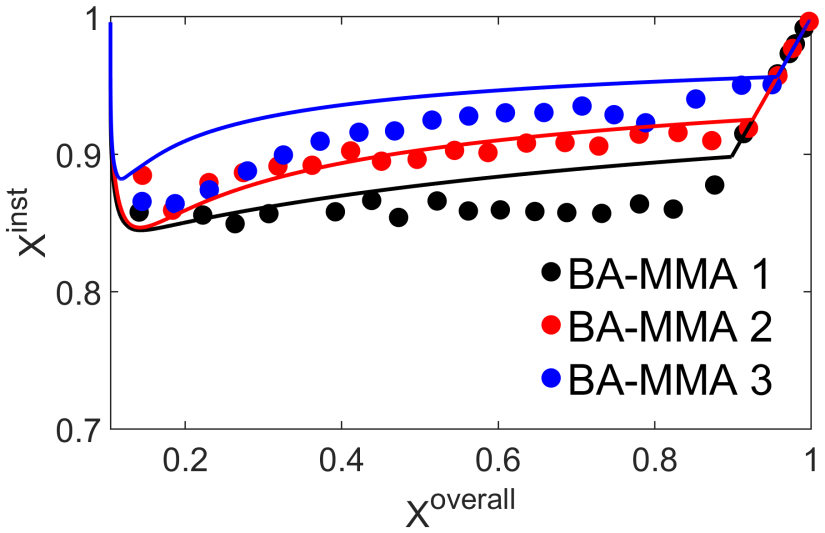

Fig. 7.5 Comparison of X^{inst} vs X^{overall} obtained from the model and the respective experimental data related to the co-polymerization of *n*-BA/MMA [119].

trend X^{inst} vs X^{overall} used for the processes involving *n*-BA. In Fig. 7.5 it is shown that the model can reproduce accurately the increase of X^{inst} with higher mole fractions of MMA in the system.

In this case the feeding time is the same, so it is evident that the reactivity of the system increases with higher amounts of methyl methacrylate. By analysing some kinetic trends this statement seems to be contradictory: in the top left of Fig.7.6 the termination rate $\langle k_{\text{t,b}} \rangle$ in bulk conditions, neglecting any gel effect, is proposed: since the homotermination rate related to two MMA radicalic species ($k_{\text{t,33}} = 9.87\ 10^8$ [L mol^{-1}s^{-1}]) is higher than the ones related to both *n*-BA terminal ends ($k_{\text{t,11}} = 6.84\ 10^8$ [L mol^{-1}s^{-1}] and $k_{\text{t,22}} = 1.26\ 10^6$ [L mol^{-1}s^{-1}]) an addition of methyl methacrylate increases the overall termination rate which is in contradiction with the experimental evidence. This means that MMA impacts the gel effect in a much stronger way than *n*-BA: by giving $a_{\text{MMA}} = 16$, a value almost three times higher than its equivalent for a_{BA}, it is possible to make sure that the termination rate in the particle phase c decreases with a more substantial presence of MMA in the latex as showed on the right hand side of Fig.7.6. At this point the average number of radicals $\tilde{n}$ showed at the bottom of Fig.7.6 foresees the expected trend of increasing with more substantial presence of methyl methacrylate allowing an accurate monitoring of the kinetic variables of interest.

The previous paragraph highlights the importance of identifying the proper monomer-specific gel effects in order to describe accurately its effect on the radical activity within the particle phase. Anyway, it is necessary to recall that the gel effect is also dependent on the latex composition according to Eq.(6.34), so a correct monitoring of the mole fractions Y_i of

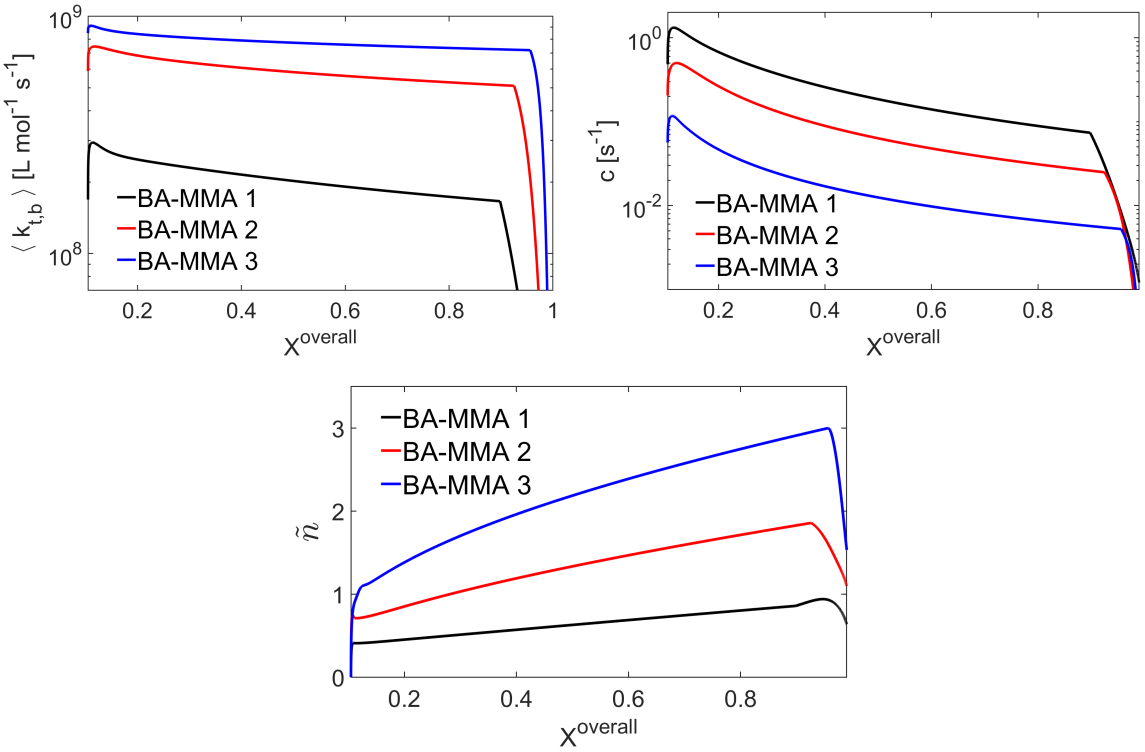

Fig. 7.6 Fundamental features influencing the co-polymerization test cases: average termination rate in bulk (left) and in the particle phase (right), together with the average number of radicals (bottom).

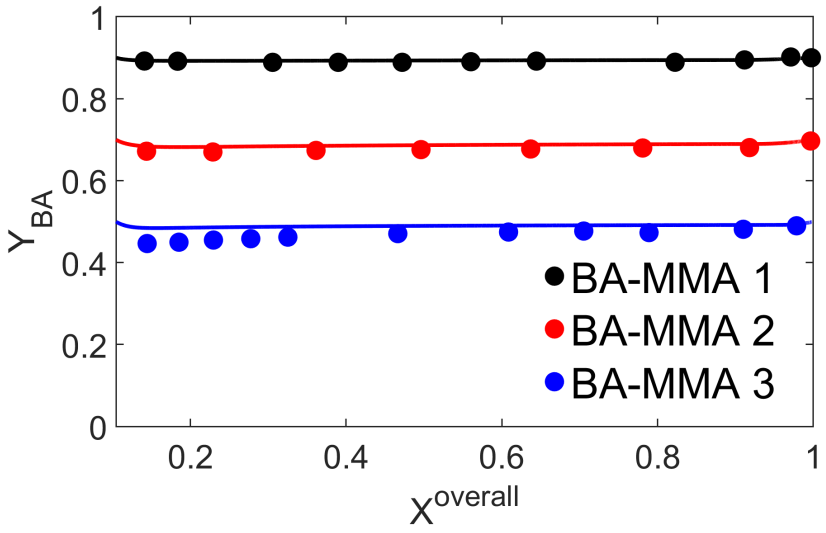

Fig. 7.7 Evolution of the molar fractions of *n*-butyl acrylate in the different runs introduced in Table 7.3 compared to experimental data [119].

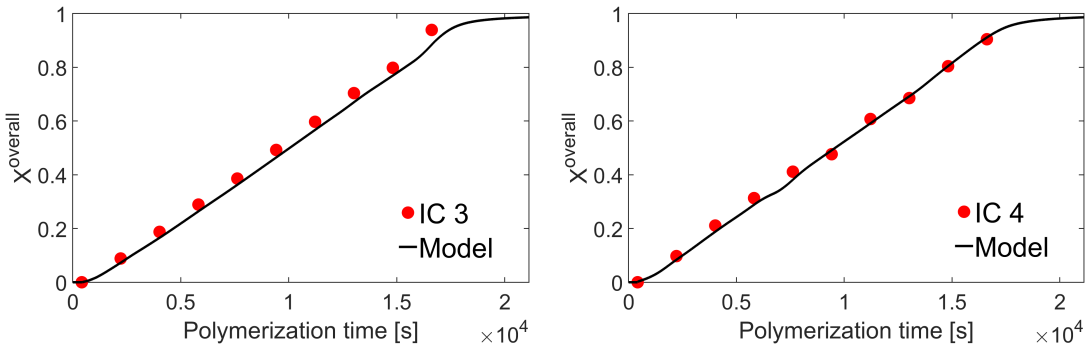

Fig. 7.8 Temporal trend of the predicted overall conversion during the ter-polymerization compared to experimental data.

each monomer in the solid phase is of pivotal importance to make sure that the monomer-specific gel coefficients assume proper values. In Fig.7.7 a comparison between the mole fractions of *n*-BA in the three latexes calculated by Eq.(6.67) and experimental data [119] is provided (since it is a co-polymer the mole fraction of MMA is its complementary to unity): it is possible to see that the model reproduces the data quite accurately except for the initial stages where the prediction of the model slightly overestimates the presence of butyl acrylate in the latex.

7.2.3 *n*-BA/MMA/2-HEMA terpolymerizations

Finally, the same procedure has been repeated on the polymerization runs of the industrial ter-polymer *n*-BA/MMA/2-HEMA where the final monomer specific gel-effect coefficient $a_{\text{2-HEMA}} = 75$ has been found by fitting temporal trends of cumulative conversions and average particle size data evaluated experimentally by Gas Chromathography and Dynamic Light Scattering; more details on the latex characterization, including a check on the hypothesis of monodispersity of the latex particles, can be found in Appendix B.
First, in Fig.7.8 the predicted X^{overall} compared to experimental data obtained by GC measurements for IC 3 and IC 4 is showed: the monitoring of these kinetic variables is really satisfactory and it shows the reliability of the model in adapting to different operative conditions, since the particle number of IC 4 is one order of magnitude lower than in IC 3.
Unfortunately, only two sets of conversion data were available for comparison so attention is turned to the monitoring of the average particle size R_{p}: the results are reported in Fig. 7.9 with a really remarkable agreement for all the considered runs.

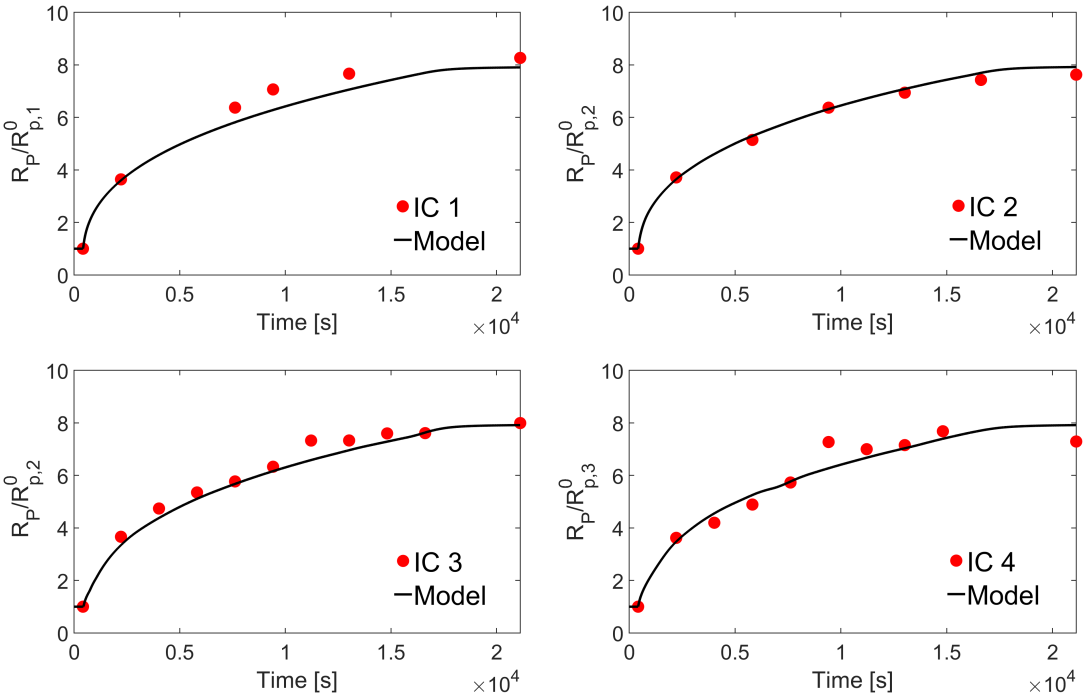

Fig. 7.9 Predicted average particle sizes compared to experimental data for all IC; each each trend has been normalized by the size of the respective seeds in order not to disclose sensitive information.

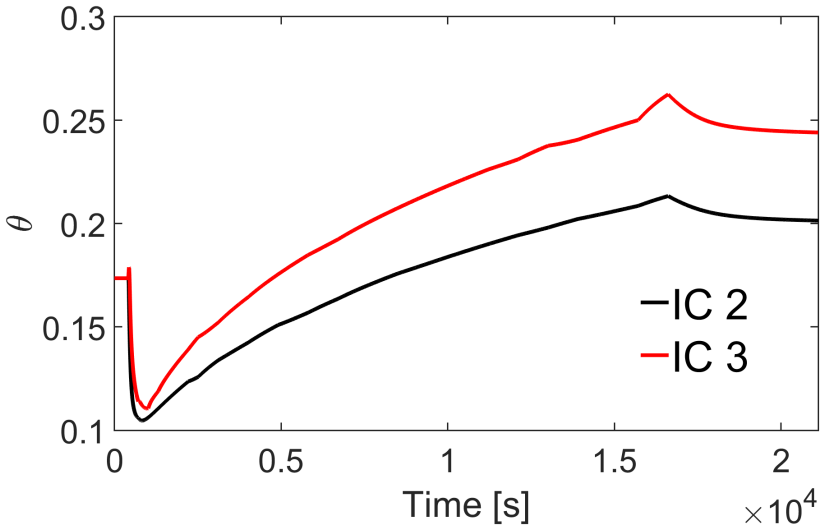

Fig. 7.10 Surface coverage difference between IC 2 and IC 3.

7.3 Interplay between surface coverage and salt content on coagulum formation

The final part of the chapter propose the application of the model to determine the optimal conditions in order to minimise the presence of coagulum for the industrial test cases. In this section two different formulations, IC 2 and IC 3, have been chosen whose only difference is the total amount of surfactant added during the delayed additions: the 0.17 % gap expressed in Table 7.5 means an increase of 20% of the total surfactant content going from IC 2 to IC 3. First, in Fig. 7.10 a comparison between the different surface coverages evaluated by the procedure in Section 6.10 is proposed. The initial value represents the surface of the seed covered by Surfactant A evaluated by Eq.(6.73): since $\theta_A \approx 0.17$ it can be said that the simplified method in Eq(6.73) adopted for surfactant A is sufficiently reliable. Once the delayed additions begin, the variations of surface coverage is caused by the consistent addition of Surfactant B only. At the beginning θ decreases for both the runs because the total surface area A_P increases with a really high rate which reaches a maximum of $\Delta A_P/\Delta t = 6000$ m^{2}s^{-1} after 7 minutes from the start of the additions. Afterwards the growth rate begins to slow down with $\Delta A_P/\Delta t$ reaching a plateau of ~ 2000 m^{2}s^{-1} and θ starts increasing until the end of the delayed additions. The total surface coverage then slightly decreases because no more emulsifier is provided, but still some free monomer needs to be converted which causes A_P to keep increasing.

It can be noticed that, since in IC 3 the amount of added surfactant is 20 % higher than in IC 2 θ will gradually be higher for the former until a maximum of 20 % difference in θ is

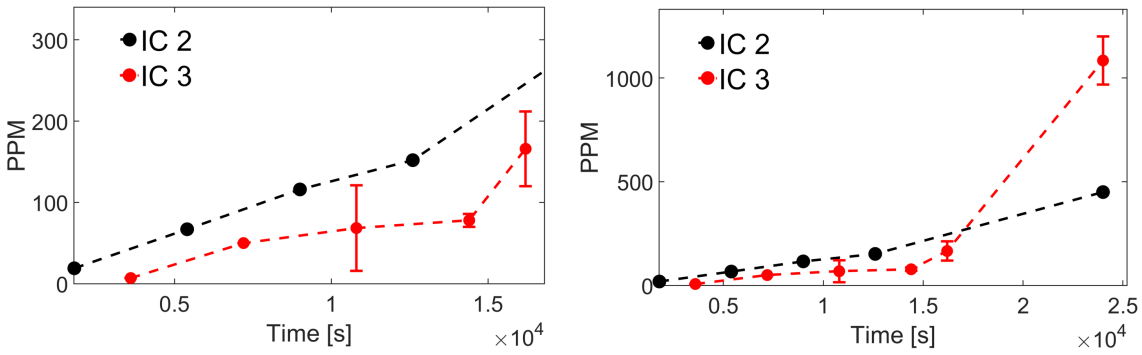

Fig. 7.11 Temporal evolution of the coagulation behavior from the grit analysis: on the left the plot is focused on the timespan of the feed additions, on the right the behavior during the whole polymerization process is shown.

reached at the end of the delayed additions. The increase of surface coverage between IC 2 and IC 3 is positively reflected by a decrease of coagulum, which is measured according to the procedure described in Appendix B, during the delayed additions: the PPMs detected in IC 3 are on average a factor $1/2$ lower than the ones in IC 2 as it can be seen on the left side of Fig. 7.11. This is easily explained by the fact that in IC 3 the surface charge density is higher than in IC 2 which guarantees a better electrostatic stabilization.

Quite the opposite, the right hand side of the same figure shows a sudden and undesired change of scenario: a steep increase of coagulum formation between the end of the feed additions and the end of the polymerization in IC 3 in which the detected amount is almost three times higher with respect to the final value in IC 2. An explanation for this behavior has been researched in Fig.7.12 where the difference in salt content due to the additional surfactant amount added in IC 3 calculated by the procedure in Section 6.11 is showed; it has been already discussed in chapter 5 how an excessive amount of salt can affect negatively the stability against the aggregation through the so-called "screening effect". At a first glance the difference is small but consistently increasing throughout the delayed additions and it reaches a maximum of 7% at the end of the feed additions which remains constant until the end of the process. Unfortunately, this small difference leads to a dramatically diverse coagulation behavior which is very likely to be linked to the fact that the concentration of counterions in IC 3 has crossed over the Critical Coagulation Concentration (CCC) between the end of the delayed additions and the end of the polymerization. This scenario is visually summarized in Figure 7.13: even if IC 2 has a lower surface coverage than IC 3 the salt content is low enough to guarantee a sufficiently high energy barrier U which limits the aggregation of the particles. On the other hand, since IC 3 probably passes the CCC the energy barrier will be overall lower than in IC 2, even if the surface coverage is higher, because of the stronger

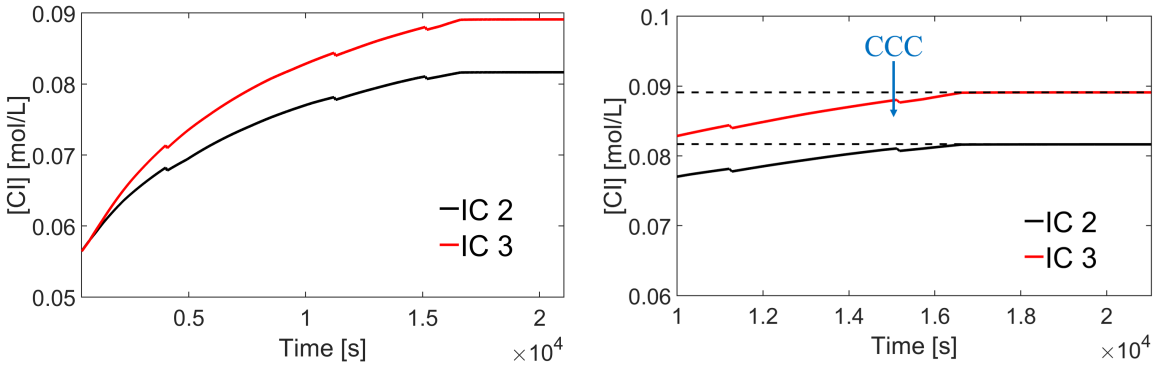

Fig. 7.12 Concentrations of counterions in the aqueous phase as a function of time during the polymerization process. The panel on the right is a zoomed in version of the plot on the left hand side focusing on the late stage of the process. The dashed lines indicate the lower and an upper bounds for the CCC, such that CCC $\approx 0.085/0.09$ [mol/L].

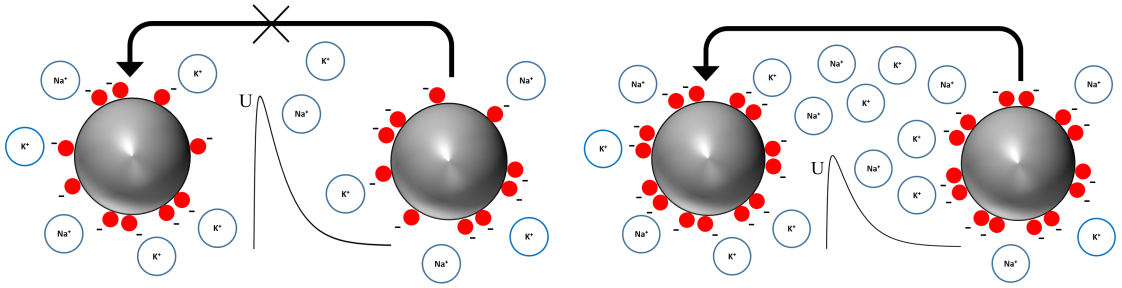

Fig. 7.13 Visual summary of the balance between the surface coverage and salt content on the energy barrier against aggregation in IC 2 (left) and IC 3 (right) at the end of the polymerization.

screening effect on the electrical double layer caused by the counterions. This ultimately triggers the colloidal instability and sudden formation of coagulum. If IC 2 never crosses the CCC whereas IC 3 does it, even a small increase of 7% in total salt content can lead to an increase of 300% of detected coagulum at the end of the polymerization.
The inspection of the right hand side of Figure 7.12 suggests that the CCC assumes a value $\approx 0.085 - 0.09$ mol/L). From a quick survey across the literature about Critical Coagulation Concentration of carboxyl-stabilized surfaces it is clear that the pH plays an important role in determining the surface charge density of the dispersion: at low pHs the probability of protonation of the carboxylic sites is very likely, meanwhile this phenomenon is avoided at pHs over the neutrality point; this leads to an important increase, even by two orders of magnitude, of the CCC going from acid to alkaline environments. Since both the industrial runs are featured by a basic environment due to the addition of ammonia during the polymerization, the CCC is ≈ 0.35 mol/L [91] for systems with pH above 7 and Na^+ or K^+ as counterions, which is sinisterly higher than the predicted one; there are two possible explanations for this discrepancy. One relies on the fact that one of the more dominant counterions in our system is the ammonium ion NH_4^+, which has a more destabilizing effect on the dispersion compared to Na^+ or K^+ according to the Hofmeister series [135]; indeed, within the Hofmeister, a difference of a factor $2-3$ upon changing the counterion is not uncommon. Furthermore, the CCCs reported across the literature are typically related to extremely dilute conditions, whereas in industrial conditions the colloidal particle concentration is much higher such that many-body effects can enhance coagulation on top of EDL screening effects. It is evident that this system is very sensitive to increase in salt content even far away from the typical CCC values because of (i) the stronger destabilizing effect of the ammonium ion, and (ii) the much higher solids content typical of the industrial emulsion polymerization processes.

7.4 Conclusions

In this work a mathematical model to predict the seeded-emulsion polymer reaction kinetics of homo-, co- and ter-polymerizations has been developed. The model takes advantage of state-of-art models for radical exchange between particle and aqueous phase within the pseudo-homopolymerization framework.
Unknown parameters related to the monomer-specific influence on the gel effect are calibrated by fitting literature data of monomer conversion for *n*-BA homo-polymerizations and *n*-BA/MMA co-polymerizations. Finally, the predictive model has been tested using a ter-polymerization of *n*-butyl acrylate and methyl methacrylate with 2-hydroxyethyl methacrylate (2-HEMA). This time the model predictions are compared with DLS and GC characterizations

of the time-evolution of average particle size and the cumulative conversion, respectively; good agreement is found for both the literature and the industrial runs with a very limited number of fitting parameters.
Then two industrial test cases, IC 2 and IC 3, whose formulations differ from the amount of added anionic surfactant only, have been adopted to start studying the optimal conditions in order to minimize the formation of undesired coagulum. This stage of the project is mainly focused on studying the interplay between different surface coverages and salt contents on the formation of coagulum. The analysis shows that the surfactant-rich system displays significantly less coagulation, which is guaranteed by an higher colloidal stability due to a better electrostatic stabilization, during all steps of the industrial polymerization process except at the end where the PPMs of coagulum increases by 300 % in IC 3 than in IC 2. This can be explained by the extra amount of counterions dosed during IC 3 due to the extra Surfactant B, in this case a potassium salt, which is likely to bring the concentration of counterions in the system above the critical coagulation concentration (CCC) and to uncontrolled coagulation resulting in a much larger amount of detected coagulum at the end of the process. Hence, the proposed modelling-based methodology offers the possibility to rationalize the interplay of surfactant and counterion concentrations on colloidal coagulation during emulsion polymerization.

7.5 Future Steps

7.5.1 Quantitative prediction of coagulum formation

For now, the results provided by the model shows a clear, but still qualitative, interconnection between the stabilizing effect provided by the surface coverage and the destabilizing one from the counterions dissolved into the liquid medium.
The logical next step is quantitatively evaluating the impact of the aforementioned contributions on the colloidal stability through a systematic evaluation of the Fuchs stability ratio for the latex particles whose particle size R_P will be tracked by the polymerization kinetics:

$$W = \int_{2R_P}^{\infty} \frac{\exp(\beta U)}{\chi^{-1}(r) r^2} dr \tag{7.1}$$

In particular the interaction potential U will be evaluated by the classic DLVO theory proposed in Eq.(5.5-5.6-5.7): the Debye length κ^{-1} will be calculated as a function of the overall ionic strength of the system (Eq.(5.9)), meanwhile the zeta potential ζ in Eq.(5.7) will be linked to the effective surface charge density σ_{eff} through the integration of the Poisson-Boltzmann

equation under appropriate approximations:

$$\zeta = \frac{\sigma_{\text{eff}}}{\varepsilon_0 \varepsilon_r (1 + \kappa R_P)}. \tag{7.2}$$

σ_{eff} depends on the surface coverage θ which provides a surface charge density equal to σ_0 via Eq.(5.10). In order to obtain σ_{eff} it is important to remove from σ_0 the charge density σ_d of opposite sign provided by the adsorption of the counterions on the Stern layer:

$$\sigma_{\text{eff}} = \sigma_0 - \sigma_d \tag{7.3}$$

Another possible development is adding the influence of the flow field due to the mixing conditions inside the reactor by introducing the formalism proposed by Zaccone et al. [54] recalled here:

$$W_G = \int_{2R_P}^{\delta} \left\{ \frac{1}{\chi^{-1} r^2} \exp\left[\int_{\delta}^{r} \left(\beta \frac{dU}{dr} + \text{Pe} v_r \right) dr \right] \right\} dr, \tag{7.4}$$

where $\delta = R_P \sqrt{(\kappa^{-1}/R_P)/\text{Pe}}$.
The first and more simplified approach would be the evaluation of an average Péclet number by evaluating the average shear rate G which depends on the power provided to the impeller and the total volume of the system according to Eq.(5.13).

7.5.2 Extension to other polymerization modes

Once the quantitative evaluation for seeded systems is reliable, it is possible to extend the model from external seeded procedures to emulsion polymerization modes which includes Interval I, the particle formation. In these scenarios the total number of particles N_P varies with time and it is the superposition of two contributions:

$$\frac{dN_P}{dt} = \frac{dN_{P,\text{homo}}}{dt} + \frac{dN_{P,\text{mic}}}{dt} \tag{7.5}$$

The first contribution is the one by homogeneous nucleation which forsees a very similar mechanism to the entry of oligomers in the mature particles: within the aqueous phase the oligomers have to reach the critical degree of oligomerization j_{cr} for which they become completely water insoluble. This leads to the following final balance for the number of particles formed by the homogeneous mechanism $N_{\text{P,homo}}$:

$$\frac{dN_{P,\text{homo}}}{dt} = k_{\text{p}} [M]_{\text{w}} [\text{R}^{\bullet}_{\text{j}_{\text{cr}}-1}]_{\text{w}}. \tag{7.6}$$

On the other hand, the micellar nucleation is described as the absorption of oligomers with a degree of polymerization higher than the surface active threshold R_{capt}, so that they can be captured by micelles:

$$\frac{dN_{P,\text{mic}}}{dt} = \frac{k_{\text{cm}} N_{\text{AV}}}{r_{\text{mic}}} [\text{R}^{\bullet}]_{\text{capt,w}}, \tag{7.7}$$

where k_{cm} is the rate with which the oligomers are captured by the micelles with radius r_{mic}.

Part III

Biological systems

Chapter 8

Study of the *in vivo* growth dynamics of a Poly-glutamine

In this chapter an application of the Smoluchowski equation to a biological system will be proposed: the main topic is the demonstration of the primary role of the diffusion in the growth dynamics of perinuclear "aggresomes", big proteinaceous agglomerates, inside mammalian cells.

8.1 Introduction

Computational modelling of biological systems has seen an important increase of interest over the last two decades: the increasing available computational power allows the study of more and more complex dynamics which take place inside fundamental biological units such as the cells. The development of Molecular Dynamics (MD) has allowed the description of material transport across biological membranes by using spatial and temporal resolutions currently unattainable by experimental methods [137].
Among the application of MD has also been used to study protein folding and unfolding mechanisms inside biological cells [138, 139]. The former is the process by which linear chains of amino-acids are converted into three dimensional structures which provide functional properties to that particular molecule. It can happen that this procedure may instead fail (unfolding), causing the exposition of hydrophobic sides of the protein to the liquid cytosol which, for certain proteins such as Poly-glutamine, ultimately leads to formation of small aggregates which then form a big proteinaceous agglomerate named "aggresome" [140].
These big clusters have first been thought to be beneficial since they capture all of the mis-

folded proteins which are toxic for the cell [141], but recent studies have contradicted this theory showing a connection between the presence of the aggresomes and nuclear malfunctioning whose major observable features are DNA double strand breaks, cell cycle arrests, mitotic defects and apoptosis [142].
Meanwhile the mechanism behind the folding/unfolding reaction has been widely modelled, a computational scheme which describes the aggregation process itself is still missing and the proposed mechanisms until now are based on *in vitro* experimental procedures only. The currently accepted mechanism foresees the build-up of the initial core at the centre of a spiderweb of microtubules called MicroTubes Organized Centre (MTOC) or centresome: the small proteinaceous aggregates in the cytosol are marked by an enzyme named HDAC6 (Histone deacetylases 6) which enables them to be attached to the Microtubes with a protein named dynein and finally transported along almost linear trajectories to the centresome.
On the other hand, there is still debate on the mechanism behind the later stages of the growth: it is still widely accepted that the active transport plays the most important role during the later stages as well, but the fact that its growth has been mainly studied *in vitro* weakens this hypothesis even because recent *in vivo* studies have instead hypothesized that the diffusion is the major contributor to the growth of the aggresome during the later stages [143], a theory which will be backed up by the following computational model which, together with proposing itself as the first framework to describe aggregation kinetics inside a biological cell, is an ulterior step forward the understanding of the link between protein aggregation and neurodegenerative illnesses such as the Hungtington Disease (HD).

8.2 Theoretical framework

The starting point is visually summarized in Fig.8.1 where the initial scenario is proposed: the cytosol is homogeneously populated by proteinaceous aggregates with the same size R_P which will constitute the primary particles inside the "aggresome". The two possible transport mechanisms are also highlighted: on one hand the disordered Brownian motion in the cytosol, on the other the active transport along the Microtubes according to the aforementioned mechanism. This physical scenario can be mathematically described by an initial value problem whose main equation has an identical structure to the 2-Body Smoluchowski equation under shear flow, but this time $\mathbf{v}$ describes the velocity with which the aggregates move along the Microtubes and, since no hydrodynamic interactions have

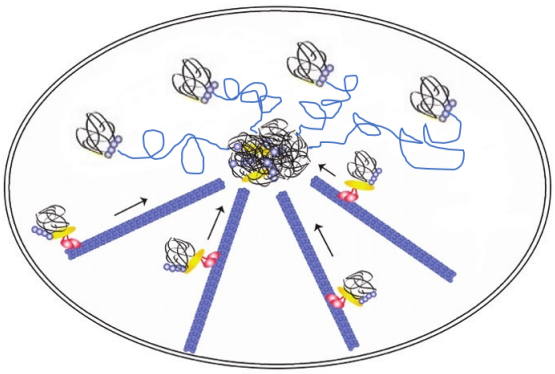

Fig. 8.1 Scheme of the aggresome growth with the contemporary presence of vibrating Brownian motion inside the cytosol and active transport on the MTOC; it is possible to see the presence of the HDAC6 (yellow) and the dynein (pink).

been considered, it is featured by a null divergence:

$$\begin{cases} \partial_t C_{\text{liq}} = \nabla \cdot \left(D \nabla C_{\text{liq}} - \mathbf{v} C_{\text{liq}} \right) & R(t) < r < R_{\text{cell}} \\ C_{\text{liq}}(r,t) = 0 \quad r = R(t) \\ \partial_r C_{\text{liq}}(r,t) = 0 \quad r = R_{\text{cell}} \\ C_{\text{liq}}(r,t) = C_{\text{liq},0} \quad t = 0. \end{cases} \tag{8.1}$$

C_{liq} is instead the number concentration of aggregates inside the cell, D the diffusion coefficient and $C_{\text{liq},0}$ the initial concentration of aggregates which has been estimated by image analysis to be $C_{\text{liq},0} = 6.0\ 10^{17}[\text{m}^{-3}]$. From Fig 8.1 it is evident that the transport properties are basically dependent on the radial coordinate only, so a radial symmetry will be imposed and, considering also $\nabla \cdot \mathbf{v} = 0$, Eq.(8.1) becomes

$$\partial_t C_{\text{liq}} = D \partial_r^2 C_{\text{liq}} + \frac{2D}{r} \partial_r C_{\text{liq}} - v_r \partial_r C_{\text{liq}}. \tag{8.2}$$

The second hypothesis is based on the independence between the two different transport methods: when an aggregate is captured by the microtubes it will not be possible for it to re-enter the cytosol once again; for this reason Eq.(8.2) can be split as follows:

$$\partial_t C_{\text{liq}} = \partial_t C^B_{\text{liq}} + \partial_t C^C_{\text{liq}} = D \partial_r^2 C^B_{\text{liq}} + \frac{2D}{r} \partial_r C^B_{\text{liq}} - v_r \partial_r C^C_{\text{liq}}, \tag{8.3}$$

where C^B_{liq} is the concentration of clusters transported by Brownian motion, and C^B_{liq} the concentration of aggregates transported by pure advection to the aggresome.

The final formalism is then composed two different Cauchy problems: the one related to the diffusive transport which can be written as

$$\begin{cases} \partial_t C^B_{\text{liq}} = D\partial_r^2 C^B_{\text{liq}} + \dfrac{2D}{r}\partial_r C^B_{\text{liq}} \quad R(t) < r < R_{\text{cell}} \\ C^B_{\text{liq}}(r,t) = 0 \quad r = R(t) \\ \partial_r C^B_{\text{liq}}(r,t) = 0 \quad r = R_{\text{cell}} \\ C^B_{\text{liq}}(r,t) = C^B_{\text{liq},0} \quad t = 0, \end{cases} \tag{8.4}$$

meanwhile the one related to the active transport in the microtubes includes the pure-advection equation with its boundary conditions:

$$\begin{cases} \partial_t C^C_{\text{liq}} = -v_r \partial_r C^C_{\text{liq}} \quad R(t) < r < R_{\text{cell}}; \\ \partial_r C^C_{\text{liq}}(r,t) = 0 \quad r = R_{\text{cell}}; \\ C^C_{\text{liq}}(r,t) = C^C_{\text{liq},0} \quad t = 0, \end{cases} \tag{8.5}$$

where $R(t)$ is the radius of the growing aggresome corresponding to the position of the solid-liquid interface, R_{cell} the characteristic size of the cell taken to be spherical. Concerning the evaluation of the initial concentrations $C^B_{\text{liq},0}$ inside the cytosol and $C^C_{\text{liq},0}$ on the microtubes, trajectory analyses conducted by Prof. Clemens Kaminski and his research group have been estimated that, on average, only 5% of aggregates undergoes active transport during the growth of the aggresome; their final values are proposed in Table 8.1.

Concerning the other input data the radius of the cell R_{cell} and of the aggregates R_{P} have been evaluated by image analysis, meanwhile the evaluations of the diffusion coefficient D needs a deeper explanation: during the formation of the aggresome, the presence of aggregates keeps on reducing, so at the beginning there will be a slower diffusion, meanwhile at the end it will be much quicker due to the lower presence of obstacles in the cytosol. For this reason D has been calculated by making a geometric average between its value at the beginning of the growth measured by mean square displacement evaluations and the one at the end estimated by the application of the Stokes-Einstein theory.

The strength of the model is based on the fact that the only adjustable parameter in Table 8.1 is v_r: its sign has to be negative since the direction of the active transport is opposite with respect to the radial direction which starts from the centre of the aggresome pointing outward.

Since the solid phase, the aggresome, is growing one of the two boundaries of the liquid phase is not fixed, but its value will change as a function of time; so Eq.(8.4-8.5) are defined as *moving boundary problems*.

Property	**Value**
R_{P}	$1.95\ 10^{-7}$ [m]
R_{cell}	$1.5\ 10^{-5}$ [m]
D	$1.36\ 10^{-15}$ [$\mathrm{m^2\ s^{-1}}$]
v_r	$-7.0\ 10^{-10}$ [$\mathrm{m\ s^{-1}}$]
$C^B_{\mathrm{liq},0}$	$5.7\ 10^{17}$ [$\mathrm{m^{-3}}$]
$C^C_{\mathrm{liq},0}$	$3.0\ 10^{16}$ [$\mathrm{m^{-3}}$]

Table 8.1 Input data adopted for the solution of the Cauchy problems.

The update of the position of the solid-liquid interface $R(t)$ requests a model to describe the growth of the aggresome. To do so it has been applied a principle commonly used in heat transfer moving boundary problems, also known as Stefan problems [144]. The first step is the enforcement of the conservation of matter at r = R(t): the RHS of Eq.(8.6) represents the flux of matter that is included in the solid phase during the time span δt. This leads to the deposition of an external shell of aggregates to the surface of the aggresome that causes the increase of its mass (in this case defined as the number of aggregates inside the cluster) expressed in the LHS of Eq.(8.6):

$$q\frac{4}{3}\pi\Big(R(t+\delta t)^3-R(t)^3\Big)=4\pi\int_t^{t+\delta t}R(\tau)^2\Big[D\partial_r C^B_{\mathrm{liq}}(R(\tau),\tau)-v_r C^C_{\mathrm{liq}}(R(\tau),\tau)\Big]d\tau. \quad (8.6)$$

Here τ represents the temporal variable integrated between t and $t+\delta t$, meanwhile q represents a "growing factor", the amount of primary particles necessary to increase the system by a unit of volume which will be described later when the morphology of the aggresome will be introduced. Even though $q(t)$ varies with time overall, it will be considered constant over the small time-step δt taken for the discretization of the transport equations. Dividing both intervals by δt and doing the limit for $\delta t \to 0$ the following formalism is obtained:

$$\lim_{\delta t\to 0}\frac{4\pi q}{3}\frac{R(t+\delta t)^3-R(t)^3}{\delta t}= \\ =\lim_{\delta t\to 0}\frac{4\pi}{\delta t}\int_t^{t+\delta t}R(\tau)^2\Big[D\partial_r C^B_{\mathrm{liq}}(R(\tau),\tau)-v_r C^C_{\mathrm{liq}}(R(\tau),\tau)\Big]d\tau \quad (8.7)$$

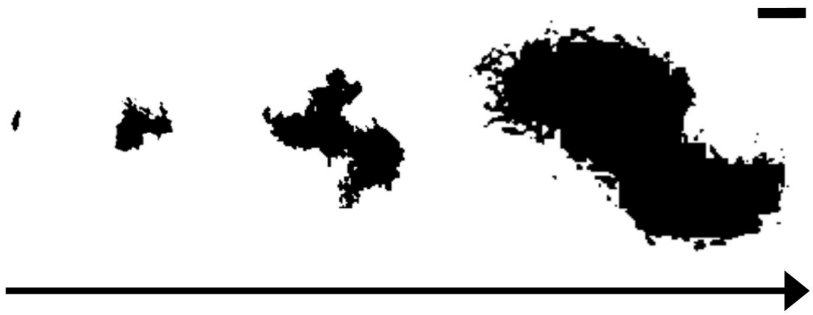

Fig. 8.2 One of the possible growing paths of the aggresome which is used to evaluate the parameters in Eq.(8.11) (adapted from [143]); the scale bar represents 1μm .

Because the integrated function in Eq.(8.6) is continuous and limited inside every interval [t,t+δt] it is possible to apply the Mean Value Theorem (MVT):

$$\frac{\int_t^{t+\delta t} R(\tau)^2 \left[D\partial_r C^B_{\text{liq}}(R(\tau),\tau) - v_r C^C_{\text{liq}}(R(\tau),\tau) \right]}{\delta t} = \\ = R(t_{\text{int}})^2 \left[D\partial_r C^B_{\text{liq}}(R(t_{\text{int}},t_{\text{int}}) - v_r C^C_{\text{liq}}(R(t_{\text{int}}),t_{\text{int}}) \right], \quad (8.8)$$

where t_{int} is an intermediate point inside the interval $[t, t+\delta t]$.
The application of Eq.(8.8) together with the definition of the first derivative to Eq.(8.7) leads to the following expression:

$$\frac{4\pi q}{3}\partial_t [R(t)^3] = \lim_{\delta t \to 0} 4\pi R(t_{\text{int}})^2 \left[D\partial_r C^B_{\text{liq}}(R(t_{\text{int}}),t) - v_r C^C_{\text{liq}}(R(t_{\text{int}}),t_{\text{int}}) \right]. \quad (8.9)$$

Finally, Eq.(8.9) can be reduced to the following initial value problem:

$$\begin{cases} \partial_t R(t) = \dfrac{D}{q(t)}\partial_r C^B_{\text{liq}}(R(t),t) - \dfrac{v_r}{q(t)} C^C_{\text{liq}}(R(t),t) \quad t > 0 \\ R = R_0 \quad t = 0, \end{cases} \quad (8.10)$$

where R_0 is the initial aggresome size expressed as radius of gyration which is defined as the root mean square distance of the aggregate forming the aggresome from its centre of mass. In this work R_0 has been found by image analysis using R_0 = 6.67 10^{-7} m as initial value.

8.2.1 Morphology of the aggresome

The only variable which still needs to be described to solve the Cauchy problems is the growing factor $q(t)$ which has been introduced as a number concentration, the number of aggregates which are needed to increase the volume of the system by 1 m^3; the problem is now linking $q(t)$ to the microscopical structure of the aggresome.
To do so, it has been hypothesized that the morphology of the aggresome is comparable to the one of a fractal object. This family of clusters is characterised by scale invariance [145], which means that their shape remains more or less the same during their growth. This hypothesis is backed up by visual analysis of the growth dynamics in Fig.8.2 in which one example of a series of very similar growing paths is proposed: it is possible to observe that the agglomerates start developing an elongated structure whose ends are featured by the growth of almost symmetric lobes.
Nonetheless, this hypothesis needs a quantitative confirmation: it is necessary to make sure that the N number of primary particles contained in the cluster scales with the the aggresome normalized size $R(t)/R_P$ according to Eq.(8.11):

$$N = k_f \left(\frac{R(t)}{R_P} \right)^{d_f}. \tag{8.11}$$

In particular k_f is a simple scaling factor, meanwhile d_f is the fractal dimension, the key parameter for the description of the structure of a cluster: if its value is closer to unity, it has an almost fibrillate shape, meanwhile if $d_f \to 3$ the shape will be nearly spherical. The two missing parameters have been found by image analysis conducted by Prof. Clemens Kaminski and its group: from estimating N and R(t) from Fig.8.2 it has been possible to find a very good linear fit on the double logarithmic scale showed in Fig.8.3 from which the values $k_f = 1.75$ and $d_f = 2.08$ have been evaluated.
Since it is possible to say that the aggresome behaves as a fractal, its packed fraction ϕ_P, the total volume occupied by the primary units in the aggresome, can be formalized as:

$$\phi_P = k_f \left(\frac{R(t)}{R_\mathrm{P}} \right)^{d_f - 3} = \frac{N V_\mathrm{P}}{V_\mathrm{agg}}, \tag{8.12}$$

where V_P is the volume of a primary unit and V_agg the one of the aggresome. Since the growing factor is a number concentration it will be expressed as the total number of aggregates per unit volume of the aggresome, obtaining the following expression for $q(t)$:

$$q(t) = \frac{N}{V_\mathrm{agg}} = \frac{k_f (R(t)/R_\mathrm{P})^{d_f - 3}}{4/3 \pi R_\mathrm{P}^3}. \tag{8.13}$$

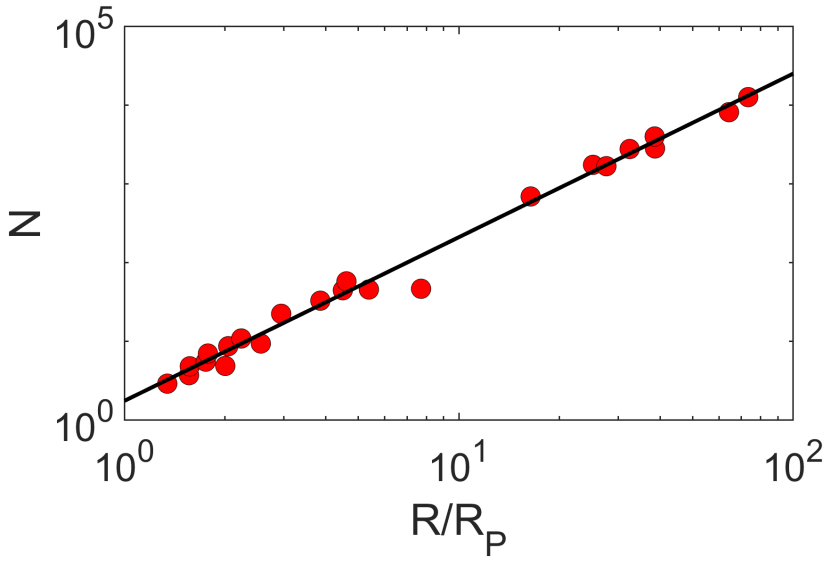

Fig. 8.3 Number of particles inside the growing aggresome N with respect to its dimensionless radius R/R_{P} (adapted by [143]).

8.3 Mathematical methods

At this point it is possible to focus on the actual resolution of the Cauchy problems.
Regarding the one related to the active transport on the Microstubes, Eq.(8.5), it is well known that the analytic solution of a pure convection equation, knowing the initial concentration distribution $C^{C}_{\mathrm{liq},0}$, is

$$C^{C}_{\mathrm{liq}}(r,t) = C^{C}_{\mathrm{liq},0}(r - v_r t, t). \tag{8.14}$$

Thanks to Eq.(8.14), the active transport of aggregates inside the micro-tubes can be modelled as a plug flow of matter from the liquid medium to the aggresome.
On the other hand, the initial value problems related to the diffusive motion of the aggregates in the cytosol (Eq.(8.4)) and the growth of the aggresome (Eq.(8.10)) are solved numerically: the continuous space coordinate is divided into a series of N discrete intervals and the time span between t_{in} = 0 h and t_{fin} = 16 h in M timesteps.
Eq.(8.4) is solved by implementing a *Crank-Nicholson* scheme over the spatial coordinates r_j with $j = n+1,..,N$ where $r_{n+1} = R(t)$ is the node related to the position of the solid-liquid interface.
As it is well known, the Crank-Nicholson methodology is an implicit method which solves the following differential equation (C =$C^{\mathrm{B}}_{\mathrm{liq}}$ for better clarity)

$$\frac{\partial C}{\partial t} = F\left(r, C, t, \frac{\partial C}{\partial r}, \frac{\partial^2 C}{\partial r^2}\right) \tag{8.15}$$

through a combination of the forward and backward Euler methods:

$$\frac{C_{\mathrm{i}}^{\mathrm{j+1}} - C_{\mathrm{i}}^{\mathrm{j}}}{\delta t} = \frac{1}{2}\left[F_{\mathrm{i}}^{\mathrm{j+1}}\left(r, C, t, \frac{\partial C}{\partial r}, \frac{\partial^2 C}{\partial r^2}\right) + F_{\mathrm{i}}^{\mathrm{j}}\left(r, C, t, \frac{\partial C}{\partial r}, \frac{\partial^2 C}{\partial r^2}\right)\right] \tag{8.16}$$

This methodology leads to the formulation of a linear system which has to be solved at every timestep whose general line is proposed in Eq.(8.17):

$$-A(\mathrm{r_j})C_{j+1}^{i+1} + (1+B)C_j^{i+1} - E(\mathrm{r_j})C_{j-1}^{i+1} = A(\mathrm{r_j})C_{j+1}^{i} + (1-B)C_j^{i} + E(\mathrm{r_j})C_{j-1}^{i}, \tag{8.17}$$

where the coefficients $\mathrm{A(r_j)}$, B and $\mathrm{E(r_j)}$ are computed as

$$\begin{cases} A(r_j) = \left(\dfrac{D\delta t}{2\delta r^2} + \dfrac{D\delta t}{2r_j\delta r}\right); \\ B = \dfrac{D\delta t}{\delta r^2}; \\ E(r_j) = \left(\dfrac{D\delta t}{2\delta r^2} - \dfrac{D\delta t}{2r_j\delta r}\right). \end{cases} \tag{8.18}$$

Finally, the two boundary conditions in Eq.(8.4) are written as

$$\begin{cases} C_{\mathrm{liq}}^{B}(n+1,t) = 0; \\ C_{\mathrm{liq}}^{B}(N-1,t) = C_{\mathrm{liq}}^{B}(N+1,t). \end{cases} \tag{8.19}$$

The second one represents the null flux at $r = R_{\mathrm{cell}}$ which is implemented by applying symmetry condition thanks to the use of the ghost node $N+1$: the N^{th} point of the grid can be used as a mirror between neighbouring cells; so the coefficients of the last line of the linear system become

$$B(R_{\mathrm{cell}}) = E(R_{\mathrm{cell}}) = \left(\frac{D\delta t}{\delta r^2}\right). \tag{8.20}$$

Once the concentration profile C_{liq}^{B} is updated, it is possible to calculate the particle size of the aggresome $R(t)$ by solving Eq.(8.10) for each timestep with a forward Euler method. This is an explicit scheme which means that the following formalism

$$\frac{\partial R}{\partial t} = G(R, r, t, C_{\mathrm{liq}}^{\mathrm{C}}) \tag{8.21}$$

Property	Value
δt	3.6 s
δr	9.25 10^{-9} m

Table 8.2 Time and spatial steps adopted in the numerical frameworks.

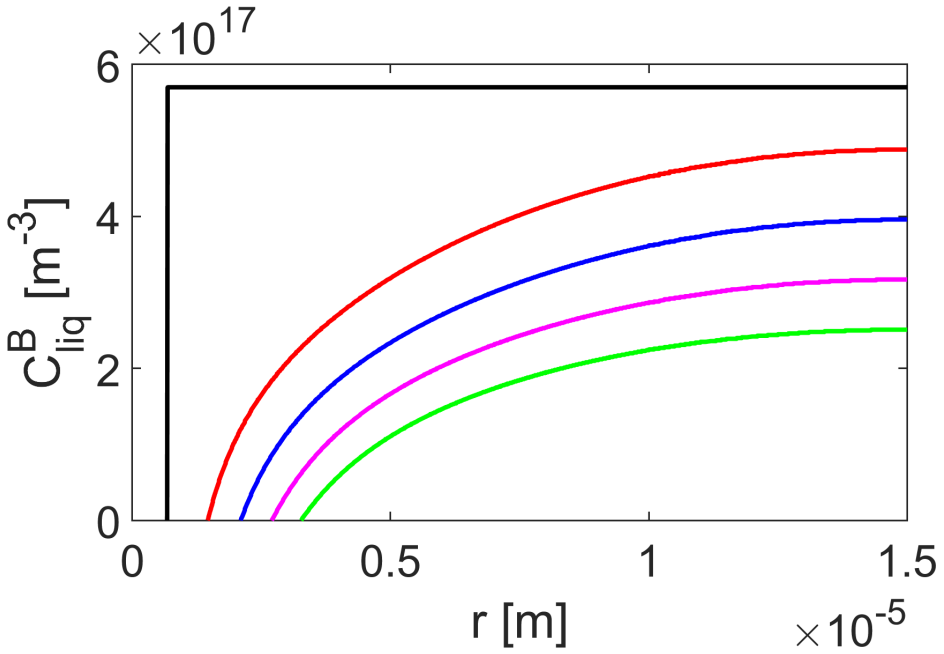

Fig. 8.4 Aggregates concentration profile inside the cytosol at the beginning of the process (black), after 4h (red), 8h (blue), 12h (magenta) and 16h (green).

is solved through the following scheme:

$$\frac{R^{j+1}-R^{j}}{\delta t}=G^{j}\left(R,r,t,C^{C}_{liq},\frac{\partial C^{B}_{liq}}{\partial r}\right). \tag{8.22}$$

This leads to the following final expression

$$R^{j+1}=R^{j}+\left(\frac{D}{q_i}\frac{C^{B}_{liq,i}(n+2)-C^{B}_{liq,i}(n+1)}{\delta r}-\frac{v_r}{q_i}C^{C}_{liq,0}\right)\delta t. \tag{8.23}$$

It is important to stress that a proper time and spatial step need to be chosen in order to obtain reliable results; the final values for δt and δr are proposed in Table 8.2.

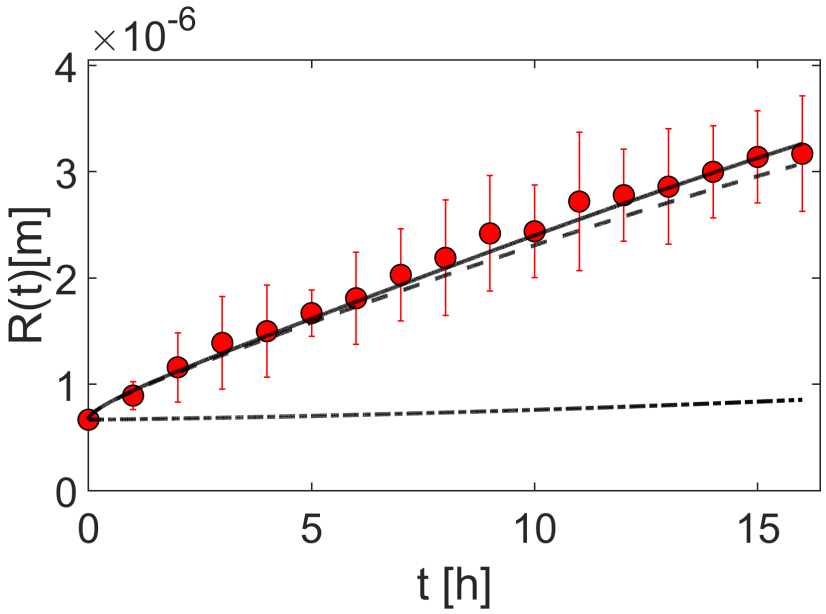

Fig. 8.5 Analysis of the contributions of the diffusive motion (dashed line), active transport (dashed-dot line) and their combined contribution (solid line) to the "aggresome" growth coupled with a comparison to experimental data (red dots and linked error bars).

8.4 Discussion

Plots of the concentration profile C^B_{liq} related to different times of the agglomerate growth are represented in Fig. 8.4. It is useful to remind that the starting point of each line is different because the solid-liquid interface, where the immediate stick condition forces the concentration to be null, is moving towards the external border of the cell because of the growth of the "aggresome" according to Eq.(8.10). Overall it is found that the presence of the aggregates inside the liquid medium decreases consistently with time but, after 16 hours, the cluster concentration is slightly over-estimated, especially in the section closer to the border of the cell. This is justified by the observation of other little "aggresomes" inside the cell which consume extra aggregates, instead one of the hypothesis of the model is the growth of a singular proteinaceous agglomerate near the nucleus of the cell.

Finally, the position of the moving solid-liquid interface calculated by Eq.(8.23), the external border of the growing "aggresome", is proposed compared to experimental data provided by image analysis on the size of the aggresome: the increase of the size depends on the superposition of the Brownian motion and active transport contributions inside the MTOC which are independent from one another. Thanks to this observation it is possible to analyse the two effects separately to check the one with the bigger impact on the "aggresome" self-assembly. Everything is sum up in Fig. 8.5: the model can catch quite accurately the

growing path of the aggresome which has been obtained by experimental data related to 7 different cases. Moreover, it is clear that the diffusion of the aggregates inside the cytosol plays the dominant role in the formation of the aggresome, instead the active transport inside the microtubes is only marginal during this stage since it never intersects neither the lower limit provided by the error bars in Fig. 8.5. This final result finds a good agreement with the experimental analysis which shows the diffusion as the key factor during the final stages of the self-assembly.

Finally, considering the superposition of the effects, an optimal fitting with experimental data from both a quantitative and a qualitative point of view can be seen: this is the indication that without an approach like the one proposed in this chapter, the modelling of the aggregation kinetics inside the aggresome would have been very difficult, if not impossible.

The only negative aspect of the proposed model is the failure to reproduce the plateau observed at the end of the process. This can be explained by the overestimation of the concentration of aggregates inside the cytosol which does not allow the driving force of the matter transport from the bulk to the agglomerate surface to slow down.

Chapter 9

Epilogue

This thesis has addressed several problems concerning the dynamic of colloids. The considered soft matter systems share the pivotal role played by Brownian motion in diverse physico-chemical environments where complex dynamics arises from the interplay between Brownian motion, physico-chemical interactions, and external fields.

The first part of the thesis has focused on the microstructure, that is the spatial arrangement, of hard-spheres dispersions suspended into a fluid under conditions of creeping flow. A new theoretical framework has been proposed which, by analytically solving the 2-Body Smoluchowski equation, studies the microstructure (also named pair correlation function) of strongly sheared suspensions under semi-dilute conditions. The methodology described in chapter 3 foresees the application of an angular average over the compressing and the extensional regions of the flow field generated by the application of an external stress: the final result is the evaluation of two separated solutions, one for each quadrant, which can be determined by the application of a singular perturbation methodology. In particular, the formalism of the obtained solutions indicates that this framework can be considered as an improvement of already existing theories [47, 48]. Chapter 4 is dedicated to the proposal of the results obtained by the theory. It has been first adopted to study the behavior of an hard-spheres suspension: it has been compared to Stokesian dynamics simulations demonstrating that the new analytic framework can capture sufficiently accurately the main features of these physical systems. Next, by showing the quadrant-dependent microstructures it has been showed that the theory can accurately represent the typical anisotropy of strongly sheared conditions characterized by an important difference in the trends the pair correlation function related to the compressing and the extensional regions, a feature which has already been confirmed by experimental works [61] and by running simulations [32].
Next, the work has focused on complex interacting systems by analysing an attractive fluid,

in which the particles interact by a 12-6 Lennard-Jones interaction potential, and a charge stabilized suspension, in which the colloidal particles interact by a Debye-Hückel potential. A new wealth of physical phenomena has been unveiled in case the Peclet number is sufficiently low (Pe = 10): considering the pair correlation function of attractive fluids related to compressing quadrants, the presence of a pronounced depletion effect resulting in a minimum or undershoot in the pcf at separations right after the accumulation peak has been discovered; this effect is already visible at modest values of the attraction energy, and becomes more and more important upon increasing the strength of the inter-particle interactions. Concerning the analysis of the charge-stabilized suspension it has been highlighted that, in the compression sectors, an accumulation peak near contact is visible which can be lowered upon increasing the repulsion parameters of the Debye-Hückel potential. As the Debye length increases a secondary maximum has been discovered: it is the effect of the competition between the advecting action of the flow and the effect of screened electrostatic repulsion. In the extensional sectors, instead, no accumulation peak is visible but there is the occurrence of a depletion layer, where the pair correlation function is identically zero, whose width increases upon increasing either the charge repulsion strength or the Debye length.

The Brownian motion also influences the aggregation behavior of colloidal particles: in chapter 1 it has been showed how the flow rate of Brownian particles colliding with a "stationary" one (not influenced by the jiggling motion) can be used to study the entry and the desorption of radicalic species from particles during an emulsion polymerization. The second part of the thesis has then centred on this particular polymerization procedure: a numerical framework has been developed which is capable of tracking crucial kinetic variables such as the conversion and latex composition. In chapter 6 the full explanation behind the mechanistic aspects of the model are proposed; in particular the kinetics have been described by using the well-known pseudo-homopolymerization approach. In chapter 7 the monitoring of the aforementioned targets has been tested with test cases of increasing difficulty: the simpler ones, a series of homo-polymerizations of n-Butyl Acrylate [121] and one of co-polymerizations of n-BA and MMA [119] have been taken from the literature, meanwhile the third one, a *n*-BA/MMA/2-HEMA terpolymer, has been produced and characterized by Synthomer LTD. Next, the model has been used to study the interplay between the fraction of the surface of the latex actually covered by the emulsifier and the salt content in the formation of undesired coagulum: a higher surface coverage reduces the reactor fouling because of an improved electrostatic stability, but if the salt content is too high then the system becomes unstable leading to a sudden increase of coagulum formation. These are absolutely reasonable and meaningful, but for now the model shows just a qualitative comparison, meanwhile future steps aim to use

this model as a first step towards the building of an industrial software which can quantitatively predict the colloidal stability of the suspension and link it to the formation of coagulum.

Finally, the Brownian motion also plays an important role in studying physical phenomena in biological systems [9], so the third and final part analyses the growth dynamics of a poly-glutamine (Poly-Q) agglomerate, usually named "aggresome", inside a mammalian cell in which the genes related to the Poly-Q have been overexpressed, so that the cytosol has been filled with small proteinaceous aggregates which will be the primary particles constituting the aggresome. The formation and growth of the aggresome is the interplay between the active transport of the aggregates through a spiderweb of microtubes centred on the Microtubes Organized Centre (MTOC) and the diffusion of the primary particles from the cytosol to the growing aggresome; in particular this work will not discuss the formation of the big agglomerate, but it will analyse the later stages of its growth.
Based upon a numerical resolution of the macroscopic version of the Smoluchowski equation, that is the advection-diffusion equation, it has been possible to demonstrate that these later stages are dominated by the diffusion of the small aggregates in the liquid medium, contrarily to what the current theory which supports that the active transport is the most dominant mechanism through the whole formation and growth of the aggresome.

References

[1] R. Brown, *A brief account of microscopical observations made in the months of June, July and August 1827, on the particles contained in the pollen of plants; and on the general existence of active molecules in organic and inorganic bodies*, The Philosophical Magazine **4**(21), 161-173 (1828).

[2] A. Fick, *Uber Diffusion*, Annalen der Physik **170**(1), 59-86 (1855).

[3] A. Einstein, *Investigation on the theory of Brownian Movement*, Translated and reprinted (1956).

[4] M. von Smoluchowski, *Zur kinetischen Theorie der Brownschen Molekular Bewegung und der Suspensionen*, Annalen der Physik **21**, 756-780 (1906).

[5] F.F. Brady, G. Bossis, *Stokesian dynamics*, Annual Review of Fluid Mechanics **20**, 111-157 (1988).

[6] M. von Smoluchowski, *Drei vortrage uber diffusion, brownsche bewegung und koagulation von kolloidteilchen*, Zeitschrift fur Physik **17**, 557-585 (1916).

[7] R.G. Gilbert, *Emulsion polymerization: a mechanistic approach*, Academic Press (1995).

[8] D. Holchman, Z. Schuss, *Stochatic Narrow Escape*, Springer (2015).

[9] D. Holcman, N. Hoze, Z. Schuss, *Analysis and interpretation of superresolution single-particle trajectories*, Biophysical journal **109**(9), 1761-1771 (2015).

[10] M. Lu, N. Williamson, C. Boschetti, T. Ellis, T. Yoshimi, A. Tunnaclife, *Expression-level dependent perturbation of cell proteostasis and nuclear morphology by aggregation-prone polyglutamine proteins*,Biotechnology and bioengineering **112**(9), 1883-1892 (2015).

[11] J.K.G. Dhont, *An Introduction to Dynamics of colloids*, Elsevier (1996).

[12] P. Langevin, *Sur la théorie du mouvement brownien*, Comptes rendus de l'Académie des Sciences **146**, 530-533 (1908).

[13] J. Larsen, *Foundations of High-energy-density Physics: Physical Processes of Matter at Extreme Conditions*, (Cambridge University Press, 2017).

[14] J.P. Hansen, *Statistical mechanics of dense ionized matter. I. Equilibrium properties of the classical one-component plasma* Physical Review A **8**, 3096-3109 (1973).

[15] S. Kim, S.J. Karrila, *Microhydrodynamics: Principles and Selected Applications*, Butterworth-Heinemann (1991).

[16] G.K. Batchelor, *Brownian diffusion of particles with hydrodynamic interaction*, Journal of Fluid Mechanics **74**(1), 1-29 (1976).

[17] H. Brenner, *The slow motion of a sphere through a viscous fluid towards a plane surface*, Chemical Engineering Science **16**, 242-251 (1961).

[18] M. Stimson, G. B. Jeffrey, *The Motion of two spheres in a viscous fluid*, Proceedings of the Royal Society A **22**, 110-116 (1926).

[19] E.P. Honig, G.J.Roebersen, P.H. Wieresema, *Effect of hydrodynamic interaction on the coagulation rate of hydrophobic colloids*, J. Coll. Interface Sci. **36** 97 (1971).

[20] C. Ness, A. Zaccone, *Effect of hydrodynamic interactions on the lifetime of colloidal bonds*, Industrial & Engineering Chemical Research **56**, 3726-3732 (2017).

[21] P.M. Adler, *Interaction of unequal spheres. I. Hydrodynamic interaction: colloidal forces*, Journal of colloidal and interface science **84**, 461-473 (1981).

[22] C.J. Lin, K.J. Lee, N.F. Sather, *Slow motion of two spheres in a shear field* Journal of Fluid Mechanics **43**, 35-57 (1970).

[23] G.K. Batchelor, J.T. Green, *The hydrodynamic interaction of two small freely-moving spheres in a linear flow field*,Journal of Fluid Mechanics **56**, 375-400(1972).

[24] S. Melis, M. Verduyn, G. Storti, M. Morbidelli, J. Baldyga, *Effect of fluid motion on the aggregation of small particles subject to interaction forces*, AlChe Journal **45**, 1383-1393 (1999).

[25] J. F. Morris, B. Katyal, *Microstructure from simulated Brownian suspension flows at large shear rate*, Physics of Fluid **14**, 1920-1937 (2002).

[26] É Guazzelli, J. Morris, S. Pic, *Physical Introduction to Suspension Dynamics* Cambridge University Press (2011).

[27] G.K. Batchelor, *The effect of Brownian motion on the bulk stress of a suspension of spherical particles*, Journal of Fluid Mechanics **83**, 97-117 (1977).

[28] W.B. Russel, A.P. Gast, *Nonequilibrium statistical mechanics of concentrated colloidal dispersions: Hard spheres in weak flows*, The Journal of chemical physics **84**(3), 1815-1826 (1986).

[29] R. A. Lionerger, W.B. Russel, *A Smoluchowski theory with simple approximations for hydrodynamic interactions in concentrated dispersions*, Journal of Rheology **41**(2), 399-425 (1997).

[30] J. F. Brady, *The rheological behavior of concentrated colloidal dispersions*, The Journal of Chemical Physics **99**(1), 567-581 (1993).

[31] R.H. Ottewill, N.S.J. Williams, *Study of particle motion in concentrated dispersions by tracer diffusion*, Nature **325**(6101), 232-234 (1987).

[32] T.N. Phung, *Behaviour of concentrated colloidal dispersions by Stokesian dynamics*. PhD thesis, California Institute of Technology (1993).

[33] E.Nazockdast, J.F. Morris, *Microstructural theory and the rheology of concentrated colloidal suspensions*, Journal of Fluid Mechanics **713**, 420-452 (2012).

[34] A. Rice, J. Lekner, *On the Equation of State of the Rigid-Sphere Fluid*, The Journal of Chemical Physics **42**, 3559-3565 (1965).

[35] J. M. Brader, M. E. Cates, M. Fuchs, *First-Principles Constitutive Equation for Suspension Rheology*, Phys. Rev. Lett. **101**, 138301 (2008).

[36] M. Fuchs and M.E. Cates, *A mode coupling theory for Brownian particles in homogeneous steady shear flows*, J. Rheol. **53**, 957-1000 (2009).

[37] A. Onuki,*Phase Transition Dynamics* Cambridge University Press, (2004).

[38] N. A. Clark and B.J. Ackerson, *Observation of the Coupling of Concentration Fluctuations to Steady-State Shear Flow*, Phys. Rev. Lett. **44**, 1005 (1980).

[39] B.J. Ackerson and N.A. Clark, *Sheared colloidal suspensions*, Physica A **118**, 221 (1983).

[40] D. Ronis, *Theory of fluctuations in colloidal suspensions undergoing steady shear flow*, Phys. Rev. A **29**, 1453 (1984).

[41] B.J. Ackerson, *Shear induced order in equilibirum colloidal liquids*, Physica A **174**, 15-30 (1991).

[42] J.F. Schwarzl and S. Hess, *Shear-flow-induced distortion of the structure of a fluid: Application of a simple kinetic equation*, Phys. Rev. A **33**, 4277 (1986).

[43] J.K.G. Dhont, *On the distortion of the static structure factor of colloidal fluids in shear flow*, Journal of Fluid Mechanics **204**, 421-431 (1989).

[44] J. Blawzdziewicz and G. Szamel, *Structure and rheology of semidilute suspension in shear flow*, Phys. Rev. E **48**, 4632 (1993).

[45] Y.D. Yan, J.K.G. Dhont, *Shear-induced structure distortion in nonaqueous dispersions of charged colloidal spheres via light scattering*, Physica A: Statistical Mechanics and its Applications **198**(1-2), 78-107 (1993).

[46] W. Xue, G.S. Grest, *Brownian dynamics simulations for interacting colloids in the presence of a shear flow*, Physical Review A **40**(3), 1709-1712 (1989).

[47] G. K. Batchelor, J. T. Green, *The determination of the bulk stress in a suspension of spherical particles to order* c^2, Journal of Fluid Mechanics **56**, 401-427 (1972).

[48] J. F. Brady, J. F. Morris, *Microstructure of strongly sheared suspensions and its impact on rheology and diffusion*, Journal of Fluid Mechanics **348**, 103-139 (1997).

[49] J. Bergenholtz, J.F. Brady, M. Vicic, *The non-Newtonian rheology of dilute colloidal suspensions*, Journal of Fluid Mechanics **456**, 239-275 (2002).

[50] S. Chandrasekar, *Stochastic problems in physics and astronomy*, Reviews of Modern Physics **15**(1), 1-89 (1943).

[51] L. A. Spielman, *Viscous Interactions in Brownian Coagulation*, Journal of Colloid and Interface Science **33**, 562-571 (1970).

[52] D.L. Swift, S.K. Friedlander, *The coagulation of hydrosols by Brownian motion and laminar shear flow*, Journal of colloid science **19**(7),621-647 (1977).

[53] T.G.M. Van de Ven, S.G. Mason, *The microrehology of colloidal dispersions VIII. Effect of shear on perikinetic doublet formation.*, Colloid & Polymer Science **255**, 794-804 (1977).

[54] A.Zaccone, H. Wu, D.Gentili, M.Morbidelli, *Theory of activated process under shear with application to shear-induced aggregation of colloids*,Physical Review E **80**, 051404 (2009).

[55] M. Smoluchowski, *Versuch einer Mathematischen Theorie der Koagulationskinetik Kolloider Loesungen*, Z. Phys. Chem **92** 120-168 (1917).

[56] T.G.M. Van de Ven, S.G. Mason, *The microrehology of colloidal dispersions VII. Orthokinetic doublet formation of spheres.*, Colloid & Polymer Science **255**(5), 468-479 (1977).

[57] D.L. Feke, W.R. Schowalter, *The effect of Brownian diffusion on shear-induced coagulation of colloidal dispersions*, Journal of Fluid Mechanics **133**, 17-35 (1983).

[58] C. M. Bender, S.A. Orszag, *Advanced mathematical methods for scientists and engineers I: Asymptotic methods and perturbation theory* (Springer Science & Business Media, New York, 1999).

[59] J.Hinch, *Perturbation methods*, (Cambridge University Press, 1991).

[60] M. Van Dyke, *Perturbation methods in fluid mechanics*, (Parabolic Press, Stanford, 1975).

[61] F. Parsi, F. Gadala-Maria, *Fore-and-Aft Asymmetry in a Concentrated Suspension of Solid Spheres*, Journal of Rheology **31**(8), 725-732 (1987).

[62] M. Cloitre, R. T. Bonnecaze, *A review on wall slip in high solid dispersions*, Rheologica Acta **56**, 283–305 (2017).

[63] P. Chaudhuri, L. Berthier, L. Bocquet, *Inhomogeneous shear flows in soft jammed materials with tunable attractive forces*. Physical Review E **85**, 021503 (2012).

[64] A. Montesi, A.A. Pena, M. Pasquali, *Vorticity alignment and negative normal stresses in sheared attractive emulsions*, Physical Review Letters **92**(5), 058303 (2004).

[65] Z. Varga, J.W. Swan, *Large scale anisotropies in sheared colloidal gels*, Journal of Rheology **62**(2), 405-418 (2018).

[66] Z. Varga, V. Grenard, S. Pecorario, N. Taberlet, V. Dolique, S. Manneville, T. Divoux, G.H. McKinley, J.W. Swan, *Hydrodynamics control shear-induced pattern formation in attractive suspensions*, Proceedings of the National Academy of Sciences **116**(25), 12193-12198 (2019).

[67] Z. Varga, J.W. Swan, *Linear viscoelasticity of attractive colloidal dispersions*, Journal of Rheology **59**(5), 1271-1298 (2015).

[68] S. Asakura, Fumio Oosawa, *Interaction between particles suspended in solutions of macromolecules*,Journal of polymer science **33**(126) 183-192 (1958).

[69] S.R. Rastogi, N.J. Wagner, S.R. Lustig,*Rheology, self-diffusion, and microstructure of charged colloids under simple shear by massively parallel nonequilibrium Brownian dynamics*, The Journal of chemical physics **104**(22), 9234-9248 (1996).

[70] E. Nazockdast, J. F. Morris, *Effect of repulsive interactions on structure and rheology of sheared colloidal dispersions*, Soft Matter **8**, 4223-4234 (2012).

[71] S.O. Yurchenko, *The shortest-graph method for calculation of the pair correlation function in crystalline systems*, The Journal of Chemical Physics **140**, 134502 (2014).

[72] V. Nosenko, A.V. Ivlev, G.E. Morfill, *Microstructure of a Liquid Two-Dimensional Dusty Plasma under Shear*, Physical Review Letters **108**, 135005 (2012).

[73] T. Ott, M. Bonitz, L. G. Stanton, and M. S. Murillo, *Coupling strength in Coulomb and Yukawa one-component plasmas*, Phys. Plasmas **21**, 113704 (2014).

[74] D. Toneian, C. N Likos and G. Kahl, *Controlled self-aggregation of polymer-based nanoparticles employing shear flow and magnetic fields*, J. Phys.: Condens. Matter **31**, 24LT02 (2019).

[75] S.C. Thickett, R.G. Gilbert, *Emulsion polymerization: State of the art in kinetics and mechanisms*, Polymer **48**(24), 6965-6991 (2007).

[76] W.D. Harkins, *A general theory of the mechanism of emulsion polymerization*, Journal of the American Chemical Society **69**(5), 1428-1444 (1947).

[77] W.V. Smith, R.H. Ewart, *Kinetics of emulsion polymerization*, The journal of chemical physics **16**(6), 592-599 (1948).

[78] R.M. Fitch, C.H. Tsai, *Particle formation in polymer colloids, III: Prediction of the number of particles by a homogeneous nucleation theory*, Polymer Colloids, 73-102, Springer (1971).

[79] R.M. Fitch, C.H. Tsai, *Homogeneous nucleation of polymer colloids, IV: the role of soluble oligomeric radicals*, Polymer Colloids, 103-116, Springer (1971).

[80] J. Asua, *Polymer reaction engineering*, John Wiley & Sons (2008).

[81] M. Vanni, G. Baldi, *Coagulation efficiency of colloidal particles in shear flow*,Advances in colloid and interface science **97**(1-3), 151-177 (2002).

[82] D.H. Napper, *Steric stabilization*, Journal of colloid and interface science **58**(2), 390-407 (1977).

[83] R. Hogg, T.W. Healy, D.W. Fuerstenau, *Mutual coagulation of colloidal dispersions*, Transactions of the Faraday society **62**, 1638-1651 (1966).

[84] S.Melis, *A model for the coagulation of polyvinyl acetate particles in emulsion*, Chemical engineering science **55**(16), 3101-3111 (2000).

[85] E. Unzueta, J. Forcada, *Modeling the effect of mixed emulsifier systems in emulsion copolymerization*, Journal of Applied Polymer Science **66**(3), 445-458 (1997).

[86] M.J.J. Mayer, J. Meuldijk, D. Theones, *Dynamic modeling of limited particle coagulation in emulsion polymerization*, Journal of applied polymer science **59**(1), 83-90 (1996).

[87] S. Sajjadi, *Particle formation and coagulation in the seeded semibatch emulsion polymerization of butyl acrylate*, Journal of Polymer Science Part A: Polymer Chemistry **38**(19), 3612-3630 (2000).

[88] J. Šňupárek, *Particle coagulation at semicontinuous emulstion polymerization. I. Some factors affecting the process*, Journal of Applied Polymer Science **24**(4), 909-914 (1979).

[89] A. Zaccone, H. Wu, M. Lattuada, M. Morbidelli, *Charged molecular films on brownian particles: Structure, interactions, and relation to stability*, The Journal of Physical Chemistry B **112**(22), 6793-6802 (2008).

[90] Z. Jia, C. Gauer, H. Wu, M. Morbidelli, A., Chittofrati, M. Apostolo, *A generalized model for the stability of polymer colloids*, Journal of colloid and interface science **302**(1), 187-202 (2006).

[91] L. Ehrl, Z. Jia, H. Wua, M. Lattuada, M. Soos, M. Morbidelli, *Role of counterion association in colloidal stability*, Langmuir **25**(5), 2696-2972 (2009).

[92] S.H. Behrens, D.I. Christl, R. Emmerzael, P. Schurtenberger, M. Borkovec, *Charging and aggregation properties of carboxyl latex particles: Experiments versus DLVO theory*, Langmuir **16**(6), 2566-2575 (2000).

[93] Von Smoluchowski, M.,*Grundriß der Koagulationskinetik Kolloider Losungen*, Kolloid-Zeitschrift und Zeitschrift für Polymere,**21**,98–104 (1917).

[94] T.R. Camp, P.C. Stein, *Velocity gradients and internal work in fluid motion*, Journal of Boston Society Civil Engineering **30**, 219-230 (1943).

[95] A. Matějíček, A. Pivoňková, J. Kaška, P. Ditl, L. Formánek, *Influence of agitation on the creation of coagulum during the emulsion polymerization of the system styrene–butylacrylate–acrylic acid*, Journal of Applied Polymer Science **35**(3), 583-591 (1988).

[96] L.L.M. Krutzer, *The influence of the type of flow on the orthokinetic coagulation rate*, Journal of colloid and interface science **171**(2), 429-438 (1995).

[97] V. Lowry, M.S. El-Asser, J.W. Vanderhoff, A. Klein, C.A. Silebi, *Kinetics of agitation-induced coagulation of high-solid latexes*, Journal of colloid and interface science **112**(2), 521-529 (1986).

[98] M. Zubitur, J.M. Asua, *Factors affecting kinetics and coagulum formation during the emulsion copolymerization of styrene/butyl acrylate*, Polymer **42**(14), 5979-5985 (2001).

[99] *Applications of n-Butyl Acrylate*, https://www.gantrade.com/blog/applications-of-n-butyl-acrylate (2018).

[100] H.M. Vale, T.F. McKenna, *Modeling particle size distribution in emulsion polymerization reactors*, Progress in polymer Science **30**(10), 1019-1048 (2005).

[101] J.B. Rawlings, W.H. Ray, *The modeling of batch and continuous emulsion polymerization reactors. Part I: Model formulation and sensitivity to parameters*, Polymer Engineering & Science **28**(5), 237-256 (1988).

[102] E. Saldivar, P. Dafnotis, W.H. Ray, *Mathematical Modeling of Emulsion Copolymerization Reactors. I. Model Formulation and Application to Reactors Operating with Micellar Nucleation*, Journal of Macromolecular Science, Part C **38**(2), 207-325 (1998).

[103] J. Gao, A. Penlidis, *Mathematical modelling and computer simulator/database for emulsion polymerizations*, Progress in polymer science **27**(3), 403-535.

[104] M.A. Dubé, J.B.P. Soares, A. Penlidis, A.E. Hamielec, *Mathematical modeling of multicomponent chain-growth polymerizations in batch, semibatch, and continuous reactors: a review*, Industrial & engineering chemistry research **36**(4), 966-1015 (1997).

[105] R.D. Sudduth, *A new method to predict the maximum packing fraction and the viscosity of solutions with a size distribution of suspended particles. II*, Journal of applied polymer science **48**(1), 37-55 (1993).

[106] D. Satas, *Handbook of Pressure Sensitive Adhesive Technology*, 2nd Edition Van Nostrand Reinhold, New York (1989).

[107] C. Plessis, G. Arzamendi, J.R. Leiza, H.A.S. Schoonbrood, D. Charmot, J.M. Asua, *Kinetics and Polymer Microstructure of the Seeded Semibatch Emulsion Copolymerization of n-Butyl Acrylate and Styrene*, Macromolecules **34**(15), 5147-5157. (2001).

[108] Lee, D.I. In J.M. Asua (ed.), *Polymeric Dispersions: Principles and Applications*. Kluwer Academic Publishers, Dordrecht, pp. 497–513 (1997).

[109] J.L. Gardon, *Emulsion polymerization. II. Review of experimental data in the context of the revised Smith-Ewart theory*, Journal of Polymer Science Part A-1: Polymer Chemistry **6**(3), 643-664 (1968).

[110] X.S. Chai, F.J. Schork, A. DeCinque, K. Wilson, *Measurement of the solubilities of vinylic monomers in water*, Industrial & engineering chemistry research **44**(14), 5256-5258 (2005).

[111] F. Khan, S.R. Ahmad, *Graft copolymerization and characterization of 2-hydroxyethyl methacrylate onto jute fiber by photoirradiation*, Journal of applied polymer science **101**(5), 2898-2910 (2006).

[112] L.M. Gugliotta, G. Arzamendi, J.M. Asua, *Choice of monomer partition model in mathematical modeling of emulsion copolymerization systems*, Journal of applied polymer science **55**(7), 1017-1039 (1995).

[113] H.H. Chu, E.D. Ou, *Emulsion polymerization of 2-hydroxyethyl methacrylate and partition of monomer between particles and water phase*, Polymer Bulletin **44**(3), 337-344 (2000).

[114] I.M. Boristov, R.S. Luksha, S.T. Rashidova, *Kinetic features of ammonium persulfate decomposition in aqueous medium*, Russian Chemical Bulletin International Edition **64**(10), 2512-2513 (2015).

[115] S. Beuermann, M. Buback, *Rate coefficients of free-radical polymerization deduced from pulsed laser experiments*, Progress in Polymer Science **27**(2), 191-254 (2002).

[116] C. Plessis, G. Arzamendi, J.M. Alberdi, A.M. Van Herk, J. Leiza, J.M. Asua, *Evidence of Branching in Poly (butyl acrylate) Produced in Pulsed-Laser Polymerization Experiments*, Macromolecular rapid communications **24**(2), 173-177 (2003).

[117] J. Barth, M. Buback, P. Hesse, T. Sergeeva, *Termination and transfer kinetics of butyl acrylate radical polymerization studied via SP-PLP-EPR*, Macromolecules **43**(9), 4023-4031 (2010).

[118] D.S. Achilias, P.I. Siafaka, *Polymerization kinetics of poly (2-hydroxyethyl methacrylate) hydrogels and nanocomposite materials*, Processes **5**(2) 21 (2017).

[119] O. Elizalde, G. Arzamendi, J.R. Leiza, J.M. Asua, *Seeded semibatch emulsion copolymerization of n-butyl acrylate and methyl methacrylate*, Industrial & engineering chemistry research **43**(23), 7401-7409 (2004).

[120] I.K. Varma, S. Patniak, *Copolymerization of 2-hydroxyethyl methacrylate with alkyl acrylates*, European Polymer Journal **12**(4), 259-261 (1976).

[121] C. Plessis, G. Arzamendi, J.R. Leiza, H.A.S. Schoonbrood, D. Charmot, J.M. Asua, *Modeling of seeded semibatch emulsion polymerization of n-BA*, Industrial & engineering chemistry research **40**(18), 3883-3894 (2001).

[122] J. Barth, M. Buback, *SP–PLP–EPR Investigations into the Chain-Length-Dependent Termination of Methyl Methacrylate Bulk Polymerization*, Macromolecular rapid communications **30**(21), 1805-1811 (2009).

[123] S. Maeder, R.G. Gilbert, *Measurement of transfer constant for butyl acrylate free-radical polymerization*, Macromolecules **31**(14), 4410-4418 (1998).

[124] M. Stickler, G. Meyerhoff, *Die thermische polymerisation von methylmethacrylat, 1. Polymerisation in substanz*, Die Makromolekulare Chemie: Macromolecular Chemistry and Physics **179**(11), 2729-2745 (1978).

[125] D.F. Sangster, J. Feldthusen, J. Strauch, C.M. Fellows, *Measurement of Transfer Coefficients to Monomer for n-Butyl Methacrylate by Molecular Weight Distributions from Emulsion Polymerization*, Macromolecular Chemistry and Physics **209**(15), 1612-1627 (2008).

[126] G. Storti, S. Carrà, M. Morbidelli, G. Vita, *Kinetics of multimonomer emulsion polymerization. The pseudo-homopolymerization approach*, Journal of applied polymer science **37**(9), 2443-2467 (1989).

[127] L. Hlalele, B. Kluperman, *In situ NMR and modeling studies of nitroxide mediated copolymerization of styrene and n-butyl acrylate*,Macromolecules **44**(17), 6683-6690 (2011).

[128] L. Hlalele, B. Kluperman, *Reversible nitroxide trapping of the mid-chain radical in n-butyl acrylate polymerization*, Macromolecules **44**(17), 5554-5557 (2011).

[129] A. Ghielmi, D. Cuccato, G. Storti, *Particle state dependent radical desorption and its effect on the kinetics of emulsion polymerization*, Industrial & Engineering Chemistry Research **53**(22), 9049-9057 (2014).

[130] I.A. Maxwell, D.H. Napper, R.G. Gilbert, *Emulsion polymerization of butyl acrylate. Kinetics of particle growth*, Journal of the Chemical Society, Faraday Transactions 1: Physical Chemistry in Condensed Phases **83**(5), 1449-1467 (1987).

[131] M.J. Ballard, D.H. Napper, R.G. Gilbert, *Kinetics of emulsion polymerization of methyl methacrylate*, Journal of Polymer Science: Polymer Chemistry Edition **22**(11), 3225-3253 (1984).

[132] I.A. Maxwell, B.R. Morrison, D.H. Napper, R.G. Gilbert, *Entry of free radicals into latex particles in emulsion polymerization*, Macromolecules **24**(7), 1629-1640 (1991).

[133] M. Morbidelli, G. Storti, S. Carrà, *Role of micellar equilibria on modelling of batch emulsion polymerization reactors*, Journal of Applied Polymer Science **28**(3), 901-919 (1983).

[134] R.X.E. Willemse, A.M. Van Herk, E. Panchenko, T. Junkers, M. Buback, *PLP- ESR Monitoring of Midchain Radicals in n-Butyl Acrylate Polymerization*, Macromolecules **38**(12), 5098-5103 (2005).

[135] M. van der Linden, B. O Conchúir, E. Spigone, A. Niranjan, A. Zaccone, P. Cicuta, *Microscopic origin of the Hofmeister effect in gelation kinetics of colloidal silica*, The journal of physical chemistry letters **6**(15), 2881-2887 (2015).

[136] A. Zaccone, H. Wua, D. Gentili, M. Morbidelli, *Theory of activated-rate processes under shear with application to shear-induced aggregation of colloids* Physical Review E **80**(5), 051404 (2009).

[137] F. Khalili-Araghi, J. Gumbart, P.C. Wen, M. Sotomayor, E. Tajkhorshid, K. Schulten, *Molecular dynamics simulations of membrane channels and transporters*, Current Opinion in Structural Biology **19**, 128-137 (2009).

[138] V. Daggett, *Molecular dynamics simulations of the protein unfolding/folding reaction*, Accounts of chemical research **35**(6), 422-429 (2002).

[139] A. Das, C. Mukhopadhyay, *Application of principal component analysis in protein unfolding: An all-atom molecular dynamics simulation study*, The journal of chemical physics **127**(16), 10B625 (2007).

[140] J.A. Johnston, C.L. Ward, R.R. Kopito,*Aggresomes: a cellular response to misfolded proteins*, The Journal of cell biology **143**(7), 1883-1898 (1998).

[141] J.P. Taylor, F. Tanaka, J. Robitschek, C.M. Sandoval, A. Taye, S. Markovic-Plese, K.H. Fischbeck, *Aggresomes protect cells by enhancing the degradation of toxic polyglutamine-containing protein*, Human molecular genetics **12**(7), 749-757 (2003).

[142] M. Lu, C. Boschetti, A. Tunnacliffe, *Long term aggresome accumulation leads to DNA damage, p53-dependent cell cycle arrest, and steric interference in mitosis*, Journal of Biological Chemistry **290**(46) 27986-28000 (2015).

[143] M. Lu, L. Banetta, L.J. Young, E.J. Smith, G.P. Bates, A.Zaccone, G.S. Schierle-Kaminskim C.F. Kaminski, *Live-cell super-resolution microscopy reveals a primary role for diffusion in polyglutamine-driven aggresome assembly*, Journal of Biological Chemistry **294**(1) 257-268 (2019).

[144] V. Alexiades and A.D. Solomon. *Mathematical Modelling of Melting and Freezing Processes*. Hemisphere Publishing Corporation, Washington (1993).

[145] C.M. Sorensen, *Light Scattering by Fractal Aggregats: A Review*, Aerosol Science & Technology **36**(2), 648-687 (2001).

[146] V. Foderá, A. Zaccone, M. Lattuada, A.M. Donald, *Electrostatics Controls the Formation of Amyloid Superstructures in Protein Aggregation*, Physical Review Letters **111**, 108105 (2013).

[147] C.R. Wilke, P. Chang, *Correlation of diffusion coefficients in dilute solutions*, AIChE journal **1**(2), 264-270 (1955).

[148] *Viscosity of Water*, https://www.engineersedge.com/physics/water__density_viscosity_specific_weight_13146.html.

[149] *Polymer Database*, https://polymerdatabase.com.

Appendix A

Supporting information of Part I

A.1 Derivation of the Einstein's diffusion equation

Starting from Eq.(1.3) Einstein expanded the left hand side (LHS) in Taylor series with respect to the observation time τ and the right hand side (RHS) with respect to the displacement Δ, under the hypothesis that they are sufficiently small:

$$C(x,t)+\tau\frac{\partial C}{\partial t}+...=\int_{-\infty}^{\infty}\left(C(x,t)+\frac{\partial C}{\partial x}\Delta+\frac{\partial^2 C}{\partial x^2}\frac{\Delta^2}{2}+...\right)Q(\Delta)d\Delta+...= \\ =C(x,t)\int_{-\infty}^{\infty}Q(\Delta)d\Delta+\frac{\partial C}{\partial x}\int_{-\infty}^{\infty}\Delta Q(\Delta)d\Delta+\frac{\partial^2 C}{\partial x^2}\int_{-\infty}^{\infty}\frac{\Delta^2}{2}Q(\Delta)d\Delta+... \quad \text{(A.1)}$$

From the properties of the probability Δ proposed here in Eq.(A.2)

$$\int_{-\infty}^{\infty}\phi(\Delta)d\Delta=1 \qquad \phi(\Delta)=\phi(-\Delta) \quad \text{(A.2)}$$

it follows that

$$\int_{-\infty}^{\infty}\Delta^{2n+1}Q(\Delta)d\Delta=0 \quad \forall n\in N^{+} \quad \text{(A.3)}$$

which means that Eq.(A.1) can be simplified as

$$C(x,t)+\tau\frac{\partial C}{\partial t}+...=C(x,t)\cdot 1+\frac{\partial^2 C}{\partial x^2}\int_{-\infty}^{\infty}\frac{\Delta^2}{2}Q(\Delta)d\Delta+... \quad \text{(A.4)}$$

At this point, by imposing the correlation between the diffusion coefficient and the displacement provided in Chapter 1, Eq.(1.4), it Eq.(A.4) becomes Fick's second law of diffusion:

$$\frac{\partial C}{\partial t}=D_0\frac{\partial^2 C}{\partial x^2}. \quad \text{(A.5)}$$

A.2 Stokes-Einstein-Smoluchowski correlation

In the first section of the same work Einstein studied the Brownian motion of a suspension of N particles contained in a volume V (which means $C = N/V$); he assumed that in conditions of thermodynamic equilibrium the diffusion is regulated by an equilibrium between the variation of osmotic pressure derived by a concentration gradient and the viscous force acting on the particles themselves:

$$\mathbf{F}^{\text{visc}}C = Z\mathbf{v}C = \frac{\partial P}{\partial x}, \tag{A.6}$$

where $Z = 6\pi\eta R_P$ is recalled to be the Stokes friction coefficient.
If the osmotic pressure is expressed according to the well known formula derived for the first time by Van't Hoff (formally identical to the law of perfect gases)

$$P = k_B T C \rightarrow \frac{\partial P}{\partial x} = k_B T \frac{\partial C}{\partial x} \tag{A.7}$$

and replace the definition of the pressure gradient in Eq.(A.6), we obtain

$$\mathbf{F}^{\text{visc}}C = k_B T \frac{\partial C}{\partial x} \tag{A.8}$$

Einstein noted that the ratio $\mathbf{F}^{\text{visc}}C/Z$ has as dimension [#particles/(m^{2}s)]; basically it is a flux, so he related it to the concentration gradient according to Fick's first law:

$$\frac{\mathbf{F}^{\text{visc}}C}{Z} = D_0 \frac{\partial C}{\partial x} \rightarrow \mathbf{F}^{\text{visc}}C = D_0 Z \frac{\partial C}{\partial x}. \tag{A.9}$$

Finally, by comparing the second term Eq.(A.9) with its equivalent in Eq.(A.8), it is possible to extract the Stokes-Einstein-Smoluchowski correlation:

$$D_0 = \frac{k_B T}{6\pi\eta R_P} \tag{A.10}$$

A.3 Development of the calculations of Section 2.1

In order to continue the calculations on Eq.(2.14) it is necessary to express al the quantities in a *super-vector notation* which means expressing all the vectors as follows:

$$\begin{cases} \mathbf{r} = (\mathbf{r}_1, ..., \mathbf{r}_N) \\ \mathbf{p} = (\mathbf{p}_1, ..., \mathbf{p}_N) \\ \mathbf{F}_{\mathrm{Br}} = (\mathbf{F}_{\mathrm{Br},1}, ..., \mathbf{F}_{\mathrm{Br,N}}) \\ \nabla_{\mathbf{r}} U(\mathbf{r}) = (\nabla_{\mathbf{r}_1} U(\mathbf{r}_1, ..., \mathbf{r}_N), ..., \nabla_{\mathbf{r}_N} U(\mathbf{r}_1, ..., \mathbf{r}_N)) \end{cases} \tag{A.11}$$

and the friction matrix is now introduced as

$$\underline{\mathbf{Z}} = \begin{bmatrix} \underline{\mathbf{Z}}_{11} & \underline{\mathbf{Z}}_{12} \cdots \underline{\mathbf{Z}}_{1N} \\ \underline{\mathbf{Z}}_{21} & \underline{\mathbf{Z}}_{22} \cdots \underline{\mathbf{Z}}_{2N} \\ \vdots & \vdots \quad \vdots \\ \underline{\mathbf{Z}}_{N1} & \underline{\mathbf{Z}}_{N2} \cdots \underline{\mathbf{Z}}_{NN} \end{bmatrix} \tag{A.12}$$

According to the following notation Eq.(2.14) can be rewritten as:

$$0 = -\underline{\mathbf{Z}} \cdot \frac{\mathbf{p}}{M} - \nabla_{\mathbf{r}} U(\mathbf{r}) + \mathbf{F}_{\mathrm{Br}}. \tag{A.13}$$

Since $\underline{\mathbf{Z}}$ is invertible it is possible to rearrange the previous equation as

$$\mathbf{p}/M = \underline{\mathbf{Z}}^{-1} \cdot \left(-\nabla_{\mathbf{r}} U(\mathbf{r}) + \mathbf{F}_{\mathrm{Br}} \right). \tag{A.14}$$

Introducing the Stokes-Einstein correlation it is possible to rewrite Eq.(A.14) as

$$\mathbf{p}/M = \beta \underline{\mathbf{D}} \cdot \left(-\nabla_{\mathbf{r}} U(\mathbf{r}) + \mathbf{F}_{\mathrm{Br}} \right), \tag{A.15}$$

from which Eq.(2.14) in the main text is obtained.

A.4 Gauge functions used in Sections 3.4.1

The 12-6 LJ interaction potential after the application of the inner transformation Eq.(3.40) becomes

$$\tilde{U} = \tilde{U}_{\min} \left((\xi \delta(\varepsilon) + \tilde{r}_c)^{-12} - (\xi \delta(\varepsilon) + \tilde{r}_c)^{-6} \right). \tag{A.16}$$

and previous equation can be differentiate with respect to ξ obtaining:

$$\begin{cases} \dfrac{\mathrm{d}\tilde{U}}{\mathrm{d}\xi} = \tilde{U}_{\min}\delta(\varepsilon)\left[\dfrac{-12}{(\xi\delta(\varepsilon)+\tilde{r}_c)^{13}} + \dfrac{6}{(\xi\delta(\varepsilon)+\tilde{r}_c)^{7}}\right] = \delta(\varepsilon)W(\xi) \\ \dfrac{\mathrm{d}^2\tilde{U}}{\mathrm{d}\xi^2} = \tilde{U}_{\min}\delta(\varepsilon)^2\left[\dfrac{156}{(\xi\delta(\varepsilon)+\tilde{r}_c)^{14}} - \dfrac{42}{(\xi\delta(\varepsilon)+\tilde{r}_c)^{8}}\right] = \delta(\varepsilon)^2X(\xi). \end{cases} \tag{A.17}$$

Applying the same procedure to the Debye-Hückel potential

$$\tilde{U}(\xi) = \frac{\exp(-\kappa(\xi\delta+\tilde{r}_c+))\lambda}{\xi\delta+\tilde{r}_c} \tag{A.18}$$

it is possible to obtain the same gauge functions obtained for the 12-6 LJ potential:

$$\begin{cases} \dfrac{\mathrm{d}\tilde{U}}{\mathrm{d}\xi} = \delta(\varepsilon)\left[-\dfrac{\exp(-\kappa(\xi\delta+\tilde{r}_c))\lambda}{(\xi\delta+\tilde{r}_c)^2} - \dfrac{\exp(-\kappa(\xi\delta+\tilde{r}_c))\kappa\lambda}{\xi\delta+\tilde{r}_c}\right] = \delta(\varepsilon)W(\xi); \\ \dfrac{\mathrm{d}^2\tilde{U}}{\mathrm{d}\xi^2} = \delta^2(\varepsilon)\left[\dfrac{2\exp(-\kappa(\xi\delta+\tilde{r}_c))\lambda}{(\xi\delta+\tilde{r}_c)^3} + \dfrac{2\exp(-\kappa(\xi\delta+\tilde{r}_c))\kappa\lambda}{(\xi\delta+\tilde{r}_c)^2} + \right. \\ \left. + \dfrac{\exp(-\kappa(\xi\delta+\tilde{r}_c))\kappa^2\lambda}{\xi\delta+\tilde{r}_c}\right] = \delta(\varepsilon)^2X(\xi). \end{cases} \tag{A.19}$$

Appendix B

Supporting Information of Part II

B.1 Evaluation of the diffusion coefficents of the monomers in water

As mentioned in the main text the evaluation of the diffusion coefficients $D_{w,j}$ in water has been carried on by applying the Wilke-Chang equation [147]:

$$D_{w,j}\ [m^2 s^{-1}] = \frac{1.173\ 10^{-13}(\phi M_{w,s})^{0.5} T}{\mu_w V_{M,j}^{0.6}}. \tag{B.1}$$

In particular $V_{M,j}$ is the molar volume of the monomer, T the temperature which has been fixed to be 348 K for all the scenarios, ϕ is a coefficient specific for the solvent, $M_{w,s}$ its molecular mass and μ_w its viscosity which has been evaluated according to the following empirical law [148]:

$$\mu[\text{mPa s}] = 2.414\ 10^{-2} 10^{[247.8/(T[K]-140)]}. \tag{B.2}$$

Property	Value
T	348
ϕ	2.6
$M_{w,s}$	18 [g mol^{-1}]
$V_{M,BA}$ [149]	0.1187 [m^3 kmol^{-1}]
$V_{M,MMA}$ [149]	0.087 [m^3 kmol^{-1}]
$V_{M,STY}$ [149]	0.0992 [m^3 kmol^{-1}]

Table B.1 Input data for Eq.(B.1).

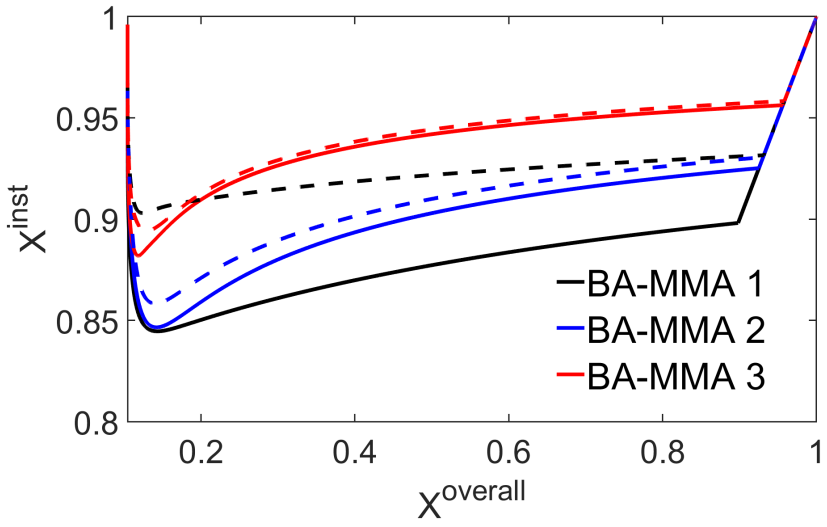

Fig. B.1 Plots of Instantaneous vs Overall conversion for the co-polymerization test cases considering (solid lines) and neglecting (dashed lines) the presence of tertiary radicals in the reacting scheme.

The remaining input data are proposed in Table B.1. In order to test the reliability of the methodology it has been decided to use Eq.(B.1) to calculate the diffusion coefficient of styrene at T = 323 K and compare it to literature data: it has emerged that $D_{w,STY} = 1.81\ 10^{-9}\ m^2s^{-1}$ which is sufficiently similar to the value $D_{w,STY} = 1.3\ 10^{-9} m^2s^{-1}$ found in [7].

B.2 Impact of the backbiting on the kinetic variables of BA/MMA copolymerizations

This small section has then the intent of analysing the effect provided by the backbiting on the three test cases considered for the co-polymerizations.
The absence of MCRs in the particle phase has been simulated by imposing $k_{fp,2} = 0$, meanwhile in the aqueous phase their presence has been neglected by considering $k_{t,w}^{BA} = k_{t,11}$ (it is not an adjustable parameter anymore).
In Fig.B.1 it can be seen that there is an important difference between neglecting and considering the presence of MCRs for BA-MMA 1 only in which the mole fraction of methyl methacrylate is 0.1, meanwhile there is a very small difference on the trends related to BA-MMA 2 and BA-MMA 3, where the mole fraction of MMA is 0.3 and 0.5 respectively. By analysing the pieces of literature which focus on the role of the backbiting in co-polymerizations [127, 128] it emerges that the experimental data, which have been gath-

ered from a *n*-BA/styrene copolymer, have been obtained by considering a minimal mole fraction of styrene of 0.3, the lower limit for which the model provides with almost identical results considering or neglecting the presence of tertiary radicals.
Concluding, the data reveal that the backbiting and the mid-chain radicals still play an important role in the polymerization kinetics of a copolymer involving really high mole fractions of n-Butyl Acrylate, meanwhile its effect can be neglected in case of mole fraction of the second monomer higher than 0.3 as it has been demonstrated experimentally.

B.3 Polymerization procedure

B.3.1 Materials

n-Butyl acrylate (Arkema), Methyl methacrylate (Dow) and 2-HydroxyEthyl Methacrylate (Dow) have been used as monomers, a sodium salt (Univar) and an ammonium salt (Univar) have been used as initiators, meanwhile a carboxylate salt of potassium (Synthomer LTD) has been used as surfactant and ammonia (Univar) as the buffer solution; every material has been used as received. We can not disclose the exact composition of the surfactant for proprietary reasons. All industrial runs have been conducted using de-ionized water.

B.3.2 Polymerization process

The industrial test cases were carried out in a 1 m^3 mechanically stirred reactor. First, the temperature of the reactor is raised to 350 K by an external coil where steam is injected. The seeds (solids content = 30% with different particle sizes $R^0_{p,i}$) has then been loaded followed by a shot of the sodium salt (Initiator A). Immediately thereafter, a stream of pre-emulsified monomers together with the surfactant and a second stream containing the ammonium salt (Initiator B) has been slowly added for about 270 minutes; this interval of time will be referred to subsequently as "*feed additions*". During the feed additions, the reactor was cooled down by flushing water in the coil in order to maintain the temperature at the desired value. The rotational speed of the impeller is increased during this interval from 40 to 60 rpm to guarantee a proper mixing, which is hindered during the polymerization by the increase of the solids content. Moreover, a series of shots of ammonia has been added during the feed additions in order to maintain the pH as alkaline as possible to facilitate post-processing treatments. At the end of the polymerization, a final shot of buffer solution is added after 90 minutes from the end of the feed additions.

B.4 Latex characterizations

A series of samples has been collected during the feed additions and a final one at the end of the polymerization.

B.4.1 Free monomer evaluation

The amount of free monomer contained in every sample has been measured by *Gas Chromatography* using a Shimadzu 2010 gas chromatograph and AOC 6000 auto sampler together with a FID detector; the author here acknowledges the help from Christopher Davis and Lawrence Cook at Synthomer Limited pilot plant in Stallingborough who carried on the experimental evaluations. From this procedure the concentration of free monomer [FM] (expressed in PPM) inside the sample could be measured which, under the condition of perfect mixing, we have associated to the experimental overall conversion $X_{\text{exp}}^{\text{overall}}$ as:

$$X_{\text{exp}}^{\text{overall}} = \frac{(\sum_{i=1}^{N_m} m_i^t) - [\text{FM}]\ 10^{-6}\ m_{\text{system}}}{\sum_{i=1}^{N_m} m_i^{\text{tot}}}, \tag{B.3}$$

where m_{system} is the overall mass contained inside the reactor.

B.4.2 Particle size evaluation

The average particle sizes have been evaluated through *Dynamic Light Scattering* (DLS) using a Malvern ZetaSizer. The measurements involving IC 2, IC 3 and IC 4 have been carried out at the pilot plant in Stallingborough, meanwhile particle sizes related to IC 1 have been measured by the author at the department of Chemical Engineering & Biotechnology. Since the solid content in the samples is really high (up to 50%) the measurements can not be run after sampling, but a procedure of successive dilutions is requested: a predefined volume is taken from each intermediate and it is diluted in a certain amount of water (Round 1). The series of successive dilutions foresees the gathering of a certain sample from the previous round and dilute it with an ulterior predefined volume of water which will constitute the following round; the complete series is proposed in Table B.2. In this way it is possible to obtain a good quality of the signal from the DLS in order to achieve reliable values of particle size which have been proposed in Fig.7.9.
It is also possible to demonstrate that the original hypothesis of monodispersity of the population of particles is actually valid by proposing in Table B.3 the Polydispersity Index (PDI) for IC 1 and IC 3: since the values have an order of magnitude of 10^{-2} it has been demonstrated that all of the particles have basically the same particle size.

Round	Sample [ml]	Water [ml]
1	1	5
2	0.5	5
3	0.25	5
4	0.25	5

Table B.2 Volumes of samples and water adopted in the successive dilutions.

Time [min]	IC 1	IC 3
30	0.025	0.02
120	0.042	0.002
150	0.025	0.016
210	0.048	0.015
345	0.036	0.053

Table B.3 Temporal trend of Polydispersity Indexes for IC 1 and IC 3 with time = 0 set as the beginning of the monomers' additions.

B.4.3 Grit analysis

Finally, concerning the grit analysis, a certain mass m_s has been gathered from each sample which has been filtered through a disposable sieve with empty mass m_0 and a cutoff size of 45 μm. Afterwards the sieves were dried at 80° for 10 minutes to eliminate any remaining liquid and, finally, they were weighted a second time m_f. The amount of coagulated colloid, expressed in PPM, has been measured as follows:

$$\text{PPM}\left(\frac{\text{mg}}{\text{Kg}}\right) = \frac{m_f - m_0}{m_{\text{sample}}}\ 10^6 \tag{B.4}$$